wind turbine aerodynamics in yaw

unravelling the measured rotor wake

wind turbine
aerodynamics in yaw
unravelling the measured rotor wake

PROEFSCHRIFT

ter verkrijging van de graad van doctor
aan de Technische Universiteit Delft,
op gezag van de Rector Magnificus Prof. ir. K.C.A.M. Luyben,
voorzitter van het College voor Promoties,
in het openbaar te verdedigen
op woensdag, 21 september 2011 om 12.30 uur
door

Wouter Haans

ingenieur luchtvaart en ruimtevaart
geboren te Haaren.

Dit proefschrift is goedgekeurd door de promotoren:

Prof. dr. ir. G.A.M. van Kuik
Prof. dr. G.J.W van Bussel

Samenstelling promotiecommissie:

Rector Magnificus	voorzitter
Prof. dr. ir. G.A.M. van Kuik	Technische Universiteit Delft, promotor
Prof. dr. G.J.W van Bussel	Technische Universiteit Delft, promotor
Prof. dr. ir. drs. H. Bijl	Technische Universiteit Delft
Prof. dr. ir. H. Hoeijmakers	Universiteit Twente
Prof. C.P. van Dam, B.S., M.S., D.Engr	University of California, Davis
R. Mikkelsen, MSc. PhD.	Technical University of Denmark
Ir. G.J. Schepers	Energy Research Centre of The Netherlands ECN

To Irene, for her patience, support and love

Summary

Wind energy currently provides a modest contribution to the global energy mix. Growth of the wind energy piece is driven by its Cost of Energy CoE, relative to other means of producing energy. Fundamental research and technology development have been demonstrated to substantially reduce CoE from wind. Improved technology is still anticipated to lower CoE, one of the keys being better rotor aerodynamics modeling.

The Blade Element Momentum BEM model couples an airfoil model to steady, one-dimensional inviscid actuator disc theory. Empirical models fix the code when conditions violate original assumptions; with the rotor misaligned to the flow, i.e. in yaw, actuator disc theory is e.g. replaced with the Glauert momentum equation. Its low computational demand makes BEM codes better suited then more advanced aerodynamic methods to integrate into aero-servo-elastic models. Industry thus uses BEM codes to compute the loads needed for component design.

Wind tunnel tests on model rotors illustrate the substantial modeling uncertainty of BEM codes. Whilst even axial flow conditions are nontrivial to model, uncertainties are particularly large in yaw. Navier-Stokes models tend to be more accurate, but their prohibitive computational demand renders Navier-Stokes based aero-servo-elastic tools impractical in an industry setting.

BEM modeling uncertainty impacts the required structural margins of the turbine and hence CoE. To reduce modeling uncertainty, wind tunnel tests on model rotors study fundamental rotor aerodynamic phenomena. In light hereof, this thesis addresses experimental rotor aerodynamics in yaw, aiming:

- to quantify the effects of experimentally observed yaw misalignment on rotor inflow and blade loads

- to identify the aerodynamic mechanisms governing the effects of yaw misalignment on rotor inflow and blade loads

- to assess the validity of semi-empirical submodels that are used to patch BEM theory in yaw; unsteady airfoil models, the Glauert momentum equation, induction non-uniformity corrections

An experimental campaign is run in an open jet wind tunnel at the TUDelft on a $1.2m$ diameter model rotor with two nontapered, twisted blades. A suite of measurements is performed in yaw and the reference axial flow state;

- rotor thrust recordings with strain gauges in the blade root

- quantitative flow visualization in the wake with smoke to measure tip vortex paths up to about $1R_t$ downstream, with R_t the rotor radius

- flow visualization on the blades with tufts to identify unsteady flow separation across the span in yaw

- three-dimensional flow velocity measurements at three near-wake planes with single-sensor hot-film Constant Temperature Anemometry CTA

All measurements are unsteady and are reduced to Phase Locked Average PLA data. Furthermore, a detailed measurement uncertainty analysis is presented for each experimental technique and wind tunnel wall corrections are methodically quantified; both analyzes yield satisfactory results.

Traditional data reduction for single-sensor CTA PLA data only solves for the magnitudes of the three PLA flow velocity components; the experimenter must explicitly specify the direction. Especially in yaw, this would not be a trivial task. A novel CTA data reduction technique is therefore proposed that implicitly derives both magnitude and direction of the three-dimensional PLA flow velocity. Its capabilities are confirmed in a comparison with Navier-Stokes wake modeling , making it the preferred data reduction technique in yaw.

First, axial flow is studied, as this forms the reference for yaw. Measured rotor thrust coefficient C_T, tip vortex paths and near-wake flow velocity generally comply with published experiments and theory. Recorded C_T matches that found from the one-dimensional inviscid actuator disc model, the latter using rotor inflow that is linearly extrapolated from the near-wake measurements. This model forms the momentum part of BEM in axial flow.

In yaw, measured flow features are typical for misalignment. Tip vortex paths demonstrate wake skewness, the near-wake flow velocity is distributed asymmetrically across the measurement planes and C_T reduces with increased yaw angle. To the author's knowledge, this experiment is the first to record PLA three-dimensional flow velocity in the skewed near-wake and the EU-funded MEXICO project is the only alternative source.

Quantification of the experimental inflow *at* the rotor plane is pivotal to achieve the objectives of this thesis. The measurements clearly demonstrate the nonlinear downwind convection of the skewed wake. Linearly extrapolating the measured near-wake velocity to derive the inflow at the rotor plane would thus be inappropriate. A further challenge towards meeting the objectives is the lack of measured sectional loads, due to model restrictions.

Both inflow and loads are addressed through the development of a physics based measurement analysis tool. This inverse vortex wake model reconstructs the wake vortex geometry from measurements, uses conservation of circulation and the Biot-Savart law to relate measured induced velocity with unknown bound circulation and solves the system of equations for the latter. Airfoil tables are not needed, loads are estimated instead using the Kutta-Joukowsky law, where required inflow and bound circulation are both derived from the inverse vortex wake model. Earlier TUDelft studies lay the foundation of present model, where the most notable improvement is the extension from axial into yawed flow. Model verification and validation are completed successfully.

The thesis aims to base BEM model validation (objective 3) on the experimental findings of the phenomena governing yawed rotor aerodynamics (objective 2). The analyzes with the inverse vortex wake model are thus performed in the context of BEM theory.

The analyzes focus on three items; unsteady blade aerodynamics and resulting loads, the relation between C_T and induced axial flow at the rotor plane and the mechanisms driving the unsteady inflow at the blade. From the BEM perspective, this translates to validating unsteady airfoil models, the Glauert momentum model and induction factor non-uniformity corrections. The axial and both yawed flow cases have marginal stall, thus avoiding the added complexity that stall would introduce to the analysis of inflow and loads.

A testimony to the unsteadiness of blade aerodynamics is the observed lift hysteresis, even for these non-stalled conditions. Actuator line modeling with either the Øye or Beddoes-Leishman dynamic stall model does not reproduce the extent of the hysteresis. Differences are attributed to measurement uncertainty and to boundary layer dynamics typical for the chord Reynolds number Re of the experiments, $Re\,\epsilon\,10^5$, that the dynamic stall codes ignore.

Sectional c_t derived from experimental blade load estimates is compared to that found from the Glauert momentum equation, using estimated annular averaged induced axial velocity in the rotor plane. Reasonable agreement is found across the blade span, for all cases including the most extreme with $45°$ yaw angle. Based hereupon, BEM codes do not require an engineering correction to the Glauert momentum model.

The inverse vortex wake model quantifies the nonuniformity in the inflow at the rotor plane in yaw. Furthermore, this study is the first to decompose the experimental induced velocity into the constituting components from tip and root vortices and the vortex sheet. The experiments clearly demonstrate, next to the strong effects from tip vortices, the importance of the root vortices on the induced axial velocity locally in the inboard, downwind region.

In summary, the thesis contributes to the reduction of BEM modeling uncertainty through the experimental analysis of yawed rotor aerodynamics. The reduced uncertainty could lead to a reduced CoE for wind energy.

Samenvatting

Windenergie levert momenteel een bescheiden bijdrage aan de globale energiemix. De energiekosten van wind ten opzichte van andere energieproductiemethoden bepalen de groei van het windenergieaandeel. Fundamenteel onderzoek en technologieontwikkeling hebben aantoonbaar de energiekosten van wind substantieel gereduceerd. Nog altijd wordt technologische vooruitgang geacht een verdere verlaging te geven, met als een van de speerpunten een verbeterde modellering van de rotoraerodynamica.

Het Blad Element Impuls BEI model koppelt een profielmodel aan de stationaire, een-dimensionale, niet-visceuze trekkende schijf theorie. Empirische modellen repareren de BEI code wanneer de oorspronkelijke aannames niet gelden. Zo wordt met de rotor scheef op de wind, d.w.z. in scheefstand, het trekkende schijf model vervangen door het Glauert impulsmodel. De BEI methode is geschikter als aerodynamisch submodel in aero-servo-elastische codes dan geavanceerdere methoden vanwege haar relatief lage eisen aan computerkracht. In de industrie worden daarom belastingen, benodigd voor componentontwerp, vrijwel uitsluitend uitgerekend met behulp van BEI codes.

Windtunneltesten aan modelrotoren illustreren de substantiële modelonzekerheid behorende bij BEI codes. Zelfs axiale instroomcondities blijken lastig te modeleren. De modelonzekerheid is echter bijzonder groot in scheefstand. Hoewel Navier-Stokes alternatieven ernaar neigen nauwkeuriger te zijn, maakt de enorme vereiste computerkracht ze onpraktisch voor inpassing in industiële aero-servo-elastische modellen.

De onzekerheid van BEI modellering beïnvloedt de vereiste structurele marges van de turbine en daarmee de energiekosten van wind. Fundamentele stromingsfenomenen worden dus bestudeerd in de windtunnel aan modelrotoren teneinde de modelonzekerheid te reduceren. In het licht hiervan richt dit proefschrift zich op rotoraerodynamica in scheefstand, ernaar strevend:

- de effecten te kwantificeren van experimenteel waargenomen scheefstand op bladbelastingen en de instroming in het rotorvlak

- de aerodynamische mechanismen te identificeren, welke bepalend zijn voor de scheefstandseffecten op de rotorinstroming en bladbelastingen

- semi-empirische submodellen te valideren, welke gebruikt worden om BEI methoden te repareren in scheefstand; instationaire profielmodellen, de Glauert impulsvergelijking, correcties voor de niet-uniforme inductie

Hiertoe wordt een meetcampagne uitgevoerd in een open straal windtunnel van de TUDelft aan een $1.2m$ diameter modelrotor met twee niet-tapse, getordeerde bladen. Verscheidene metingen worden uitgevoerd in scheefstand en de axiale referentietoestand;

- metingen van de rotor-axiaalkracht met rekstrookjes in de bladwortel

- kwantitatieve stromingsvisualisatie in het zog met rook om tipwervelpaden te meten tot ongeveer $1R_t$ stroomafwaarts, met R_t de rotorradius

- stromingsvisualisatie op de bladen met woldraadjes om instationaire stromingsloslating in scheefstand langs het blad te identificeren

- metingen van de drie-dimensionale stroomsnelheid in drie vlakken in het nabije zog, met enkel-sensor hittefilm Constant Temperatuur Anemometrie CTA

Alle metingen zijn instationair en worden teruggebracht tot Fase Vergrendelde (of ensemble) Gemiddelde FVG waarden. Daarnaast wordt een gedetailleerde meetonzekerheidsanalyse gepresenteerd voor elke meettechniek en worden windtunnelwandcorrecties methodisch gekwantificeerd; beide analyses geven bevredigende resultaten.

Traditionele datareductie voor enkel-sensor CTA FVG data bepaalt alleen de grootte van de drie FVG stroomsnelheidscomponenten; de experimentator moet expliciet de richting opgeven. Dit zou vooral in scheefstand geen triviale taak zijn. Een nieuwe CTA datareductietechniek wordt daarom geïntroduceerd, welke zowel de grootte als de richting van de drie-dimen-sionale FVG stroomsnelheid afleidt. Vergelijking met Navier-Stokes zogmodellering bevestigt het functioneren van deze techniek. Daarmee verdient deze datareductietechniek de voorkeur in scheefstand.

Ten eerste wordt rechte aanstroming bestudeerd, daar het de referentie vormt voor scheefstand. Experimentele rotor axiaalkrachtscoëfficiënt C_T, tipwervelpaden en stroomsnelheid in het nabije zog komen in het algemeen overeen met experimentele en theoretische publicaties. Verder wordt overeenstemming gevonden tussen de gemeten C_T en die bepaald met het een-dimensionale, niet-visceuze, trekkende schijf model. De benodigde instroming in het rotorvlak is verkregen door lineaire extrapolatie van de metingen in het nabije zog. Het moet opgemerkt worden dat dit model het impulsdeel vormt van BEI modellering in rechte aanstroming.

De in scheefstand gemeten stromingsfenomenen zijn typisch voor deze conditie. Tipwervelpaden vertonen scheefheid, de stroomsnelheid in het nabije zog is asymmetrisch verdeeld over de meetvlakken en C_T neemt af met toenemende scheefstandshoek. Naar weten van de auteur is dit het eerste experiment waarbij de FVG drie-dimensionale stroomsnelheid wordt gerapporteerd in het scheve zog en is het enige alternatief het EU-gefinancierde MEXICO project.

Om de doelstellingen van het proefschrift te halen is het essentieel de experimentele instroming *in* het rotorvlak te kwantificeren. De metingen laten duidelijk de niet-lineaire stroomafwaartse convectie van het zog in scheefstand zien. Het zou dus ongepast zijn om de instroming in het rotorvlak af te leiden met lineaire extrapolatie van de metingen in het nabije zog. Naast de noodzaak tot het ontwikkelen van een niet-lineaire extrapolatiemethode ten behoeve van de instroming in het rotorvlak, is ook het ontbreken van gemeten sectionele bladbelastingen een belemmering om de gestelde doelen te bereiken.

De uitdagingen betreffende de instroming en de belasting worden beide opgepakt met de ontwikkeling van een fysisch analysemodel van de metingen. Dit inverse wervelzogmodel 1) reconstrueert de geometrie van het wervelzog uit metingen, 2) gebruikt behoud van circulatie en de Biot-Savart wet om gemeten geïnduceerde snelheden te relateren aan de onbekende gebonden circulatie en 3) lost het systeem van vergelijkingen op voor laatstgenoemde. Profieltabellen zijn niet nodig, in plaats daarvan worden belastingen geschat met de Kutta-Joukowsky wet, waarbij het model de benodigde instroming en gebonden circulatie bepaalt. Eerdere studies aan de TUDelft leggen het fundament voor het huidige model, met als belangrijkste verbetering de uitbreiding van axiaalstroming naar scheefstand. Verificatie en validatie worden succesvol afgerond.

Het proefschrift beoogt de bevindingen van de experimentele studie naar de dominante stromingsfenomenen in scheefstand (doelstelling 2) te gebruiken voor de validatie van BEM theorie (doelstelling 3). De analyses met het inverse wervelzogmodel worden derhalve uitgevoerd in de context van BEI theorie.

De analyses betreffen drie aspecten van scheefstand; instationaire bladaerodynamica en resulterende belasting, de relatie tussen C_T en geïnduceerde axiaalstroming in het rotorvlak en de mechanismen achter de instationaire instroming op het blad. Vanuit het BEI-perspectief vertaalt dit zich naar validatie van instationaire profielmodellen, van het Glauert impulsmodel en van correcties voor de niet-uniformiteit van de inductiefactor. Het moet opgemerkt worden dat de drie bestudeerde stromingscondities, een axiale en twee met scheefstand, marginale overtrek hebben, waardoor de extra complexiteit, die geïntroduceerd zou worden door overtrek, vermeden wordt.

Het instationaire gedrag van de bladaerodynamica in scheefstand spreekt uit de waarnemingen van lift hysterese, zelfs voor de huidige condities zonder overtrek. Deze mate van hysterese wordt niet voorspeld door modellering

gebaseerd op trekkende lijn theorie, waarbij twee verschillende instationaire profielmodellen worden gebruikt; het Øye en het Beddoes-Leishman instationair profielmodel. Dit verschil in hysterese wordt toegeschreven aan meetonzekerheid en aan instationaire grenslaagdynamica typisch voor het Reynoldsgetal Re van de modelrotor, $Re \, \epsilon \, 10^5$, welke genegeerd wordt door deze profielmodellen.

Sectionele c_t bepaald uit de experimentele bladbelasting wordt vergeleken met die gevonden uit de Glauert impulsvergelijking, die gebruik maakt van de experimentele annulair-gemiddelde geïnduceerde axiaalstroming in het rotorvlak zoals afgeschat met het inverse wervelzogmodel. De conditie met $30°$ scheefstandshoek en zelfs die met $45°$ scheefstandshoek geven allebei, langs het gehele blad, redelijke overeenstemming in c_t. Afgaand op deze resultaten behoeft het Glauert impulsmodel van BEI codes geen correctie.

Het inverse wervelzogmodel kwantificeert de niet-uniformiteit van de intoming in het rotorvlak in scheefstand. Verder is dit de eerste experimentele studie die de geïnduceerde snelheid ontleedt in de bijdragen van de wortel en tip wervel en het wervelvlak. De metingen laten, naast sterke tipwerveleffecten, duidelijk de bijdrage zien van de wortelwervels, welke zelfs dominant is aan de binnenkant van het rotorvlak, wanneer een blad stroomafwaarts wijst.

Samenvattend levert dit proefschrift, door haar experimentele analyse van rotoraerodynamica in scheefstand, een bijdrage aan de reductie van BEI modelonzekerheid. De verminderde onzekerheid zou kunnen leiden tot een afname in de kosten van windstroom.

Contents

Chapter 1

Introduction - the thesis and its link to cost of wind energy

1.1 Wind energy: renewable and economic

The world needs energy; society comes to a halt without a reliable and affordable supply of energy, as is illustrated throughout history. A famed example is Easter Island, where the decline of its civilization is understood to be related to the deforestation of the island [25].

Our society is no exception to the rule. The preferred energy source being fossil fuel, see Figure 1.1, current generations are fortunate to harvest from up to 2 billion years of maturation[1]. The contrast between the steadily increasing worldwide demand for energy [12, 9] and the near-future decline in global oil production due to depleting economically viable resources, predicted by the peak-oil scenario [93], could mean that future generations will not be so lucky. Besides this anticipated global rise in the cost of energy, reliability of supply issues have already materialized, recall e.g. the oil crises of the 1970's and the disputes with Russia in the 2000's over natural gas deliveries. All this, complemented with the wide scientific consensus [7] on the relation between climate change and the man-made rise in atmospheric CO_2-levels, resulting a.o. from burning fossil fuels, has made decision makers worldwide rethink their energy strategies.

In contrast to fossil fuels, renewable energy by definition does not deplete, is more evenly spread across the globe and has marginal CO_2-emission. Despite these advantages of renewables over fossil fuels, renewable energy sources have over the last two decades only contributed a modest, steady $6-7\%$ to the global mix of primary energy consumed [12]; conventional thermal (coal, oil & gas)

---

[1]loosely quoted from MacKay's book dedication [115], with 2 billion years the age of the eldest organisms fossilized to form fossil fuel.
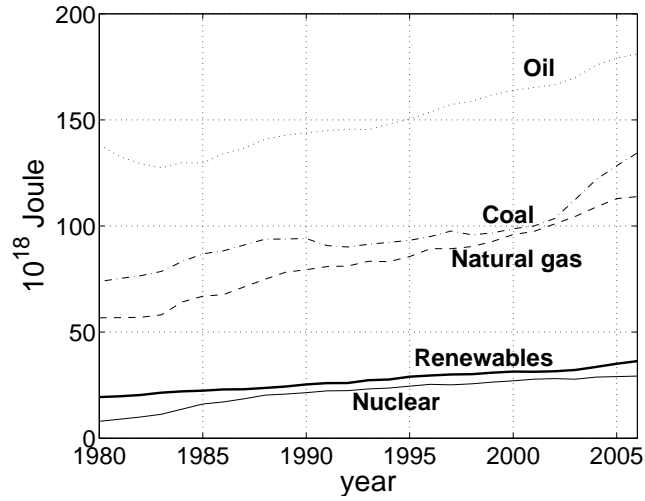
Figure 1.1: World primary energy consumption by fuel type 1990-2005. Renewables include hydro, geothermal, wind, solar, wood and waste energy. [source: Energy Information Administration [12]].

takes the bulk, see Figure 1.1. The share of renewables is expected to increase significantly however in the near future, as governments of the most energy intensive nations have set aggressive renewable energy targets; a.o. European Union legislation [1] demands 20% of the primary energy consumed in the EU in 2020 to come from renewable sources. This 20% target appears achievable without too much ado. It must be realized however that change to a 100% renewable energy supply requires a monumental, society wide effort and is only somewhat realistic if we reduce our energy consumption substantially, by e.g. electrifying transport [115][2].

At present, approximately one third of the world's energy is used to generate electricity[3]. Over the last two decades, a steady $19 - 22\%$ of the worldwide electricity has been generated with renewables [12], see Figure 1.2. Hydroelectric power claims the dominant role within the mix of renewable electricity sources, see Figure 1.3, with the other renewable sources each yielding a relatively modest contribution.

Whilst wind energy only contributed 3.66% to the global renewable elec-

---

[2]The author of this thesis highly recommends this title, as it brings quantification to the renewable energy debate in society

[3]a back-of-the-envelope check: in 2006, the total amount primary energy consumed is $5.0 \cdot 10^{20}$ Joule, whilst the amount of generated electricity totals $6.5 \cdot 10^{19}$ Joule [12]. Assuming a typical efficiency of 40% for the conversion of primary energy to electricity, 33% of the total primary energy is used to produce electricity.
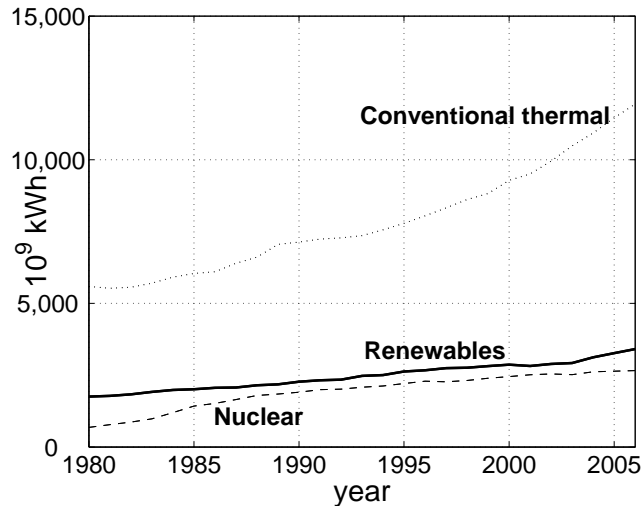
Figure 1.2: World generated electricity by fuel type 1990-2005. Renewables include hydro, geothermal, wind, solar, wood and waste energy. [source: Energy Information Administration [12]].
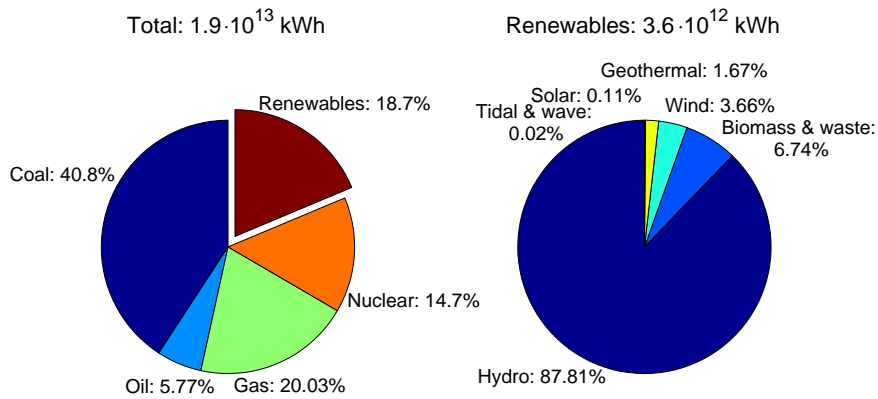
Figure 1.3: Percentage contributions per fuel type to the total (left) and renewable mix (right) of the world generated electricity in 2006. [source: International Energy Agency [9]].

tricity mix in 2006, it has come from virtually zero only two decades ago; the wind energy industry has experienced dramatic growth, with the yearly installed capacity increasing at approximately 30% per annum for the last decade [11], see Figure 1.4.
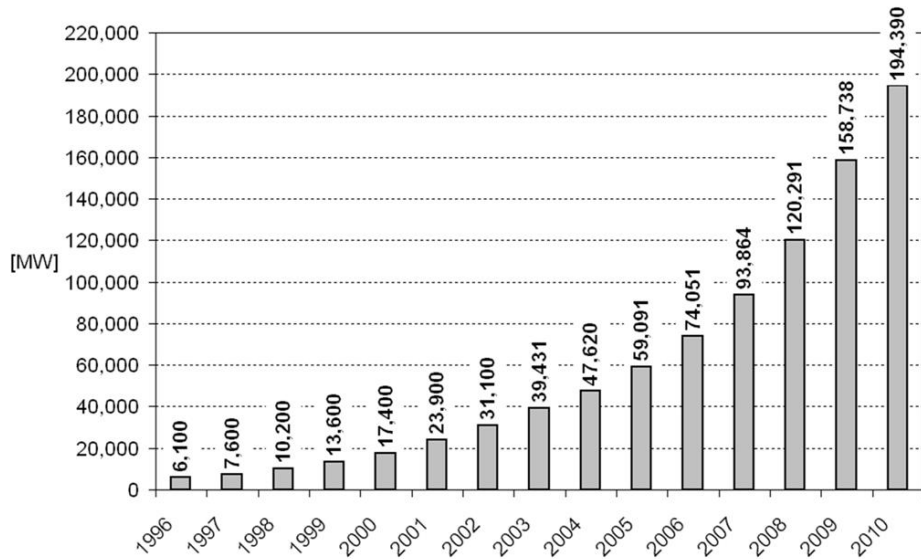
Figure 1.4: Global cumulative installed wind power capacity 1996-2010 [source: Global Wind Energy Council [11]].

This growth has been fueled by the spectacularly enhanced economics of wind turbines, which in turn has been driven by technology improvements and turbine upscaling; wind turbine sizes have increased from typically 55 kW with 15 m rotor diameter, the Vestas V15-55 which was one of the first serial produced wind turbines, to 6 MW with 126 m rotor diameter, the Enercon E-126 which currently is the most powerful wind turbine [8]. The cost of energy produced from wind has reduced by 80% since the pioneering days in the late 1970's that started the current era of electricity generation from wind.

To appreciate the economics of wind energy relative to other sources of generation, it should be realized that politics drive the definition of the economic playing field. The continued debate on energy policy is supported with e.g. scenario studies [10, 121] and research on the socio-environmental costs of energy generation [5]. In the current market conditions however, a developer of a wind park could, for a good[4] site, anticipate a cost of energy level that is similar to that for a newly developed fossil fuel power plant, see Figure 1.5. It can hence tentatively be posited that, despite popular belief, wind energy makes economic sense!

---

[4]Even though the wind resource may be better offshore, the economically best wind parks are all located onshore.
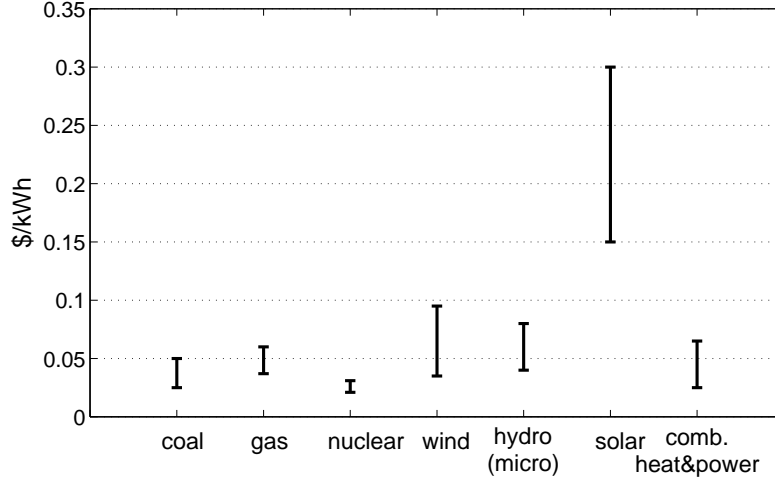
Figure 1.5: Projected levelized cost of electricity for new installations at 5% discount rate [source: Organisation for Economic Co-Operation and Development OECD 2005 [13]].

1.2 Rotor aerodynamics research: cost of wind energy reduction

1.2.1 Impact of aero-elastic modeling on cost of wind energy

The cost of energy can be conceptualized to

$$\text{Cost of energy} = \frac{\text{total investment by a utility to produce energy}}{\text{amount of energy produced}} \quad (1.1)$$

Wind turbine loads drive both the numerator as well as the denominator of this conceptual cost of energy equation 1.1. To briefly elucidate; loads impact the total investment as the dimensions and hence the costs of wind turbine components are driven by the loads they have to withstand[5]. Loads govern the amount of energy produced as well, because the kinetic energy extracted from the wind is first converted to mechanical energy, i.e. rotor torque spinning the blades, whereafter the generator converts mechanical into electric energy.

It can hence be understood that further reductions in the cost of wind energy are dictated by the ability of technological advancements to positively

---

[5]Wind turbine components are designed to keep their material stresses below given bounds. To cover uncertainties in loads and stress predictions, the design standards issued by certification bodies prescribe safety factors, refer e.g. those of the to Germanischer Lloyd[6]. For an explicitly probabilistic approach to wind turbine design, effectively doing away with safety factors, see Veldkamp [201]

impact loads. Note that "technological advancements" should be interpreted both as improvements to wind turbine hard- and software as well as enhanced modeling capability, i.e. a reduction in modeling uncertainty. This thesis focusses on the latter interpretation; the work presented here is intended to contribute to reducing the uncertainty in wind turbine loads modeling.

Wind turbine loads are governed by the dynamic interaction between aerodynamics, controls and the elastic turbine structure. The prediction of turbine loads thus requires not only a rotor aerodynamics model, but an integrated aero-servo-elastic model. The suite of rotor aerodynamics models available for use in aero-servo-elastic tools consists of three general categories; Blade Element Momentum (BEM), vortex wake and Navier-Stokes (CFD) models. BEM models come with most rigorous assumptions. For reasons of computational speed however, the aero-servo-elastic tools being used in industry generally employ BEM instead of the less restrictive vortex wake and Navier-Stokes models. This situation is not expected to change substantially in the near future, as indicated by e.g. Vermeer *et al.* [204] and Hansen *et al.* [86].

The main assumptions underlying BEM theory - inviscid, steady, one-dimensional flow - effectively constrain the operating conditions for which BEM is valid to uniform, steady rotor inflow. Wind turbines in fact never experience this 'ideal' operating condition, as they operate in the turbulent atmospheric boundary layer. Further, these BEM assumptions are based on a uniformly loaded rotor disc; a state that is not achievable in practice, even in the wind tunnel where the uniform inflow *can* be realized, due amongst others to the finite number of blades a real rotor has, in contrast to the non-rotating actuator disc that forms the basis of the wake momentum theory used with BEM modeling.

To account for the observation that "real" rotor aerodynamics violates the BEM assumptions, BEM methods are patched with several semi-empirical models. The uncertainties in BEM modeling predictions of both loads and power are considerable however, when comparing to measurements. Two general sources for the modeling uncertainties can be identified;

- limited knowledge of the turbulent inflow to a field rotor

- inaccurate modeling of the aerodynamic interaction between rotor and inflow

Note that the former source applies not just to BEM but to higher fidelity rotor aerodynamics models as well, since it concerns prescribing the appropriate boundary conditions to a vortex wake or a Navier-Stokes type problem.

1.2.2 Need for rotor aerodynamics research in the wind tunnel

The modeling uncertainty of rotor aerodynamics codes could in principle be reduced through field measurements, using them to enhance our understanding of rotor aerodynamics and validate (sub)models. Prominent field test examples are those performed in the 1990's within the international collaboration framework of the International Energy Agency (IEA) Annexes XIV [155] and XVIII [154].

Field tests are hampered however by the inadequate quantification of the turbulent atmospheric boundary layer: the inflow conditions are generally known only at a few positions, e.g. at a metmast in the vicinity of the turbine. This lack of inflow information complicates the assessment of rotor aerodynamic measurements; first, cause-effect hypotheses are difficult to verify when the cause is not well defined. Second, model validation suffers from the coarse definition of model boundary conditions, as has been marked already at the top of the list in Section 1.2.1.

Compared to metmasts, the amount of inflow data can be greatly increased by use of a Light Detection and Ranging (Lidar) system, which allow for wind velocity measurements at hundreds of arbitrary points in space each second. Even for the ideal case when the inflow in the entire space-time domain of relevance to the turbine would be known, analysis of field measurements would still be complicated, because the inflow cannot be controlled. As a consequence, rotor aerodynamics phenomena generally do not occur in isolation. A field turbine might e.g. experience a gust over part of the rotor plane whilst operating in a sheared, misaligned inflow, leading to a complex aerodynamic response, with coupled governing mechanisms. Use of field measurements for aerodynamic analysis and model validation hence is far from trivial, as concluded in IEA Annexes XIV [155] and XVIII [154].

Testing in the controlled environment of a wind tunnel mitigates the inflow issues associated with field testing, at the expense of introducing scaling problems, i.e. lack of similitude[6]. Geometric dissimilarity occurs with rotors that are simplified with blades that e.g. have no twist or a single airfoil. Kinematic similarity can typically be achieved, because the model rotor can normally be set to dimensionless operational conditions that are representative for a full-scale rotor; similar ratio of tip speed to ambient wind speed and similar blade pitch angles.

Wind tunnel tests on model rotors do by no means achieve dynamic similarity though, i.e. Reynolds numbers (Re) equal to those achieved on MW-scale wind turbines. Careful test design, based on awareness of the experimental Re and understanding of its consequences for both translating measurements

---

[6]similitude is defined as the combination of geometric, kinematic and dynamic similarity between the scale model and the full-scale object

to full-scale conditions as well as model validation, helps reduce the risk of
Re-dissimilarity. In all, the mechanisms driving rotor aerodynamic flow phe-
nomena can thus generally be maintained between model and full scale rotors.
In their recent reviews of wind turbine aerodynamics, Snel [175, 177] and
Leishman [110] acknowledge the need for wind tunnel testing to help enhance
our understanding of rotor aerodynamics, thereby reducing modeling uncer-
tainties in today's aero-servo-elastic design codes.

Within the collection of wind tunnel experiments on model rotors, see
Vermeer *et al.* [204] for an overview, the Unsteady Aerodynamic Experiment
(UAE) Phase VI, conducted by the National Renewable Energy Laboratory
(NREL) in the NASA-Ames 24 by 27 meter wind tunnel on a 10 meter diam-
eter wind turbine [52], has been instrumental, as they a.o. formed the basis
for the 2001 NREL blind comparison [173]; academic institutions across the
global wind energy community were asked to model the tests, without a-priori
knowledge of the experimental results. Contributing rotor aerodynamics tools
include BEM, vortex wake and Navier-Stokes models. The blind comparison
results are not favorable. Whilst even axial flow conditions with generally
attached flow across the blade span pose challenges, load and power modeling
uncertainties are especially considerable for yawed flow conditions.

To summarize, reduction of the uncertainties in loads and power predic-
tions of present rotor aerodynamic models aids in achieving lower cost of en-
ergy. The basis for uncertainty reduction is an enhanced insight into rotor
aerodynamics, obtained through model rotor experiments in the controlled
environment of a wind tunnel.

1.3   This thesis: motivation, objectives & scope

Motivation

The general need for experiments in a controlled environment to reduce the
uncertainty of wind turbine rotor aerodynamics modeling, sketched in Section
1.2, forms a common basis for wind tunnel research on rotor aerodynamics
performed across the wind energy academic community. This thesis is no
exception. Rooted in this general need, the specific motivation for the research
performed within this thesis is the observation that BEM-models, patched with
semi-empirical submodels, yield significant modeling uncertainties for yawed
inflow conditions. This particular inflow state, yaw, is of special interest, both
from an industry and an academic perspective;

- Wind turbines permanently operate in yaw:
  - the turbine is not able to instantaneously re-align itself with the
    continuously changing wind direction

- the nonzero tilt angle of a wind turbine, combined with the non-horizontal orientation of the wind, results in tilt misalignment that is aerodynamically identical to yaw misalignment[7]

- Yaw misalignment results in design driving unsteady loading:

  - the unsteady loads impact turbine fatigue life
  - for some turbines, yawed inflow even yields extreme loads

- The assumptions on which BEM-theory is based are violated in yaw, resulting in substantial modeling uncertainties and conservative turbine designs

- In the wind tunnel, yaw misalignment can easily be achieved; just turn the model rotor out of the wind

To summarize; enhanced insight into the aerodynamics of a rotor in yaw, obtained through wind tunnel tests, should result in more accurate yaw modeling, which, in turn, should reduce the cost of wind energy.

Objectives

The Wind Energy group at the Aerospace Engineering faculty[8] of the TUDelft initiated a study in 2003 aimed at reducing BEM modeling uncertainty in yaw misalignment through wind tunnel experiments. The approach towards this general aim can be characterized by three interacting elements, as sketched in Figure 1.6; to improve understanding of rotor aerodynamics in yaw through the execution and analysis of wind tunnel measurements, to implement suggested BEM modeling enhancements and to validate the enhanced BEM model with field measurements.

The study has been organized as a "duo-PhD" project. In good harmony, Tonio Sant [147] has been responsible for improving BEM models, whilst undersigned has been driving wind tunnel data reduction and subsequent aerodynamic assessment. It must be noted that the fourth and final step, validation with field experiments, has remained out-of-scope for this project; the updated BEM models have only been validated against wind tunnel experiments on model rotors.

This thesis hence aims to improve our understanding of rotor aerodynamics in yaw using wind tunnel experiments. Its concrete objectives are:

---

[7]Note that in contrast to yaw misalignment, present turbines cannot actively control tilt misalignment during operation; tilt misalignment at low wind speed conditions is accepted to avoid the blade striking the tower in high loading conditions.

[8]The group moved from the faculty of Civil to Aerospace Engineering in 2004.
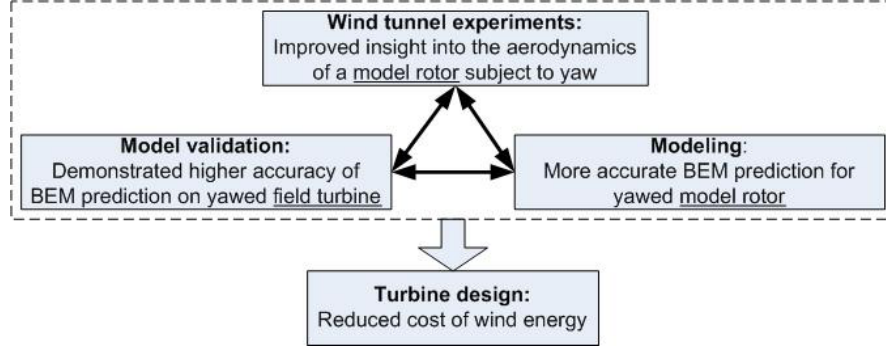
Figure 1.6: Schematic approach to reduce the uncertainty of BEM modeling in yaw, resulting in lower cost of wind energy.

- quantify the effects of experimentally observed yaw misalignment on rotor inflow and blade loads

- identify the aerodynamic mechanisms governing the effects of yaw misalignment on rotor inflow and blade loads

- assess the validity of semi-empirical submodels, used to patch BEM-theory; the Glauert momentum equation for yaw, induction non-uniformity corrections in yaw, airfoil dynamic stall models.

Note that the objectives explicitly mention both rotor inflow and blade loads; the aerodynamics of the rotor is characterized by coupled blade and wake (inflow) aerodynamics, see Figure 1.7. Comprehensive understanding of a rotor aerodynamic phenomenon can thus in essence only be obtained when both blade and wake aerodynamics are studied.

Wind tunnel experiments are generally focused on measuring either blade loads or wake properties though; in the overview of experiments given by Vermeer *et al.* [204], only one of nineteen tabulated experimental campaigns concerns both comprehensive blade and wake measurements. That campaign is MEXICO (Model Rotor Experiments in Controlled Conditions) [181], where measurements have been conducted in the German-Dutch Wind Tunnels (DNW) on a 4.5 meter diameter rotor within a EU research framework. Rotors of this size are easier to equip with distributed load and pressure sensors than the smaller rotors typically used in a university environment, hence the main reason for the scarcity of combined blade and wake wind tunnel measurements.

The model rotor available for wind tunnel testing in the context of this thesis is exemplary for university experiments; it lacks distributed loads/pressure sensors along its blades. Knowledge of both inflow and blade loads is essen-

10
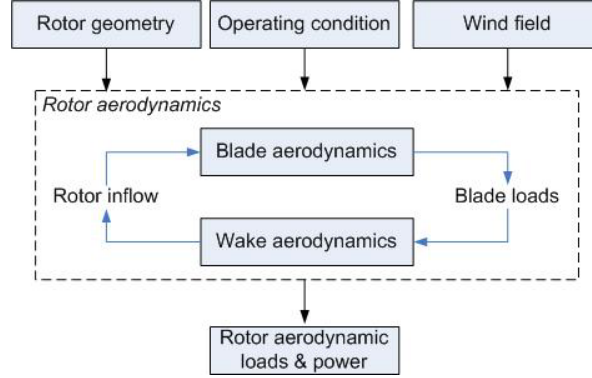
Figure 1.7: Schematic input-output type model illustrating that rotor aerodynamics in essence is composed of coupled blade and wake aerodynamics.

tial for a comprehensive understanding of yaw misalignment, as reflected by explicitly mentioning them in the thesis objectives. The thesis should consequently address a method to derive load distributions across the blade span using wake measurements of a yawed rotor.

Scope

The pursuit of these objectives in a constrained world[9] of calls for a project scope definition:

- Whilst a wind turbine rotor can operate in the helicopter, vortex ring, turbulent wake and windmill state, see e.g. Glauert [61], this thesis only considers the last operational state.

- The thesis focusses on the TUDelft model rotor in the TUDelft open jet wind tunnel. Rotor experiments in other tunnels and/or using other rotor models are discussed in the context of scientific reference only.

1.4   Outline

Part of the joy in reading a thesis stems from having foreknowledge of where to find relevant information. Hence, to assist those readers that do not read cover-to-cover[10], an overview of each section;

---

[9]A PhD in The Netherlands = 4 years = 34.944 man hours including the time spend sleeping, eating and, in the author's case, drinking approximately 600 liters of coffee.

[10]No hard feelings, the author has applied this very strategy for all theses, except his own.

Chapter 2 provides an overview of relevant previous analytical, numerical and experimental work in the field of wind turbine rotor aerodynamics, which should both result in a solid base for further work and place the problem statement of this thesis in its academic perspective.

The aerodynamic measurements, that form a pillar of the analyzes in this thesis, are described in detail in **Chapter 3**. The model rotor and open jet wind tunnel are discussed, as well as measurement techniques used.

Experimental data reduction is treated in **Chapter 4**. A new method, capable of determining the phase-locked average three-dimensional flow velocity from single-sensor constant temperature anemometry, is proposed. Wind tunnel wall corrections are derived and a measurement uncertainties are analyzed for the experimental techniques employed.

The introduction of the measurements in chapters 3 and 4 is succeeded by the study into experimentally observed near-wake flow physics, commencing in **Chapter 5** with the analysis of the axial flow conditions. **Chapter 6** discusses the experimentally observed effects of yaw misalignment on the near-wake rotor aerodynamics.

Having analyzed the rotor wake in Chapters 5 and 6, insight into the aerodynamics of the rotor would be further enhanced with the availability of blade loads, since blade and wake aerodynamics are coupled. As blade loads are not recorded, a measurement analysis tool entitled 'inverse vortex wake model' is presented in **Chapter 7** that is capable of deriving blade loads and the inflow at the rotor plane from the combination of rotor wake measurements and vortex theory, for both axial and yawed flow conditions. The inverse vortex wake model is applied to the model rotor experiments in **Chapter 8**.

The experimental insights gained form a basis for the comparison in **Chapter 9** of measurements against models. The validity of the Glauert momentum deficit model and the effect of dynamic stall model selection in the actuator line model are assessed.

Conclusions and recommendations can be found in **Chapter 10**.

Chapter 2

Wind turbine aerodynamics - models and experiments

The aerodynamics of wind turbines is a specific variant within the field of rotor[1] aerodynamics, that further includes amongst others the aerodynamics of helicopters[2] and the fluid dynamics of both arial and marine propellers. All these embodiments share a common theoretical basis, with their aerodynamics characterized by similar flow phenomena as exemplified in Figure 2.1. The unique specifics of each application have resulted in dedicated research though, performed within quasi-detached scientific communities. The discussion in this section logically focusses on the work performed on wind turbine rotor aerodynamics.
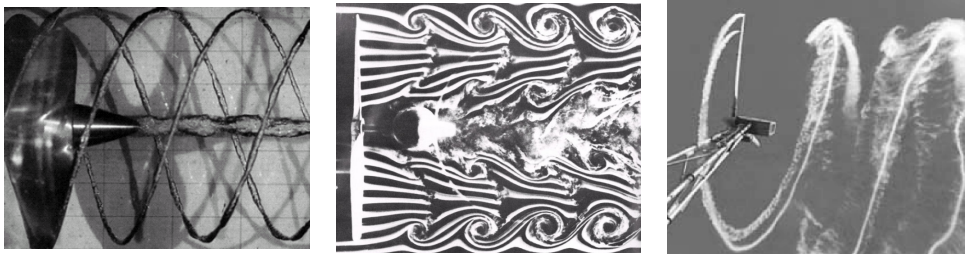
Figure 2.1: Experimental visualization of the rotor wake structure downstream of a marine propeller (left), an arial propeller (middle) and a wind turbine (right). Sources: unknown, Van Dyke [47] (photo 75 by Brown), Risø DTU

---

[1]a rotor is an assembly of blades

[2]The reader interested in helicopter aerodynamics is referred to e.g. Leishman and Bagai [111] for a specialized review of wake flow phenomena and to Conlisk [36] for a general review of experiment and model approaches and results

In Section 2.1, the fundamentals of wind turbine rotor aerodynamics modeling are introduced first, whereafter an overview is given of the modeling state-of-the-art. The literature on wind turbine rotor experiments is discussed in Section 2.2. Note that both literature surveys focus on work relevant to the study of yaw misalignment, in accordance with the thesis objectives outlined in Section 1.3. Section 2.3 reviews rotor wake measurement analysis tools, in support of the specific task identified in Section 1.3 to pursue a method capable of deriving blade load distributions from inflow measurements. Review conclusions in light of the objectives and scope of this thesis are discussed in Section 2.4.

2.1 Rotor aerodynamics modeling

The discussion on rotor aerodynamics modeling starts with its fundament; a brief introduction into actuator disc theory in Section 2.1.1. Based hereupon is Blade Element Momentum BEM modeling, the current rotor aerodynamics method of choice in the industry and focal point of this thesis. Section 2.1.2 is dedicated to BEM. More advanced rotor aerodynamics models and the insights these bring to modeling yaw misalignment are reviewed in Section 2.1.3.
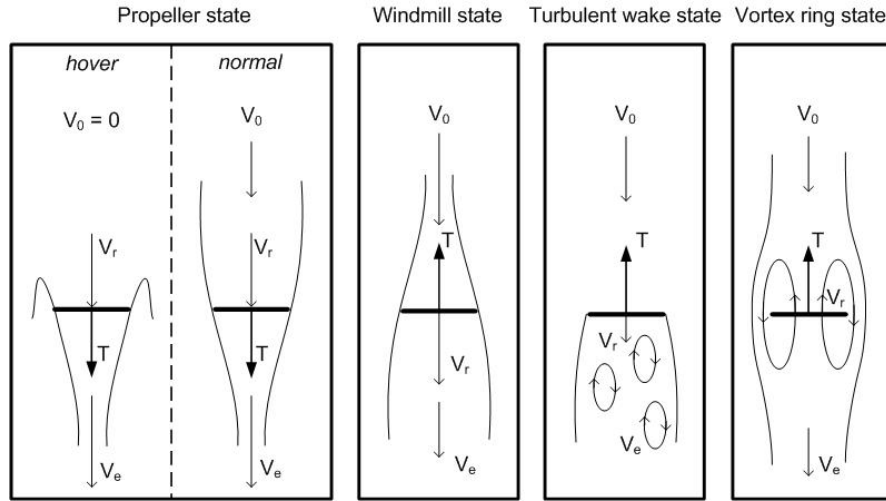
Figure 2.2: Schematic of the four general actuator disc states

2.1.1 The basics: actuator disc

In essence, a rotor changes the kinetic energy of the fluid flow as work is performed by forces on its blades. Based on this principle, in the latter half of the

14

19th century the foundation of today's rotor aerodynamics models was laid, as Froude [54], building upon Rankine's [142] propeller work, introduced the actuator disc concept; the rotor is represented by a porous disc of zero thickness on which forces equivalent to those on the actual rotor are distributed.

Four general actuator disc states are identified, see Figure 2.2, where V is the flow velocity and T is the thrust acting on the flow. Suffices 0, r and e refer to far upstream, the rotor and far downstream, respectively.

- **propeller state**: rotor thrust accelerates the flow. The rotor adds kinetic energy to the flow and thus needs to be powered. This state includes the limit case of $V_0 = 0$, known as helicopter hover.

- **windmill state**: rotor thrust decelerates the flow. Kinetic energy is extracted from the flow and drives the rotor.

- **turbulent wake state**: strong flow deceleration by the rotor yields flow reversal in the wake, $V_e \leq 0$, resulting in unsteady, recirculating wake flow. The rotor still extracts kinetic energy from the flow.

- **vortex ring state**: the rotor further decelerates the flow, resulting in $V_r < 0$. The flow field near the disc resembles vortex rings. Rotor flow field and loads are highly unsteady. The rotor adds kinetic energy to the flow and thus needs to be driven.
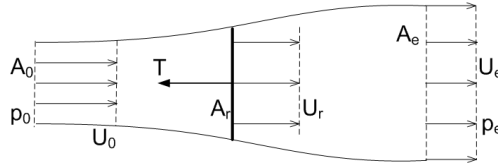
Figure 2.3: Schematic of classical one-dimensional actuator disc flow

The four actuator disc states can only be covered comprehensively by a flow model based on viscous, three-dimensional, unsteady wake flow. Classical Rankine-Froude actuator disc theory however assumes one-dimensional, non-rotating flow and a uniformly loaded disc to model the propeller and windmill states, see Figure 2.3. Notations used are identical to those in Figure 2.2, with the remark that U represents an *axial* flow velocity. Further, p is a static pressure and A is a surface. The thrust T results from a pressure jump Δp across the disc. Assuming $p_0 = p_e$, conservation of axial momentum and of energy result in

$$T = \Delta p \, A_r = \dot{m} \, (U_e - U_0) \tag{2.1}$$

and

$$P = \dot{m} \left(\frac{1}{2} U_e^2 - \frac{1}{2} U_0^2 \right) = U_r T, \tag{2.2}$$

respectively, with P the power extracted by the disc and $\dot{m}$ the mass flow. Conservation of mass is given by

$$\dot{m} = \rho U_0 A_0 = \rho U_r A_r = \rho U_e A_e, \tag{2.3}$$

where the surfaces A_0 and A_e are constructed from the limiting streamtube through the edge of the actuator disc. Combining Equations 2.1 and 2.2 yields

$$U_r = \frac{1}{2} \left(U_0 + U_e \right). \tag{2.4}$$

The flow velocity at the actuator disc hence is the average of the undisturbed wind speed far upstream and the wind speed in the wake of the disc, far downstream. With the flow axial velocity induced by the actuator disc U_i, or induced axial velocity in short, defined as

$$U_i(x) = U(x) - U_0, \tag{2.5}$$

where $U(x)$ is the flow axial velocity at given x, Equation 2.4 can be rewritten to

$$U_{i_e} = 2U_{i_r}. \tag{2.6}$$
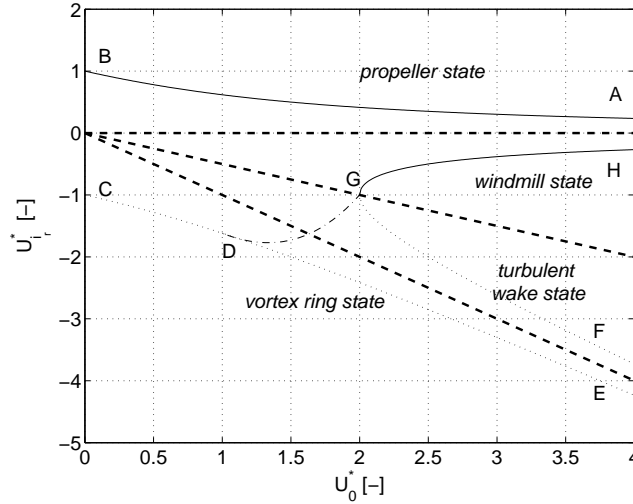
Figure 2.4: Classical actuator disc modeling result (Equation 2.7): U_{i_r} vs. U_0, both made dimensionless with $\sqrt{|T|/(2\rho A_r)}$, illustrating actuator disc states.

Combining Equations 2.1, 2.3, 2.5 and 2.6 yields an expression relating T to U_{i_r} and U_0,

$$\frac{T}{2\rho A_r} = U_{i_r}^2 + U_0 U_{i_r}. \tag{2.7}$$

The dimensionless version of Equation 2.7, obtained by dividing each velocity component with $\sqrt{|T|/(2\rho A_r)}$, is plotted in Figure 2.4, where nondimensional velocities are marked with an asterisk. By definition, $U_0^* \geq 0$, in concurrence with U_0 directed left to right in Figure 2.3, and $U_{i_r}^*$ can be positive or negative. Dashed lines indicate the bounds between the four actuator disc states, where

- propeller state: $U_{i_r} > 0$

- windmill state: $-\frac{1}{2} < U_{i_r}/U_0 \leq 0$

- turbulent wake state: $-1 < U_{i_r}/U_0 \leq -\frac{1}{2}$

- vortex ring state: $U_{i_r}/U_0 \leq -1$

The Rankine-Froude assumptions approximately hold for the propeller and windmill state only; the solution to Equation 2.7 is hence given with a solid line for these two states (lines AB and GH), whilst the results obtained for the vortex ring and the turbulent wake state are given with dotted lines (lines CDE and GF). Note that both points B and C for $U_0^* = 0$ mark the helicopter hover condition. A more detailed description of actuator disc states in general and Equation 2.7, Figure 2.4 in particular is e.g. given in Van Kuik's PhD thesis [103]. The remainder of this discussion focusses on the windmill state.

Rotor thrust T and power P are expressed in terms of dimensionless thrust and power coefficients C_T and C_P, respectively, with

$$C_T = \frac{T}{\frac{1}{2}\rho U_0^2 A_r}, \tag{2.8}$$

$$C_P = \frac{P}{\frac{1}{2}\rho U_0^3 A_r}. \tag{2.9}$$

Further, introduction of the axial induction factor a,

$$a = -\frac{U_{i_r}}{U_0} = 1 - \frac{U_r}{U_0}. \tag{2.10}$$

enables the actuator disc relations for T and P to be made dimensionless; combining Equations 2.1-2.4 and 2.8-2.10 yields

$$C_T = 4a(1 - a), \tag{2.11}$$

$$C_P = 4a(1 - a)^2, \tag{2.12}$$

17

where it must be noted that C_T and C_P concern the thrust and power on the rotor by the flow, that are both positive for the windmill state. Independent of each other, Betz [22], Lanchester [105] and Joukowsky [100][3] derived that $C_{P_{max}} = 16/27$ for $a = 1/3$. At this Betz-Lanchester-Joukowsky limit, or Betz limit in short, $C_T = 8/9$.
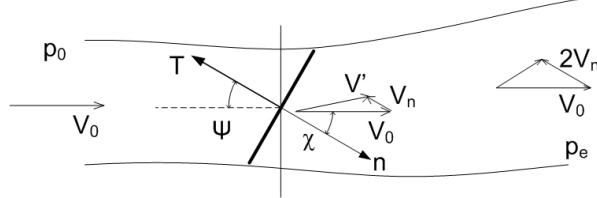
Figure 2.5: Schematic of actuator disc flow subject to yaw misalignment.

The Rankine-Froude actuator disc model is based on the assumption of one-dimensionality, i.e. the flow velocity is perpendicular to the rotor plane. This assumption is consistently violated for wind turbines operating in the field due to combined yaw and tilt misalignment, which hereafter is concisely referred to as yaw misalignment. The two-dimensionality introduced to actuator disc flow by yaw misalignment angle Ψ is shown in Figure 2.5, where it can be seen that the wake is deflected towards the downwind side of the actuator disc with skew angle χ whilst convecting downstream.

To account for yaw misalignment, the Rankine-Froude axial momentum relations are superseded by the momentum equation proposed by Glauert [60, 62];

$$ T = 2\rho A_r \left| \vec{V_0} + \vec{n} \left(\vec{n} \cdot \vec{V_i} \right) \right| \left(\vec{n} \cdot \vec{V_i} \right), \tag{2.13} $$

where velocities are written in terms of vectors instead of scalars, i.e. $\vec{V_0}$ versus U_0 and $\vec{V_i}$ versus U_i, to emphasize their direction, and $\vec{n}$ is the normal to the actuator disc, pointing downstream. Using $\vec{V_n} = \vec{n}(\vec{n} \cdot \vec{V_i})$ and $\vec{V'} = \vec{V_0} + \vec{V_n}$, see Figure 2.5, Equation 2.13 can be rewritten in a more compact form;

$$ T = 2\rho A_r |\vec{V'}| \; \vec{n} \cdot \vec{V_n}. \tag{2.14} $$

It can readily be shown that Glauert's momentum Equation 2.14 reduces to the Rankine-Froude result 2.7 for axial flow, $\Psi = 0°$. Further, for a wind turbine rotor at $90°$ yaw, Glauert's momentum Equation 2.14 corresponds to the momentum equations describing a gyrocopter in fast forward flight, see e.g. Bramwell [23, 24]. Without any formal proof, Glauert's momentum Equation 2.14 is assumed to hold for all other yaw angles other than $\Psi = 0°, 90°$ as well.

---

[3]Van Kuik [104] brought Joukowsky's contribution to the footlight.

The dimensionless expression for Equation 2.14 reads

$$C_T = 4a\sqrt{sin^2\Psi + (cos\Psi - a)^2}, \tag{2.15}$$

where a is defined according to Equation 2.10; the normal component of the induced velocity at the disc $-\vec{n}\cdot\vec{V_n}$, made dimensionless with $|\vec{V_0}|$.

In his studies [60], Glauert predicts the impact of yaw on the induced velocity distribution across the disc; in contrast to axial flow conditions, the induced velocity varies across the disc for a rotor subject to yaw misalignment, even with a uniformly loaded rotor (constant pressure jump Δp). Consequently, the velocities $\vec{V}'$ and $\vec{V_n}$ in Equation 2.14 refer to averages over the disc, not to local velocities. Glauert's momentum relation 2.14 hence cannot be used in differential form,

$$dT = 2\rho|\vec{V}'| \ \vec{n}\cdot\vec{V_n} \, dA_r. \tag{2.16}$$

to equate thrust and induced velocity locally at a point on the disc.

2.1.2   The industry workhorse: Blade Element Momentum

However indubitable the contribution of actuator disc models to our understanding of rotor aerodynamics, they lack the ability to disclose the aerodynamics at *the individual blades* of a rotor, since the rotor is simplified to a porous disc carrying a pressure jump. Glauert's[4] approach to couple the actuator disc theory with a blade element model, published in 1935 [62], thus signified a major modeling advancement and formed the first description of a complete BEM model.

To this day, BEM models have remained the industry workhorse for wind turbine rotor aerodynamic design and aero-servo-elastic loads simulation. They are expected to retain a significant position in the wind turbine designer toolbox for the foreseeable future. Note that Glauert's original BEM model has over time been patched with a variety of submodels, effectively creating a family of "modern" BEM models, each one with its own submodels and implementations thereof.

BEM models used for wind turbine applications are abundantly introduced in literature, refer to e.g. the textbooks by Burton *et al.* [27] and Hansen [85]. This section does not aim to replicate these textbooks or add novel insights. Instead, a refresher is given on the key submodels of a typical BEM code and their context. Emphasis is put on yaw misalignment, regarding both the validity of BEM assumptions in yaw as well as the implementation of yaw in BEM. The discussion intends to provide adequate basis for the subsequent BEM-related discussions in the results Chapters 8 and 9 of this thesis.

---

[4]In his brief history of wind turbine aerodynamics, Snel [178] credits Froude as the first to couple momentum and blade element theory. Glauert however "first described a full fledged BEM theory", reported in [62]
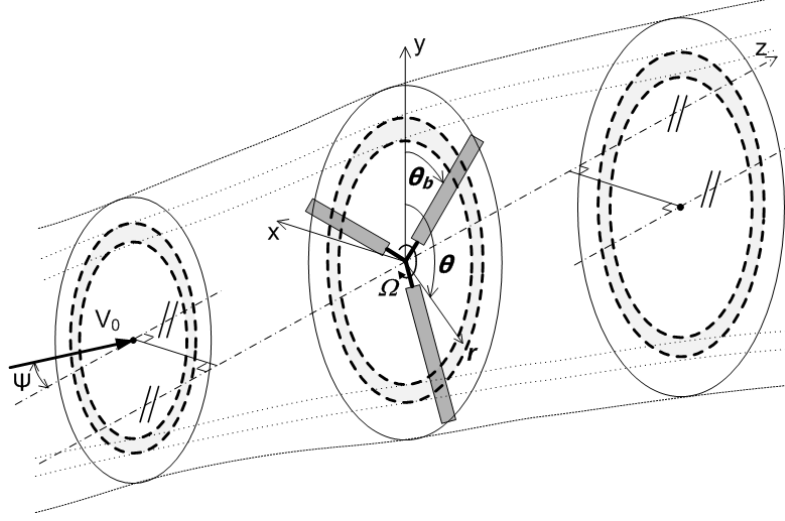
Figure 2.6: Schematic of an annulus as used in BEM modeling. $\vec{V_0}$ is not oriented perpendicular to the rotor plane, resulting in a nonzero yaw misalignment angle Ψ. Note that $\vec{V_0}$ is parallel with the (x, z)-plane.

Momentum equations

A BEM model divides the wake into a number of concentric strips or annuli, illustrated in Figure 2.6. The aerodynamic loads at the blade elements contained within an annulus are assumed to balance the wake momentum deficit. The Glauert momentum Equation 2.14 in quasi-differential form[5] is used to determine wake momentum deficit and blade element loads are found through airfoil modeling. Wake momentum deficit and blade loads are coupled through the induced velocity at the blades; equating wake momentum deficit with blade loads hence corresponds to finding the appropriate value for the induced velocity at the blades.

In concreto, the equilibrium between wake momentum change and blade loads is expressed in terms of a modified Glauert momentum Equation 2.13;

$$V_{i_n} = \frac{-BLcos\phi}{4\pi\rho r F \left| \vec{V_0} + f_g \vec{n} \left(\vec{n} \cdot \vec{V_i} \right) \right|}, \tag{2.17}$$

$$V_{i_\theta} = \frac{-BLsin\phi}{4\pi\rho r F \left| \vec{V_0} + f_g \vec{n} \left(\vec{n} \cdot \vec{V_i} \right) \right|} \tag{2.18}$$

---

[5] *quasi*-differential form, as instead of per streamtube with infinitesimal cross-section, the equation is applied per annulus; $dA_r = 2\pi r dr$

for axial and angular momentum, respectively. Note that Equation 2.18 for the induced velocity in the tangential direction V_{i_θ} is not derived from momentum theory, but is logically inferred to be similar in form to Equation 2.17 for V_{i_n}. B is the number of blades in the annulus, L the lift force, ϕ the inflow angle relative to the rotating blade section (also see Figure 2.7), F a tip loss correction factor and f_g a correction factor for highly loaded rotors.
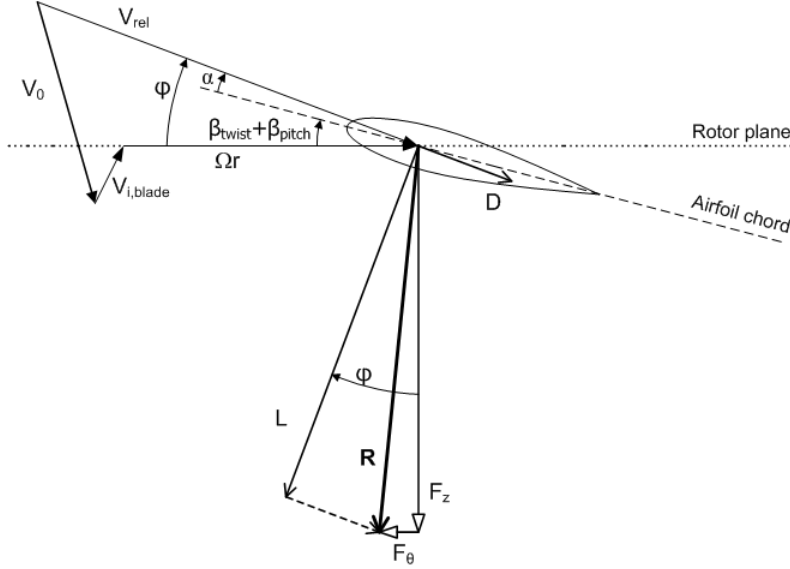
Figure 2.7: Velocity and load triangles for a blade element, generalized for yaw misalignment.

Sørensen and Mikkelsen [184] demonstrate that application of the Rankine-Froude axial momentum equation 2.1 in quasi-differential form, i.e. per annulus, is principally invalid; Equation 2.1 ignores the pressure acting on the lateral bounds of the annular streamtube. The lateral pressure contributes to the thrust though, thereby invalidating the one-dimensional actuator disc conclusion that the induced velocity at the disc is half that in the far wake, Equation 2.6. By comparison with a Navier-Stokes model of a uniformly loaded finite radius actuator disc in axial flow, Sørensen and Mikkelsen [184] conclude that the error made when applying the Rankine-Froude model per annulus is negligible at each annulus except for the tip region. The actuator disc and BEM models used in this thesis thus do not apply a lateral pressure correction to Equations 2.17 and 2.18.

Equations 2.17 and 2.18 further assume the blade elements to be positioned in the rotor plane, which is defined as the plane normal to the axis of rotation, intersecting this axis at the hub center. The generally large structural

flexibility of wind turbine blades [6] and the associated build-in blade prebend and rotor cone question this assumption in at least some operating conditions. Though BEM codes typically use Equations 2.17 and 2.18 regardless of these considerations, Crawford [40, 41] proposes an update to the BEM equations to account for large cone angles. Streamtube lateral pressure and deflection/cone effects are out-of-scope for the current study and are thus ignored.

Tip loss modeling

Actuator disc modeling of the axial flow condition yields a uniform azimuthal distribution of the induced velocity across an annulus. In BEM theory though, rotor forces act on a finite number of blades instead of a continuous actuator disc. As a result hereof, the induced velocity is nonuniformly distributed across an annulus, especially towards the blade tips. The tip loss correction factor F corrects for the induced velocity nonuniformity that results from having a finite number of blades.

Though e.g. Holierhoek [91] directly applies F on the blade sectional loads, most references, including e.g. the textbooks by Burton *et al.* [27] and Hansen [85], use F to correct the induced velocity from the actuator disc based value to that *at* the blades. F can hence be interpreted as a ratio,

$$F = \frac{V_{i_n,ann}}{V_{i_n,blade}} = \frac{a_{ann}}{a_{blade}},$$
(2.19)

where the numerator and the denominator refer to the actuator disc based inflow and that at the blade, respectively. For clarity, suffixes "ann" and "blade" have been appended to both the induced velocity normal to the disc V_{i_n} and the axial induction factor a in Equation 2.19. Note that, although explicit suffixes are omitted in compliance with literature, the induced velocity terms in Equations 2.17 and 2.18 concern those at the blade. Shen *et al.* [168] review the formulation and implementation of F, including the well known Prandtl tip loss model[7], and propose a modification hereof that better fits high fidelity CFD modeling, where tip losses are included implicitly.

Highly loaded rotors

Wind turbines occasionally operate in the turbulent wake state[8], which defies simulation with the Rankine-Froude actuator disc model, as discussed in Section 2.1.1. Anticipating on this condition of strong induced velocity ($a \geq 0.5$)

---

[6]As a rule of thumb, the blade is designed for a flapwise tip deflection of about 10% of the rotor diameter.

[7]The derivation of the Prandtl tip loss model is given by Glauert [62]

[8]A typical example: a constant speed rotor at start-up in low wind

combined with high thrust ($C_T \geq 1$), Glauert [59] proposes a factor f_g to correct the Rankine-Froude actuator disc model for highly loaded rotors, as implemented in Equations 2.17 and 2.18.

Note the empirical nature of Glauert's correction factor f_g, which has been found through experiments on a rotor with a finite number of blades, studied as a whole instead of per annulus. Consequently, f_g implicitly includes the overall effect of a finite number of blades. This could be considered an inconsistency in BEM modeling, because the correction for the finite number of blades should be handled exclusively by F.

Dynamic inflow

BEM modeling is based on the assumption of invariability with respect to time, resulting in the *steady* momentum balance. The associated steadiness of blade loads requires sectional inflow conditions and hence uniform and steady freestream flow. It's readily appreciated that this condition can only be obtained in the controlled environment of a wind tunnel; in the field, the shear and turbulence of the atmospheric boundary layer result in unsteady sectional inflow. Additionally, the rotor should not be yawed to the freestream, should run at constant RPM and should not change its blade pitch angle.

Using a quasi-steady[9] BEM approach is reasonable when the time scale of blade load variation is of the same order of magnitude as that of the change in the velocity induced by the wake. This condition constrains the rate of change in blade loads to a pace that is characteristic of a comprehensive wake adjustment, i.e. from the rotor plane up to a downstream distance of several rotor radii.

The wake time scale is given by

$$\tau_{wake} = \frac{R_t}{|\vec{V_0}|}, \tag{2.20}$$

the time it takes a flow particle to travel the distance of a rotor radius R_t at freestream wind speed $\vec{V_0}$. The particular cause of blade load variation drives its time scale τ_{bl}; e.g. the once-per-blade-rotation (1P) time periods that are thought to dominate blade loads in wind shear and yaw yield

$$\tau_{bl_{shear}} = \tau_{bl_{yaw}} = \frac{2\pi}{\Omega}, \tag{2.21}$$

with Ω the blade angular speed. The associated ratio of blade and wake time scales is

$$\frac{\tau_{bl_{shear,yaw}}}{\tau_{wake}} = \frac{\lambda}{(2\pi)}, \tag{2.22}$$

---

[9]*Quasi*-steady since unsteady blade sectional inflow conditions, due to e.g. wind shear, are "fed" into the steady momentum equation.

with λ the tip speed ratio[10], given by

$$\lambda = \frac{\Omega R_t}{\left|\vec{V_0}\right|}. \tag{2.23}$$

A 3-bladed wind turbine rotor is typically designed to operate optimally at $\lambda \approx 8$ [89]. Equation 2.22 now gives that shear and yaw induced blade time scales are of the same order of magnitude as the wake time scale, justifying the quasi-steady approach to BEM modeling.

A fast blade pitch change however can occur in less then a second on a multi-MW wind turbine; a typical time scale would be $\tau_{bl_{pitch}} = 0.5\,s$. To estimate τ_{wake} from Equation 2.20 for a multi-MW turbine, $R_t = 50\,m$ and $V_0 = 10\,m/s$ are reasonable numbers, resulting in $\tau_{wake} = 5\,s$. The fast blade pitch change hence clearly introduces an order-of-magnitude difference between τ_{bl} and τ_{wake}.

Measurements on a the 2MW Tjæreborg wind turbine during a fast blade pitch event, reported in the EU co-funded "Dynamic Inflow"[11] studies [179, 157] within the framework of the EU JOULE I & II programs confirm the consequent inaptitude of the quasi-steady BEM approach. These two projects also propose engineering fixes to the issue, that boil down to damping the variations in induced velocity obtained through the quasi-steady approach. Of these dynamic inflow models, Øye's one is applied frequently, ergo the reason for its introduction here. His model, based on an actuator disc vortex ring model including effect of wake expansion, is given by

$$V_{i_{n,int}} + \tau_1 \frac{dV_{i_{n,int}}}{dt} = V_{i_{n,qs}} + k\tau_1 \frac{dV_{i_{n,qs}}}{dt}, \tag{2.24}$$

$$V_{i_n} + \tau_2 \frac{dV_{i_n}}{dt} = V_{i_{n,int}}, \tag{2.25}$$

where $V_{i_{n,qs}}$ is the quasi-steady normal induced velocity found from Equation 2.17, $V_{i_{n,int}}$ is an intermediate induced velocity, k is a coefficient set to $k = 0.6$ and τ_1 and τ_2 are time constants, with

$$\tau_1 = \frac{1.1}{1 - 1.3a} \frac{R_t}{V_0}, \tag{2.26}$$

$$\tau_2 = \left(0.39 - 0.26 \left(\frac{r}{R_t}\right)^2\right) \tau_1. \tag{2.27}$$

---

[10]In American literature, tip speed ratio is abbreviated as TSR instead of λ.

[11]official titles are "JOULE1: Joint Investigation of Dynamic Inflow Effects and Implementation of an Engineering Method" and "Joule2: Dynamic inflow: Yawed Conditions and Partial Span Pitch".

Using Øye's dynamic inflow model, or any of the dynamic inflow engineering fixes to BEM proposed in the Dynamic Inflow reports [179, 157], dynamic loads prediction for the fast-pitching Tjæreborg wind turbine is improved substantially over quasi-static BEM, when compared with measurements.

BEM for yaw: the BEM approach of independent annuli

The flow in an annulus is assumed to be independent of the flow in other annuli. This assumption only holds for axial flow conditions without swirl that result in a uniformly loaded rotor, i.e. constant axial induction factor $a = a(r)$ and tangential induction factor $a' = 0$, where

$$a = -\frac{V_{i_n}}{W_0 cos \Psi} \tag{2.28}$$

and

$$a' = -\frac{V_{i_\theta}}{\Omega r}. \tag{2.29}$$

In practise, wind turbine rotors are neither designed for, nor experience uniform loading. Thus even when subject to axial flow conditions, wind turbine rotors generally invalidate the independent annuli approach.

Whilst the assumption of independent annuli is strictly only valid for uniformly loaded rotors subject to axial flow, its practical suitability extends to include those nonuniformly loaded rotors in axial flow conditions that can be modeled properly with the linearized Euler equation; e.g. Bramwell [23] uses the related linearized acceleration potential theory to demonstrate that, for an actuator disc model of a hovering helicopter, the axial induced velocity at a given location on the disc depends only on the local pressure difference across the disc. The Glauert momentum equation can hence be used in quasi-differential form - equivalent to assuming independent annuli in BEM.

With the rotor subject to significant yaw misalignment, the independent annuli assumption is violated. The induced velocity at a given point on the disc no longer is a function of the local disc loading only, but depends on the pressure gradient along the flow path of the fluid particle passing the disc at that point [23]. The pressure field through which the fluid particle convects is not just governed by the pressure step across the disc at the point where the fluid particle passes the disc, but by the (nonuniform) pressure step across the entire disc. As the independent annuli approach is invalid for yawed inflow, the Glauert momentum equation should, strictly spoken, not be used in quasi-differential form.

BEM for yaw: induced velocity nonuniformity correction

The invalidity of the independent annuli assumption in yaw is illustrated by Glauert's observation from his work on a momentum theory for the autogiro [60, 62] that, for a yawed actuator disc, the induced velocity is nonuniformly distributed across the disc. For a rotor in yaw, the induced velocity at a blade section, and thus the inflow at a blade section, therefore vary during a rotational cycle; the induced velocity is smaller in the upwind than the downwind region of the disc, as the upwind region of the disc is oriented away from the wake. The result is a generally stabilizing yaw moment; it intends to turn the rotor back into the wind.

To account for the induced velocity variation resulting from yaw misalignment, thereby aiming to overcome the nonphysical nature of the BEM independent annuli approach in yaw, a nonuniformity correction is applied to $\vec{V_i}$ found from Equations 2.17 and 2.18. Skewed wake correction models available in literature generally adhere to Glauert's original formulation [60],

$$\vec{V_i} = \vec{V_{i_0}} \left(1 + K \frac{r}{R} \cos\left(\theta_b - \theta_0\right) \right), \tag{2.30}$$

where $\vec{V_{i_0}}$ is the induced velocity found with the dynamic wake correction, θ_b is the actual azimuthal angle of the blade, sketched in Figure 2.6, and θ_0 is the azimuth angle where the blade is oriented furthest downstream[12]. K is a generic variable for which several formulations have been proposed, refer to e.g. Sant [147] for a tabular overview hereof. A frequently used formulation for K is that according to Coleman et al. [35],

$$K = \tan\left(\frac{\chi}{2}\right), \tag{2.31}$$

where χ is the wake skew angle, given in Figure 2.5.

Additionally, the Dynamic Inflow projects result, next to dynamic inflow tools, in a suite of wake skew correction engineering models [179, 157]. Their overall forms are generally similar to that of Equation 2.30, with differences seen in the specific reformulation of Glauert's $\left(K \frac{r}{R}\right)$-term. These engineering models for BEM are based on higher fidelity aerodynamic tools, e.g. simplified vortex wake models, and are validated with both field and wind tunnel measurements. Building hereupon, Schepers[152] presents a further refined model, based on inflow measurements by Vermeer[13]. This study is of particular relevance, because the associated experiment is the ancestor of the current work, using the same TUDelft open jet wind tunnel and a nearly identical model rotor.

---

[12]In Figure 2.6, $\theta_0 = 90°$

[13]For an overview of Vermeer's wind tunnel work, refer to [202]

Blade loads

The sectional lift force L is computed within the Blade Element part of a BEM model using a two-dimensional airfoil approach, where the sectional lift coefficient c_l is related to (the history of)[14] the sectional angle-of-attack α. The general expression for L hence is

$$L = 1/2\rho V_{rel}^2 c_l c, \tag{2.32}$$

where c is the sectional chord length. The inflow velocity relative to the rotating blade section V_{rel} is given by

$$V_{rel}^2 = \left[V_0 cos\Psi + V_{i_{n,blade}}\right]^2 + \left[-V_0 \, sin\Psi \, cos \, \theta_b + V_{i_{\theta,blade}} + \Omega r\right]^2, \tag{2.33}$$

with Ω the blade angular velocity and r the annular radius, see Figure 2.7. The composition of V_{rel} includes velocity components in the airfoil plane only; those in the rotor radial direction, perpendicular to the airfoil plane, do not contribute to V_{rel}. Note that Equation 2.33 is derived for the geometry sketched in Figure 2.6, with $\vec{V_0}$ parallel to the (x, z)-plane. To allow $\vec{V_0}$ to have any orientation, a generalized version of Equation 2.33 would have to be derived.

The contribution from airfoil drag to wake momentum change is purposely omitted from Equations 2.17 and 2.18, because the viscous nature of airfoil drag does not comply with inviscid wake momentum theory; i.e. the skin friction that causes airfoil drag does not impact the pressure distribution across the rotor disc. This approach, suggested by Wilson and Lissaman [215] and De Vries [209], is not undisputed, as e.g. airfoil stall gives rise to a substantial pressure-based drag force. Hence, both versions of the momentum equations, those in- and excluding drag, are seen in literature.

Computation procedure of an unsteady BEM code

The BEM building blocks that have been introduced need to be linked properly to arrive at a working BEM model. Whilst there is no unique way of doing things right, the computational routine presented here is typical of that used in BEM codes. The annular independency assumption of BEM allows subsequent computation of each annulus. Hence, at a given time instant after initialization, for a given annulus at radius r, for a given blade section;

1. **Inflow angle**: compute ϕ using $\vec{V_0}$ and Ω at current time instant and $\vec{V_i}$ from step 6 of the previous time instant (for a definition of ϕ, see Figure 2.7)

---

[14]In between brackets as only for unsteady airfoil models, e.g. dynamic stall models, the α-history is of relevance.

2. **Blade sectional lift**: compute L from Equation 2.32 using $\vec{V_0}$, Ω and β_{pitch} at current time instant and $\vec{V_i}$ from step 6 of the previous time instant

3. **Tip loss modeling**: compute F using ϕ from step 1 of current time instant and $\vec{V_i}$ from step 6 of the previous time instant

4. **Quasi-steady BEM**: compute $V_{i_{n,qs}}$ and $V_{i_{\theta,qs}}$ from Equations 2.17 and 2.18, respectively, using $\vec{V_0}$ and ϕ, L, F from steps 1-3, all four of current time instant, and $\vec{V_i}$ from step 6 of the previous time instant

5. **Dynamic inflow correction**: compute $V_{i_{n,0}}$ from e.g. Equations 2.24-2.27 using $V_{i_{n,qs}}$ from step 4 of current time instant

6. **Yaw induced flow nonuniformity correction**: compute V_i, from e.g. Equations 2.30-2.31 using $\vec{V_{i_0}}$ from step 5 of current time instant

7. Go to next blade section, annulus and/or time instant

Note that this scheme does not iterate to convergence of the induced velocity at given time instant. Instead, time is used to iterate as the time scales of induced velocity variations are generally larger than the temporal resolution used to model the unsteady rotor aerodynamics.

BEM concluding remarks

The discussion in this section demonstrates that BEM modeling goes with substantial simplifications of the real physics; the associated assumptions significantly restrain the validity range of turbine operating conditions. Engineering type correction models are needed to, at least in part, overcome the limitations, opening up a wide enough applicability range for BEM that, together with its computational speed, makes it the industry workhorse rotor aerodynamics tool, albeit with substantial modeling uncertainties for e.g. yaw misalignment, refer to the NREL blind comparison [173].

2.1.3   Advanced rotor aerodynamics modeling - focus on yaw

BEM is and will be the industry tool of choice for the near future. Reduction of BEM modeling uncertainties thus lowers the cost of wind energy. To this aim, improved physical insight is needed from both computational and experimental studies, as argued by Snel [175, 177] and Leishman [110] in their literature surveys.

Whilst comprehensive reviews of rotor aerodynamics models for wind turbines are given by e.g. Snel [175, 177], Vermeer *et al.* [204], Leishman [110],

Hansen *et al.* [86] and Sørensen [183], in this section the contribution of these advanced models to the understanding of yaw aerodynamics is discussed. The discussion is grouped around the acceleration potential, velocity potential and Navier-Stokes model types.

Acceleration potential models

The Euler equation for incompressible, inviscid flow relates the substantial derivative of a fluid particle to the gradient of the pressure; the pressure effectively acts as an acceleration potential function for the flow field. Assuming irrotational flow characterized by a uniform flow field with small disturbances, the Euler equation may be linearized and the acceleration potential function can be shown to satisfy the Laplace equation.

The linearized acceleration potential model has been applied to actuator disc representations of a helicopter rotor. In contrast to the steady, one-dimensional Rankine-Froude actuator disc theory, acceleration potential theory allows unsteady, three-dimensional flow. It is therefore elegantly suited for forward flight conditions[15]; Coleman *et al.* [35], Pitt and Peters [140] and Goankar and Peters [63, 64] use acceleration potential theory to propose models for skewed wake effects of helicopter forward flight.

Wind turbine studies with the acceleration potential method generally build upon helicopter work; Swift [192] applies the Pitt & Peters method to an actuator disc representation of a wind turbine rotor, thereby being the first in wind[16] to study the effects of yaw misalignment on wind turbines with acceleration potential theory. The small disturbances assumption is less applicable for wind turbines than for helicopters. Van Bussel [29] therefore derives a semi-linearized acceleration potential model for wind turbine rotors with discrete blade representation through pressure distributions, where the Laplace equation is solved by asymptotic expansion techniques. Near-wake flow velocity and rotor thrust are compared by Van Bussel [28] with TUDelft measurements on a yawed rotor that is nearly identical to the present one to find reasonable agreement in trends, but considerable bias in absolute levels.

Velocity potential models

The assumption of incompressible, inviscid, irrotational flow forms the basis for the potential flow models. Blades and wakes are modeled by a distribution of singularity elements; sources, doublets and vortices. Potential flow models

---

[15]From an actuator disc perspective, helicopter forward flight is analogous to a yaw misaligned wind turbine.

[16]According to Hansen [84].

are therefore also known as vortex wake models. For a thorough introduction to potential flow modeling, refer to e.g. Katz and Plotkin [101].

Three general subgroups can be identified within the vortex wake model family, in order of descending computational effort; panel[17], lifting surface and lifting line methods. Further, vortex wake models come in two distinct alternatives; a prescribed and a free wake method. With the former, the wake geometry is defined from e.g. measurements or semi-empirical relations and prescribed to the vortex wake model a-priori, whilst with the latter, the wake convects with the ad-hoc computed flow. The vortex wake geometry is hence implicitly computed with a free wake model. A prescribed wake method is faster to run, but its range of applicability is confined to those rotor configurations and operating conditions for which measurements are available or the semi-empirical relations hold. A free wake method is more computationally intensive, but can model configurations and conditions without the need for e.g. complimentary wake geometry measurements.

A. Panel methods

With panel models, rotor blades are represented by a distribution of sources and doublets at the blade surface and the wake is modeled by a sheet of distributed doublets. Since the exact geometry of the blade is included, sectional lift can be obtained without the need for an airfoil model. The user should specify the type of Kutta condition and its position on the blade though.

Panel methods have been applied to wind turbines for simple flow conditions in the 1980's [141, 16] and 1990's [20] and more recently for yawed flow conditions [44, 58]. Dixon [44] develops an unsteady, free-wake panel method. Geurts [58] uses Dixon's method to model a rotor with trailing edge (TE) flap actuated feedback control in yaw; compared to the reference case of no flap action, using TE flaps does not substantially reduce the unsteadiness of thrust loads during a rotational cycle in yaw.

Dixon [44] compares results from his panel method to wind tunnel measurements done within the framework of this thesis. Measured C_T and tip vortex locations up to about $1R_t$ downstream are closely predicted for both axial and yawed inflow, though the model requires an unexplained bias of $\Delta\beta_{twist} = 0.5°$ to arrive at these results. The experimentally observed absence of substantial dynamic stall for the yawed flow condition considered might in part explain the success of the code; modeling uncertainty is expected to increase with the occurrence of dynamic stall, as this panel code cannot model flow separation.

To reduce blade load modeling uncertainty over that of a normal panel method in case of separated flow, Van Garrel [56] commences the development

---

[17]Vermeer *et al.* [204], refer to the panel method as boundary integral equation method BIEM, whilst Hansen *et al.* [86] see BIEM as an equivalent alternative to panel methods.

of ROTORFLOW; a free wake panel model coupled to an integral boundary layer method. A point of fundamental concern should be raised with this type of model; for a separated flow region, where viscous effect dominate the flow, the validity of the thin vortex sheet assumption used for wake modeling is questionable.

B. Lifting surface methods

The lifting surface method simplifies the blade geometry to a lifting surface of zero thickness, coinciding with the camber lines. The most widely used subtype is the vortex-lattice method, where blade and wake are modeled as a set of panels with piecewise constant doublet distribution, which is equivalent to constant strength closed-loop vortices along the boundary of each panel. The Biot-Savart law is used to compute at any point, including locations where velocity boundary conditions are prescribed, the velocity induced by all vortex filaments. Blade lift is found either through airfoil models or through integration of the pressure across the surface with special consideration of the nose region, refer to Hansen *et al.* [86] for an introduction.

Wind turbine rotors are modeled with lifting surface methods; Kocurek [102] modifies his helicopter lifting surface prescribed wake code (LSWT code) to enable wind turbine modeling. Gerber *et al.* [57], Tangler [193, 194] and Whale *et al.* [211] all employ the LSWT model to translate blade loads, measured for axial flow conditions, into dimensionless airfoil aerodynamic properties; c_l and c_d as a function of α per blade section. Bareiss and Wagner [19] implement a free-wake vortex lattice model, which they name ROVLM. Whale *et al.* [213] compare the ROVLM code against Particle Image Velocimetry PIV measurements in a water tunnel on a model rotor in axial flow to find reasonable agreement in tip vortex trajectory and mean vorticity. Though both the LSWT and the ROVLM model are capable of modeling yaw, the author is not aware of any publications hereof.

Pesmajoglou and Graham [138] present a free wake vortex lattice method that is compared to field and wind tunnel experiments in yaw. Modeled and measured cycle averaged hub yaw moments match reasonably over a large range of yaw angles, for operating conditions where stall is expected to be of limited influence. To alleviate the computational burden of time varying yaw angle and turbulence, they further propose an indicial response method for these cases, using steady yaw computations from their code.

C. Lifting line methods

As a further simplification of the potential flow model, blade lift is lumped into a single lifting line with bound circulation Γ_b, located $\frac{1}{4}c$ from the leading

edge. Lifting line models could hence be viewed as vortex lattice lifting surface models with a resolution in blade chordwise direction of a single panel. In Prandtl's original lifting line model, Γ_b is determined from the inflow at $\frac{1}{4}c$, the appropriate $\alpha - c_l$ airfoil table and the Kutta-Joukowsky law. Alternatively, a flow tangency boundary condition can be prescribed at $\frac{3}{4}c$ to determine Γ_b directly[18]. Both approaches require the inflow at the blade, the induced velocity part of which is computed with the Biot-Savart law.

Lifting line models see wide application to wind turbines, compared to the panel and lifting surface methods. The discussion below does not intend to provide a comprehensive overview. Instead, selected studies are discussed to sketch the landscape of modeling yaw with lifting line methods.

Robison *et al.* [143, 144] develop a lifting line method named HAWT-DAWG, where the vortex wake is prescribed based on relations derived from momentum theory. Whilst for steady inflow conditions airfoil tables are used, the Beddoes-Leishman dynamic stall model [113, 114] is employed for unsteady inflow to the blades.

Two studies compare HAWTDAWG model results with measurements for both axial and yawed flow to find modest agreement; focussing on the wake, Grant *et al.* [66] find marginal agreement between modeled tip vortex trajectories and those measured in a wind tunnel. Discrepancies are in part attributed to wind tunnel wall effects; a plausible explanation as the ratio of rotor swept to test area is 0.23, which is relatively high for rotor tests in a closed test section wind tunnel.

Coton and Wang [38] compare HAWTDAWG model results to find a good match with rotor power coefficients C_P measured in the wind tunnel and modest agreement with sectional normal force coefficients C_n measured in the field. Differences with field data are attributed to the noncontrollable, partly unknown inflow conditions, to three-dimensional, rotational blade aerodynamic effects not captured with a two-dimensional airfoil model and to inadequate dynamic stall modeling.

Uncertainties associated with both three-dimensional, rotational effects as well as dynamic stall are addressed through modifications to the original Beddoes-Leishman dynamic stall model; Wang and Coton [212] use the Du and Selig correction method to update the Beddoes-Leishman model in HAWT-DAWG in order to represent three-dimensional rotational effects on unsteady airfoil aerodynamics. Beddoes-Leishman dynamic stall model uncertainty is further rooted in the substantial difference between the blade Mach number M of wind turbines and helicopters, for which the model was originally developed. To reduce modeling uncertainty for the low M of wind turbines, Sheng, Galbraith and Coton propose improvements to the dynamic stall onset criterion

---

[18]This option is equivalent to the linear model of a thin symmetric airfoil, $c_l = 2\pi\alpha$.

[170, 171] and the stall recovery mechanism [172] of the Beddoes-Leishman dynamic stall model.

Chattot [32, 33] develops a prescribed wake lifting line model for propellers and modifies it to work with wind turbines. The wake is based on the Goldstein model; regular screw surfaces are thus prescribed, without expansion and roll-up into concentrated tip and root vortices. Airfoil tables relate computed α to c_l and c_d. Using his model, Chattot [33] finds that maximization of rotor power capture at given thrust results in satisfying the Betz minimum energy condition, not at each radial station in the rotor plane, but averaged over the Trefftz plane far downstream. Besides this axial flow study, Chattot [34] also models the yawed NREL rotor in the NASA-Ames wind tunnel. Airfoil tables are used instead of a dynamic stall model. The wake is prescribed not to skew; it remains perpendicular to the rotor plane, thus ignoring the basic mechanism that governs wake deflection towards the rotor downwind side. Interestingly, sectional C_n is predicted reasonably well. Note though that the condition studied has marginal yaw misalignment; $\Psi = 10°$. In case of substantial yaw misalignment, the modeling approach to have neither a dynamic stall model nor wake skew is expected to yield considerable deviations with experiments.

Bagai and Leishman [17] present a free wake lifting line model for helicopters that Leishman [110] subsequently applies to wind turbines. Whilst the helicopter model works with a trailed vortex sheet in the near-wake that discretely rolls up into a concentrated tip vortex, the wind turbine model has a concentrated tip vortex only. Neither model includes a (concentrated) root vortex, even though inviscid theory says that the rolled-up tip and root vortices are of equal strength. Submodels for wake vortex stretching and diffusion are included. In a comparison with a BEM model, Gupta and Leishman [69] illustrate the improved capability of their lifting line tool to model the turbulent wake, vortex ring and yawed wind turbine operating states[19]. Further, Gupta and Leishman [71] model the wind tunnel measurements of a yawed rotor conducted in the framework of this thesis. Good agreement is found with tip vortex trajectories, measured up to about $1R_t$ downstream, and C_T across a range of yawed flow conditions.

The free wake lifting line code AWSM developed at ECN by Van Garrel [55] represents the wake as a vortex sheet instead of concentrated tip vortices[20]. Although the vortex wake formulation allows for instationary wake aerodynamics, an unsteady airfoil model is not implemented; airfoil tables are used instead. The modeling uncertainty of AWSM is hence expected to increase substantially for conditions where the aerodynamics are driven by

---

[19]Though this observation makes physical sense, the discussion lacks comparison with a higher fidelity (CFD) code or experiments. Pedants would argue that comparison between a BEM and a free wake code only yields relative errors, not errors with respect to the truth.

[20]AWSM is a precursor to ROTORFLOW, mentioned in the section on panel methods.

high reduced frequencies and dynamic stall. Snel and Schepers [180] compare AWSM to the MEXICO experiment, mentioned in Section 1.3, for both axial and yawed flow conditions. The comparison is inconclusive on the quality of AWSM, also because MEXICO experimental results are not thoroughly understood yet.

Sant [147] presents a free wake lifting line method, with the wake vorticity modeled as sheets of trailed and shed circulation. Blade loads, measured on the NREL rotor in the NASA-Ames tunnel, are fed to the model to arrive at sectional $(c_l, \alpha)-$ and $(c_d, \alpha)-$relations in both axial [149] and yawed inflow [150] conditions. This approach is similar to those of Tangler [193, 194] and Whale *et al.* [211], who use panel methods instead. Sant's yaw study adds physical insight though to the analysis of the experiments; he e.g. quantifies the hysteresis in the (c_l, α)-curves across the span and computes the geometry and circulation strength of the corresponding asymmetric vortex wake.

Navier-Stokes models

The Navier-Stokes equations are the direct fluid dynamic interpretation of Newton's second law, the only assumption being that the flow is a continuum. Depending on the flow problem considered, further assumptions are made, e.g. that of a Newtonian fluid or of incompressibility. Exact solutions of the Navier-Stokes equations are known for a few niche problems; the typical solution procedure consists however of discretizing the equations in the space-time domain and solving the resulting system of algebraic equations.

Of special interest is turbulence modeling; the generally large disparity in scales of flow phenomena, from the smallest turbulence scales to the largest overall scales, demands prohibitive computer resources to capture all scales with adequate resolution. Small turbulence scales are instead represented by turbulence models of reduced order, to lower computational requirements. A turbulence model is typically only suited for a specific range of flow problems; selection of a turbulence model should hence be done with due care, to limit the modeling uncertainty introduced by these semi-empiric submodels.

A somewhat related problem of scales is found in Navier-Stokes modeling of wind turbines; the rotor can be represented at three distinct scales, each one with its own level of detail, assumptions and computational requirements. In order of increasing computational cost, these are actuator disc, actuator line and detailed blade geometry modeling. This paragraph briefly touches on the three modeling options, with a focus on demonstrated performance in yaw.

A. Numerical actuator disc models

With the least demanding of three Navier-Stokes rotor modeling options, the rotor is conceptualized to a Navier-Stokes model of a porous actuator disc, where the rotor normal force is represented by a pressure discontinuity across the disc. Blades are not resolved. The model thus does not implicitly relate loads, i.e. the pressure discontinuity, to inflow at the disc. Such a relation should either be explicitly prescribed, through e.g. airfoil modeling, or the pressure jump at the disc should be frozen. Vermeer *et al.* [204], Hansen *et al.* [86] and Sørensen [183] review numerical actuator disc studies. For details on a typical numerical implementation, refer to Mikkelsen's PhD thesis [128].

The numerical actuator disc approach shows its value when modeling e.g. coned rotors [130] and turbulent wake and vortex ring states [188], when deriving wind tunnel wall corrections [187] or when assessing the validity of BEM methods [184]. The approach is further applied to compute rotor interaction in a wind farm [97, 14]. Whilst wind farm studies address yawed inflow, the analysis is complicated by wake interaction and effects of the turbulent atmosphere that both are generally included in the modeling.

Numerical actuator disc modeling is applied to yawed flow as well; Mikkelsen and Sørensen [129] model a yawed numerical actuator disc with unsteady, axisymmetric Navier-Stokes equations, where the disc loads acting on the flow are introduced through body forces that are computed with a blade element model; the inflow to a blade, computed with the Navier-Stokes equations, is fed to airfoil tables. The disc loading at given radial station is then taken to be the average of all blade loads for that radial position. Results agree reasonably with blade root flap moment measurements on the Tjæreborg 2MW field turbine in nearly axial flow and yaw. The agreement in yaw can be considered remarkable since the axisymmetric equations do not capture wake skewness, a dominant flow feature in yaw that governs the variation of inflow at a blade during a rotation. Mikkelsen [128] a.o. substitutes the steady airfoil table method with the unsteady Øye dynamic stall model to find somewhat improved prediction of the Tjæreborg measurements.

The method by Leclerc & Masson [107] does not assume axisymmetry, but employs the unsteady, *three-dimensional* Navier-Stokes equations to model an actuator disc subject to yaw. The model hence predicts a skewed wake in yaw. Disc loads are introduced in the Navier-Stokes equations through a stress discontinuity at the actuator surface, that is quantified by a blade element method; the Gormont dynamic stall model. Comparison of model results to sectional loads in yaw measured with the NREL Combined Experiment field test suggests the unsuitability of the Gormont model for this application. As a testimony to its ability to model skewed wakes, this actuator disc method is shown to predict a cyclically varying axial induced velocity at given radial

location on the disc, in accordance with Glauert's momentum studies [60] mentioned in Section 2.1.1.

The numerical actuator disc method has the potential to implicitly model an unsteady, asymmetric wake. The representation of the rotor by a disc obscures flow phenomena on the scales of blades and airfoils though. An actuator disc approach thus captures first order flow physics; for higher order effects, the blades would have to be resolved.

B. Actuator line models

Sørensen and Shen [186] propose a method where the flow is governed by the unsteady, three-dimensional Navier-Stokes equations and the rotor blades are represented by actuator lines; the detailed blade shape is not resolved. Blade loads are determined by means of a blade element method, using the inflow computed at the actuator lines, and are introduced in the Navier-Stokes equations as body forces locally near the lines.

As a first demonstration of its capabilities, a Nordtank 500 kW turbine is modeled with the actuator line technique [186]; next to rotor power and spanwise loads, detailed wake structures are captured as well, including tip and root vortices and the associated nonuniform induced velocity field near the rotor plane. A more detailed introduction into the actuator line method is given in Appendix C.

The actuator line technique is used for a range of applications; Mikkelsen [128] studies coned rotors and rotors in a closed wind tunnel test section to confirm observations from numerical actuator disc modeling. Stability and breakdown mechanisms of the vortex wake system going with a three bladed turbine are studied by Ivanell *et al.* [96, 98] as part of Ivanell's PhD-thesis [95]. An empirical relationship between turbulence intensity and wake breakdown is suggested, that should be tuned with experiments. Troldborg's PhD thesis [197] focusses on wake modeling of both solitary and clustered wind turbine rotors with the actuator line technique. In the wake of his thesis, Troldborg *et al.* [199] present the wake downstream development for a rotor subject to axial flow operating in turbulent wake and windmill states, thereby finding good agreement with C_P-measurements on the Tjæreborg turbine[21]. They further demonstrate the dominant role of atmospheric turbulence in the process of wake breakdown [198]. Mikkelsen *et al.* [131] study wake interaction in farm configurations. Similar to numerical actuator disc results, wake interaction complicates the interpretation of the aerodynamics of a yawed rotor.

Mikkelsen [128] studies a solitary rotor subject to yaw with the actuator line model. The yawed Tjæreborg turbine is modeled and compared to

---

[21]The different wake states are achieved for the constant speed Tjæreborg rotor by varying V_0 and hence λ; the turbulent wake state is found for $\lambda = 11.78$, corresponding to $V_0 = 6\,m/s$.

field measurements. Mikkelsen [128] also models these experiments with the numerical actuator disc model, where the wake is represented by the axisymmetric Navier-Stokes equations. Actuator line predictions are generally closer to measured blade root flap moments than actuator disc results, especially for the high yaw angle of $\Psi = 54°$; an observation that is attributed to the three-dimensional Navier-Stokes equation of the actuator line model that captures the skewed, three-dimensional wake structure, in contrast to the axisymmetric variant of the actuator disc model. The wake is furthermore found to develop into two dominant vortex structures in the far wake, resembling the far wake of a helicopter in forward flight.

C. Blade shape resolving models

With the actuator line approach, the wake flow is governed by the unsteady, three-dimensional Navier-Stokes equations; the aerodynamics of the wake trailing the blades is hence implicitly modeled properly. Blade aerodynamics however rely on two-dimensional airfoil models. To make explicit airfoil models redundant and hence eliminate this source of uncertainty, the detailed blade shape should be resolved within a Navier-Stokes model.

The grid required to capture both the blade boundary layer as well as the rotor wake typically exceeds $5 - 10 \cdot 10^6$ nodes, even when modelling axial inflow with the periodicity assumption that effectively reduces the computational domain by a factor of B, with B the number of blades; fully resolved Navier-Stokes modelling hence comes with high computational costs.

Navier-Stokes solutions for wind turbine rotors are presented mainly for steady axial flow conditions. For a relatively early CFD study, refer to e.g. Sørensen and Hansen [190] who relate differences with measurements to turbulence modelling and low spatial resolution near the blades. Whilst ongoing developments in computing hardware relax the grid size constraint somewhat, this comes at the expense of computational time, that generally grows with grid size [22]

To reduce the computational demands of Navier-Stokes modeling, overset methods are used, where nodes are clustered flexibly in those regions where strong solution gradients are anticipated. For examples of this approach, refer to Duque *et al.* [46] and Zahle [219]. Of special interest is the study by Iida *et al.* [94]; they apply an overset method to model the rotor that is used for the wind tunnel tests performed within the framework of this thesis. Reasonable agreement is found with experimental rotor torque and thrust across a λ-range. Comparison with BEM modeling leads to the suggestion

---

[22]For an extremely high resolution grid, see Fleig *et al.* [53] that present a Large Eddy Simulation of a wind turbine rotor at startup on a grid with $0.4 \cdot 10^9$ nodes.

that BEM over-predicts the induced velocity locally at tip and root. Whilst this observation is not disputed, the analysis does not disclose its causes.

An alternative approach to speed up Navier-Stokes codes is to limit Navier-Stokes modeling to the near-wake; flow in the far-wake is modeled with a simpler, computationally lighter model. Rather than "Navier-Stokes" methods, a more appropriate name would be e.g. "hybrid Navier-Stokes" for this family of rotor aerodynamics methods. Hybrid Navier-Stokes codes with a range of far-wake models are presented; for potential flow far-wake models, refer to Xu and Sankar [216] and to Schmitz and Chattot [160], where the far-wake is modeled with prescribed inviscid tip vortices and vortex sheets, respectively. Hansen *et al.* [88] use an axisymmetric Euler model in the far-wake.

The added value of Navier-Stokes modeling is exemplified in a study by Sørensen *et al.* [191]; for a high speed axial flow condition of the UAE Phase VI wind tunnel tests, blade flow is quantified with CFD to support measured blade pressure distributions. The CFD results thereby enlighten the mechanism driving local stall at the blade mid span, an observation that could not be obtained from pressure readings alone.

Where Navier-Stokes models are computationally intensive in axial flow, they become even more so in yaw; here, the computational domain cannot be reduced by a factor of B using periodic boundary conditions, with B the number of blades, nor can a steady formulation be applied[23]; the flow is asymmetric and unsteady in yaw.

Madsen *et al.* [116] compare Navier-Stokes results in yaw to measurements on both the NREL Phase VI tunnel measurements and a 100kW field test to find promising results, especially for the former test case. The validation is limited to spanwise inflow angles though, no sectional loads are e.g. considered. Hence, despite the agreement found for the inflow angles, the sparsity of the validation constrains a balanced assessment of rotor aerodynamics modeling quality.

To counter the high computational cost of yaw modeling, hybrid Navier-Stokes codes are used, at the expense of physical correctness. Xu and Sankar [217] modify their hybrid Navier-Stokes model, with a potential flow far wake model, from use in axial to yawed flow conditions. This model is also employed by Tongchitpakdee *et al.* [196] to study yaw; the NASA-Ames experiments of the NREL Phase VI rotor are modeled to find reasonable agreement in spanwise loads, for yaw angles from $0°$ to $45°$ and high λ-conditions that are associated with limited flow separation and stall. The agreement worsens substantially for reduced λ, when the blades are experimentally shown to exhibit large regions of dynamic stall. More advanced, more computationally

---

[23]An observer rotating with the blades experiences a steady flow field for a rotor operating in the wind turbine state, subject to axial flow. The unsteadiness of the turbulent far-wake is omitted here for simplicity.

intensive turbulence models improve the prediction. Whilst Tongchitpakdee *et al.* [196] demonstrate interesting yaw results, a mayor limitation is its narrow scope; only time averaged results are discussed, despite the strong unsteady phenomena associated with yawed flow.

Navier-Stokes models that resolve the blade boundary layer have the potential to disclose a wealth of information on rotor flow physics. Their computational costs are high though, even when simplifying to a steady, periodic problem for axial inflow. Some alleviation is found through the introduction of hybrid Navier-Stokes models. Yawed flow conditions on a utility scale wind turbine rotor present a true challenge for Navier-Stokes models. This might also explain the relative scarcity of publications on the topic.

2.2   Wind tunnel experiments

Next to modeling, physical insight can also be obtained from measurements, often in conjunction with model predictions. As argued in Section 1.2.1, the wind energy scientific community currently prefers wind tunnel above field tests to study fundamental rotor aerodynamics; the benefits of a controlled, known environment trade favorably with the disadvantage of Re-dissimilarity. This literature review thus focusses on wind tunnel work, with the objective to discuss yawed flow results. Axial flow measurements are briefly touched upon, as these form the reference for yawed flow studies. For a comprehensive review of wind tunnel work on rotors in axial flow, refer to Vermeer *et al.* [204].

The aerodynamics of a rotor is characterized by strong coupling between blade and wake flow. Quantification of both is needed to understand the rotor flow. However, wind tunnel experiments typically focus on either the blade or the wake. Universities generally engage in wake measurements on rotors up to say 1 m diameter, too small to reasonably equip with pressure taps, using their own wind tunnels. Loads are typically only recorded at the level of the rotor, i.e. rotor torque and thrust, not at the level of blade sections. Wake experiments are reviewed in Section 2.2.1. Detailed blade load measurements are conducted on larger scale rotor models, with diameters up to a few meters, in industrial wind tunnels. The two main examples hereof are the UAE Phase VI and MEXICO campaigns that are further discussed in Section 2.2.2.

2.2.1   Wake

The majority of rotor wake experiments focus on axial flow. These are the reference for yawed flow experiments, both in terms of flow physics as well as measurement techniques, and are thus briefly addressed here, next to yaw studies.

The rotor wake can be thought of as a vortex system, with bound vorticity at the rotor blades that trails and sheds from the blades to form sheets of vorticity convecting with the flow. These vortex sheets generally organize themselves into a distinct tip vortex, whilst the root vortex is typically less pronounced. The region downstream of the rotor where tip vortices are formed, up to the, relatively arbitrary, location where effects of the individual blades are no longer noticeable, is called the near-wake. In the succeeding far-wake, vorticity is convected further downstream and is ultimately dissipated.

Wake measurements can be characterized into near- and far-wake types. In this thesis, we stay close to the rotor, recall the objectives in Section 1.3 on quantification of and insight into rotor inflow and loads in yaw. This review hence focusses on near-wake measurements.

Tip vortices

The experimental investigation of tip vortices is justified from their dominant influence on the essence of rotor aerodynamics; tip vortices drive the induced velocity in the rotor plane and thus blade loads.

For a review of tip vortex measurements, refer to the wake aerodynamics review of Vermeer *et al.* [204]. Tip vortices can elegantly be visualized by simple smoke injection into the streamtubes passing the tips, as this technique yields intuitive pictures. E.g. Montgomerie and Dahlberg [132] present smoke visualization in axial flow. Tip vortex trajectories in axial flow conditions are further reported by amongst others Vermeer [202], Whale *et al.* [213] and Grant *et al.* [66]. The former uses hot-wire Constant Temperature Anemometry (CTA), the latter two employ Particle Image Velocimetry (PIV). All these measurements clearly show the widening tip vortex paths going downstream, as expected for the expanding wake of a wind turbine rotor.

Notable is the experimental campaign by Ebert and Wood [48, 49, 50], where the near-wake is measured using CTA. Their wide range of operational conditions tested, focus on both hub and tip vortices as well as mid-span flow velocity and attention to minimization of measurement uncertainty would qualify their data for study of near-wake phenomena and model validation. The cross-section of the open jet outlet equals the model rotor diameter however; the resulting large, but uncorrected, wind tunnel wall effects severely complicate interpretation of observed tip vortex phenomena [49, 50] to unconstrained rotors and general model validation.

With the turbine operating in yaw, the skewed tip vortex trajectories are studied by Grant *et al.* using visualization [68] and PIV [66]. Grant and Parkin [67] furthermore employ PIV to determine velocity and circulation of tip vortices in yaw.

The MEXICO project [158, 181] deserves to be mentioned in this overview

of tip vortex experiments; the experimental campaign where a $4.5m$ diameter rotor is tested in the $9.5m$ by $9.5m$ open jet test section of Large Scale Low Speed Facility LLF, part of the German Dutch wind tunnel DNW complex, is only rivalled in size by the UAE Phase VI tests on a $10m$ diameter rotor in the NASA-Ames tunnel [52]. MEXICO is unique though in the combination of detailed load and flow field recordings that are furthermore taken at a number of operating conditions, including yaw. The discussion on MEXICO tip vortex measurements is combined with the overall review of the campaign in Section 2.2.2.

Flow velocity

Wake vorticity feeds back to rotor loads through the induced velocity component of the inflow at the blades; rotor inflow measurements are thus relevant. BEM and lifting line vortex wake models use the inflow *at* the blade 1/4-chord line as input to the blade models. The flow velocity at 1/4-chord line does not make practical sense, as this line is located in the blade interior.

The flow velocity could be measured near the blade surface, close to the 1/4-chord location, to try to find the inflow as used in blade models. Next to the technical challenges of measuring close to a blade surface, the recorded flow velocity would be dominated by the influence of the blade. This contribution should in fact be omitted when determining the inflow as used in blade models. Measurement of the flow velocity across the near-wake, including the rotor plane, is more valuable, as it allows the inflow velocity used in blade modeling to be estimated and the downstream development of the wake to be studied.

A distinction must be made between time and cyclic averaged measurements. Recording data at a fixed, non-rotating position in the wake, the former method averages over all points in the data set. The latter method averages over the data points sampled per rotor azimuth angle. Cyclic, or phase locked, averaging PLA captures periodic wake unsteadiness, e.g. associated with blade passages; information that is lost with time averaging.

The first generation of wind tunnel measurements on rotor wakes concerns time averaged flow velocity recorded with pressure tubes, refer to Vermeer *et al.* [204] for an overview and to De Vries [210] for an example. Typically, the downstream development of the wake velocity deficit and wake expansion are disclosed. Later work by Vermeer and De Boer [203], in the context of the EU Dynamic Inflow projects, uses CTA to demonstrate the nonuniformity of time averaged near-wake flow velocity [24] in yaw. The study is of particular interest, as the model rotor used is nearly identical to the one used for present experiments. Time averaged flow velocity is also presented in recent work by

---

[24]Vermeer and De Boer [203] use dual-sensor hot-wire CTA, but it is unclear what reported velocity refers to; e.g. the axial velocity component, total velocity or effective velocity.

Parkin *et al.* [137], Dahlberg and Medici [42] and Medici and Alfredsson [124], all three using PIV and the latter two also supported by CTA. These three studies include yawed flow conditions, where they illustrate the associated asymmetry of the time averaged wake.

PLA near-wake flow velocity measurements are reviewed by Vermeer *et al.* [204]. Results include flow velocity patterns observed with the passage of a blade and its trailing wake for a fixed point in the inertial frame of reference. PLA CTA and PLA Laser Doppler Velocimetry LDV are the measurement techniques of choice for these studies. It should be mentioned that whilst the tip vortex part of Ebert and Wood's CTA-based experiments [48, 49, 50] is discarded for reasons of too large wind tunnel interference, the PLA flow velocity results in the mid-span region and the discussion hereof remain relevant; flow velocity trends with e.g. blade passage are similar to those found for measurements with substantially smaller wind tunnel interference.

Experimental studies published after the review [204] by Vermeer *et al.* include work by Massouh and Dobrev [118] and Massouh, Dobrev and Rapin [119], where PLA PIV and PLA CTA are employed. Both the general near-wake velocity field as well as tip vortex details are addressed. Results are in overall agreement with previously published observations. The MEXICO project further addresses, next to tip vortices, the inflow in the rotor plane, using PLA PIV, as will be discussed in Section 2.2.2.

Anticipating this discussion, it must be stressed that for yaw, MEXICO publications only mention the availability of PLA flow velocity recordings; no actual results are shown. To the author's knowledge, only Vermeer and De Boer [203] report near-wake phase-locked flow velocity in yaw. Despite the interesting observation that phase-locked flow velocity patterns depend on the wake azimuth, the results come with serious remarks. Only one cycle is recorded, thus disallowing determination of a PLA; only PL-data can be quantified. Further, the selected CTA implementation is unfit for the three-dimensional flow typical of skewed wakes. Both aspects contribute to measurement uncertainty, which is not quantified but expected to be significant. Lastly, use of a single measurement plane prevents the study of wake downstream convection, which is expected to be nonlinear in yaw.

Wake meandering

Medici and Alfredsson [123, 124] perform wind tunnel measurements of the flow velocity at stationary positions in the far-wake of a wind turbine model rotor with CTA to find an oscillation frequency that is an order of magnitude lower than those associated with tip vortex passages. These low-frequency flow velocity fluctuations hint at wake meandering, which Medici and Alfredsson [123, 124] hypothesize to be similar to the vortex shedding occurring in the

wake of a solid disc.

Vortex shedding phenomena are characterized by their Strouhal number St,

$$St = \frac{fL}{V_\infty}, \qquad (2.34)$$

with f the shedding/meandering frequency, L a characteristic length and V_∞ the freestream velocity. For rotor wake meandering, L is taken to be the rotor diameter D. The Medici and Alfredsson experiment demonstrates that wake meandering only occurs above a certain λ-threshold. Having passed the threshold, St associated with the meandering is a function of λ that for axial flow converges to $St = 0.12$; a value that is similar to that reported for solid disc vortex shedding. Medici and Alfredsson [123, 124] disclose wake meandering in yaw as well. In accordance with solid disc work, St is found to increase with yaw angle, though the study does not specify whether St of the yawed rotor refers to a converged value or still displays λ-dependency.

Sørensen and Okulov [185] use an analytical wake model to reproduce the flow velocity signal as measured by Medici and Alfredsson [123, 124], thereby confirming that wake meandering is indeed the phenomenon governing the recorded velocity pattern.

The mechanism that drives meandering is not disclosed though, as the vortex wake model is explicitly tuned to match measured velocity. It can i.e. not be confirmed that vortex shedding analogous to that for a bluff body/solid disc is responsible for the wake meandering observed by Medici and Alfredsson [123, 124]. Another driver may be atmospheric boundary layer turbulence, as illustrated in wind tunnel tests by Espana *et al.* [51]. Studies from the 1980's based on field data appear to hypothesize wake meandering to be caused by variations in wind direction, refer to the brief review by Larsen *et al.* [106]. The alternative hypothesis of solid disc vortex shedding is not addressed though. Note that Larsen *et al.* [106] also base their own wake meandering model on the assumption that meandering is driven by atmospheric turbulence, where they argue that the wind tunnel experiments of Medici and Alfredsson [123, 124] are not representative for field conditions due to too low ambient turbulence and too high turbine loading.

The suggestion that in the field, "random" meandering due to atmospheric boundary layer turbulence dominates "harmonic" meandering analogous to solid disc vortex shedding does not address occurrence and impact of wake meandering for wind tunnel measurements on the near-wake of model wind turbine rotors. Medici and Alfredsson [125] extend their wind tunnel experiments of [123, 124] to present operating regions, defined by the number of blades, λ and C_T, where wake meandering occurs.

These experimental findings are based on measurements $2R_t$ downstream of the rotor though. Under the assumption of gradually amplified meandering

43

whilst the wake convects downstream, it seems reasonable to assume that, in case turbine conditions suggest wake meandering according to [125], the near-wake region substantially closer to the rotor than $2R_t$, is only marginally affected by wake meandering.

2.2.2 Blade

Load distributions along the blade of model wind turbine rotors are measured for three wind tunnel campaigns, see Table 2.1. The Aeronautical Research Institute of Sweden FFA measurements in the China Aerodynamics Research and Development Center CARD tunnel have the least extensive set of operational conditions and, in contrast to the other two campaigns, lack inflow measurements along the blade. The FFA tests also see least exposure in scientific literature. This section thus omits a detailed FFA discussion and only focusses on the NREL and MEXICO measurements.

Table 2.1: Wind tunnel tests of blade loads on model wind turbine rotors

	FFA	NREL UAE Phase VI	MEXICO
Rotor diameter	$5.35m$	$10m$	$4.5m$
Test section size	$12m * 16m$	$24m * 37m$	$9.5m * 9.5m$
Open jet/closed	closed	closed	open jet
Tunnel owner	CARDC	NASA-Ames	DNW
Year of test	1989, 1992	2000	2006
References	Ronsten [145] Dexin *et al.* [43]	Fingerish *et al.* [52]	Schepers *et al.* [181]

NREL Phase VI

Between 1987 and 1999, NREL conducted field tests on a $10m$ diameter, $20kW$ rated, stall control wind turbine, referred to as the Combined Experiment [31, 30] and the Unsteady Aerodynamics Experiment UAE [174, 82]. Tested turbine configurations include e.g. upwind and downwind settings, 2- and 3-bladed rotors and tapered and rectangular blades.

In the spring of 2000, NREL tested this field turbine in a NASA-Ames facility with $24m$ by $37m$ closed test section. The turbine rotor is configured with 2 twisted and tapered blades that have a single airfoil; the S809 designed by NREL. Both the upwind and downwind setting are tested. Operating conditions include axial and yawed inflow, as well as dynamic events, e.g. fast

pitch, and parked blades. Hand *et al.* [83] discuss turbine configurations and data recordings in detail.

One blade is instrumented with flush-mounted pressure taps; these are both placed on the suction surface in pairs of 2 at 10 spanwise stations and in a distribution across the chord from leading to trailing edge at another 5 spanwise stations. Measured pressure distributions at the 5 sections are correlated to inflow through recording of local inflow angles LFA and dynamic pressures near these 5 stations using five-hole pressure probes on prongs. It must explicitly be noted that the LFA does not equal the angle of attack α.

The NREL Phase VI measurements are instrumental for the wind turbine aerodynamics scientific community, addressing flow phenomena that are relevant for power production and loads of utility-scale wind turbines in a structured manner with emphasis on measurement uncertainty. Worldwide research efforts are organized within the framework of the IEA Annex XX that finished in December 2008 with the issue of a final report [161].

A first insight from the measurements concerns the blind comparison of Simms *et al.* [173], introduced in Section 1.2.2. Even the presumably straightforward axial flow conditions without stall appear difficult to model, with large variation amongst the participating BEM, vortex wake and CFD codes and between modeled and measured data. For more complicated cases with stall and/or yaw, the agreement worsens.

The best performing code of the blind comparison, a blade resolving Navier-Stokes model presented by Sørensen *et al.* [191], does yield reasonable predictions of distributed loads. Only axial flow results were submitted to the blind comparison however, yaw could not be handled at the time. Later work by Madsen *et al.* [116] on the same code does present yaw results; across the span, modeled unsteady LFA generally shows good correlation with measurements at $45°$ yaw and $7m/s$ wind speed. Whilst the agreement suggests that this CFD code adequately captures blade aerodynamics in yaw, this cannot be confirmed as a comparison of sectional blade loads is not included.

Causes for the generally poor performance of the participating models are categorized in blade or wake related, analogous to the constituting elements of BEM and vortex wake models. Starting with the blade, Simms *et al.* [173] point out that synthesis of airfoil tables from available sets of wind tunnel data, including corrections for stall delay effects, adds considerably to modeling uncertainty.

Axial flow studies by e.g. Tangler [193] and Sant *et al.*[149] confirm that the blade model introduces a significant contribution to the model uncertainty. Further confirmation is given by Coton *et al.* [39] in a comparison with their HAWTDAWG vortex wake model[25] for both axial and yawed flow

---

[25]refer to Section 2.1.3 for details on this code

conditions, where they add that including a dynamic stall model improves predictions. Leishman [110] notes, in reaction to the blind comparison results, that unsteady blade aerodynamics require continued consideration. He also emphasizes though that dynamic stall cannot be understood in isolation from wake dynamics.

Focussing on wake modeling uncertainties, Leishman [110] argues that vortex wake codes yield more physical models of three-dimensional, unsteady rotor wakes; a hypothesis that is generally accepted in the wind turbine rotor aerodynamics research community. The blind comparison does not yield convincing evidence though. Both BEM and vortex wake codes perform generally rather poor in e.g. yaw, which can be attributed to the uncertain blade models shared between the 2 code families. Further note that the NREL Phase VI campaign is not ideally suited to validate or benchmark wake submodels, as flow data is only available at the 5 probe locations near the blade. Tip vortices are e.g. not recorded.

The experimental analyzes that are of relevance to the current yaw-oriented study include those on stall delay in the root region and dynamic stall. Schreck and Robinson [162, 163] compare data for a parked blade with that for a rotating blade subject to axial flow to find dramatically increased loads and altered pressure distributions due to rotation. The effects are strongest near the root but persist up to at least 50% span. Similar results are presented by Gonzalez and Munduate [65], where the comparison is furthermore extended to include 2d airfoil data.

Dynamic stall is addressed by Schreck *et al.* [164, 166]. Operating conditions with nonzero yaw angle that experience dynamic α-excursions beyond the static stall α are selected. A study of the unsteady loads reveals the substantial hysteresis, including an overshoot compared to static stall. Pressure distributions further record the downstream convection of the dynamic stall vortex from leading towards trailing edge. This vortex appears to be of a three-dimensional nature, with spanwise deformation of the vortical structure. Note that the experimentally observed three-dimensionality of dynamic stall is currently not comprehensively included in airfoil dynamic stall modeling.

MEXICO

An EU-sponsored research collaborative [158] performs extensive blade and wake measurements in on a $4.5m$ diameter model rotor in a DNW open jet wind tunnel with $9.5m$ by $9.5m$ test section in December 2006. Each of the three rotor blades is instrumented with Kulite dynamic pressure sensors, chordwise distributed at spanwise sections that partly overlap between the blades, thereby allowing for data repetition checks. In all, pressure distributions are recorded at 5 spanwise stations. Loads are further measured at the

blade roots with strain gauges and at the tower base with a balance.

Next to these load measurements, near-wake PLA PIV measurements are conducted; both the inflow in the rotor plane as well as near-wake tip vortices are recorded. Combined blade loads and flow velocities are recorded for a range of axial and yawed flow conditions. The interdependence of blade and wake aerodynamics motivates the value of having both load and flow velocity measurements. As illustrated in this literature survey of wind tunnel tests on model rotors, MEXICO is in a unique position with its combination of measurements.

Project delays result in minimal analysis of the experimental data within the framework of MEXICO [158]. More substantial efforts are coordinated instead through the currently ongoing IEA Annex 29, entitled Mexnext[26]. Since Annex 29 is a work in progress, this paragraph cannot present a comprehensive review. Instead, a status-update is given, with a focus on flow physics, not model validation, studies.

Snel *et al.* [182, 181] present initial results; sectional pressure distributions, the inflow in the rotor plane and tip vortex trajectories are sketched.

A more detailed analysis by Schepers *et al.* [156] includes a basic comparison of axial rotor loads, determined from blade pressure and balance measurements, yielding good agreement. PLA PIV inflow measurements in axial flow conditions demonstrate the deceleration of the flow through the rotor, commencing about one rotor diameter upstream and reaching an equilibrium about one rotor diameter downstream of the rotor. Overall flow deceleration is reasonably well modeled by a simple cylindrical vortex wake code with constant bound vorticity in the rotor plane, similar to an actuator disc. Inflow at and near the rotor plane however typically defies predictions with this simple model. Trends in the PLA flow measurements near the rotor plane during a cycle agree with those presented in e.g. the review by Vermeer *et al.* [204].

In yaw, recorded tip vortex trajectories reveal the skewed wake pattern characteristic of misaligned flow conditions, with stronger wake expansion at the downwind than the upwind side of the rotor. Flow velocity recordings in the mid-span region further clearly demonstrate the highly asymmetric flow patterns in yaw.

Schepers *et al.* [156] further present, for the design axial flow operating condition, tip vortex circulation at different downstream locations, found from the integral of measured flow velocity along contours enclosing the vortex core; tip vortex circulation remains approximately constant going downstream, whilst the vortex core diffuses, as expected for the near-wake up to about 1 radius downstream. Tip vortex circulation is also compared to bound circulation at the blade. Though the agreement is interesting, the comparison has to be

---

[26]For details, see http://www.mexnext.org/resultsstatus/

reviewed with caution, because of the simplistic approach to base blade inflow on one-dimensional momentum theory in the derivation of bound circulation, even though inflow measurements are available.

MEXICO analysis by Schepers *et al.* [151] focusses on Navier-Stokes model based studies of wind tunnel effects, suggesting that these are negligible at design operating conditions. Effects are not quantified, though. Further, wind tunnel effects are not studied at high λ, where the turbulent wake state with its associated high C_T is approached, whilst this condition would suffer most from tunnel effects. More study is hence needed to get a comprehensive, quantified understanding on tunnel effects.

The article also briefly compares measured inflow and loads with results from rotor aerodynamics models to yield, according to the authors, contradicting findings; whilst induced velocity in the rotor plane is under-predicted, thrust is over-predicted. Inflow velocity is however presented at a single blade azimuth angle only. The average inflow velocity across an annulus would be a more representative metric of wake momentum loss.

Schepers *et al.* [151] further present rotational augmentation of the normal force on the inboard part of the MEXICO rotor. This phenomenon is analyzed in-depth by Schreck *et al.* [165], including a comparison with stall delay on the UAE Phase VI rotor, tested in the NASA-Ames tunnel. General similarities are observed in the steepening of the C_n-α curve for attached flow and the delayed stall and amplified C_n for partly separated flow at higher α. Chordwise pressure distributions suggest markedly different stall mechanisms however; trailing edge separation for the MEXICO rotor and leading edge separation with subsequent shear layer impingement for the UAE Phase VI rotor. These differences in stall are attributed to the variation in airfoil shape between the two rotors.

2.3 Measurement analysis tools

The interpretation of rotor experiments is generally complicated by inadequate information on wake and/or blade aerodynamics; both are needed to close the loop on rotor aerodynamics. Tools developed to aid in the analysis of such "incomplete" rotor measurements are briefly reviewed here. Methods to derive sectional α are discussed first in Section 2.3.1, whereafter tools that also estimate sectional blade loads are presented in Section 2.3.2.

2.3.1 Angle of attack in blade & wake measurements

BEM and vortex wake methods utilize airfoil models to determine sectional loads for a given inflow distribution in the rotor plane. Airfoil models typically require the input of sectional α.

For a two-dimensional airfoil, α is defined as the angle between the undisturbed flow and the chord. On a rotating blade however, a revised definition should be used, due to additional flow velocity components from blade motion - including the bent streamlines from blade rotation - and induced by the three-dimensional wake vortex system.

Use of α in rotor aerodynamics codes is limited to BEM and vortex wake models, thus justifying a definition of α within the context of lifting line theory. On a rotating blade, α could be defined as the angle in the plane of the airfoil section between the chord and the inflow velocity at $1/4c$, given by the vectorial summation of undisturbed flow velocity, relative flow velocity from blade motion and induced velocity from the vortex wake, except the contribution from the bound vortex *at* the given section.

Sectional α cannot be measured directly, because its definition is based on the flow velocity *at* the theoretical lifting line. Tools have thus been proposed to estimate α for rotor measurements.

First however, a work-around; issues with the definition of α are avoided by using an alternative sectional inflow angle that is measurable and explicitly described for the experimental rotor. Schreck and Robinson e.g. take this approach to discuss the NREL UAE Phase VI NASA-Ames tests [162]. Such a method is generally limited to study experimentally observed flow phenomena, instead of model validation, as the inflow angle correlates, but is not identical to α.

When both blade loads and the rotor wake velocity at least a single point near the blade are recorded, a combined load-velocity method by Shen *et al.*[167] could be applied to estimate α. Hua *et al.* [92] apply Shen's method to the MEXICO rotor to derive airfoil characteristics at various blade sections that are subsequently used in a BEM model of the MEXICO rotor. Despite the coarse resolution of the resulting blade sectional aerodynamics, the agreement between measured and modeled normal force is encouraging, thus suggesting the usefulness of Shen's method to find α.

Combined measurements of blade and wake are scarce and Shen's method therefore sees limited applicability. For measurements of the rotor wake only, Hansen *et al.* [87] present a method to determine α that is based on the azimuthal averaged axial velocity in the near-wake.

Methods that only require load recordings to find α include an approach by Van Rooij *et al.*[146] based on blade pressures. Further, both Whale *et al.* [211] and Tangler [194] use a prescribed wake lifting surface method to estimate α from measured loads only. Similarly, Sant *et al.* propose a free wake lifting line method and apply it to find α for the NREL UAE Phase VI rotor in axial [149] and yawed conditions [150].

The combination of measured loads and estimated α enables the sectional lift and drag to the determined on the rotating blade. Contrary to airfoil data

obtained through two-dimensional wind tunnel tests, these airfoil characteristics implicitly include three-dimensional and rotational effects; their use in BEM and vortex wake codes could thus assist to reduce the substantial modeling uncertainty introduced in these codes by blade models.

2.3.2   Angle of attack & loads in wake measurements

The conditions at the rotor blade are not directly measured for rotor wake experiments. Methods based on inviscid, incompressible vortex theory are proposed in literature to derive blade loads and the corresponding α. This theory allows the flow velocity at any point in a domain to be be expressed as the vectorial summation of flow velocity induced by all circulation in the domain, found through the Biot-Savart law, and a uniform flow velocity.

An analysis tool by Vermeer and Van Bussel [208] approximates the strength of the bound circulation on the blade for axial flow conditions. The measured velocity is assumed to only have induced velocity contributions from the bound circulation, with the blade represented by a two-dimensional translating line vortex. The Biot-Savart equation is solved for the bound circulation strength. Vermeer [207] subsequently incorporates three-dimensional effects to the model; the blades have finite length, bound circulation is allowed to vary in spanwise direction and the blades rotate. Wake circulation effects are however not included.

Conservation of circulation is applied in a measurement analysis model by Mast *et al.* [120, 122], where the induced velocity is modeled to include contributions from both bound and trailed circulation. The vortex wake geometry is reconstructed from measurements. A Legendre polynomial function series represents the bound circulation distribution. The method is referred to as an "inverse vortex wake method", since the complete blade-wake vortex system is considered, where the term "inverse" indicates it's use as a measurement analysis tool, instead of a prediction tool. The shapes of the Legendre polynomials are not ideally suited to represent the bound circulation distribution, adding computational effort. The model is further only applied in axial flow.

2.4   Conclusions

The workhorse aero-servo-elastic models all base their aerodynamic part on BEM theory. The review of BEM modeling highlights the engineering fixes applied to correct for the violation of the assumptions underlying BEM theory when modeling dynamic and/or asymmetric flow conditions.

In contrast to BEM codes, the vortex wake methods implicitly model wake unsteadiness and asymmetry in a physically sound manner, especially with the free-wake formulation. Their blade models are essentially equal to those used

in BEM codes though; blade related modeling uncertainties are hence not reduced compared to BEM. Comparisons with measurements yield mixed results, where especially for yawed flow conditions the fair agreement is thought to originate from uncertainties related to blade modeling.

Navier-Stokes equations based methods provide an attractive alternative from the perspective of physically correct modeling; both concerning the wake and blade. Their excessive computational demands however restrain widespread use in an engineering environment. At present time, they should serve the purpose of providing increased physical understanding of rotor aerodynamics, often in conjunction with measurements. As such, a basis is formed to develop simplified engineering models for application in design codes.

A call for rotor aerodynamic tests in controlled wind tunnel conditions is shared generally within the scientific community. Both smaller scale, university driven, rotor wake experiments as well as larger scale tests with comprehensively instrumented rotor blades, i.e. NREL UAE Phase VI and MEXICO, provide the opportunity to study physical phenomena as well as to validate and further develop rotor aerodynamics codes. MEXICO has most potential to achieve both goals, because of its combined wake and blade experiment.

The interpretation of rotor measurements is hampered by the fact that α cannot be recorded directly, due to the lifting line nature of its definition. The dependency on α of the blade part in BEM and vortex wake codes calls for the experimental quantification of α, though. Tools to estimate α from near-wake flow measurements, possibly combined with load recordings, are proposed in literature, their scope encompassing both axial and yawed flow conditions.

Specifically for measurements of the rotor wake only, where blade load details are not available, analysis tools based on potential flow theory estimate both α and sectional loads from near-wake measurements. Whilst methods are presented for axial flow conditions, the author is not aware of successful attempts to address asymmetric flow conditions.

Concluding, the review of the state-of-the-art in rotor aerodynamics modeling and measurements demonstrates the clear need to reduce BEM and vortex wake modeling uncertainties through wind tunnel experiments on model rotors. Asymmetric, e.g. yawed, inflow conditions form a particular focus, as complex flow phenomena on the blade and in the wake interact to increase modeling uncertainty.

The call for wind tunnel tests on yawed model rotors comes with the explicit request to provide both experimental flow velocity and loads, due to the strongly coupled blade and wake aerodynamics of a rotor. In case rotor model constraints prevent blade load measurements, this limitation could - at least in part - be circumvented through development and implementation of a measurement analysis tool that estimates blade loads from measured flow velocity in yaw.

Chapter 3

The model rotor experiment

A measurement campaign is conducted at a TUDelft wind tunnel to study the near-wake aerodynamics of a model wind turbine rotor. In Section 3.1, the experimental setup and the test conditions are discussed and the coordinate systems used throughout the thesis are introduced. Measurement techniques and procedures are discussed in Section 3.2.
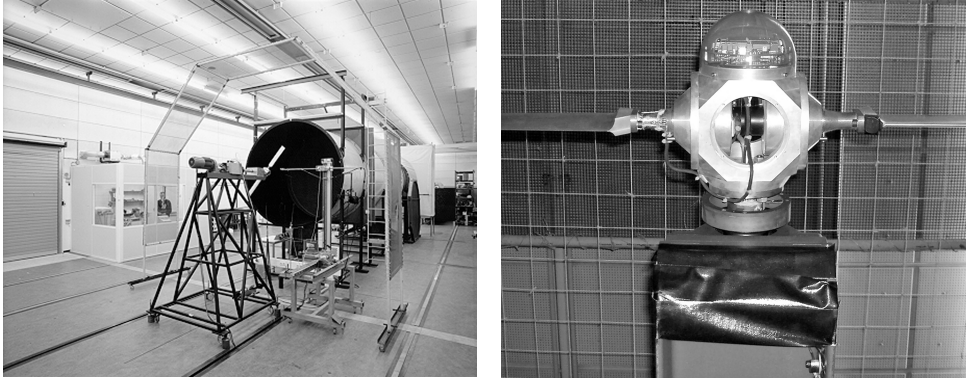

Figure 3.1: The model rotor in the open jet wind tunnel (left picture) and a close up of the model.

3.1 Experimental setup and conditions

Tests are conducted on a model wind turbine rotor placed in an open jet wind tunnel. Photographs of the setup are given in Figure 3.1. The main geometric features of the two-bladed $1.2\,m$ diameter rotor model are given in Table 3.1. The variable-pitch, non-tapered rotor blades have a linear twist distribution of $4°$ from tip to root. An automated blade pitch mechanism controls the

blade pitch angle β_{pitch} to $\pm 0.1°$ accuracy. Both β_{pitch} and β_{twist} are defined positive when pitching and twisting the blade leading edge into the wind, see Figure 3.2.
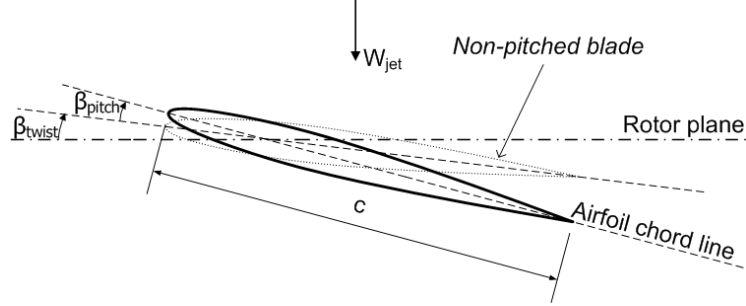

Figure 3.2: Schematic of a blade section. W_{jet} is directed from top to bottom.

The wind tunnel jet speed W_{jet} is derived by combining the ideal gas law and the Bernoulli equation [214],

$$W_{jet} = \sqrt{\frac{2RT\Delta p}{p}}, \qquad (3.1)$$

with Δp the pressure difference reading from three interconnected Pitot-static tubes, mounted in the jet outflow plane, p the ambient pressure recording, T the jet temperature recording and R the ideal gas constant. The operator of the open jet wind tunnel manually controls the flow speed by adjusting the RPM of the wind tunnel fan and monitoring W_{jet}.

The jet outflow plane of the open jet wind tunnel has a $2.24\,m$ diameter, resulting in a ratio of rotor swept area to jet outflow plane area of 0.29. The model rotor hub, i.e. the center of the rotor plane, is positioned $1\,m$, or 1.7 rotor tip radii R_t, downstream of the jet exit and coincides with the center axis of the jet, $2.33\,m$, or $3.9R_t$, above the tunnel hall floor, see Figure 3.3. The open jet wind tunnel is of the open-return type; instead of a separate flow return channel, the tunnel hall is used for recirculation. The distance from the rotor hub to the downstream tunnel wall is $11\,m$ or $18.4R_t$. In Table 3.2 the main wind tunnel characteristics are summarized. For further details on the model rotor and the open jet wind tunnel, see Vermeer [202].

The coordinate systems used are displayed in Figure 3.3. The cartesian wind tunnel coordinate system $(x_{jet}, y_{jet}, z_{jet})$ is used to express W_{jet}. Aligned with the model rotor are inertial, i.e. non-rotating, cartesian (x_m, y_m, z_m)- and cylindrical (r, θ, z)-coordinate systems. The z- and z_m-axes are equivalent. The origins of both coordinate systems are located in the rotor hub center,

Table 3.1: Model rotor main geometric features

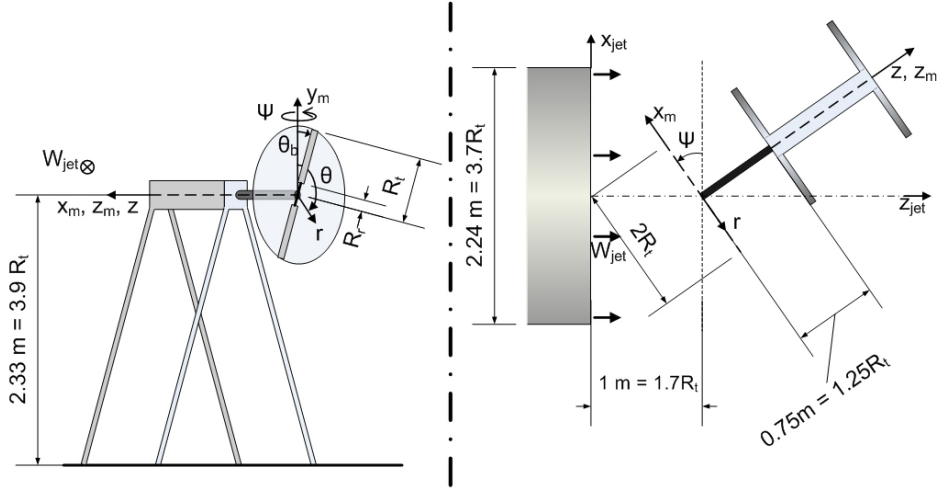| Quantity	Unit	
Number of blades	-	2
Airfoil section	-	NACA0012
Rotor tip radius R_t	$[m]$	0.6
Rotor root radius R_r	$[m]$	0.18
Chord c	$[m]$	0.08
Blade pitch angle β_{pitch}	$[°]$	test input
Blade twist angle $\beta_{twist}(r/R_t)$	$[°]$	$6 - 6.67 r/R_t$ $\quad 0.3 \leq r/R_t \leq 0.9$
		0 $\qquad\qquad 0.9 < r/R_t \leq 1$

Figure 3.3: Schematic of the model rotor set up in the open jet wind tunnel. Left plot: front view, looking in downwind direction, right plot: top view.

with the rotor plane given by $z, z_m = 0$. The blades rotate clockwise, when observing the rotor from an upwind position, with θ_b the blade azimuth angle and Ω the rotational frequency.

The yaw angle Ψ is generally defined as the angle between the undisturbed wind velocity and the normal to the rotor plane. For the current wind tunnel setup, Ψ is set by rotating the model rotor with respect to its y_m-axis. For $\Psi > 0°$, the downstream and upstream halves of the rotor plane are given by $0° \leq \theta \leq 180°$ and $180° \leq \theta \leq 360°$, respectively, corresponding to a righthanded cartesian coordinate system.

A rotor operating condition for the given model rotor is defined by W_{jet},

Table 3.2: Wind tunnel characteristics

Quantity	Unit	
Jet exit diameter	$[m]$	2.24
Maximum wind speed $W_{jet_{max}}$	$[m/s]$	14.5
Turbulence intensity Tu	$[\%]$	1.2 ± 0.2 @ $W_{jet} = 5.5\,m/s$
		1.4 ± 0.1 @ $W_{jet} = 8.0\,m/s$

Ψ, Ω and β_{pitch}. Consequently, the tip speed ratio λ, given by

$$\lambda = \frac{\Omega R_t}{W_{jet}}, \tag{3.2}$$

can be determined. For a rotating blade at e.g. the 70% span section, the chord Reynolds number $Re_{0.7R}$ and reduced frequency $k_{0.7R}$ are determined. To estimate $Re_{0.7R}$ and $k_{0.7R}$, the flow velocity relative to the blades $\vec{V}_{rel}$ is assumed to consist of the W_{jet}- and (Ωr)-contributions only, induced velocity is ignored. $\vec{V}_{rel}$ is expressed in the cylindrical coordinate system attached to the rotor, shown in Figure 3.3,

$$\begin{pmatrix} V_{r_{rel}} \\ V_{\theta_{rel}} \\ V_{z_{rel}} \end{pmatrix} (r, \theta_b, \Psi, W_{jet}) = \begin{pmatrix} W_{jet} sin\Psi sin\theta_b \\ W_{jet} sin\Psi cos\theta_b - \Omega r \\ W_{jet} cos\Psi \end{pmatrix}. \tag{3.3}$$

With $|V_{0.7R_{rel}}|$ the magnitude of the estimated flow velocity relative to the rotating blade at the 70% span section, $Re_{0.7R}$ and $k_{0.7R}$ can consequently be written as

$$Re_{0.7R} = \frac{c|V_{0.7R_{rel}}|}{\nu}, \tag{3.4}$$

$$k_{0.7R} = \frac{\omega c}{2\overline{|V_{0.7R_{rel}}|}}, \tag{3.5}$$

with c the airfoil chord, ν the kinematic viscosity, ω the frequency of the inflow fluctuations and $\overline{|V_{0.7R_{rel}}|}$ the average of $|V_{0.7R_{rel}}|$ over a blade cycle.

With the model rotor set to $\Psi \neq 0°$, $|V_{0.7R_{rel}}|$ and consequently $Re_{0.7R}$ are a function of θ_b. Furthermore, in contrast to the approximately steady inflow seen by a rotating blade section in axial flow conditions, the inflow is unsteady for $\Psi \neq 0°$; ω and thus $k_{0.7R}$ become nonzero with the model rotor subject to yawed flow. The value for ω in Equation [3.5] is approximated by the once-per-period (1P) harmonic, $\omega = \Omega$.

Note that the turbulence intensity for a point fixed on a rotating blade is reduced compared to the freestream turbulence intensity, given in Table 3.2, as a consequence of the increased apparent flow velocity due to blade rotation.
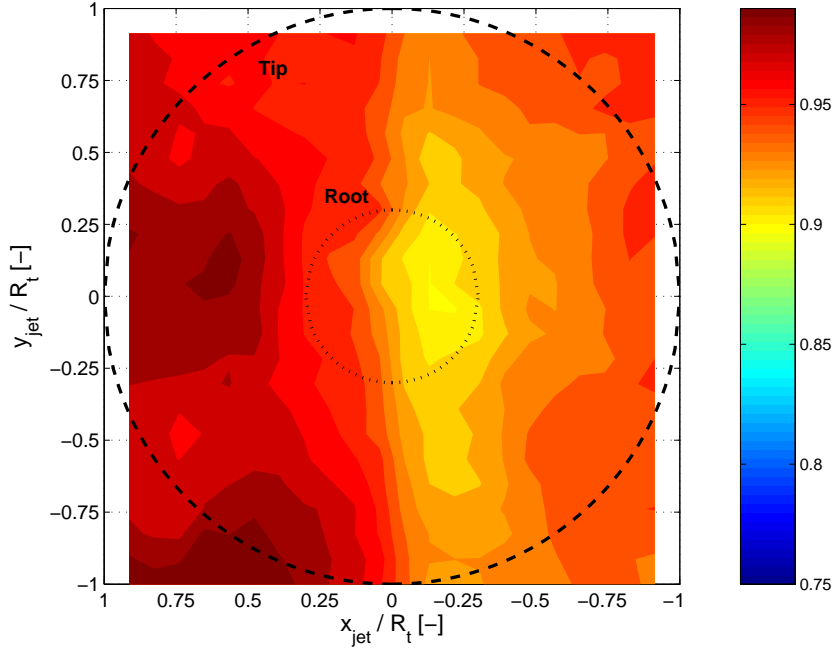
Figure 3.4: Empty tunnel W/W_{jet} at $z_{jet} = 1\,m$, with W the axial flow velocity from hot-film CTA and W_{jet} according to Equation 3.1. Local W/W_{jet} is normalized with the maximum across the plane. Test at $W_{jet} = 5.5\,m/s$. Model rotor tip and root outlines are indicated. Viewpoint is from upwind.

On the other hand, the jet flow velocity field is nonuniform, non-axisymmetric, as indicated with hot-film Constant Temperature Anemometry CTA in Figure 3.4, resulting in additional 'turbulence' at a point fixed on the rotating blade.

The axial velocity reduction near the center of the empty jet is associated with the wake trailed from the nacelle of the wind tunnel fan located upstream of the test section [195]. Further empty jet asymmetry could be induced by the interaction between the jet flow and the returning flow, as a separate flow return channel is absent.

Asymmetric inflow not only results from empty jet phenomena; the space frame supporting the rotor (see Figure 3.1) could cause local flow blockage, thereby inducing further asymmetry to the rotor inflow. Possible flow disturbances from the support structure are not further investigated however, since the $1.25R_t$ distance between the support structure and the rotor plane, see Figure 3.3, is deemed adequate to render the effects of the asymmetric support structure on the near-wake rotor flow insignificant.

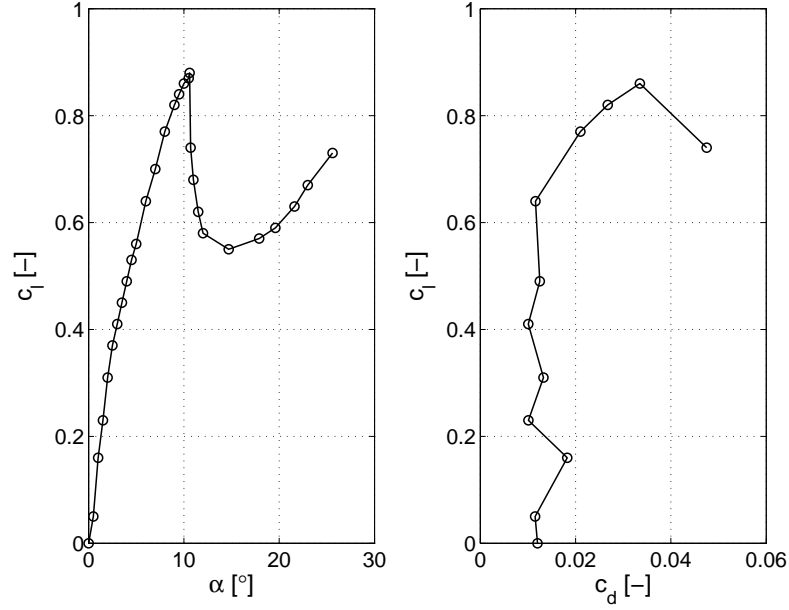For all operating conditions considered during the measurement campaign,

Figure 3.5: Measured NACA0012 airfoil characteristics at $Re_c = 1.5 \cdot 10^5$. Left: c_l versus α, right: the drag polar.

the range of chord Reynolds numbers Re_c across the blade is estimated at $0.4 \cdot 10^5 \leq Re_c \leq 3.1 \cdot 10^5$ from Equation [3.4]. These relatively low Re_c are prone to the presence of laminar separation bubbles, refer e.g. to Baragona [18] for a literature review hereof.

NACA0012 airfoil measurements at $Re_c \epsilon 10^5$ are scarce. Within the framework of the design of current model rotor, Vermeer and Timmer measure the NACA0012 in the TUDelft Low Turbulence Tunnel LSL for $Re_c = 1.5 \cdot 10^5$, see Figure 3.5. Unfortunately, these experiments are not published in literature. The synthesized c_l-, c_d-tables in Appendix N of the second "dynamic inflow" report [157] are mainly based on aforementioned measurements though.

Measured airfoil performance in Figure 3.5 suggests the presence of laminar separation bubbles; the nonlinear behavior at low α could result from bubbles, with the boundary layer failing to reattach before reaching the trailing edge. These long bubbles seem to be mitigated with higher α, until stall abruptly occurs at $\alpha_{stall} = 10.6°$, suggesting sudden bubble bursting at the leading edge.

Interestingly, NACA0012 measurements at $1.7 \cdot 10^5 \leq Re_c \leq 3.3 \cdot 10^5$ in the NACA Variable Density Tunnel by Jacobs and Sherman [99] do not yield abrupt stall. More benign behavior is found instead, suggesting either trailing edge or thin-airfoil stall. Below stall, the performance is similar though, with

58

comparable $c_{l_{max}}$, c_{d_0} and α_{stall}.

When the present study demands airfoil tables to e.g. relate sectional loads to estimated α, the Vermeer and Timmer recordings are used. This choice is motivated by the excellent reputation of the LSL.

In line with the wind tunnel experiments reviewed in Section 2.2, the model rotor lacks similitude with typical MW-scale wind turbines; the model rotor is two- instead of three-bladed, model blades do not have taper and the symmetrical, relatively thin NACA0012 airfoil[1] is used, whereas modern full-scale blades are constructed with thicker, cambered airfoils. Furthermore, experimental Re is at least one order of magnitude smaller than that in the field.

Recall from Section 1.2.2 that lack of similitude need not invalidate tunnel tests. The rotor is operated at representative λ, β_{twist} and β_{pitch}, yielding blade flow similarity between experiment and full scale. The Re-disparity is further not expected to drive near-wake rotor aerodynamics; model and full-scale rotors have similar near-wake vortex systems.

Further actions to mitigate lack of similitude include the availability of NACA0012 airfoil tables at $Re_c = 1.5 \cdot 10^5$, a representative value for the tests, for use with rotor aerodynamics codes in their comparisons with the experiments. Dynamic stall tests are further performed with trip strips applied near the blade leading edge to avoid unsteady laminar separation bubbles, a phenomenon which is unlikely to occur on fullscale rotors. Summarizing, it can be concluded that lack of similitude does not substantially negate the relevance of current measurements for wind turbine aerodynamics studies.

3.2 Measurement techniques and procedures

The present experimental campaign employs strain gauge, quantitative smoke visualization, tuft and hot-film CTA measurements. Each technique, the corresponding procedure and the tested rotor operating conditions are discussed in this section. The conditions presented are those *desired* by the operator, not the actual ones accounting for wind tunnel wall corrections. Differences are of the order of a few percent. For the full test matrix of experimental techniques and wind tunnel wall corrected conditions, refer to Appendix A.

3.2.1 Rotor thrust: strain gauges

It is recommended to commence every rotor aerodynamics experiment with performance tests. Quantification of the rotor performance enables identification of the rotor operating states as a function of rotor settings. Based

---

[1]The NACA0012 airfoil has been used in general aviation aircraft and helicopters, see e.g. http://www.ae.uiuc.edu/m-selig/ads/aircraft.html for an extensive list of airfoil usage.
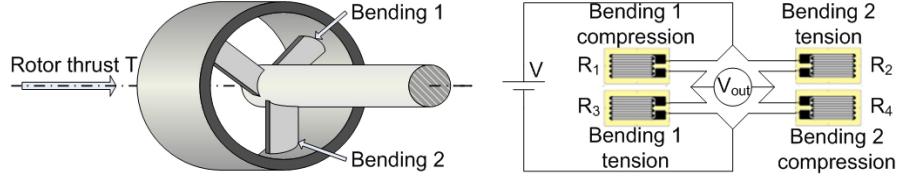
Figure 3.6: Schematic of the flexible ring-element that transfers the rotor thrust T to the shaft (left) and the corresponding strain gauge electric scheme: a double Wheatstone bridge.

hereupon, operating conditions can be selected that are of interest for further study. Moreover, the performance data is valuable for validation and construction of rotor aerodynamics models.

Rotor thrust T, the force normal to the rotor plane and hence also known as axial force, is recorded by means of strain gauges. The deformation of a strain gauge alters its electric resistance. A flexible connector is applied between the rotor hub and the shaft in the form of a ring-element, see the close-up in Figure 3.1, in order to obtain measurable sensitivity of strains to T-variations. The bending-type deflection of the elements indicated with 'bending 1' and 'bending 2' in Figure 3.6 deforms the strain gauges glued to the compression and tension side. The strain gauges are placed in a double Wheatstone bridge circuit, see Figure 3.6, that records a potential difference V_{out} when T is applied to the rotor, according to

$$V_{out} = V \left(\frac{R_4}{R_4 + R_2} - \frac{R_3}{R_3 + R_1} \right),$$ (3.6)

with V the voltage applied and R the electrical resistance of a strain gauge. This electric layout is automatically temperature compensated. Calibration with known axial loads on the rotor shaft yields a relation between T and V_{out}.

T is recorded over a range of operating conditions, all with $W_{jet} = 5.5\,m/s$; for each of the seven yaw angles $\Psi = -45°, -30°, -15°, 0°, 15°, 30°$ and $45°$, measurements of T are taken with the rotor set to all nine combinations of $\lambda = 6, 8, 10$ and $\beta_{pitch} = 0°, 2°, 4°$. For each rotor operating condition, T is recorded at a $\Delta\theta_b = 6°$ interval, during 36 cycles. Concurrently, W_{jet} and Ω are recorded twice and once per cycle, respectively.

Strain gauge calibrations are performed frequently during the measurement campaign. Furthermore, zero-measurements are performed, where T is recorded in wind-off conditions on a slowly rotating rotor, $\Omega \approx 3\,rad/s$. The resulting nonzero, θ_b-dependent T_{offset} is treated as a non-aerodynamic offset, since at these tip speeds below $2\,m/s$, the contribution from aerodynamic
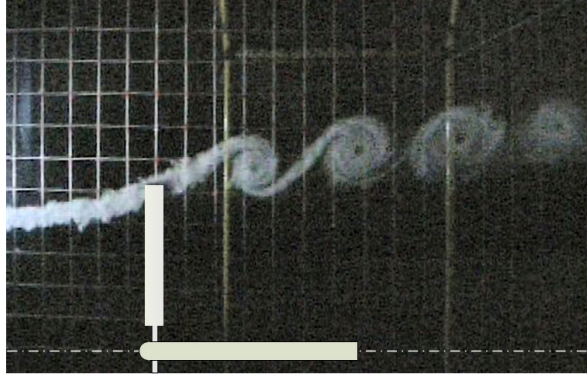
Figure 3.7: A smoke visualization photo showing the tip vortices downstream of the model rotor, for $\Psi = 0°$, $\lambda = 8$, $\beta_{pitch} = 2°$. The background grid can be seen, a sketch of the rotor is appended for clarity.

loads to T is ignored[2]. T_{offset} is consequently subtracted from T-recordings.

Aerodynamic drag from the relatively large hub, see Figure 3.1, could complicate interpretation of the T-recordings; the experimental analysis should only focus on blade effects and model validations would be hampered by the fact that rotor aerodynamic tools typically exclude hub drag. Tests in wind-on conditions with the blades removed yield negligible T-values though, compared to those on a rotor with blades. Thrust measurements are thus not corrected for hub drag.

The rotor thrust coefficient C_T, corrected with the zero-measurements, can be determined for each of the 36 cycles, using

$$C_T = \frac{T - T_{offset}}{1/2\rho W_{jet}^2 A_r}. \tag{3.7}$$

3.2.2 Tip vortex geometry: quantitative smoke visualization

Air is transparent, smoke can therefore be used to visualize the flow of air. An image of the smoke released from an emitter into an unsteady flow displays streaklines; lines traced out by the instantaneous loci of all particles passing through a given point. When smoke is injected upstream of a rotating rotor, at $r \approx R_t$, the smoke trails are influenced by the concentrated tip vortices and yield the characteristic image of Figure 3.7. The visualizations do not

---

[2]For current experiments, the tip speed is 33 to 55 m/s. The resulting dynamic pressure at the blade tips is at least 272 times that of the tests with $2m/s$ tip speed. Aerodynamic loads thus are marginal for these zero-measurements relative to "wind-on" recordings.
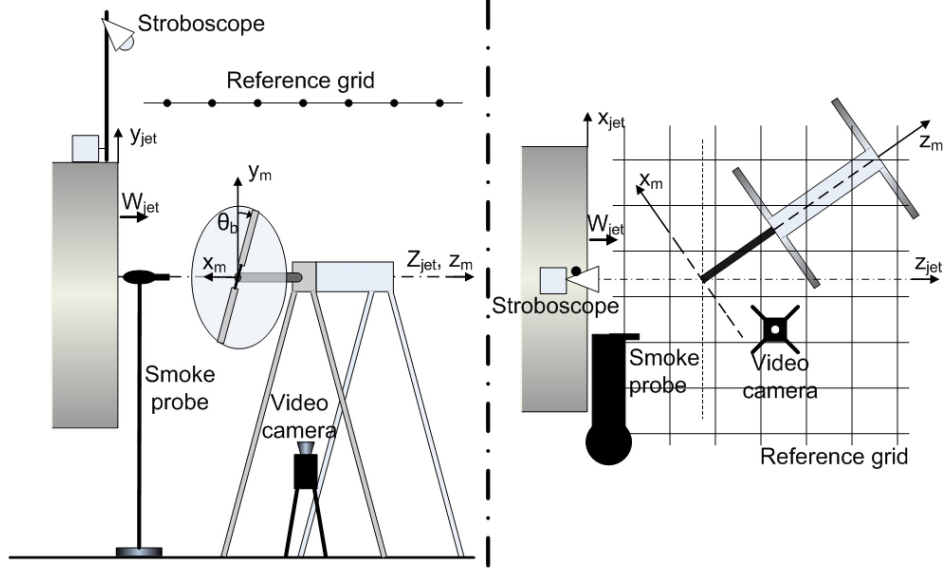
Figure 3.8: Schematic of the experimental setup employed with the smoke visualization measurements. Left plot: side view, right plot: top view. The stroboscope, smoke probe, photo-camera and reference grid are indicated.

only yield instructive qualitative information, they can also be used to derive quantitative data of the tip vortex geometry. For a general discussion on smoke visualization, see e.g. Yang [218].

With the present measurements, smoke is injected in the (x_m, z_m)-plane upstream of the rotor using a streamlined smoke probe, see Figure 3.8 for the experimental setup. The exact location of the smoke probe varies with the rotor operating condition for optimal capture of the tip vortex, the axial distance (parallel to z_{jet}) of the smoke probe to the rotor hub however is larger than $0.8R_t$ for all measurements, aiming at reduced intrusiveness.

A stroboscope, synchronized to the rotor rotational frequency $\Omega/(2\pi)$ and with phase angle $\theta_b = 90°$, illuminates the setup. Images are recorded with a digital video camera. The stroboscope used is a point light source, a light sheet that would illuminate only the (x_m, z_m)-plane is not used. The post-processing procedure however assumes that the smoke streaklines are located in the (x_m, z_m)-plane. A frame harnessed with equidistant wires forms a reference grid that is positioned horizontally above the setup, outside the jet. The reference grid is aligned with the x_{jet}- and z_{jet}-direction.

Smoke visualization is done at $\Psi = 0°, -15°, -30°, -45°$ and $45°$. For each Ψ, all nine combinations of $\lambda = 6, 8, 10$ and $\beta_{pitch} = 0°, 2°, 4°$ are studied. W_{jet}
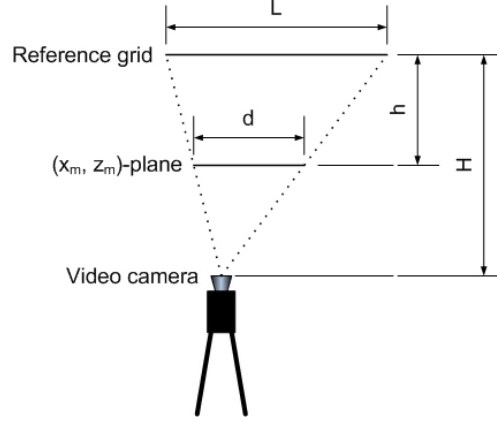
Figure 3.9: Schematic of the smoke visualization parallax correction

is set to $5.5\,m/s$ throughout. Images are taken on the upwind and downwind side of the rotor when $\Psi \neq 0°$. Two symmetry checks are performed on the visualization data; both for $\Psi = 0°$ and $\Psi = \pm 45°$, smoke is injected to the (x_m, z_m)-plane with the phase angle of the stroboscope at $\theta_b = 90°$ and $270°$.

Each operating condition yields at least six useful smoke visualization photos at both the upwind and downwind side of the rotor. For an example, see Figure 3.7. The photos appear to be stills of the unsteady helical tip vortex structure. A tip vortex is identified by the swirling smoke pattern, with the center of the vortex indicated by the smoke void[3]. Observed wake expansion and the sense of the flow rotation induced by the tip vortices (clockwise in Figure 3.7), are typical of the wind turbine operating state.

The distances on the visualization photos, e.g. between a tip vortex center and the blade tip, are first expressed in terms of a reference grid unit. To translate these to actual distances in the (x_m, z_m)-plane, a parallax correction is needed. Hereto, the relative distances between camera, rotor hub center and the reference grid are measured. The actual distance d is given by

$$d = \frac{H - h}{H} L, \tag{3.8}$$

with L a distance measured on a photo, h the vertical distance between (x_m, z_m)-plane and reference grid and H the vertical distance between camera and reference grid, see Figure 3.9. Tip vortex center locations are given relative to the blade tips and made dimensionless through division by R_t.

---

[3]Leishman [108] theoretically derives that the convection of smoke particles away from the tip vortex centers is governed by vortex swirl induced centrifugal forces.

3.2.3 Flow velocity: hot-film CTA

This CTA section starts with an introduction on the physical background of the technique, tapping from Bruun's comprehensive work [26], where the interested reader can find more details.

Hot-wire measurements are based on heat transfer. The hot-wire, with electric resistance R_w, is heated when set to an electric current I_w and voltage V_w. The heat generated in the wire W is given by

$$W = I_w^2 R_w = V_w^2/R_w. \tag{3.9}$$

Note that R_w depends on T_w, the temperature of the heated wire. T_w corresponds to a wire thermal energy E of

$$E = c_w T_w, \tag{3.10}$$

with c_w the wire heat capacity. Heat is transferred from the wire by convection, conduction and radiation, indicated with H. The thermodynamic balance between W, E and H is given by

$$\frac{dE}{dt} = W - H. \tag{3.11}$$

The design of a hot-wire results in a convection dominated heat transfer for low speed flow; the flow passing by cools the hot-wire. The amount of cooling is affected by the flow speed and temperature.
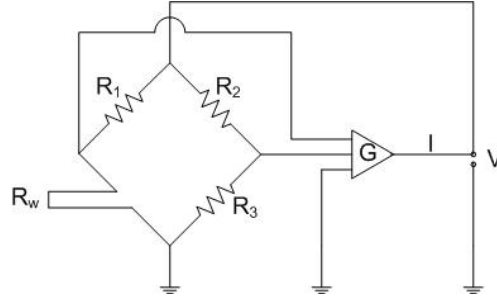
Figure 3.10: Schematic of the hot-wire CTA electric circuit.

Constant Temperature Anemometry CTA is applied to measure the heat transfer. The hot-wire is connected to one arm of a Wheatstone bridge, see Figure 3.10. Electric resistances are indicated with R, where R_w is the hot-wire. The bridge remains balanced when R_w and consequently T_w are kept constant. A servo amplifier G thus aims to balance the bridge by controlling I. Constant R_w and T_w yield $W = H$, according to equations [3.10] and [3.11].

Furthermore, voltage V can be related to a flow velocity U through King's law,

$$V^2 = (T_w - T_a)(A + BU^n), \qquad (3.12)$$

with T_a the measured flow temperature. A, B and n are speed calibration constants. A speed calibration relates measured V to a known flow speed W_p oriented normal to the hot-wire, i.e. in the z_p-direction, see Figure 3.11 for the local hot-wire coordinate system (x_p, y_p, z_p). U in equation [3.12] can hence be replaced by the known W_p and A, B and n can be solved for.
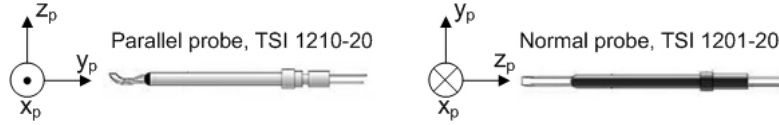

Figure 3.11: The normal and parallel types of single-film hot-film probes. The cartesian coordinate systems (x_p, y_p, z_p), attached to the probe, are included.

Hot-wire cooling is also sensitive to the relative flow direction; flow parallel to the hot-wire does not cool as effectively as flow normal to the hot-wire. Generally, the flow direction is unknown. The value for U, found from equation [3.12], should thus be interpreted as the flow speed when the flow would have been normal to the hot-wire, in the z_p-direction, named effective velocity V_{eff} in short. Jørgensen's equation for the flow direction dependency is given by

$$V_{eff}^2 = h^2 U_p^2 + k^2 V_p^2 + W_p^2, \qquad (3.13)$$

where the flow velocity is expressed in terms of the local hot-wire coordinate system (x_p, y_p, z_p), see Figure 3.11. h and k are constants derived from angular calibrations, where the relation between measured V_{eff} and known flow angle for a given flow speed is determined.

The present experiments are conducted with hot-films instead of hot-wires, since hot-films are more robust than hot-wires. Hot-film recordings at multiple orientations are required to estimate the flow velocity magnitude and direction [26]. The instantaneous flow velocity can be measured with a three-sensor hot-film probe. At present however, phase-locked flow velocity is subject of study. The cyclic character of the flow enables reconstruction of the phase-locked flow velocity using a single-sensor hot-film with successively varying orientations. Both single- and three-sensor hot-film measurements require the flow conditions to be constant throughout the experimental campaign. An additional requirement for the single-sensor hot-film is the repeatability of the (r, θ, z)-coordinate and of the θ_b-phase, as multiple recordings at a given (r, θ, z, θ_b)-point are needed to estimate the phase-locked flow velocity.

Since single-sensor probes are relatively inexpensive, calibration-friendly and expendable, compared to three-sensor types, single-sensor hot-films are used.

In order to cover all required sensor orientations, two types of hot-film probes are used, see Figure 3.11; the TSI 1201-20 with the sensor normal to the probe and the TSI 1210-20 with the sensor parallel to the probe, in brief the normal and parallel probe, respectively. Main characteristics, applicable to both probe types, are given in Table 3.3.

Table 3.3: Hot-film characteristics

Quantity	
Hot-film material	platinum film on fused-quartz substrate
Hot-film diameter	$50.8\,\mu m$
Hot-film length	$1.02\,mm$
Upper frequency limit	$75\,Khz$ @ $10\,m/s$ [26]
Probe diameter	$3.9\,mm$

It appears from C_P measurements on the model rotor in axial flow by Vermeer [202] that the rotor operating condition of $\Psi = 0°$, $\lambda = 8$, $\beta_{pitch} = 2°$ is near the C_P-optimum. This condition is selected as the baseline case for CTA near-wake flow velocity measurements. With $\lambda = 8$ and $\beta_{pitch} = 2°$ kept constant, CTA near-wake flow velocity experiments are also conducted with the rotor subject to $\Psi = 30°, 45°$. W_{jet} is set to $5.5\,m/s$ throughout.

Hot-film traverses are conducted in three downstream measurement planes that are oriented parallel to the rotor plane, $z/R_t = 5.83 \cdot 10^{-2}$, $1.00 \cdot 10^{-1}$ and $1.50 \cdot 10^{-1}$, see Figure 3.12. Hot-film CTA recordings are also taken in a measurement plane $z/R_t = 1.00 \cdot 10^{-1}$ upstream. These measurements are ignored however due to their unacceptable quality; the setup with the hot-film traverse upstream of the rotor disturbs the flow significantly more than the downstream setup. Whereas for the downstream setup, the probe longitudinal axis is aligned with the rotor z_m-axis, lack of space between the upstream measurement plane and the rotor plane forces the probe longitudinal axis to be aligned with the rotor y_m-axis, thereby clearly introducing a large disturbance to the flow.

At a given measurement plane, the traverse covers a circular disc, co-axial to the rotor, with inner radius R_r and outer radius R_t. The spatial resolution of the measurements is $\Delta\theta = 15°$ and $\Delta(r/R_t) = 0.1$ in the azimuthal and radial direction, respectively. Recordings are phase-locked with a blade azimuth resolution of $\Delta\theta_b = 2°$. The corresponding temporal resolution is approximately $2.1\,kHz$, from equation [3.2]. According to the Nyquist criterium, the maximum resolved frequency hence is $1.0kHz$. The upper frequency limit
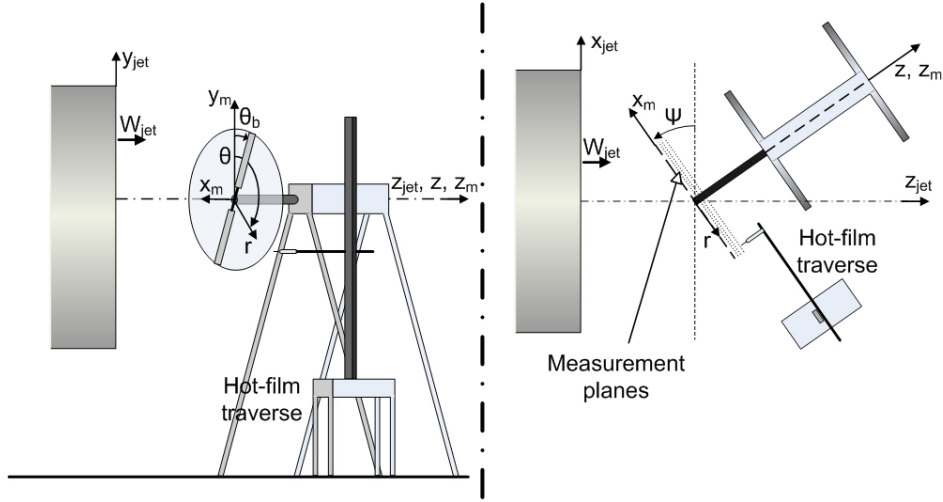
Figure 3.12: Schematic of the experimental setup employed with the hot-film CTA measurements. Left plot: side view, right plot: top view. The hot-film traverse and the three downstream measurement planes, at $z/R_t = 5.83 \cdot 10^{-2}$, $1.00 \cdot 10^{-1}$ and $1.50 \cdot 10^{-1}$, are indicated.

for a cylindrical hot-film is about $75 \, kHz$ at $10 \, m/s$ [26]. The maximum frequency response of the current hot-film measurements is thus dictated by the temporal resolution of the recordings, not by the physical limit of the hot-film. For a given (r, θ, z)-location, hot-film readings are taken for a total of 54 rotor cycles, resulting in 54 recordings per (r, θ, z, θ_b)-point.

At a given (r, θ, z, θ_b)-point, measurements with six hot-film orientations are required to reconstruct the flow velocity vector according to a new data reduction technique proposed by Haans *et al.* [75]. The resulting flow velocity is made dimensionless through division by $(W_{jet} \, cos\Psi)$.

The limited range of the traversing rig necessitates performing multiple runs at given rig position as well as shifting the rig to a new position to cover the full measurement plane; a run for the axial and the yawed flow cases spans half and quarter of a measurement plane, respectively. Errors between intended and actual (r, θ, z)-positions due to random shifts of the traversing rig accumulate and result into an offset when returning to the starting point upon completion of a traverse. After each traverse, the offset is determined and the position of the hot-film probe is reset. Both speed and angular calibrations are performed regularly to compensate for hot-film ageing.

3.2.4   Boundary layer separation: blade tufts & CTA

Yawed flow conditions result in a cyclic variation of inflow conditions at the blades. Under certain conditions, part of the blades could experience dynamic stall, with associated flow separation over the blade suction side.

A means to distinguish between attached and separated flow around a body is to study the behavior of tufts, attached to the surface. The tuft reacts to all forces exerted on it, hence also to the aerodynamic force component. Generally, attached flow is characterized by marginal tuft movement, the tuft pointing steadily in the direction of the flow, and separated flow is associated with rapid tuft motion.

When the tufts are attached to a rotating body, the centrifugal force acting on the tufts complicates the analysis. Glued to rotating rotor blades, the centrifugal force contribution biases the tuft orientation towards the outboard radial direction. Aerodynamic forces on the tuft are drag related and are proportional to $D\left(\Omega r\right)^2$, while centrifugal forces on the tufts scale with $D^2\Omega^2 r$, with D the tuft diameter. Hence, to minimize the ratio of centrifugal to aerodynamic forces, the tufts should have a small diameter and be located outboard. Corten [37] remarks that the tufts that are biased radially outboard could act as vortex generators, postponing separation. A comprehensive discussion on tuft techniques is given in Yang [218].

The blade boundary layer is convected into the wake as a viscous shear layer. Blade stall should hence also be observable in the near-wake velocity field associated with the viscous wake. A general correlation between tuft and hot-wire CTA recordings is found by Vermeer and Timmer [205] for the current model rotor subject to axial flow conditions. Similar correlation is obtained for yawed flow conditions by Haans *et al.* [76], increasing the confidence in the capability of both experimental methods to detect stall; tufts and CTA.

Two rotor operating conditions are considered for boundary layer separation studies. For both, $\Psi = 45°$ and $\beta_{pitch} = 2°$. λ is varied by altering W_{jet} while keeping Ω constant at $73.3\,rad/s$. W_{jet} is set to $5.5\,m/s$ and $8.0\,m/s$ for $\lambda = 8.0$ and 5.5, respectively. Constant Ω yields equal centrifugal force at a given tuft for the two conditions. Differences in tuft orientations are due to changes in tuft aerodynamic loads only.

Two rows of approximately $1.4\,cm$ $(0.18c)$ long tufts are glued to one of the two blades. Tufts extend from $r/R_t = 0.37$ up to $r/R_t = 0.97$, see Figure 3.13. The tuft equipped blade is illuminated with a stroboscopic light source, synchronized with Ω. The phase angle of the stroboscope is adjusted with a resolution of $\Delta\theta_b = 30°$. A minimum of two useful photos per θ_b-setting is taken with a digital camera, positioned outside of the jet flow.

Hot-film CTA is applied in the near-wake of the model rotor. The TSI 1201-20 single-sensor hot-film, see Figure 3.11, is mounted on a traversing rig that
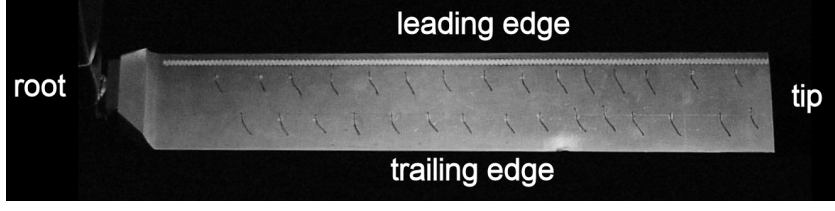
Figure 3.13: Rotor blade equipped with two rows of tufts, from $r/R_t = 0.37$ to 0.97.

traverses automatically through a plane located $z/R_t = 5.83 \cdot 10^{-2}$ downstream of the rotor plane. For the given rotor model, $z/R_t = 5.83 \cdot 10^{-2}$ is equivalent to $z/c = 0.44$. The spatial resolution of the phase-locked measurements is $\Delta\theta = 15°$ and $\Delta(r/R_t) = 0.1$ in the azimuthal and radial direction, respectively. Samples are taken with a blade azimuth resolution of $\Delta\theta_b = 2°$ during 54 cycles. For each $(r/R_t, \theta, z/c, \theta_b)$-point, 54 recordings are hence available.

Present CTA measurements do not aim to determine the three-dimensional PLA flow velocity. The goal is more modest; to identify the spanwise region of stall on the blade during the rotational cycle from observed trends in the hot-film signal. It is not necessary to calibrate the hot-film, since the trends in the hot-film signal, measured in the wake, are independent of the calibration routines. Furthermore, a single hot-film probe orientation is adequate to study trends in the hot-film signal. Within the restrictions of the given traversing rig, alignment of the probe z_p-axis to the rotor z_m-axis is considered to yield minimum flow intrusiveness. The hot-film sensor is oriented vertically; the probe y_p-axis is parallel to the rotor y_m-axis.

Note that all hot-film CTA measurements in the near-wake are taken without tufts glued to the blade.

Chapter 4

Experimental data reduction

The model rotor is tested in the open jet wind tunnel with an extensive range
of measurement techniques for a large set of rotor operating conditions, as
discussed in Chapter 3. Analysis of the recorded data requires data reduction.
A first step, discussed in Section 4.1, is to apply the concept of phase-locked
data, owing to the typically cyclic character of wind turbine rotor near-wake
data. A new hot-film single-sensor data reduction technique that enables de-
termination of both the magnitude and direction of the flow velocity vector, is
presented in Section 4.2. The traditional approach only yields the flow velocity
magnitude, not its direction. Wind tunnel wall corrections are discussed in
Section 4.3. Finally, the uncertainties associated with the measured variables
are assessed in Section 4.4.

4.1 Phase-locked analysis

The variables measured at a fixed, non-rotating position in the near-wake of a
rotating rotor are unsteady. The recorded data displays a cyclic character, see
i.e. Figure 4.1, owing to the cyclic repetition of the flow field boundary con-
ditions. The cycle period T_{cycle} is selected to be the rotor period $T_{rotor-cycle}$,
given by

$$T_{rotor-cycle} = \frac{2\pi}{\Omega}. \tag{4.1}$$

T_{cycle} could also be set to $T_{rotor-cycle}/B$, with B the number of blades, when
the blades are identical. Consider a general variable X that is measured during
N number of cycles at $(r/R_t, \theta, z/R_t)$. The phase-locked average and standard
deviation for a given θ_{b_k} can consequently be expressed by equations [4.2] and
[4.3], respectively,

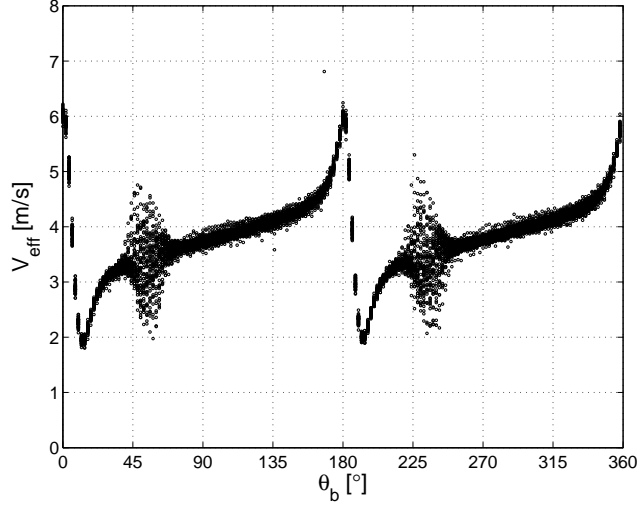$$<X>(\theta_{b_k}) = \frac{1}{N}\sum_{i=1}^{N} X(t_i), \tag{4.2}$$

Figure 4.1: Example of the cyclic character of hot-film CTA in the near-wake. V_{eff}, recorded during 54 cycles, is plotted versus θ_b for the rotor operating condition $\Psi = 0°$, $\beta_{pitch} = 2°$, $\lambda = 8$, at $(r/R_t, \theta, z/R_t) = (0.7, 180°, 5.83 \cdot 10^{-2})$.

$$s_X(\theta_{b_k}) = \left(\frac{1}{N} \sum_{i=1}^{N} [X(t_i) - <X> (\theta_{b_k})]^2 \right)^{1/2}. \tag{4.3}$$

Here, t_i is the time instant at which $\theta_b = \theta_{b_k}$, hence

$$t_i = t_k + (i-1)T_{cycle}, \quad i = 1, 2, \ldots N, \tag{4.4}$$

with t_k the first occurrence of $\theta_b = \theta_{b_k}$. $X(t_i)$ can hence be written as

$$X(t_i) = <X> (\theta_{b_k}) + x(t_i), \tag{4.5}$$

with $x(t_i)$ the instantaneous fluctuation from $<X> (\theta_{b_k})$.

For the current experimental campaign, Phase-Locked Averaging (PLA) is applied to the CTA measurements of the flow velocity in the near-wake. The general variable X can hence be substituted by V_{eff}.

The PLA-technique obscures physical phenomena that result in a cycle with a period other than T_{cycle} or a higher harmonic of T_{cycle}, since these cyclic variations are smoothed out by PLA. An example of such a physical phenomenon is wake meandering that however is not likely to influence the near-wake CTA measurements, as discussed in Section 2.2.1.

72

4.2 Hot-film data reduction method

Phase-locked CTA hot-film measurements are taken in the near-wake behind the model rotor, see Figure 3.12 for the experimental setup and the rotor co-ordinate systems used and Figure 3.11 for the probes and their coordinate systems. The PLA flow velocity is reconstructed using multiple sequential single-sensor hot-film CTA recordings with the sensor at various orientations. The traditional data reduction method, using three probe orientations, is discussed first, in Section 4.2.1. In order to overcome the drawbacks of the traditional data reduction method, a new data reduction method, using six probe orientations, is presented in Section 4.2.2.

4.2.1 Traditional method

The traditional single-sensor PLA CTA data reduction method, discussed by e.g. Bruun [26], requires three successive recordings with the sensor in three orthogonal orientations to reconstruct the PLA flow velocity vector at given $(r/R_t, \theta, z/R_t)$-location. Here, this traditional method is reviewed in light of current rotor near-wake measurements.

Basis of the traditional data reduction technique is Jørgensen's equation [3.13], defined for an instantaneous V_{eff}-measurement. Equation [3.13] is rewritten with all velocities, "effective" and "true", in the form of equation [4.5]; a v-term and a $<V>$-term. V is a generic velocity representing both the "effective" and "true" velocities. Deriving the PLA of Jørgensen's equation, $<v^2>$ is generally found to be several orders of magnitude smaller than $<V>^2$. The contributions from the fluctuation terms are thus assumed to be negligible, resulting in

$$\langle V_{eff} \rangle^2 = h^2 \langle U_p \rangle^2 + k^2 \langle V_p \rangle^2 + \langle W_p \rangle^2 . \qquad (4.6)$$

Recordings with three successive hot-film orientations and probes, given in Table 4.1, are used to construct a system of equations from the PLA Jørgensen's equation [4.6] per (r, θ, z, θ_b)-point,

$$\begin{bmatrix} h_1^2 & k_1^2 & 1 \\ k_2^2 & h_2^2 & 1 \\ h_3^2 & 1 & k_3^2 \end{bmatrix} \begin{bmatrix} \langle U_m \rangle^2 \\ \langle V_m \rangle^2 \\ \langle W_m \rangle^2 \end{bmatrix} = \begin{bmatrix} \langle V_{eff,1} \rangle^2 \\ \langle V_{eff,2} \rangle^2 \\ \langle V_{eff,3} \rangle^2 \end{bmatrix}, \qquad (4.7)$$

System of equations 4.7 is solved for $<U_m>^2$, $<V_m>^2$ and $<W_m>^2$. Note that the flow velocity is expressed in the non-rotating model rotor cartesian coordinate system (x_m, y_m, z_m), see Figure 3.12. Suggested probes and orientations are summarized in Table 4.1.

Table 4.1: hot-film probes and orientations: traditional method.

Number	1	2	3
probe type	normal	normal	parallel
x_p *parallel to*	x_m	y_m	x_m
y_p *parallel to*	y_m	x_m	z_m
z_p *parallel to*	z_m	z_m	y_m
sensor orientation	vertical	horizontal, in-plane	horizontal, downwind

System of equations [4.7] does not yield the direction of the flow velocity, since the squares of the flow velocity components are determined. The direction of the flow velocity hence has to be guessed. For the axial and yawed flow conditions currently under consideration, with $\Psi \leq 45°$, the PLA axial flow velocity component $<W_m>$ can readily be assumed to be in the downstream direction, $<W_m> > 0$. The directions of the in-plane velocity components, $<U_m>$ and $<V_m>$, are generally unknown beforehand.

Furthermore, the combined effect of small in-plane velocity components and uncertainties in measurement and data reduction yields $<U_m>^2 < 0$ and/or $<V_m>^2 < 0$ at several (r, θ, z, θ_b)-points; a nonphysical result. The magnitude of the in-plane flow velocity components hence cannot be determined at these (r, θ, z, θ_b)-points.

4.2.2 New method

Determination of the PLA in-plane flow velocity components $<U_m>$ and $<V_m>$ with the traditional data reduction method is hampered by the general inability of this method to derive the direction and the occasional incapacity to even determine the magnitude of $<U_m>$ and $<V_m>$, as discussed in Section 4.2.1. A new data reduction method, proposed by Haans *et al.* [75], overcomes these issues.

The determination of the PLA axial flow velocity component $<W_m>$ with the new data reduction method is identical to that of the traditional method; the single parallel probe and two normal probe orientations summarized in Table 4.1 each yield a $<V_{eff}>$-value, system of equations [4.7] is used to derive $|<W_m>|$ and $<W_m>$ is assumed to be directed downwind.

The new method differs from the traditional one in the derivation of $<U_m>$ and $<V_m>$. To appreciate the new method, first note that the flow angle α in

the (y_p, z_p)-plane is given by

$$\alpha = atan\left(\frac{W_p}{V_p}\right), \tag{4.8}$$

with V_p and W_p the flow velocity components parallel and normal to the sensor, see Figure 3.11 for probe geometries and coordinate systems.

The new method is based on an observation first made during an angular calibration of the parallel hot-film probe: V_{eff}-recordings of the parallel hot-film probe are asymmetric with respect to α due to partial shielding of the sensor by the prongs, see Figure 4.2. Expressed in the cartesian hot-film coordinate system (x_p, y_p, z_p), parallel probe V_{eff}-recordings are thus asymmetric to the velocity in z_p-direction W_p, also see Figure 4.3. Both the direction and the magnitude of $<U_m>$ and $<V_m>$ are derived using this W_p-asymmetry.
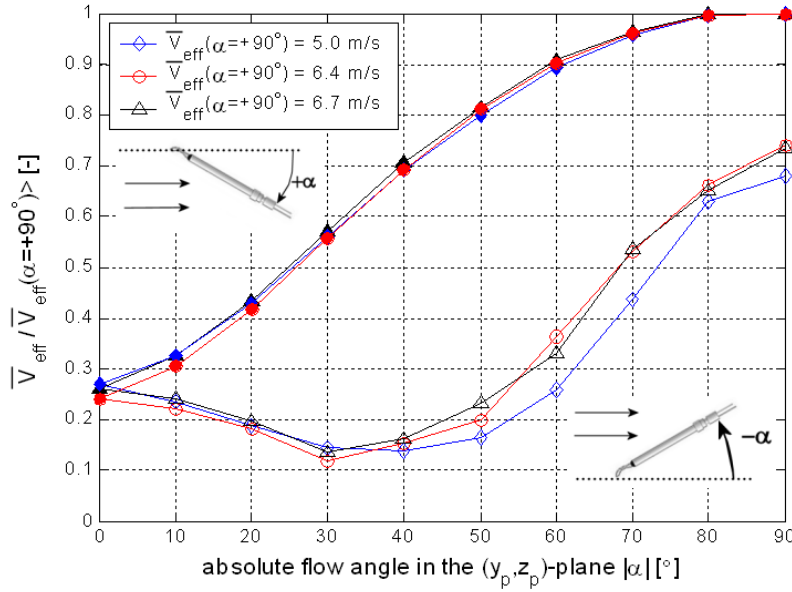
Figure 4.2: Asymmetry of parallel probe V_{eff}-recordings to the flow angle α in the (y_p, z_p)-plane, illustrated with plots of $\overline{V}_{eff}$, normalized with $\overline{V}_{eff_{\alpha=+90°}}$, as a function of $|\alpha|$ for both positive (top) and negative (bottom) α-sweeps.

in-plane flow velocity direction

During angular calibration, the parallel hot-film probe is oriented such that the flow is in the (y_p, z_p)-plane only. For known flow speed, consider two parallel

Figure 4.3: The two parallel probe orientations in the (y_m, z_m)-plane used to determine the direction of the V_m-component.

probe orientations for which the flow velocity component in z_p-direction is of equal magnitude, but opposite direction; $W_{p_1} < 0$ and $W_{p_2} > 0$, respectively. The two parallel probe orientations thus yield $|W_{p_1}| = |W_{p_2}|$ and $W_{p_1} = -W_{p_2}$. The V_{eff}-asymmetry 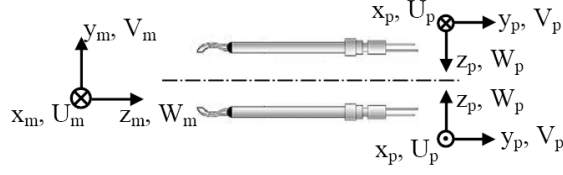to W_p results in the highest V_{eff}-value being measured when the sensor is not shielded from W_p by the prongs,

$$V_{eff}(W_p = W_{p_2}) \; < \; V_{eff}(W_p = W_{p_1}). \tag{4.9}$$

In order to determine the direction of the PLA in-plane flow velocity component $<V_m>$, two parallel probe orientations are applied, see Figure 4.3, with

$$V_m = -W_p \tag{4.10}$$

and

$$V_m = W_p, \tag{4.11}$$

for the top and bottom probe orientation, respectively. $<V_{eff}>$ is determined for both probe orientations. The direction of $<V_m>$ is subsequently derived using relations [4.9] to [4.11]; when the top probe orientation in Figure 4.3 gives the highest $<V_{eff}>$-value, $<V_m>$ is directed vertically up, in the same direction as the y_m-axis. When, on the other hand, the bottom probe orientation in Figure 4.3 gives the highest $<V_{eff}>$-value, $<V_m>$ is directed vertically down, in the direction opposite to the y_m-axis.

Note that the flow velocity includes a component normal to the (y_p, z_p)-plane, $U_p = U_m$, see Figure 4.3. The U_p-contribution to V_{eff} is generally assumed to be uncoupled from the V_p- and W_p-contributions, as can e.g. also be seen in equation [3.13]. The U_p-component hence does not influence detection of the $<V_m>$-direction.

Using an equivalent approach, the $<U_m>$-direction can be detected. Four different parallel probe orientations are hence employed to determine the direction of the PLA in-plane flow velocity.
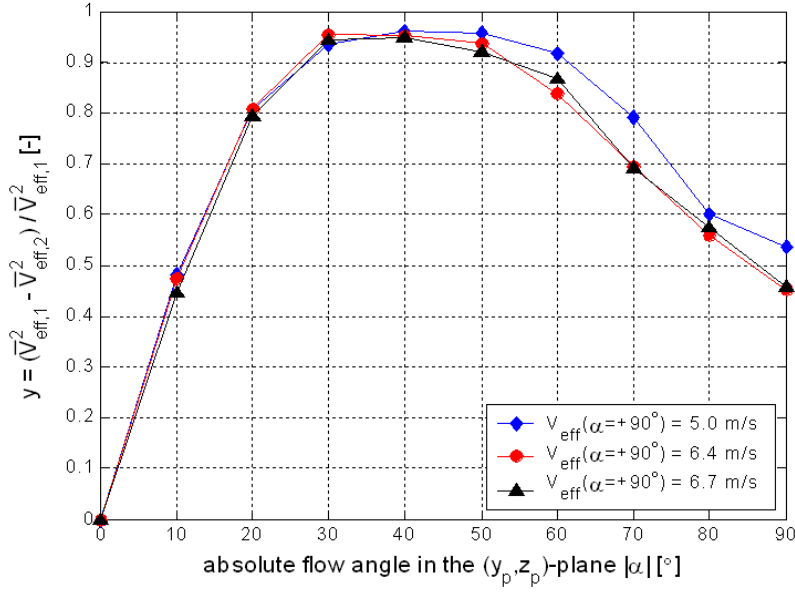
Figure 4.4: $(\overline{V}^2_{eff_1} - \overline{V}^2_{eff_2})/\overline{V}^2_{eff_1}$ as a function of $|\alpha|$, derived from parallel probe angular calibrations for the flow in the (y_p, z_p)-plane only. Suffixes 1 and 2 indicate non-shielded and a partly shielded probe orientations, respectively.

in-plane flow velocity magnitude

The V_{eff}-asymmetry of the parallel hot-film probe to W_p forms the basis of estimating the magnitude of $<U_m>$ and $<V_m>$. The method is discussed for $<V_m>$ only, since the $<U_m>$-magnitude is derived in similar fashion.

Parallel probe angular calibrations for the flow in the (y_p, z_p)-plane are used to relate the absolute flow angle $|\alpha|$ in the (y_p, z_p)-plane with the V_{eff_1}- and V_{eff_2}-recordings, see Figure 4.2. Suffixes 1 and 2 are added to distinguish between recordings for a non-shielded and a partly shielded probe orientation, respectively. For given $|\alpha|$, $V_{eff_2} < V_{eff_1}$. The relation retrieved from the calibrations,

$$\frac{V^2_{eff_1} - V^2_{eff_2}}{V^2_{eff_1}} = f\left(|\alpha|\right), \tag{4.12}$$

is plotted in Figure 4.4. The definition of $|\alpha|$ is readily inferred from that of α in Equation 4.8.

The pair of parallel probe orientations applied to detect the direction of $<V_m>$ in the rotor wake, see Figure 4.3, is also used to estimate its magnitude. The $<V_{eff}>$-recordings generally contain contributions from all three flow

Table 4.2: hot-film probes and orientations: new method.

Number	1	2	3	4	5	6
probe type	normal	normal	parallel	parallel	parallel	parallel
x_p parallel to	x_m	y_m	x_m	x_m	y_m	y_m
y_p parallel to	y_m	x_m	z_m	z_m	z_m	z_m
z_p parallel to	z_m	z_m	y_m	y_m	x_m	x_m
sensor orientation	vertical	hor., in-plane	hor., downw.	hor., downw.	hor., downw.	hor., downw.
sensor-prong (y_p, z_p)-plane	-	-	vert.	vert.	hor.	hor.
z_p-direction	-	-	same as y_m	opposite to y_m	same as x_m	opposite to x_m

velocity components, which should be acknowledged in the data reduction equations. $<V_{eff_1}>$ derived for the non-shielded orientation is related to the PLA flow velocity according to Equation [4.6]. With the PLA flow velocity expressed in the rotor cartesian coordinate system, Equation [4.6] is rewritten,

$$\left\langle V_{eff_1} \right\rangle^2 = h^2 \left\langle U_m \right\rangle^2 + \left\langle V_m \right\rangle^2 + k^2 \left\langle W_m \right\rangle^2 . \tag{4.13}$$

For the other, partly shielded, probe orientation, a more general formulation is used,

$$\left\langle V_{eff_2} \right\rangle^2 = f \left(\left\langle U_m \right\rangle, \left\langle V_m \right\rangle, \left\langle W_m \right\rangle \right). \tag{4.14}$$

From parallel probe angular calibrations with the flow in the (x_p, y_p)-plane only, it is observed that U_p yields a symmetrical V_{eff}^2-contribution, equal to $h^2 U_p^2$. Equation [4.14] can hence be rewritten,

$$\left\langle V_{eff_2} \right\rangle^2 = g \left(\left\langle V_m \right\rangle, \left\langle W_m \right\rangle \right) + h^2 \left\langle U_m \right\rangle^2 . \tag{4.15}$$

By subtracting the $<U_m>$-contribution from both $<V_{eff_1}>$ and $<V_{eff_2}>$, the angular calibration situation with flow in the (y_p, z_p)-plane only can be reconstructed for the rotor wake measurements. Equations [4.8] and [4.12] can hence be combined to find, for the rotor wake measurements,

$$\frac{\left\langle V_{eff_1} \right\rangle^2 - \left\langle V_{eff_2} \right\rangle^2}{\left\langle V_{eff_1} \right\rangle^2 - h^2 \left\langle U_m \right\rangle^2} = f \left(atan \left| \frac{\left\langle V_m \right\rangle}{\left\langle W_m \right\rangle} \right| \right). \tag{4.16}$$

The denominator of Equation [4.16] can be rewritten using Equation [4.13], yielding

$$\frac{\left\langle V_{eff_1} \right\rangle^2 - \left\langle V_{eff_2} \right\rangle^2}{\left\langle V_m \right\rangle^2 + k^2 \left\langle W_m \right\rangle^2} = f \left(atan \left| \frac{\left\langle V_m \right\rangle}{\left\langle W_m \right\rangle} \right| \right). \tag{4.17}$$

Recall that $<W_m>$ is determined using the approach of the traditional method. The remaining unknown, $|<V_m>|$, is solved for using the iterative Newton-Raphson method.

In conclusion, the new single-sensor hot-film CTA data reduction method derives the PLA flow velocity vector in a three-dimensional, cyclic flow field where the direction of one velocity component is known. The near-wake behind a rotor is typical of such a flow field, the axial velocity can readily be assumed to be oriented downstream. The new method requires a total of six different consecutive phase-locked single-sensor hot-film CTA measurements. In Table 4.2, the hot-film type and orientation for each of the six measurements is summarized.

4.3 Wind tunnel wall corrections

The setup of the model rotor in the open jet wind tunnel does not perfectly replicate the condition of a model rotor subject to unbounded flow that is uniform far upstream of the rotor. Two possible corrections are identified:

- blockage correction: the ratio of the model rotor area to the wind tunnel jet area is finite

- non-uniformity correction: the pitot-static tubes that record the dynamic pressure used to derive W_{jet} are in proximity to the rotor plane

The distance between the rotor hub and the wind tunnel jet exit of $1\,m$ or $1.7R_t$ and the wind tunnel jet diameter of $2.24\,m$ are small compared to the wind tunnel hall dimensions. The flow near the rotor and consequently the two corrections are thus considered to be governed by the interaction between an axisymmetric wind tunnel jet and the model rotor; the effects of the detailed wind tunnel hall layout are expected to be of second-order importance.

4.3.1 Euler flow model

Both corrections are studied by analyzing numerical solutions to an Euler flow model of a simplified wind tunnel setup, see Figure 4.5. The two-bladed rotor is modeled by a uniformly loaded actuator disc. Instead of the detailed wind tunnel hall, a circular cylinder, concentric with the wind tunnel jet axis, is implemented. The radii and the relative positions of the actuator disc and the wind tunnel jet exit are modeled to actual dimensions however.

Axial flow cases are modeled in a domain that is axisymmetric with respect to the wind tunnel jet center axis, see Figure 4.5, since an actuator disc in the windmill brake state can be assumed to yield axisymmetric flow. With the disc rotated about its vertical yaw-axis to $\Psi \neq 0°$, the resulting asymmetry violates
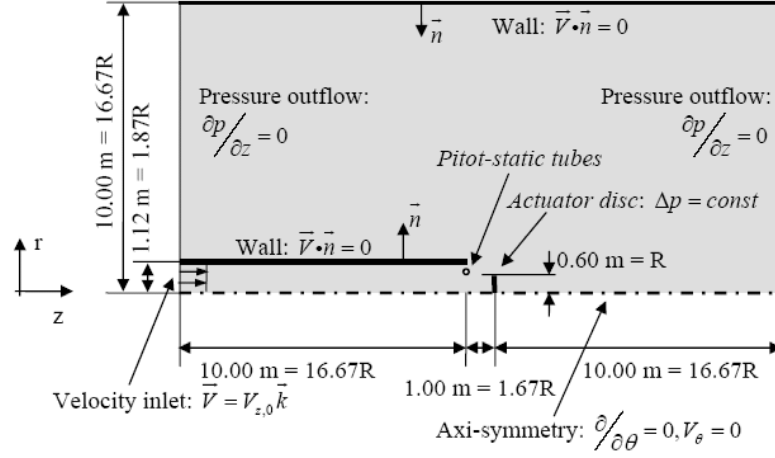
Figure 4.5: The conceptual model of a simplified wind tunnel setup for axial flow conditions. Flow direction is from left to right.

the axisymmetry assumption. Flow symmetry still applies with respect to a horizontal plane through the jet center. The three-dimensional domain used in yaw hence only includes the upper half of the setup.

The finite volume, cell centered flow solver Fluent 6.0.12 is used in the incompressible formulation, with the mass conservation and momentum equations solved sequentially. The SIMPLEC algorithm, combined with the Rhie-Chow procedure to prevent checkerboarding of the pressure, is used for pressure-velocity coupling.

The domain dimensions and grid resolution of the axisymmetric model used for the axial flow cases are determined with domain and grid dependency studies, respectively. For the resulting domain dimensions, see Figure 4.5. Highest grid resolution is found in the jet between the wind tunnel jet exit and the actuator disc; the size of the square grid cells is dictated by the discretization of the actuator disc with 21 equidistant cell nodes from center to tip. In the remainder of the domain, maximum cell stretching in both the $z-$ and $r-$direction is set to 1.05.

For the three-dimensional models used with yawed flow cases, domain and grid dependency studies would become very resource consuming and are therefore not performed. The domain dimensions and grid resolution of the three-dimensional model are similar to those of the axisymmetric model instead, since the flow field changes are not dramatic going from axial flow to yaw.

4.3.2 Blockage correction

To correct for wind tunnel blockage, the approach suggested by Glauert [62] is pursued; an equivalent unbounded air speed far upstream W_0^* is determined which yields equal velocity at the actuator disc and thrust as the undisturbed velocity $V_{z,0} = W_0$ set in the wind tunnel. For an actuator disc set to arbitrary Ψ, the equivalent velocity concept can be written as

$$C_T W_0^2 = C_T^* (W_0^*)^2 \tag{4.18}$$

$$\vec{V'^*} = \vec{V'}, \tag{4.19}$$

where the superscript * indicates the equivalent unbounded condition. W_0 is the undisturbed flow speed (scalar), C_T the thrust coefficient and V' the flow velocity at the actuator disc (vector), see Figure 4.6.
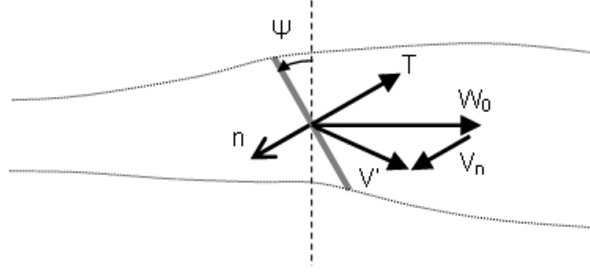
Figure 4.6: Top view of a yawed actuator disc. In contrast to related Figure 2.5, current plot does not specify far-wake induced velocity. Further, T currently acts on disc, not on flow.

In the unbounded condition, T^* acting on an actuator disc set to arbitrary Ψ is assumed to be given by Glauert's momentum relation [27],

$$T^* = \frac{1}{2}\rho A_r C_T^* (W_0^*)^2 = 2\rho A_r |\vec{V'^*}| \; \vec{n}{\cdot}\vec{V_n^*}, \tag{4.20}$$

refer to the discussion on Equation 2.14 and Figure 4.6 for the definition of the variables. For $\Psi = 0°$, Equation [4.20] reduces to the one-dimensional Rankine-Froude actuator disc theory.

Similar to the derivation for axial flow conditions by Sørensen *et al.* [187], combining Equations [4.18], [4.19] and [4.20] yields for an actuator disc set to arbitrary Ψ

$$\vec{n}{\cdot}\vec{V_n^*} = \frac{1}{4}C_T \frac{W_0^2}{|\vec{V'}|}. \tag{4.21}$$

With the vector additions

$$\vec{V'} = \vec{W_0} + \vec{V_n} \tag{4.22}$$

and

$$V'^{\vec{*}} = \vec{W}_0^* + \vec{V}_n^* \tag{4.23}$$

and Equation 4.19, Equation 4.21 can be rewritten to an expression for the blockage correction ratio,

$$\frac{W_0^*}{W_0} = \frac{1}{cos\Psi} \left(\frac{1}{4}C_T \frac{W_0}{|\vec{W}_0 + \vec{V}_n|} - \frac{\vec{n} \cdot \left(\vec{W}_0 + \vec{V}_n \right)}{W_0} \right) \tag{4.24}$$

Because C_T, W_0 and V_n are derived from the numerical model, the ratio W_0^*/W_0 can be quantified from Equation 4.24. Blockage correction results are summarized in Figure 4.7.
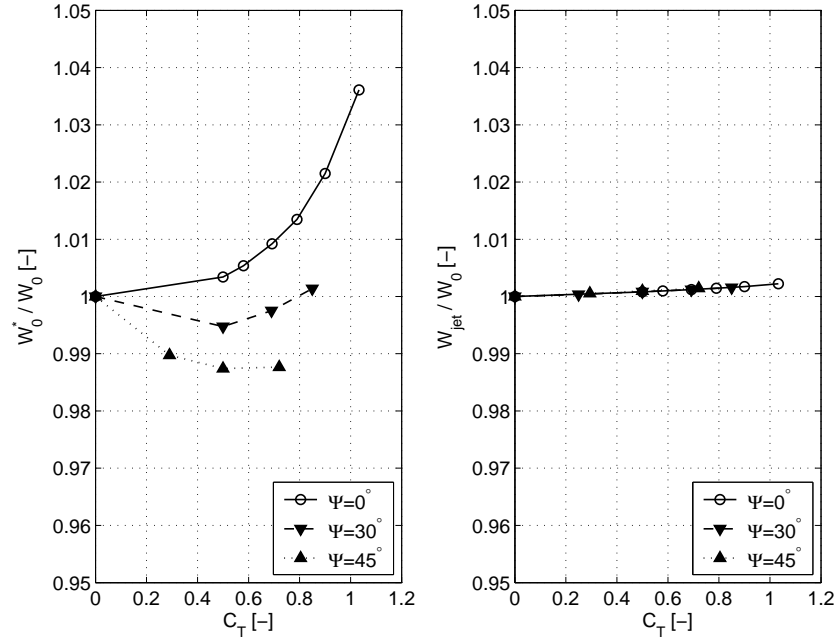
Figure 4.7: Left plot: blockage correction - (W_0^*/W_0) versus C_T. Right plot: nonuniformity correction - (W_{jet}/W_0) versus C_T. Both corrections derived from numerical inviscid actuator disc model for $\Psi = 0°, 30°, 45°$.

4.3.3   Non-uniformity correction

The distance between the rotor hub and the wind tunnel jet exit plane is $1\,m$ or $1.7R_t$. The flow in the wind tunnel exit plane, where three interconnected pitot-static tubes measure the dynamic pressure used to derive W_{jet},

is influenced by the rotor due to its close proximity, resulting in a general non-uniformity. The ratio W_{jet}/W_0 that corrects for non-uniformity is found using the flow speeds at the three pitot-static tube locations in the tunnel jet exit W_{jet_i} as found from the inviscid numerical actuator disc model, with

$$\frac{W_{jet}}{W_0} = \frac{1}{W_0}\sqrt{\frac{1}{3}\left(W_{jet_1}^2 + W_{jet_2}^2 + W_{jet_3}^2\right)}. \qquad (4.25)$$

The non-uniformity correction is marginal compared to that from wind tunnel blockage, see Figure 4.7.

4.3.4 Combined correction

The wind tunnel wall correction to arrive at the equivalent unbounded velocity W_0^* from the measured W_{jet} can be written as

$$W_0^*/W_{jet} = W_0^*/W_0 \cdot \frac{1}{W_{jet}/W_0}. \qquad (4.26)$$

The W_{jet}-dependent variables that define a rotor operating condition are subsequently corrected for wind tunnel wall effects by replacing W_{jet} with $(W_0^*/W_{jet}) \times W_{jet}$ in the expressions for λ, $Re_{0.7R}$ and $k_{0.7R}$, see Equations [3.2] to [3.5]. C_T, given in Equation 3.7, is corrected in identical fashion. In order to discriminate between uncorrected variables and those corrected for wind tunnel wall effects, the notation for the latter includes superscript *, e.g. C_T versus C_T^*.

Table 4.3 illustrates, for the three operating conditions explored with PLA CTA in the near-wake, W_0^*/W_{jet}-values and the impact on associated variables. Whereas uncorrected λ and W_{jet} are constant for all three experimental cases, wind tunnel wall corrections yield variations in λ^* and W_0^*. The relative variations are small however; up to 1.4%. Across all measurements, a typical value would be 1%, whilst the extreme goes up to 3.4%. Due to their quadratic dependency on W_0^*, C_T^*-corrections are amplified; the maximum in Table 4.3 is 3.9%, whilst a typical value and the extreme across all measurements would be 2-3% and 6.9%, respectively.

4.4 Measurement uncertainties

The quality of experimental results is assessed with an analysis of the measurement uncertainty. The methodology presented by the American Institute of Aeronautics and Astronautics (AIAA) in their measurement uncertainty standard [3] and guide [4] is applied to the present experimental campaign as it is structured and comprehensive. A further reason to apply the AIAA-approach

Table 4.3: Illustration of wind tunnel wall corrections and corrected variables

	$\frac{W_0^*}{W_0}$ [-]	$\frac{W_{jet}}{W_0}$ [-]	$\frac{W_0^*}{W_{jet}}$ [-]	W_{jet} [m/s]	λ [-]	C_T [-]	W_0^* [m/s]	λ^* [-]	C_T^* [-]
$\Psi = 0°$	1.014	1.002	1.012	5.5	8.0	0.80	5.57	7.90	0.78
$\Psi = 30°$	0.998	1.001	0.996	5.5	8.0	0.70	5.48	8.03	0.70
$\Psi = 45°$	0.987	1.001	0.986	5.5	8.0	0.51	5.43	8.11	0.53

is the authority of the AIAA in the field of aerospace wind tunnel testing, adding weight to their experimental uncertainty assessment methodology.

The AIAA-approach towards measurement uncertainty analysis is introduced in Section 4.4.1. An overview of the analyzes applied to C_T, tip vortex center locations and PLA flow velocity is given in Sections 4.4.2 to 4.4.4. The discussions focus on the approach of the analyzes, whilst typical results are given to get an appreciation of measurement uncertainties achieved.

4.4.1 Measurement uncertainty methodology

Experiments aim to uncover the real world. The relative closeness of agreement between an experimentally determined value of a quantity and its true value is termed accuracy. The experimental error ε is defined as the difference between an experimentally determined value and the true value, see Figure 4.8. ε can be considered to be composed of a random (precision) component γ and a bias (systematic) component β. An error is classified as random when it contributes to the data scatter with repeated measurements; else, it is a bias error.

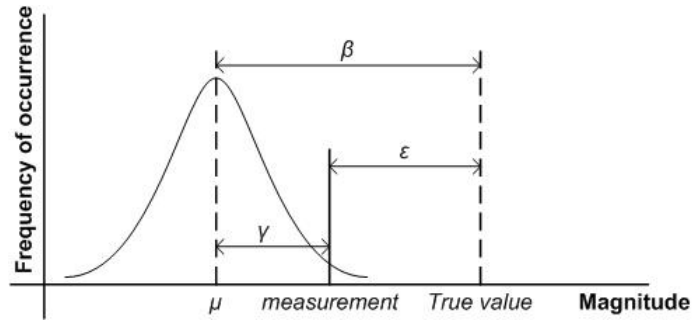Figure 4.8: Schematic of error ε between measured and true value of a quantity.

Since the true value is generally unknown, ε must be estimated by an uncertainty U, made at a confidence level determined by the experimenter. A 95

% confidence level, typically used for wind tunnel measurements, means that the true value is expected to lie within the $\pm U$-interval about the measured value 95 times out of 100.

Estimates of β and γ are given by a systematic uncertainty or bias limit B and a random uncertainty or precision limit P, respectively. For B at 95 % confidence level, the experimenter is 95% confident the true β would be within the $\pm B$-range. P at 95 % confidence level means that the $\pm P$-interval about the measured value should contain the (biased) parent population mean μ 95 times out of 100.

For most experiments, the value of the variable of interest r is derived from measured values of J independent variables X_i, using a Data Reduction Equation (DRE), written in a general form as

$$r = r\left(X_1, X_2, \ldots X_J\right). \tag{4.27}$$

γ and β associated with each X_i propagate through the DRE, resulting in γ and β of r. The corresponding estimated U_r is given by

$$U_r = \left(B_r^2 + P_r^2\right)^{1/2}. \tag{4.28}$$

The B_r- contribution to U_r can be found from analysis at the independent variable level,

$$B_r^2 = \sum_{i=1}^{J} \theta_i^2 B_i^2 + 2\sum_{i=1}^{J-1}\sum_{k=i+1}^{J} \theta_i \theta_k B_{ik}, \tag{4.29}$$

with

$$\theta_i = \frac{\partial r}{\partial X_i}. \tag{4.30}$$

Equation [4.29] is an approximation that can be derived using a first order Taylor series expansion about r. B_i is the orthogonal summation of all M elemental bias limits for each individual X_i,

$$B_i = \left[\sum_{j=1}^{M} (B_i)_j^2\right]^{1/2}. \tag{4.31}$$

The relations between elemental bias limits of different independent variables are included in Equation 4.29 through the covariance term B_{ik},

$$B_{ik} = \sum_{\alpha=1}^{L} (B_i)_\alpha (B_k)_\alpha, \tag{4.32}$$

where independent variables X_i and X_k have L identical elemental bias limits in common.

The availability of the results r from multiple tests at the same test condition allows straightforward determination of the P_r-contribution to U_r, see Equation [4.28], at the r-level, in contrast to the B_r-contribution to U_r that is derived from an analysis at the independent variable level. P_r is hence given by

$$P_r = KS_r, \tag{4.33}$$

with S_r the standard deviation for r and K the coverage factor that is dependent on the desired confidence level and the sample size; K equals 2 for a 95% confidence level and large sample size, at least 10 readings. Note that P_r derived using Equation [4.33] only incorporates those random uncertainty sources that are triggered while performing the multiple tests.

4.4.2 C_T measurement uncertainty

The rotor thrust on the model wind turbine is recorded with strain gauges that are placed on the rotor shaft. Subsequently, C_T is derived. For details on the C_T-measurements, see Section 3.2.1.

The AIAA-methodology outlined in Section 4.4.1 is employed to estimate the measurement uncertainty of C_T, U_{C_T}, at 95% confidence level. The combination of Equations [3.1], [3.7] and the ideal gas law yields C_T, written as a function of its independent variables,

$$C_T = \frac{T - T_{offset}}{A_r \Delta p}. \tag{4.34}$$

The random uncertainty P_{C_T} is studied at the level of C_T, while the bias uncertainty B_{C_T} is analyzed at the independent variable level. For all test conditions studied, B_{C_T} dominates P_{C_T}. In general, the main contributor to B_{C_T} and hence to U_{C_T} is the bias uncertainty associated with pressure difference Δp measurements by the Pitot-static tubes at the jet exit.

Typical results, given as a percentage of C_T, are a bias uncertainty of 10%, a random uncertainty of 3% and a total uncertainty of 11%, all at 95% confidence level.

4.4.3 Tip vortex center location measurement uncertainty

Quantitative smoke visualization measurements yield the location of the tip vortex centers in the near-wake behind the model rotor. For details, see Section 3.2.2. The measurement uncertainty of the tip vortex center locations is estimated at 95% confidence level. The analysis is conducted for the tip vortex center location expressed in the cartesian wind tunnel coordinate system $(x_{jet}, y_{jet}, z_{jet})$, see Figure 3.8 for the experimental setup. The measured tip

vortices are assumed to be positioned in the (x_{jet}, z_{jet})-plane, hence y_{jet} is assumed zero. The uncertainty is estimated in both in-plane directions.

The random uncertainty is studied at the level of the tip vortex center location, the bias uncertainty is analyzed at the level of the independent variables. Bias errors in the dimensions of the experimental setup, required for the parallax correction, contribute to the bias uncertainty. Furthermore, the contribution from the bias error in locating the blade tip is included. Finally, the bias uncertainty introduced by the offset in the tip vortex center position from $y_{jet} = 0$, an ignored effect with the data reduction, is also taken along.

Marked differences are observed when comparing the resulting uncertainties in the x_{jet}- and z_{jet}-direction; both B and P, and consequently U, are significantly larger in the z_{jet}- than in the x_{jet}-direction, since the vortices trailing from the blade tip are convected mainly in the downstream z_{jet}-direction.

For both directions, the term relating to the tip vortex center location offset from $y_{jet} = 0$ and the blade tip position term dominate B. The bias uncertainties of $1\,cm$ in the dimensions of the experimental setup yield negligible contributions to B, due to the relatively large dimensions; the distances between the camera and the (x_{jet}, z_{jet})-plane and between the (x_{jet}, z_{jet})-plane and the background grid are about $1.5\,m$ and $1.3\,m$, respectively, see again Figure 3.8 for the experimental setup. Typical values for the uncertainty in both in-plane directions are given in Table 4.4.

Table 4.4: The uncertainty at 95% confidence level, for measurements of the tip vortex center location, made dimensionless with R_t.

		x_{jet}	z_{jet}
B	[-]	0.01	0.05
P	[-]	0.03	0.05
U	[-]	0.03	0.07

4.4.4 Flow velocity measurement uncertainty

The three-dimensional PLA flow velocity $<\vec{V}>$ in the near-wake behind the model rotor is measured using hot-film CTA. $<\vec{V}>$ is subsequently made dimensionless through division by $(W_{jet}\,cos\Psi)$. The CTA technique, the experimental procedure and the tested conditions are discussed in Section 3.2.3, the hot-film data reduction methods are presented in Section 4.2.

The measurement uncertainty of the dimensionless three-dimensional PLA flow velocity, derived with the new data reduction method, is estimated at 95% confidence level. The data reduction yields the PLA flow velocity expressed in the cartesian non-rotating model coordinate system (x_m, y_m, z_m), see Figure

87

3.12 for the experimental setup. For all three components of the dimensionless PLA flow velocity, at all measured (r, θ, z, θ_b)-points, the measurement uncertainty $U_{<V>}$ is estimated.

Bias uncertainty $B_{<V>}$ is analyzed at the level of the independent variables. Included is bias uncertainty associated with the calibration of the hot-film probe for flow speed, see Equation [3.12]. Furthermore, the bias uncertainties in the determination and application of the angular calibration constants h and k are considered. h and k are used to express the sensitivity of the hot-film recordings to the flow direction relative to the hot-film probe, see Equation [3.13]. Finally, the bias uncertainty introduced by dividing the flow velocity through $(W_{jet} cos\Psi)$, done in order to obtain a dimensionless result, is taken along.

Random uncertainty $P_{<V>}$ is studied at the level of V_{eff}, instead of $\vec{V}$, since multiple tests of V_{eff} at the same test condition are not available for all hot-film orientations required to derive $\vec{V}$. The random uncertainty estimate obtained for V_{eff} is assumed to also hold for all three $\vec{V}$-components.

$P_{<V>}$, expressed as a fraction of W_{jet}, can be approximated at 95% confidence level by a constant; $P_{<V>} = 0.08$. $B_{<V>}$ cannot be considered constant though, the value for a given dimensionless PLA flow velocity component $<V_i>$ depends on the PLA flow velocity vector $<\vec{V}>$. At given Ψ, $U_{<V_i>}$ e.g. reduces with increased magnitude of $<V_i>$. Two typical cases of the near-wake PLA flow velocity and the associated measurement uncertainty are given in Table 4.5. All variables are made dimensionless with $W_{jet} cos\Psi$.

Table 4.5: The uncertainty at 95% confidence level, for two typical cases of a near-wake PLA flow velocity measurement. Both velocity and uncertainty are made dimensionless with $W_{jet} cos\Psi$.

		case I: $\Psi = 0°$			case II: $\Psi = 45°$		
		$<V_x>$	$<V_y>$	$<V_z>$	$<V_x>$	$<V_y>$	$<V_z>$
$\frac{<V>}{W_{jet} cos\Psi}$	[-]	0.0	-0.15	0.7	-1.0	-0.2	0.7
$B_{<V>}$	[-]	0.15	0.06	0.03	0.1	0.35	0.2
$P_{<V>}$	[-]	0.08	0.08	0.08	0.11	0.11	0.11
$U_{<V>}$	[-]	0.17	0.10	0.085	0.15	0.37	0.23

4.5 Conclusions

Experimental data reduction concerns wind tunnel wall corrections, measurement uncertainties and derivation of the PLA three-dimensional velocity from the near-wake CTA recordings.

A numerical Euler model of the simplified open jet wind tunnel is used to derive both the traditional blockage correction as well as a tunnel specific nonuniformity correction. Combined, the effects yield to a typical correction of about 1% on the undisturbed wind speed.

Measurement uncertainty analyzes follow AIAA standards and guidelines [3, 4]. Measurement uncertainty bounds are established at 95% confidence level. A typical 95% confidence uncertainty bound of 11% is found for strain gauge recordings of C_T. Those for near-wake tip vortex trajectories, found through quantitative smoke visualization, typically amount to $0.03R_t$ and $0.07R_t$ in the radial and axial direction, respectively. Uncertainty bounds at 95% confidence for the PLA three-dimensional flow velocity in the near-wake is furthermore quantified at typically $0.1W_{jet}$ for axial flow and $0.2W_{jet}cos\Psi$ for the yawed flow condition with $\Psi = 45°$.

A novel CTA data reduction method is proposed that derives the PLA three-dimensional flow velocity from single-film PLA CTA measurements. The traditional method only solves for the magnitudes of the three flow velocity components; their directions are left to the experimenter to prescribe. The novel method uses the asymmetric response of a parallel single-film probe - where the film is parallel to the longitudinal axis of the probe - to find both magnitude as well as direction of all three components of PLA flow velocity.

Chapter 5

Experimental analysis of the rotor near-wake in axial flow

This Chapter discusses the analysis of the near-wake measurements in axial flow, which forms the reference condition for yaw. Measured rotor thrust and power are presented in Section 5.1. The associated tip vortex paths are discussed in Section 5.2. For one selected operating condition, the near-wake PLA flow velocity is analyzed in detail in Section 5.3. Note that the experimental setup, measurement techniques and procedures are given in Chapter 3, whilst the experimental data reduction is discussed in Chapter 4.

5.1   Rotor performance

The near-wake studies commence with model rotor performance tests. It is recommended practise to begin every rotor aerodynamics experiment with measurements of C_T and C_P for a range of operating conditions; the results enable general performance assessment of the rotor, allow validation of and comparison with rotor aerodynamics codes, help to analyze the various operating states as a function of the rotor settings and aid in selecting operating conditions for further study.

The current experimental campaign includes C_T-measurements as a function of λ and β_{pitch} [73, 74]. For a rotor model and wind tunnel that are similar to the ones applied for the current campaign, Vermeer [206] presents C_T, C_P and tip vortex center locations. These recordings are also reported in Vermeer *et al.* [204].

Elaborating on the differences, the current rotor model is identical to the one used by Vermeer, apart from the hub; currently, it has a semi-spherical shape, with Vermeers experiments it has a sharp-edged cubic shape. After completion of Vermeer's measurements, the open jet wind tunnel moved to a
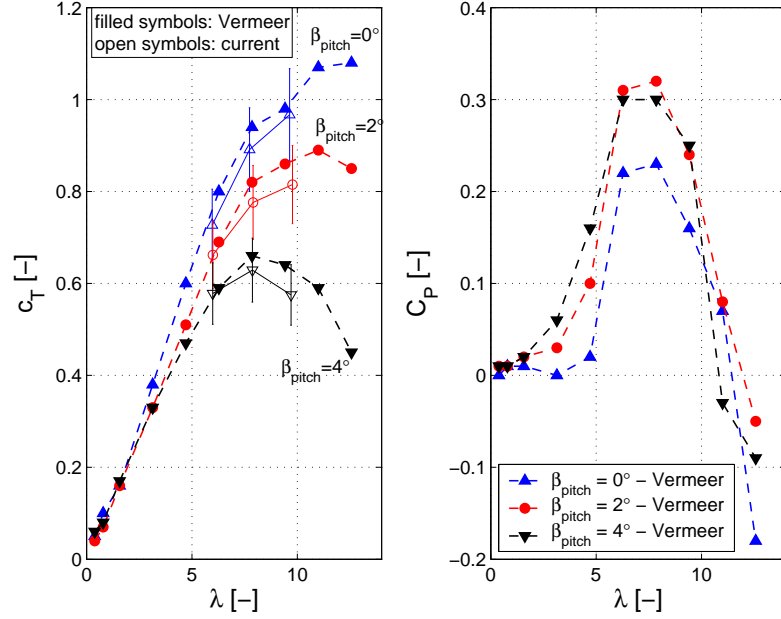
Figure 5.1: Model rotor performance in axial flow versus λ, β_{pitch}. Left plot: C_T, current and Vermeer's [206] measurements. Right plot: C_P, Vermeer's Prony brake measurements [206] only.

larger wind tunnel hall; main difference between the two wind tunnel layouts is the distance from the jet exit plane to the downstream tunnel wall, which is 6.5 m or $10.8R_t$ for Vermeers experiments and currently is 11 m or $18.4R_t$. Also note that the values for λ at which measurements are taken are not exactly identical, see Figure 5.1. Finally, Vermeer's data are not corrected for wind tunnel wall effects.

The agreement between the two sets of C_T-data is good, see Figure 5.1; the difference lies within the 95% confidence uncertainty bounds derived for the current C_T-measurements. Considering the small differences in the experimental setup and in λ between Vermeer's experiments and current measurements, the comparison strengthens confidence in the data quality.

5.2   Tip vortex characteristics

Rotor aerodynamics is dominated by the tip vortices, because of their strong circulation. To understand the phenomena governing the tip vortex geometry in the near-wake, the relation between tip vortex paths, rotor operating conditions and C_T is studied. The present discussion is based on [73, 74].
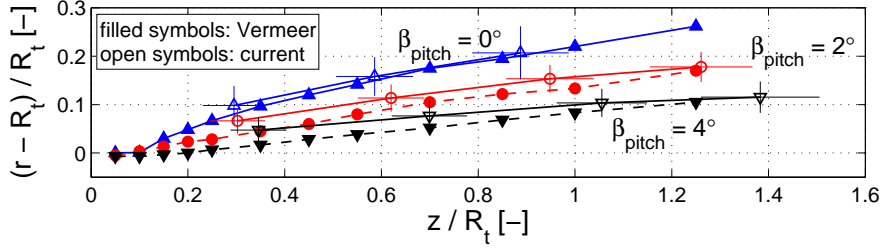
Figure 5.2: Dimensionless tip vortex center locations, relative to the blade tip, as a function of β_{pitch}. Vermeer [202]: $\lambda = 7.85$, Haans *et al.* [74]: $\lambda = 7.82, 7.90, 7.95$ for $\beta_{pitch} = 0°, 2°, 4°$, respectively.

First though, the currently measured tip vortex center locations are compared to those recorded by Vermeer [202], see Figure 5.2. The differences between the two experimental setups are discussed in Section 5.1. Furthermore, Vermeer utilizes CTA, by means of a hot-wire probe, traversing through the wake, to locate the tip vortex centers, instead of quantitative smoke visualization.

Whereas for the current measurements, the tip vortex centers are found with the blades locked at $\theta_b = 90°$, since the frequency of the stroboscopic
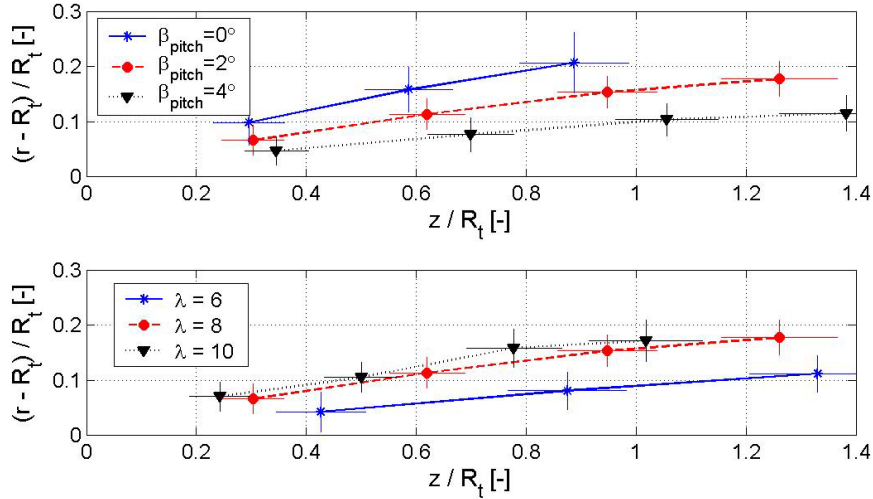

Figure 5.3: Dimensionless tip vortex center location, relative to blade tip. Top plot: $\beta_{pitch}=0°,2°,4°$ for $\lambda=8$. Bottom plot: $\lambda = 5.96, 7.90, 9.85$ for $\beta_{pitch}=2°$.

93

light source coincides with that of the rotor, for Vermeer's measurements, the blades are not locked to a particular θ_b, explaining the general mismatch between the tip vortex center *locations*. Good agreement is found for the *paths* of the tip vortex centers however; for each of the three operating conditions, the difference is smaller than the 95% confidence uncertainty bounds derived for the current quantitative smoke visualization measurements. Just as for the C_T-measurements, discussed in Section 5.1, the close match strengthens confidence in the data quality.

The tip vortex paths indicate the rotor wake boundary; the diverging tip vortex paths when going downstream, seen in Figure 5.2, hence imply wake expansion. For a rotor operating in the wind turbine state, T acting on the rotor is balanced by a reduced axial momentum, and consequently a reduced axial flow velocity, downstream of the rotor. Conservation of mass then implies an expanding wake.

The effects on the tip vortex paths of varying the rotor operating condition are illustrated in Figure 5.3. Changes in wake expansion are positively correlated with C_T-variations, compare Figures 5.3 and 5.1; the stronger wake expansion seen when altering the rotor operating condition from $\beta_{pitch} = 4°$ to $2°$ and $0°$ with constant $\lambda = 8$, corresponds to a monotonic C_T-increase. The same trend is found when changing the rotor operating conditions from $\lambda = 6$ to 8 and 10 with constant $\beta_{pitch} = 2°$.

The tip vortex pitch p is defined in Figure 5.4 as the distance in the z_m-direction between two successive tip vortex centers trailed from the same blade. Due to the limited downstream extent of the measurement domain, p is determined for the first full rotor cycle only. The average dimensionless tip vortex axial convection velocity W_{tv}/W_0 over the first rotational cycle is then given by

$$\frac{W_{tv}}{W_0} = \frac{p}{R_t} \frac{\lambda}{2\pi}. \tag{5.1}$$

The main variable governing p is λ, see Figure 5.5, as λ is inversely proportional to the distance traveled by a fluid particle in undisturbed flow, moving at W_0, within the time period of one full rotor rotation. W_{tv} is of the order of W_0, as also shown in Figure 5.5. With further downstream convection of the tip vortices from their location one rotor cycle after being shed from the tip, W_{tv} is expected to decrease, due to continued deceleration of the wake.

For given λ, the β_{pitch}-dependency of p and W_{tv} is explained by the relation between β_{pitch} and C_T, see Figure 5.1. When increasing β_{pitch} from $0°$ to $2°$ and $4°$, C_T lowers. The reduced axial flow deceleration in the near-wake associated with smaller C_T yields higher W_{tv} and hence larger p. Tip vortices generally convect downstream slower than the freestream flow, $W_{tv}/W_0 < 1$ see Figure 5.5, a feature also observed experimentally by Whale *et al.* [213].
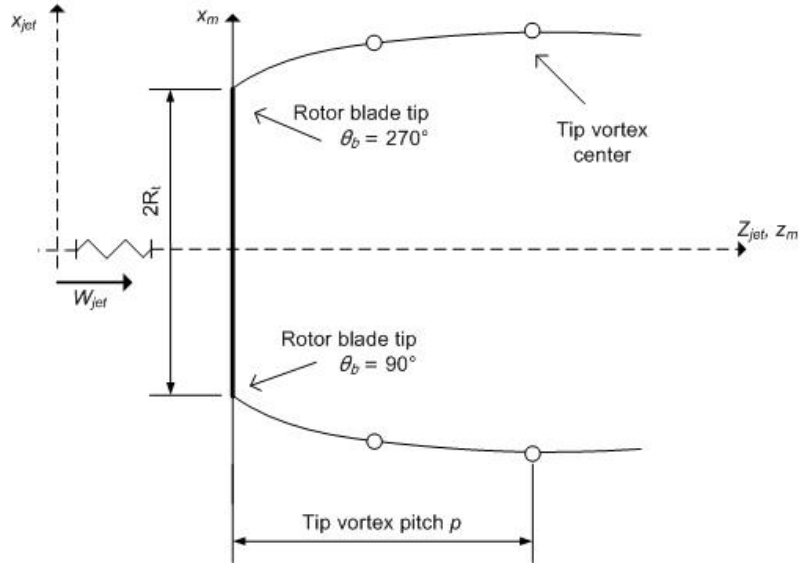
Figure 5.4: Schematic top view of the (x_m, z_m)-plane, with tip vortices trailing the two-bladed model rotor, for axial flow conditions.
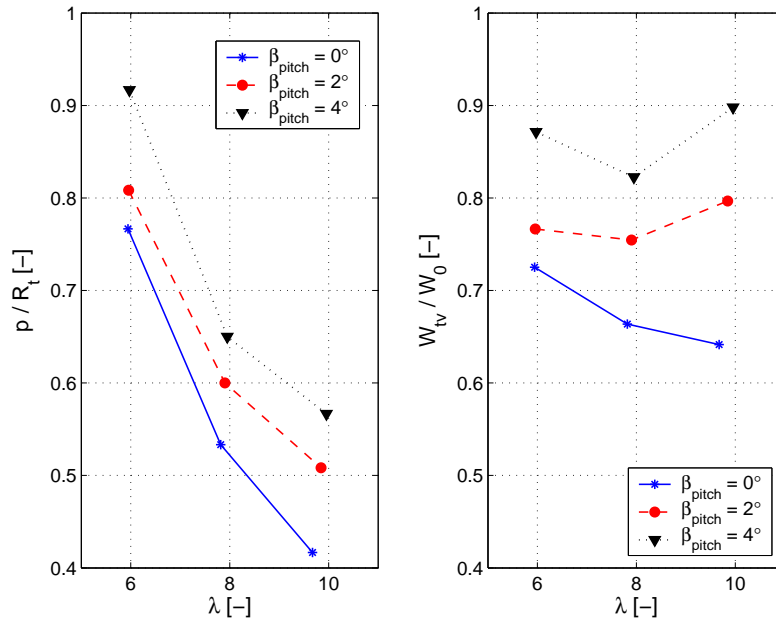

Figure 5.5: Tip vortex pitch p/R_t (left plot) and tip vortex axial convection velocity W_{tv}/W_0 (right plot) as a function of λ and β_{pitch}.

95

5.3 Near-wake flow velocity field

In contrast to the quantitative smoke visualizations, PLA CTA measurements are extremely time-consuming. The operating conditions should hence be selected with due consideration. In order not to complicate the assessment of the yaw misalignment effects on the near-wake flow velocity field, the reference axial flow operating conditions should yield attached blade flow. The operating condition of $\lambda = 7.9$, $\beta_{pitch} = 2°$ is chosen for measurements of the PLA near-wake flow velocity distribution, since the proximity of the corresponding C_P to $C_{P_{max}}$, see Figure 5.1, suggests generally attached blade flow.

The annular averaged axial induction factor is studied first, in Section 5.3.1. More insight is obtained by analyzing PLA instead of annular averaged data; to start with, measurement repeatability and the influence of the data reduction method on the PLA flow velocity are analyzed in Section 5.3.2. Thereafter, the trends observed in the PLA flow velocity with blade and wake passages are discussed in Section 5.3.3. Furthermore, the PLA flow velocity is used to reconstruct the local angle of attack, see Section 5.3.4 and to derive the viscous wake convection velocity, see Section 5.3.6. The foundation for the present discussion is laid in the first article of the series of two articles on the CTA measurements [78] and in a precursor hereof [75].

For the same rotor, wind tunnel and operating conditions, Schepers [152] presents measured PLA flow velocity at a plane $z/R_t = 1.00 \cdot 10^{-1}$ downstream of the rotor[1]. The sample used to determine the PLA consists of 10 recordings per (r, θ, z, θ_b)-point, instead of 54 recordings for the present measurements. To assess the quality of the current flow velocity measurements, both the annular averaged and the PLA flow velocity are compared to Schepers' results in Sections 5.3.1 and 5.3.2, respectively.

5.3.1 Annular averaged induction

The availability of the PLA axial flow velocity $<V_z>$ at all three downstream measurement planes, located at $z/R_t = 5.83 \cdot 10^{-2}$, $1.00 \cdot 10^{-1}$ and $1.50 \cdot 10^{-1}$, allows for the determination of the annular averaged axial velocity $\overline{<V_z>}_{ann}$, expressed analytically as

$$\overline{<V_z>}_{ann}(r, z, \theta_b) = \frac{1}{2\pi} \int_0^{2\pi} <V_z> (r, \theta, z, \theta_b) \, \mathrm{d}\theta. \tag{5.2}$$

The finite measurement resolution requires discretization of Equation [6.5]; $\overline{<V_z>}_{ann}$ is determined for given θ_b at given annulus with radius r, located at one of the three downstream measurement planes, by averaging $<V_z>$

---

[1]These recordings are performed by Vermeer within the framework of constructing an engineering inflow model for yaw, refer to [152].

over all available θ-points. The annular averaged axial induction factor a is subsequently given by

$$a = 1 - \frac{\overline{<V_z>}_{ann}}{W_0}. \tag{5.3}$$

For each annulus, a is thus determined per given θ_b; the data sample of a contains 180 recordings, since $\Delta \theta_b = 2°$.

The value for a at the rotor plane is derived using the recordings at the three downstream measurement planes, since no measurements are performed in the rotor plane itself. For given θ_b and r, the assumed linear function $a = a(z)$ is fitted in the Least Squares sense to the measured data at the three z-locations and used to extrapolate a to the rotor plane.
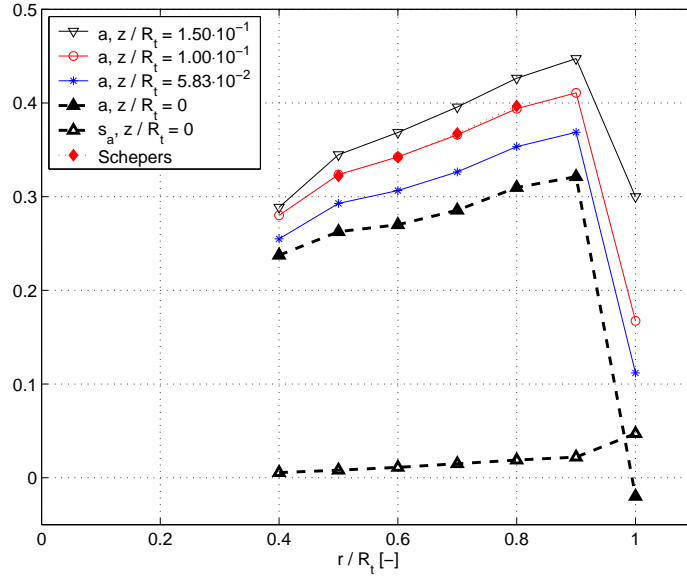

Figure 5.6: Recorded $\overline{a}$ in near-wake measurement planes and estimated $\overline{a}$, s_a in the rotor plane. Included is $\overline{a}\,(z/R_t{=}0.10)$, presented by Schepers [152].

The average $\overline{a}$ and standard deviation s_a of the 180 a-recordings per annulus are subsequently determined, see Figure 5.6. For clarity, only s_a at the rotor plane is plotted.

The axial flow condition considered ideally results in stationary near-wake flow variables for an observer rotating with the blades. Such a condition is here referred to as "rotating stationary flow", refer to Appendix B for more details. Perfect measurements of a rotating stationary flow would hence yield constant $a(\theta_b)$ and $s_a = 0$ at given annulus. As here $s_a \neq 0$, the measurements

are not perfect and/or the flow is not perfectly rotating stationary. Observed deviations from $a(\theta_b)$ are considered acceptable though.

The expected gradual $\bar{a}$-increase when going downstream and a radial dependency in $\bar{a}$ can be observed in Figure 5.6. The increased s_a in the rotor plane near the blade tip can be explained by small asymmetries in the strong tip vortex. The good agreement between measurements presented by Schepers [152] and present data by Haans et $al.$ [78] for $\bar{a}$ at $z/R_t = 1.00 \cdot 10^{-1}$ strengthens confidence in the results.

Application of the one-dimensional, steady, inviscid momentum theory to a at given annulus in the rotor plane yields the local thrust and power coefficients $c_t(r)$ and $c_p(r)$, recall Equations [2.11] and [2.12], respectively. Next, rotor level C_T is computed by integrating $c_t(r)$ across the rotor disc under the assumption of a piecewise constant c_t-distribution. Furthermore, c_t is assumed to be zero at the root and tip. For each recorded θ_b, a C_T-value is available. Averaging over the rotational cycle yields $\overline{C_T}$. An identical procedure is conducted to find $\overline{C_P}$.

The near-wake flow velocity measurements result in $\overline{C_T} = 0.75$ and $\overline{C_P} = 0.53$. Force measurements on the rotor[2], using strain gauges, yield $C_T = 0.78 \pm 0.08$. For a rotor model and wind tunnel that are similar to the ones applied for the current campaign, as explained in Section 5.1, Vermeer's [202] strain gauge and Prony brake measurements at $\lambda = 7.9$, $\beta_{pitch} = 2°$ yield $C_T = 0.82$ and $C_P = 0.32$, respectively. The observation that Vermeer's C_T-measurement is within the uncertainty bound of present recordings adds confidence to the data.

The difference in C_T from momentum theory and current force measurements also is within the uncertainty bounds of the latter. An exact match is not expected however; even when the flow would be rotating stationary, resulting in steady annular averaged flow velocity for each annulus, the momentum theory assumption of a one-dimensional, inviscid flow does not hold in reality. The significant difference[3] in C_P is considered to be mainly caused by invalid modeling assumptions; C_P obtained by the momentum model is thought to be unrealistically high for the Re-number under consideration, $Re_{0.7R} = 1.6 \cdot 10^5$, as the model inappropriately assumes inviscid flow. In reality, viscous drag effectively constitutes a loss-term for blade torque and rotor power.

---

[2]Note the force and power measurements "loose" the average-symbol, e.g. C_T versus $\overline{C_T}$, since these variables are not formally averaged from independent values per θ_b; underlying W_0 and T are e.g. determined 59 and 2 times per cycle.

[3]The difference between results is named significant when their uncertainty bandwidths do not overlap. Because the measurement uncertainty of Vermeer's C_P-recordings is unknown, the difference between C_P recorded and obtained by applying momentum theory to near-wake measurements can in principle only be $assumed$ to be significant.
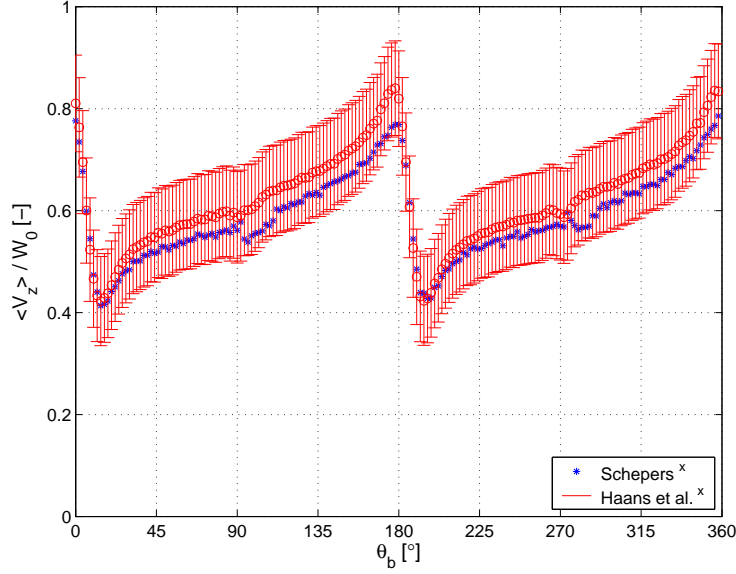
Figure 5.7: Dimensionless PLA axial flow velocity $<V_z>/W_0$ versus θ_b at $(r/R_t, \theta, z/R_t) = (0.7, 180°, 0.10)$ for Schepers [152] and Haans *et al.* [78], the latter including uncertainty intervals. Blade passage: $\theta_{b_{blade}} = 0°, 180°$, wake passage: $\theta_{b_{wake}} \approx 90°, 270°$.

5.3.2 Data quality of PLA velocity

The analysis of $<\vec{V}>$ commences with an assessment of data quality. The influence of the data reduction method is studied by employing both the traditional and new data reduction methods, discussed in Section 4.2, to derive $<\vec{V}>$. Recall that the new method is based on the asymmetric response of the parallel hot-film probe. Furthermore, repeatability is studied by comparison of the present data with the results published by Schepers [152]. Note that Schepers' results are derived using the traditional data reduction technique.

Comparisons at an inertial position in the midspan region of a measurement plane $z/R_t = 1.00 \cdot 10^{-1}$ downstream of the rotor are given in Figure 5.7 for $<V_z>$ and in Figure 5.8 for $<V_r>$ and $<V_\theta>$. For $<V_z>$, only the repeatability can be studied as the procedure to derive $<V_z>$ is identical for both data reduction techniques.

The agreement between present and Schepers' $<V_z>$-data is within the measurement uncertainty bounds of the present tests, see Figure 5.7; the maximum and average of the absolute difference in $<V_z>/W_0$, determined over a rotational cycle, are 0.08 and 0.04, respectively. Finding this repeatability between the two measurement campaigns adds confidence to the present data.
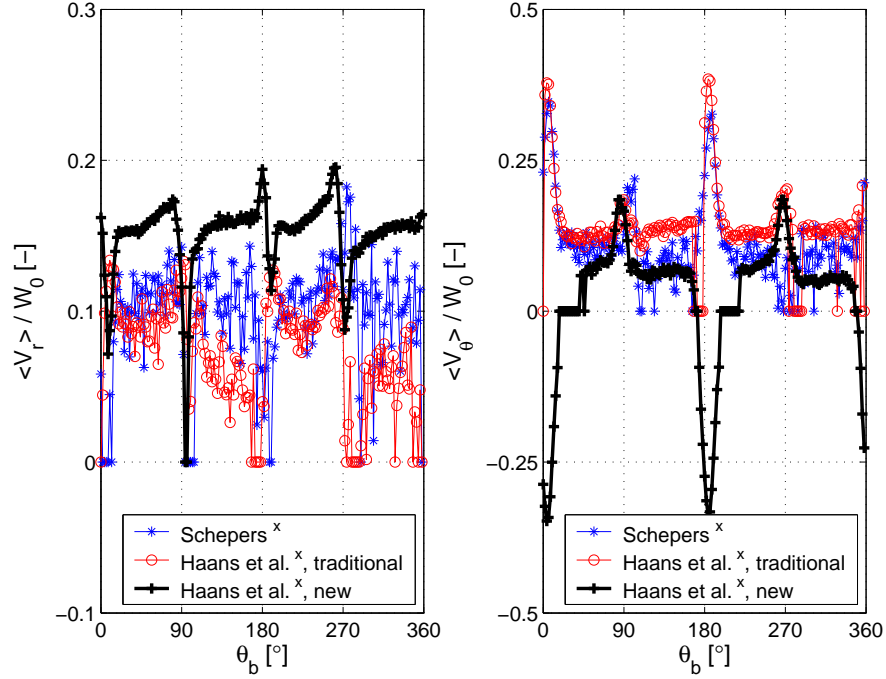
99

Figure 5.8: Left plot: dimensionless PLA radial flow velocity $<V_r>/W_0$ versus θ_b at $(r/R_t, \theta, z/R_t) = (0.7, 180°, 0.10)$ for Schepers [152] and Haans *et al.* [78]. Right plot: idem, but dimensionless *azimuthal* PLA flow velocity $<V_\theta>/W_0$. Blade passage: $\theta_{b_{blade}} = 0°, 180°$, wake passage: $\theta_{b_{wake}} \approx 90°, 270°$.

The three approaches to derive $<V_r>$ and $<V_\theta>$ predict equal order of magnitudes for given flow velocity component, see Figure 5.8. The characteristics of the $<V_r>$- and $<V_\theta>$-distribution as a function of θ_b differ significantly however between the two data reduction methods. The wiggles of the traditional approach are reduced for the new method, thereby better identifying blade and wake passages. The ability of the new data reduction method to derive the direction of the flow velocity vector as part of the solution is illustrated in the right plot of Figure 5.8; whereas the traditional approach predicts $<V_\theta>$ to be positive everywhere, the new data reduction method yields sign changes. Qualitative comparison with near-wake velocity measurements by Ebert and Wood [48] and Vermeer [202] confirms the shape of the $<V_\theta>$-distribution.

The new method predicts zero PLA flow velocity for a few phase angles, e.g. $<V_r>= 0$ at $\theta_b = 94°$ and $<V_\theta>= 0$ at $\theta_b = 30°$. Though it cannot be ruled out that given PLA flow velocity component is actually zero, the new method returns a zero when the set of $<V_{eff}>$-recordings at given θ_b yields

inconsistent predictions; $|<V_{r,\theta}>|<0$. Note the relation to measurement uncertainty; with increased uncertainty, these zero-cases occurs more often and for larger true amplitudes of given flow velocity component. The limited number of zeros and their occurrence at low expected true amplitudes of the given velocity component seen when using the new method to current recordings, as exemplified in Figure 5.8, suggests that its robustness is acceptable.

The reduction of nonphysical wiggles and the inclusion of the direction for the flow velocity $<V_r>$- and $<V_\theta>$-components enables more physical insight to be obtained with the application of the new data reduction method compared to the traditional data reduction technique. The remainder of the discussion is hence based upon the PLA flow velocity derived using the new data reduction method.

5.3.3 Trends in PLA velocity

Not only the PLA velocity $<\vec{V}>$, but also the phase locked standard deviation of the effective velocity s_{Veff}, determined over 54 blade rotations per (r,θ,z,θ_b)-data point, yields information on the wake flow. As shown in [75], s_{Veff} is an effective measure of the viscous wake passage. Fluctuations due to wake turbulence result in a local s_{Veff}-increase with a wake passage.
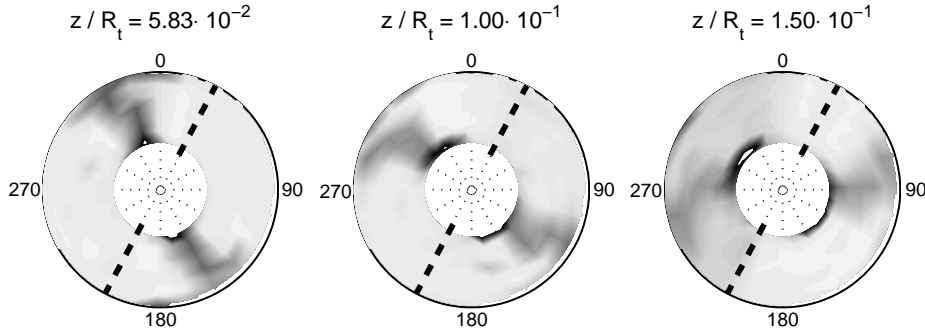
Figure 5.9: $(1-s_{veff})$ at three downstream measurement planes for $\theta_b = 28°$. Viewpoint: upstream of the rotor, facing downstream, blades rotate clockwise.

The evolution of the viscous wake in the near-wake region is illustrated in Figure 5.9. While convecting downstream, the viscous wake diffuses and is deformed. Nonuniform induction yields deformation of the wake from its original nearly linear shape when trailed from the blade trailing edge. The concentrated tip vortices induce a strong induced flow field locally near the tip vortex, with corresponding large induced velocity gradients. Wake deformation hence increases towards the tip vortices.

Figure 5.10: Nondimensional velocity versus θ_b at $(\theta, z/R_t) = (90°, 0.0583)$ for radial locations $r/R_t = 0.4, 0.6$ and 0.9. $\overline{\langle V_r \rangle}/W_0 : *$, $\overline{\langle V_\theta \rangle}/W_0 : +$, $\overline{\langle V_z \rangle}/W_0 : \circ$

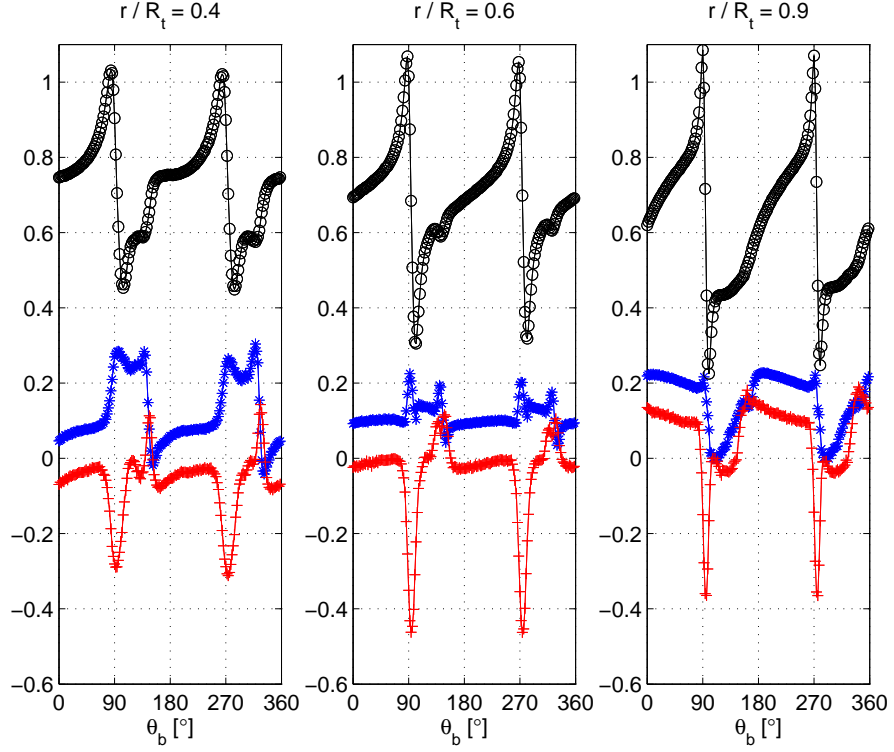Using the axial flow property of a rotating stationary near-wake, refer to Appendix B, the phase angle of PLA flow velocity recordings can be rewritten to $\Delta\theta = (\theta_b - \theta)\, mod\, 360°$. The phase lag between measurements at different azimuthal locations for given $(r/R_t, z/R_t)$ is thus effectively eliminated. Consequently, the $15°$ azimuthal resolution of the current measurements provides 24 data points per sample of $\langle\vec{V}\rangle\,(r/R_t, \Delta\theta, z/R_t)$.

Averaging over a sample of 24 data points yields $\overline{\langle\vec{V}\rangle}$. For three radial stations, $\overline{\langle V_r \rangle}$, $\overline{\langle V_\theta \rangle}$ and $\overline{\langle V_z \rangle}$ are plotted in Figures 5.10 to 5.12 for the three downstream locations. Whilst the distributions are a function of $\Delta\theta$ for given r and z, they are presented as a function of θ_b for $\theta = 90°$. Further, for better legibility, the notation used for the analysis is $\langle\vec{V}\rangle$, instead of $\overline{\langle\vec{V}\rangle}$.

To help explain the trends observed in the near-wake velocity, a typical lifting line wake vortex model is presented in Figure 5.13. The blade is represented by a bound vortex, the lifting line, with circulation Γ_b. Vorticity is

102
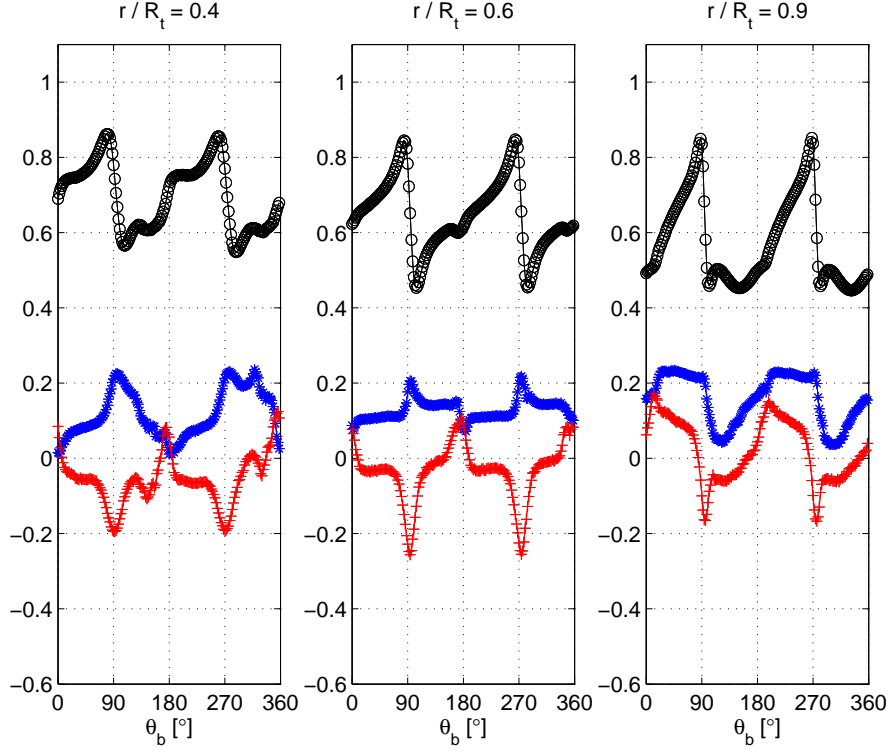
Figure 5.11: idem as Figure 5.10, but then at $z/R_t = 0.100$.

trailed into the wake to form a vortex sheet with circulation Γ_t. The velocity induced by a vortex segment is dictated by the Biot-Savart law. The flow velocity at a given location is the summation of the undisturbed flow velocity and the velocity induced by all vortices in the system, both bound and in the wake.

For a given (r, θ, z)-location, the phase angle of the blade passage is known a priori,

$$\theta_{b_{blade}} = \theta + i\frac{360°}{B} \quad mod\, 360°, \tag{5.4}$$

with $i = 0, \ldots, B{-}1$ and B the number of blades. The trends in the induced velocity during the blade passages, here located at $\theta_{b_{blade}} = 90°$ and $270°$, are analyzed by comparison with predictions from a simplified version of the lifting line model vortex model shown in Figure 5.13. The simplified model does not have a wake; it consists of the two bound vortices only, one for each blade, with constant circulation Γ_b oriented outboard. The experimental operating condition is modeled, with prescribed $\Gamma_b/(W_0 R_t) = 0.15$.

103
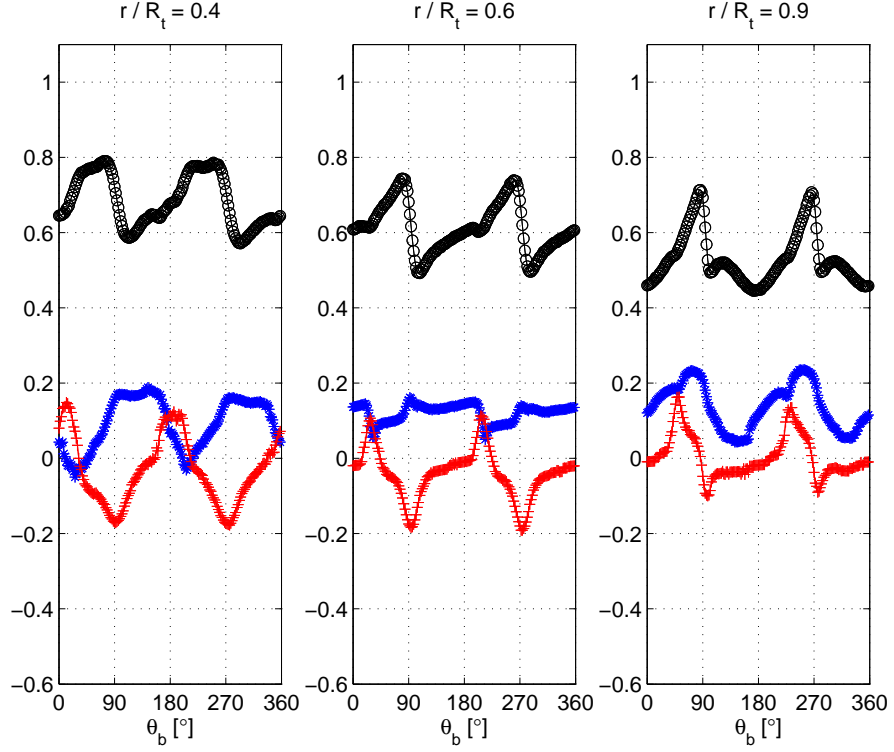
Figure 5.12: idem as Figure 5.10, but then at $z/R_t = 0.150$.

The results from the simplified lifting line model, see Figure 5.14, are compared with the measurements, see Figures 5.10 to 5.12. The observation that the local maximum and subsequent local minimum in the $<V_z>$-signal and the local $<V_\theta>$-minimum at blade passage are induced by the bound vortex is confirmed by experimental analyzes of the near-wake flow by e.g. Ebert and Wood [48], Vermeer [202] and Massouh *et al.* [119]. The amplitude of the peaks is reduced when going downstream for a given radial position, since the distance to the bound vortices is increased.

Comparing results from the simplified lifting line model (Figure 5.14) with the measured findings (Figures 5.10 to 5.12), the bound vortex is also seen to induce a local minimum followed by a local maximum for $<V_r>$ at blade passage when $r/R_t = 0.6$. This phenomenon is attributed to blade rotation; the bound vortex of a translating lifting line does not induce a spanwise flow. When the lifting line is set to rotate, the bound vortex does induce a radial flow.

The increase and decrease in $<V_r>$ measured during a blade passage at

Figure 5.13: Typical lifting line vortex wake model. The position of a hot-film sensor recording the flow velocity is indicated. Note flow is from right to left.

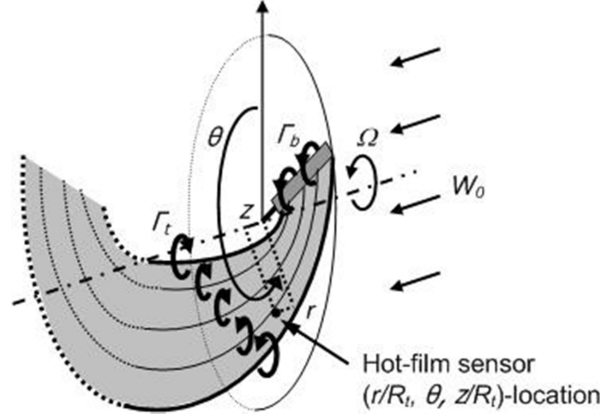$r/R_t = 0.4$ and 0.9, respectively, is hypothesized to originate from the radial component of the flow rounding the blade root and tip, driven by the pressure difference between the blade pressure and suction side. This phenomenon is out-of-scope for the simplified lifting model and therefore not seen in its predictions. Note that in general, $<V_r>$ is positive during a blade cycle, corresponding to an expanding flow.

Whereas for given (r, θ, z)-location, the phase angle of the blade passage $\theta_{b_{blade}}$ is known a priori, recall Equation [5.4], the phase angle of the wake passage $\theta_{b_{wake}}$ depends both on the operating condition and the (r, θ, z)-location. For reasons explained later in this section, $\theta_{b_{wake}}$ corresponds to θ_b at which local $<V_\theta>$-maxima are found, see Figures 5.10 to 5.12. Note that the phase difference between the wake and blade passage increases when going downstream, as expected.

The vorticity bound to the blade is confined to the blade boundary layer. The boundary layer trails the blade to form the viscous wake. The wake flow is assumed to be irrotational except for the viscous wake, where vorticity is concentrated. Combined vorticity and turbulent kinetic energy measurements in the near-wake by Ebert and Wood [49] confirm this assumption. The flow velocity at wake passage is hence affected both by viscous and by inviscid vorticity effects.

The only flow velocity trend measured at wake passage that can be explained from inviscid vorticity is that for the $<V_r>$-component. Passage of the vortex sheet induces the step-like change seen for $<V_r>$. The sign of the $<V_r>$-change is determined by the orientation of the circulation in the trailed vortex sheet Γ_t, see Figure 5.13 for a schematic representation. The orienta-

105
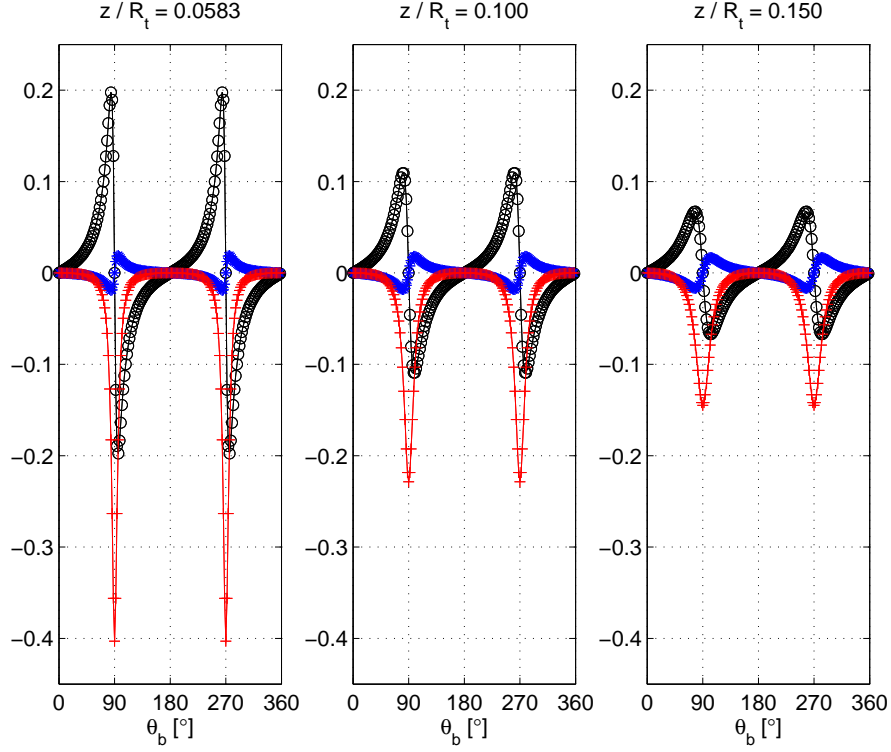
Figure 5.14: Modeled nondimensional induced velocity versus θ_b at $(\theta, r/R_t) = (90°, 0.6)$ for downstream planes $z/R_t = 0.0583, 0.100$ and 0.150. $V_r/W_0 : *$, $V_\theta/W_0 : +$, $V_z/W_0 : \circ$

tion of Γ_t at the time of trailing is in turn related to the sign of the spanwise gradient of bound circulation $d\Gamma_b/dr$, a consequence of conservation of circulation. $d\Gamma_b/dr > 0$ yields Γ_t oriented upstream, leading to a step decrease in $<V_r>$ at wake passage. For $d\Gamma_b/dr < 0$, opposite results are obtained.

Step-like $<V_r>$-decreases and -increases are found for $r/R_t = 0.4, 0.6$ and $r/R_t = 0.9$, respectively. The assumption of purely axial wake convection then results in $\partial\Gamma_b/\partial r > 0$ for blade sections with $r/R_t = 0.4, 0.6$ and $\partial\Gamma_b/\partial r < 0$ for $r/R_t = 0.9$. Since the Γ_b-shape expected for a rotating blade satisfies these $d\Gamma_b/dr$-criteria, confidence in the $<V_r>$-measurements is strengthened.

Viscous effects are responsible for the trends in $<V_\theta>$ and $<V_z>$ with wake passages. The local $<V_z>$-minimum and $<V_\theta>$-maximum represent the momentum loss due to viscous drag associated with the boundary layer that trails from the blade surface into the wake. For the current high-λ condition, the viscous drag mainly acts in the tangential direction, its effect in the axial

direction is small.

The local $<V_z>$-minimum at the wake passage represents an axial momentum loss, hence the viscous drag contribution to the thrust. The observation that $<V_\theta> > 0$ at the wake passage indicates that the wake is dragged along in the rotor rotation direction, a remnant of the no-slip condition on the blade surface. The local $<V_\theta>$-maximum corresponds to a reduction in angular momentum of the flow and hence a reduction in rotor torque.

5.3.4 Angle of attack

BEM and vortex wake methods utilize airfoil models to determine blade sectional loads for a given velocity distribution in the rotor plane. The airfoil models describing the blade section aerodynamics are based on two-dimensional theory and require an angle of attack α.
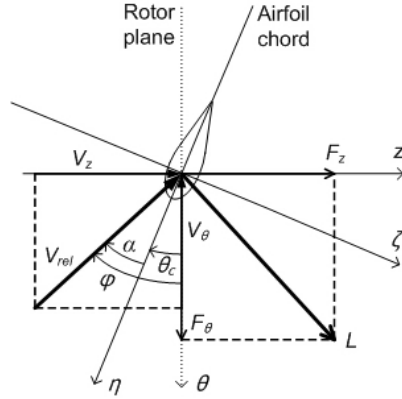
Figure 5.15: Angle of attack α on a rotating blade section.

For a two-dimensional airfoil, equivalent to a wing of infinite span, α is defined by the angle between the undisturbed flow and the airfoil chord. For a translating, finite wing, the spanwise Γ_b-variation results in the formation of a trailed vortex sheet that induces a velocity at the wing. α is subsequently defined as the angle between the local flow velocity relative to a wing section V_{rel} and the sectional chord. V_{rel} should be constructed with induced velocity contributions from all vortices, except for the local bound vortex. Note that for wing sections near the tip, the assumption of two-dimensional sectional flow does not hold due to three-dimensional tip vortex effects.

The two-dimensionality assumption is further violated on a rotating blade, as the flow passing a blade section is bent due to the blade rotation. Further-

more, possible rotational augmentation in the blade root region results in significant three-dimensional effects on the blade. The definition of α on a rotating blade, shown in Figure 5.15, is identical however to that on a translating wing.

Since α cannot be measured directly, methods have been proposed to derive α from rotor experiments, refer to Section 2.3.1 for a discussion hereof. Methods can generally be divided into those that need both blade load and flow velocity measurements and those that only require flow velocity data.

At present, blade loads are not recorded; only approaches based on inflow data can thus be applied. First, the annular averaged axial velocity method of Hansen *et al.* [87] is used. The procedure to arrive at the annular average $\overline{<V_z>}_{ann}$ in the rotor plane is similar to the determination of a in the rotor plane, see Section 5.3.1.

Furthermore, α is determined from the present measurements with a modified version of the blade passage method by Sant [147]. The method is based on the observation that, with the blade represented by a lifting line, the contribution from the bound vortex to the $<V_z>$-signal at given (r, θ, z)-location is antisymmetric around $\theta_{b_{blade}}$. The PLA axial flow velocity at the blade passage $<V_z>_{blade}$, obtained by averaging the characteristic local $<V_z>$-maxima and -minima associated with a blade passage, see Figure 5.16,

$$<V_z>_{blade} = \frac{<V_z>_{max} + <V_z>_{min}}{2}, \tag{5.5}$$

is hence assumed not to be influenced by the local bound vortex[4]. The definition of α is based on V_{rel} that excludes the flow induced by the local bound vortex. When $<V_z>_{blade}$ is estimated in the rotor plane, it would essentially represent this V_{rel}, thereby allowing α to be estimated.

Sant averages $<V_z>_{blade}$ over all available θ-positions per annulus for the measurement planes $z/R_t = 0.100$ upstream and $z/R_t = 0.0583$ downstream, whereafter a linear interpolation yields the spanwise $<V_z>_{blade}$-distribution in the rotor plane.

At present however, the upstream hot-film CTA measurements are ignored, as mentioned in Section 3.2.3. Hence, in contrast to Sant's approach, a linear relation between $<V_z>_{blade}$ and z is fitted in the Least Squares sense using data at the three downstream measurement planes per θ at given annulus. Extrapolation of the linear function yields $<V_z>_{blade}$ in the rotor plane that is subsequently used to determine α. Next, the average $\overline{\alpha}$ and standard deviation

---

[4]Besides the lifting line representation, a second requirement is needed to ensure that $<V_z>_{blade}$ does not contain a component induced by the bound vortex: the axial component of the flow velocity induced by wake vorticity should vary linearly between θ_b at the $<V_z>$-maximum and -minimum. This second requirement is generally not met.

s_α are determined for the sample of 24 θ-points per annulus. Note that perfect measurements of a rotating stationary flow would yield $s_\alpha = 0$.
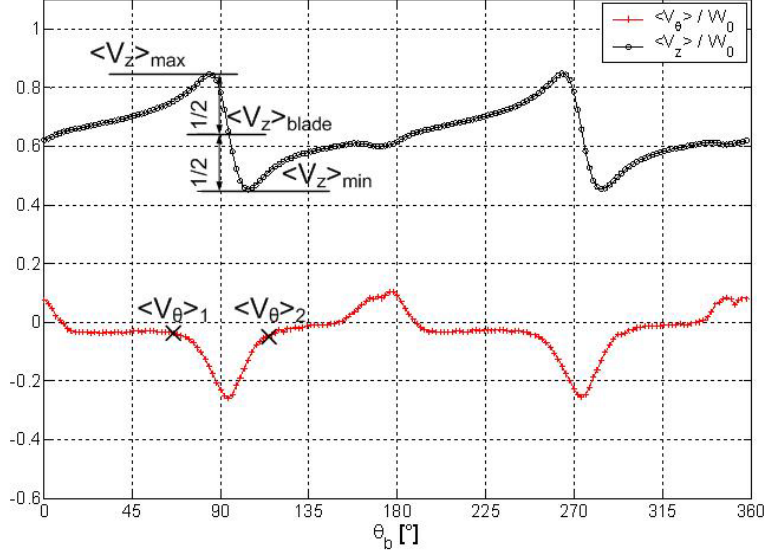
Figure 5.16: The determination of $<V_\theta>_{blade}$ and $<V_z>_{blade}$, illustrated for $(r/R_t, \theta, z/R_t) = (0.6, 90°, 0.100)$.

The azimuthal component of V_{rel} used to define α consists of contributions from blade rotation and velocity induced from wake vorticity. The latter, termed the PLA azimuthal flow velocity at the blade passage $<V_\theta>_{blade}$, is estimated from the near-wake measurements; for a given (r, θ, z)-location, visual inspection yields two θ_b-positions near $\theta_{b_{blade}}$ where the $<V_\theta>$-decrease induced by the local bound vortex is deemed insignificant, see Figure 5.16. $<V_\theta>_{blade}$, found by averaging $<V_\theta>$ at the two points,

$$<V_\theta>_{blade} = \frac{<V_\theta>_1 + <V_\theta>_2}{2}, \qquad (5.6)$$

appears to be small compared to the blade rotation component for the axial flow condition studied and is readily ignored in the determination of α.

For $0.4 \leq r/R_t \leq 0.9$, the difference in $\overline{\alpha}(r)$ between Hansen's method and the blade passage method is smaller than their corresponding s_α, see Figure 5.17. For the model rotor with its relatively high solidity, the difference between the annular averaged and the local axial induction factor, both in the rotor plane, thus is insignificant. For a rotor having lower solidity, differences in α-prediction between the two methods are expected.

109
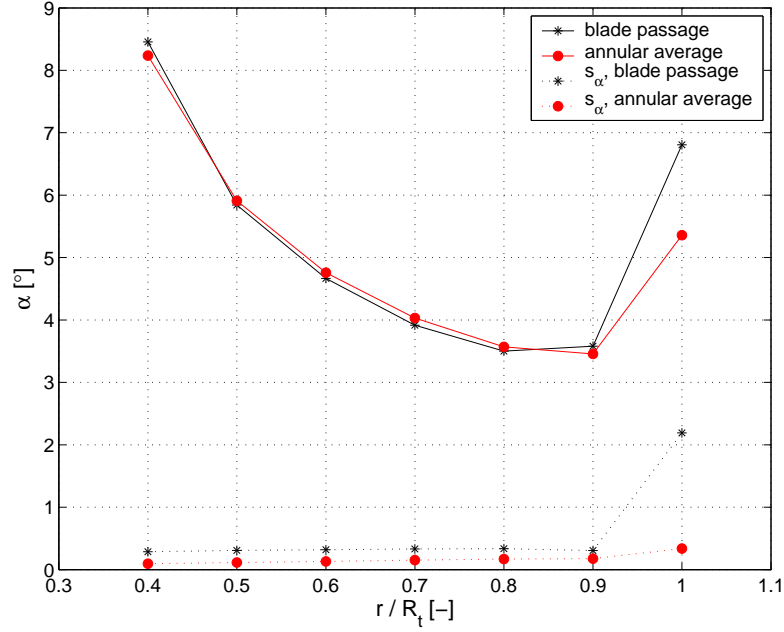
Figure 5.17: $\overline{\alpha}$ and s_α versus r/R_t, determined with both the annular average (Hansen *et al.* [87]) and the blade passage (modified Sant [147]) method.

Both models indicate an $\overline{\alpha}$-increase towards the tip, but show a significantly different $\overline{\alpha}$ for $r/R_t = 1$. The cause could be the difference between local and annular averaged axial flow velocity near the tip. In theory, the blade passage method would yield more accurate α-results near the tip, as it considers local instead of the annular averaged axial induction; the former is used in the definition of α. In practise however, its higher s_α suggests that the blade passage method is less precise than the annular averaged axial velocity method. Results from both methods are hence questionable at $r/R_t = 1$.

The maximum angle of attack is found at the most inboard measurement position, $\overline{\alpha}_{max} = 8.5°$ at $r/R_t = 0.4$. Measurements on the NACA0012 airfoil at $Re = 0.15 \cdot 10^6$ yield $\alpha_{stall} = 10.6°$, see Figure 3.5, suggesting that stall is not present on the blades. Detailed blade loads that could confirm this suggestion are not measured however.

5.3.5   Blade loads

The availability of an approximate $\overline{\alpha}$-distribution enables the blade loads to be estimated using an appropriate airfoil model. Here, the airfoil model is given by (c_l, α)-tables found from NACA0012 wind tunnel measurements, see

Figure 3.5. In accordance with Wilson and Lissaman [215] and De Vries [209], drag is not included, in view of the comparison with results obtained for the one-dimensional *inviscid* momentum approach, discussed in Section 5.3.1.
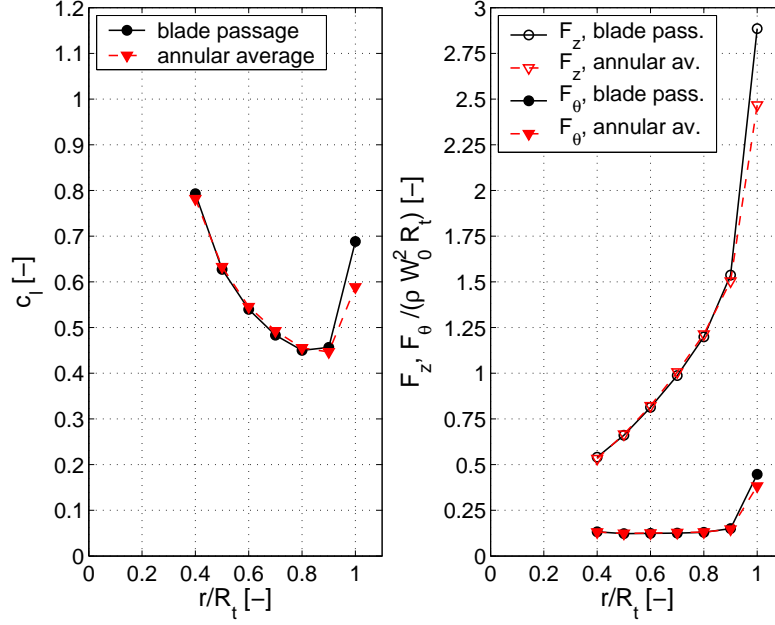
Figure 5.18: c_l (left plot) and F_z, F_θ (right plot, open en filled symbols, respectively) versus r/R_t. Results obtained by applying airfoil measurements to α determined with the blade passage method: $\circ$, idem, but α determined with annular averaged axial flow method: $\triangledown$.

The $\overline{\alpha}$-estimates at all available blade sections are hence related to c_l-values. The lift per unit span L is subsequently determined with Equation [2.32]. L is decomposed into a force per unit span normal and tangential to the rotor plane, using

$$F_z = L \cos \phi, \qquad (5.7)$$

$$F_\theta = L \sin \phi, \qquad (5.8)$$

with ϕ the flow angle, see Figure 5.15.

The resulting spanwise distributions of c_l, F_z and F_θ, derived with the two methods to determine $\overline{\alpha}$, are given in Figure 5.18. The dimensionless blade loads at the tip should be treated with caution, since the $\overline{\alpha}$-estimate at the tip is questionable, as has been argued in Section 5.3.4.

The spanwise distributions of F_z and F_θ can be integrated along the blade

span to arrive at T and P, using

$$T = B \int_{R_r}^{R_t} F_z \, dr, \tag{5.9}$$

$$P = \Omega \, B \int_{R_r}^{R_t} F_\theta \, r \, dr, \tag{5.10}$$

Since F_z and F_θ omit airfoil drag contributions, resulting T and P are interpreted to be inviscid variables.

Equations [5.9] and [5.10] are discretized using piecewise constant load distributions. At the root and tip, the loads are assumed to be zero; the loads derived for $r/R_t = 1$ thus are ignored. The dimensionless coefficients are subsequently derived using Equations [2.8] and [2.9], resulting in $C_T = 0.86$ and $C_P = 0.61$, respectively for both methods to determine α.

Figure 5.19: c_t (left plot) and c_p (right plot) versus r/R_t, derived from blade loads and the one-dimensional, inviscid momentum model.

Recall from Section 5.3.1 that the estimate of the inflow at the rotor plane obtained with the annular averaged axial velocity method is also used by the one-dimensional inviscid momentum model to find $\overline{C_T} = 0.75$ and $\overline{C_P} = 0.53$.
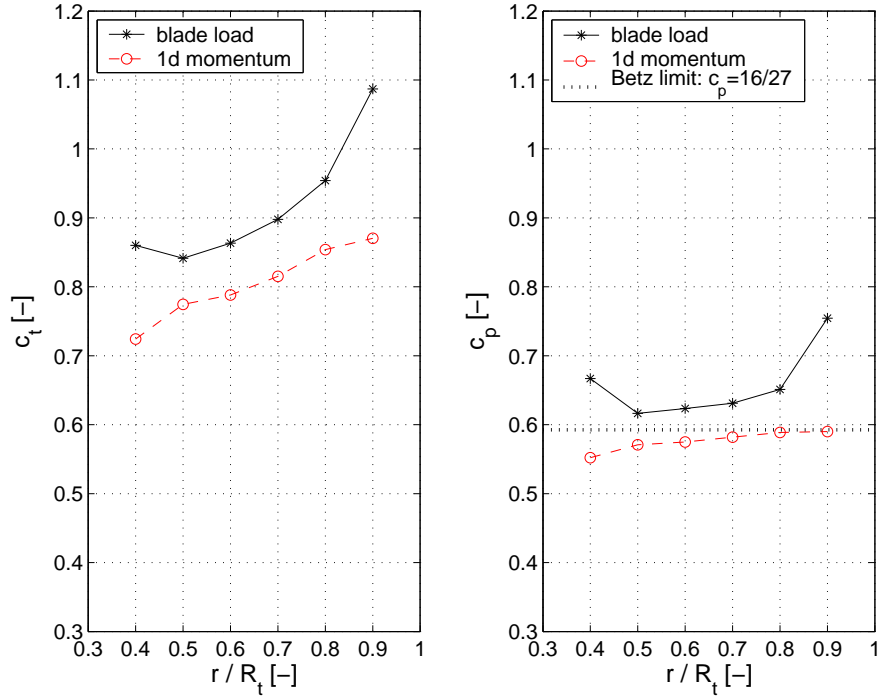
112

The substantial difference in C_T is explained from the spanwise distribution of the sectional thrust coefficient c_t, given in Figure 5.19 for both approaches. Across the span, a discrepancy is seen that increases towards the tip. Since the area of an annulus increases with r, the discrepancy near the tip has a dominant effect on the difference in C_T between the blade and the momentum method.

To put this inviscid analysis in perspective, recall from Section 5.1 that strain gauge measurements yield $C_T = 0.78 \pm 0.08$. Both inviscid estimates of C_T are within the measurement uncertainty interval.

C_P is clearly overestimated by the inviscid blade load method, it even surpasses the Betz-limit of $C_P = 16/27$ for one-dimensional, steady, inviscid flow. This observation on the level of the rotor is repeated for the sectional power coefficient c_p, which is also given in Figure 5.19. Note that c_p found with the one-dimensional, inviscid actuator disc model stays below the Betz-limit.

BEM theory equates the momentum deficit from the one-dimensional inviscid momentum model with the rotor thrust found from airfoil modeling at given annulus. Figure 5.19 can hence be interpreted as a validity check of BEM-theory; for the axial flow condition considered, the agreement between the Blade Element and the Momentum part would be marginally acceptable at all measured sections except for $r/R_t = 0.9$, the tip region. Current measurement uncertainties as well as the uncertainty associated with the approach to find the inflow at the rotor plane from linearly extrapolating near-wake recordings diffuse the assessment of BEM-theory however. A more thorough assessment into the limitations of BEM theory for both axial and yawed flow conditions is given by Sant [148, 147].

5.3.6 Wake convection

The viscous wake passage at given hot-film location (r, θ, z) is detected by a distinct increase in the standard deviation of the effective velocity s_{Veff}, as illustrated in Figure 5.9. The wake age $\Delta\theta_{b_{wake}}$ is the phase lag between the passage of the blade trailing edge and the passage of the corresponding viscous wake,

$$\Delta\theta_{b_{wake}} = \theta_{b_{wake}} - \theta_{b_{te}} + k \cdot 360°. \tag{5.11}$$

Here, $\theta_{b_{te}}$ is the blade azimuth angle at which the blade trailing edge passes the given hot-film location. It is hence assumed that the wake trails the blade at the trailing edge. k equals the number of blade passages through the vertical upwards position (where $\theta_b = 360°, 0°$) in the time between the blade trailing edge passage and the corresponding viscous wake passage.

For given hot-film location (r, θ, z),

$$\theta_{b_{te}} = \theta + i\frac{360°}{B} + atan\left(\frac{\frac{3}{4}\,c\,cos\,(\beta_{pitch} + \beta_{twist})}{r}\right) \quad mod\,360°, \qquad (5.12)$$

with $i = 0, \ldots, B{-}1$, B the number of blades and c the airfoil chord. The $atan$-term corrects for the phase difference between blade $\frac{1}{4}$-chord and trailing edge passage, compare Equations [5.4] and [5.12].

The bounds of the wake passage, expressed in θ_b, are selected by visual inspection of the s_{Veff}-distribution. $\theta_{b_{wake}}$ is then assumed to be the wake passage midpoint. The viscous wake convection velocity $\vec{V}_{wc}$ is found by averaging the measured PLA flow velocity over the wake passage.

The average and standard deviation of $\Delta\theta_{b_{wake}}$ and $\vec{V}_{wc}$ are subsequently determined for the sample of 24 θ-points per given (r, z)-coordinate. The standard deviation for perfect measurements of a rotating stationary flow would equal zero.
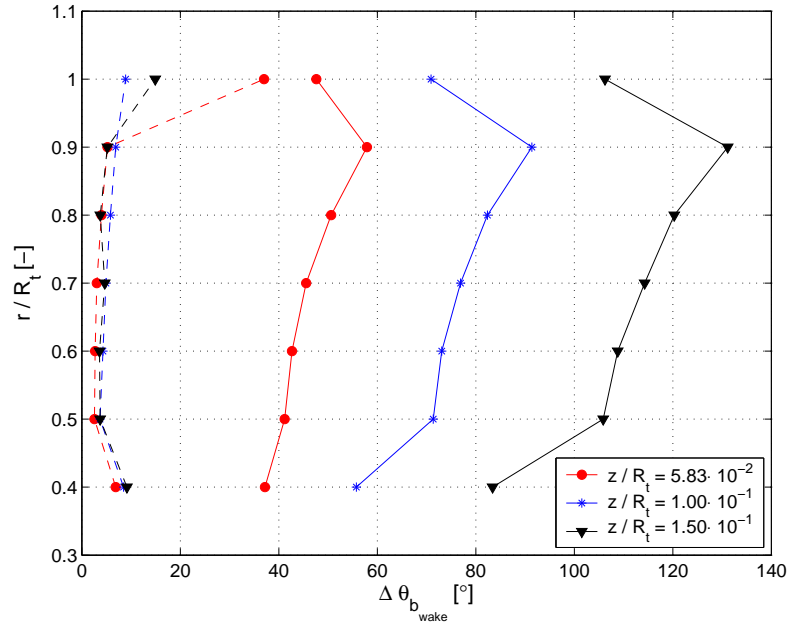
Figure 5.20: Average (solid line) and standard deviation (dashed line) of the wake age $\Delta\theta_{b_{wake}}$.

In the mid-span region, $\Delta\theta_{b_{wake}}$ increases when going outboard, see Figure 5.20. Correspondingly, $V_{z_{wc}}$ decreases when going outboard, see Figure 5.21. Both observations agree with the higher axial induction when going outboard,

see Figure 5.6. Furthermore, $V_{r_{wc}}, V_{\theta_{wc}} > 0$ found in the mid-span region suggests that the viscous wake is convected outboard and rotates in the same direction as the blades, respectively. Recall the discussion in Section 5.3.3 on the trends in the wake passage velocity signals.
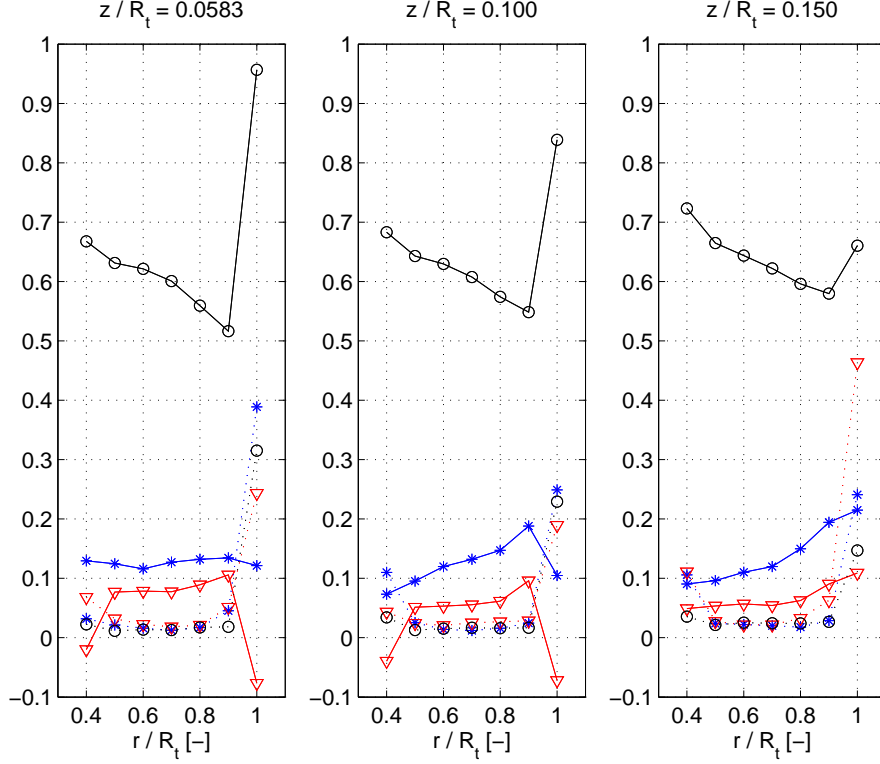
Figure 5.21: Average (solid line) and standard deviation (dashed line) of the viscous wake convection velocity $\vec{V}_{wc}$ versus r for downstream planes $z/R_t = 0.0583$, 0.100 and 0.150. $V_{r_{wc}}/W_0 : *$, $V_{\theta_{wc}}/W_0 : \triangledown$, $V_{z_{wc}}/W_0 : \circ$.

The tip vortex convects faster downstream than the wake in the mid-span region, as illustrated by comparison of e.g. Figures 5.5 and 5.21. The $\Delta\theta_{b_{wake}}$-reduction and $V_{z_{wc}}$-increase from $r/R_t = 0.9$ to 1.0, shown in Figures 5.20 and 5.21 respectively, hence indicate roll-up of the viscous wake into the tip vortex. Without roll-up of the viscous wake into the tip vortex, $V_{z_{wc}}$ would be further reduced instead of increased when approaching $r/R_t = 1.0$, due to the dominant contribution of the tip vortex to the axial induced velocity near $r/R_t = 1.0$. Note that for $r/R_t = 1.0$, the standard deviations in both $\Delta\theta_{b_{wake}}$ and $V_{z_{wc}}$ are increased significantly, suggesting a significantly increased uncertainty of the $\Delta\theta_{b_{wake}}$- and $V_{z_{wc}}$-averages.

5.4   Conclusions

The axial flow state forms the reference for yawed inflow. Analysis of the axial flow measurements thus sets the stage for the experimental assessment of yaw.

The axial flow study in this section demonstrates the quality and comprehensiveness of current measurements; data reduction techniques appear to work properly, including the proposed technique to derive the PLA three-dimensional flow velocity from PLA CTA recordings. Further, the rotor aerodynamics is as expected from published experimental and numerical studies. These results thus prove to be a sound basis for the experimental study of rotor aerodynamics in yaw.

Chapter 6

Experimental analysis of yaw effects on the rotor near-wake

Building on the knowledge obtained from the aerodynamic assessment of the baseline axial flow conditions, presented in Chapter 5, in this Chapter the effects of yaw misalignment on the near-wake rotor aerodynamics are discussed. The overall performance of the rotor in yaw is illustrated by the rotor thrust coefficient, measured for an extensive range of rotor operating conditions, see Section 6.1. The corresponding tip vortex geometries in the skewed near-wake are analyzed in Section 6.2. The effects of yaw misalignment on the near-wake PLA flow velocity are assessed by comparison of two yawed flow rotor operating conditions with a baseline axial flow condition in Section 6.3. The regions of dynamic stall on a blade during a rotational cycle, identified using both hot-film CTA in the near-wake and tuft visualization on the blades, are presented in Section 6.4. Main conclusions drawn from the experimental analyzes are given in Section 6.5. Note that details on the experimental setup, measurement techniques and procedures are given in Chapter 3, whilst the experimental data reduction is discussed in Chapter 4.

6.1 Rotor performance

Measurements of C_T are conducted for the model rotor subject to a range of both axial and yawed flow operating conditions [73, 74]. In contrast to the axial flow conditions, where Vermeer [202] measures C_P on a similar setup, he does not record C_P in yaw. When ignoring the data at $\Psi = \pm 15°$, C_T is approximately symmetric with respect to Ψ for given λ and β_{pitch}, see Figure 6.1. Furthermore, an increase from $\Psi = 0°$ to $|\Psi| = 30°, 45°$ for given λ and β_{pitch} results in a monotonic C_T-decrease. Both the C_T-symmetry and C_T-decrease are as expected.
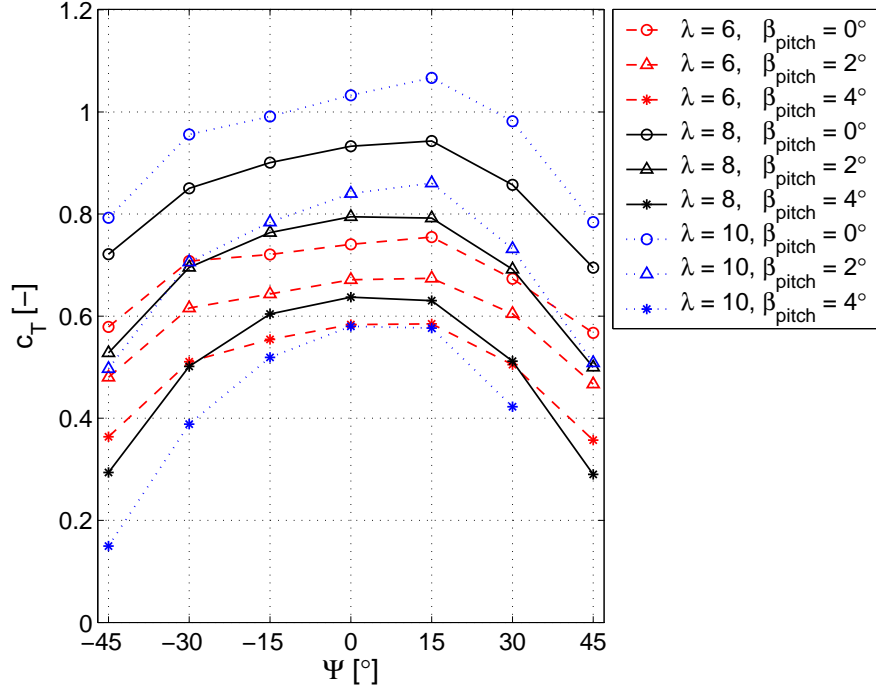
Figure 6.1: C_T versus Ψ for all measured combinations of λ and β_{pitch}.

The C_T-asymmetry for $\Psi = \pm 15°$ is thought to originate from the nonuniformity of the empty wind tunnel jet flow, see Figure 3.4. The causes for the empty jet flow disturbances are discussed in Section 3.1.

To further explain the C_T-asymmetry, first note that yaw introduces cyclicly unsteady blade inflow. Consider two cases with identical $\lambda_{1,2}$ and $\beta_{pitch_{1,2}}$, but antisymmetric yaw, $\Psi_1 = -\Psi_2$. Assume operation in uniform undisturbed flow $\vec{W}_0$. The two wakes then are each others mirror image, resulting in wake induced velocities that are 180° out-of-phase, $\vec{V}_{ind_1}(\theta_b) = \vec{V}_{ind_2}(\theta_b + 180°)$. The total velocities relative to a blade section $\vec{V}_{rel_{1,2}}$ also have a 180° phase lag,

$$\vec{V}_{rel} = \vec{V}_{ind} - \vec{\Omega} \times \vec{r} + \vec{W}_0 \tag{6.1}$$

$$\vec{V}_{rel_1}(\theta_b) = \vec{V}_{rel_2}(\theta_b + 180°) \tag{6.2}$$

Both $\vec{\Omega} \times \vec{r}$ and $\vec{W}_0$ are unchanged for the two cases and are further independent of θ_b. C_T, averaged over a cycle, would now be identical for the two conditions.

Nonuniform undisturbed flow yields a θ_b-dependent contribution to blade inflow, $\vec{W}_0(\theta_b)$. Hence,

$$\vec{V}_{rel_1}(\theta_b) \neq \vec{V}_{rel_2}(\theta_b + 180°) \tag{6.3}$$

since in general, $\vec{W}_0(\theta_b) \neq \vec{W}_0(\theta_b + 180°)$. The two cases now no longer yield equal $\vec{V}_{rel}$-patterns that are 180 out-of-phase. The $\vec{V}_{rel}$-patterns are dissimilar instead, leading to different C_T for the two cases: C_T hence is asymmetric with respect to Ψ for a non-uniform wind tunnel jet flow.

Table 6.1: $|\Delta(C_T)|$ per case, averaged over all 9 (λ, β_{pitch})-cases at given $|\Psi|$

	$\overline{|\Delta(C_T)|}$ [%]
$|\Psi| = 15°$	7.6
$|\Psi| = 30°$	2.7
$|\Psi| = 45°$	1.1

To quantify the asymmetry, $|\Delta(C_T)|$ per operating condition at given $|\Psi|$ is determined and expressed as a fraction of the lowest of the two C_T-values. Subsequent averaging over all 9 combinations of λ and β_{pitch} per $|\Psi|$ yields $\overline{|\Delta(C_T)|}$, see Table 6.1.

C_T-asymmetry diminishes with stronger yaw misalignment. The undisturbed flow nonuniformity is not notably different though between the various yawed flow cases. It is hence concluded that with increased $|\Psi|$, the influence of undisturbed flow nonuniformity on the aerodynamics of the yawed model rotor is successively reduced in favor of "clean" yawed flow phenomena.

For $|\Psi| = 15°$, undisturbed flow nonuniformity effects currently are considered too large to perform meaningful studies of the effects of yaw on rotor aerodynamics. Cases with $|\Psi| = 30°, 45°$ demonstrate minor C_T-asymmetry and are thus used for yawed flow studies in the remainder of this thesis.

6.2   Tip vortex characteristics

The availability of both tip vortex center locations and C_T for a range of yawed flow rotor operating conditions allows assessment of yaw misalignment effects on the near-wake tip vortex paths. Wake expansion and, in yaw, wake deflection can hence be studied, as the rotor wake bounds are marked by the tip vortex paths. In [73, 74] the basis for the current analysis is presented.

A schematic of the skewed near-wake tip vortex geometry, measured in the rotor (x_m, z_m)-plane downstream of the model rotor set to $\Psi \neq 0°$, is shown in Figure 6.2. Two additional coordinate systems, one for each blade tip, are introduced to express the locations of the tip vortex centers; with the origin located at the blade tip, z_t and r_t are aligned with z_{jet} and x_{jet}, respectively, where it must be noted that r_t is always directed outboard.

Figure 6.2: Schematic top view of the (x_m, z_m)-plane, with tip vortices trailing the two-bladed rotor, in yaw.

Typical plots showing the tip vortex center locations relative to a blade tip are presented in Figures 6.3 and 6.4. Recall that a tip vortex center with $r_t > 0$ is located outboard of the blade tip. For the axial flow condition in Figure 6.3, only one tip vortex trajectory is plotted; asymmetric wake expansion effects in axial flow are included in the measurement uncertainty.

The deflection of the expanding rotor near-wake in the direction of the downwind blade that is observed with the yawed model rotor in Figures 6.3 and 6.4 confirms measurements by e.g. Grant *et al.* [68, 66]. The mechanism driving the downwind deflection of the rotor wake can be explained with Glauert's momentum model for the actuator disc [60, 62]. T is oriented normal to an actuator disc. Compared with the undisturbed flow velocity, the flow velocity at the disc is thus reduced in the direction normal to the disc only, it is unchanged in the direction parallel to the disc. Vectorial addition yields a downwind deflection of the flow, see the schematic of Figure 4.6 and actual measurements of Figures 6.3 and 6.4.

For axial flow conditions, the changes in the wake expansion correlate positively with C_T-variations, as discussed in Section 5.2. The yawed flow conditions also show a positive correlation; the reduced wake expansion observed
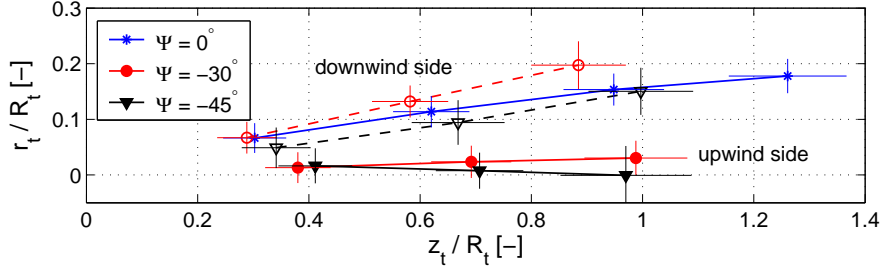
120

Figure 6.3: Dimensionless tip vortex center locations, relative to the blade tip, for $\Psi = 0°, -30°, -45°$ with $\lambda = 8$, $\beta_{pitch} = 2°$. Dashed lines, open symbols and solid lines, filled symbols for the downwind and upwind side, respectively.

in Figure 6.3 when Ψ is decreased from $-30°$ to $-45°$ with constant $\lambda = 8$ and $\beta_{pitch} = 2°$ corresponds to a C_T-decrease, see Figure 6.1. Similarly, the reduced wake expansion seen for the β_{pitch}-increase with constant $\Psi = -30°$ and $\lambda = 8$ in Figure 6.4 corresponds to a C_T-decrease, see Figure 6.1.

The positive correlation between changes in the skewed wake expansion and C_T-variations can intuitively be understood with the uniformly loaded actuator disc theory. The insignificant change in the wake expansion on the upwind side with variations in the rotor operating conditions correlates with a balance between increased expansion and increased wake skew with higher rotor thrust.

The wake skew angle χ, i.e. the angle between the wake flow velocity and the normal to the rotor plane, quantifies wake skewness. It is not uncommon
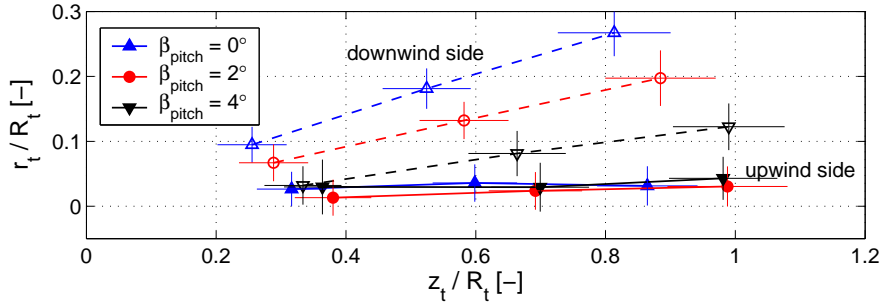

Figure 6.4: Dimensionless tip vortex center locations, relative to the blade tip, for $\beta_{pitch} = 0°, 2°, 4°$ with $\lambda = 8$, $\Psi = -30°$. Dashed lines, open symbols and solid lines, filled symbols for the downwind and upwind side, respectively.
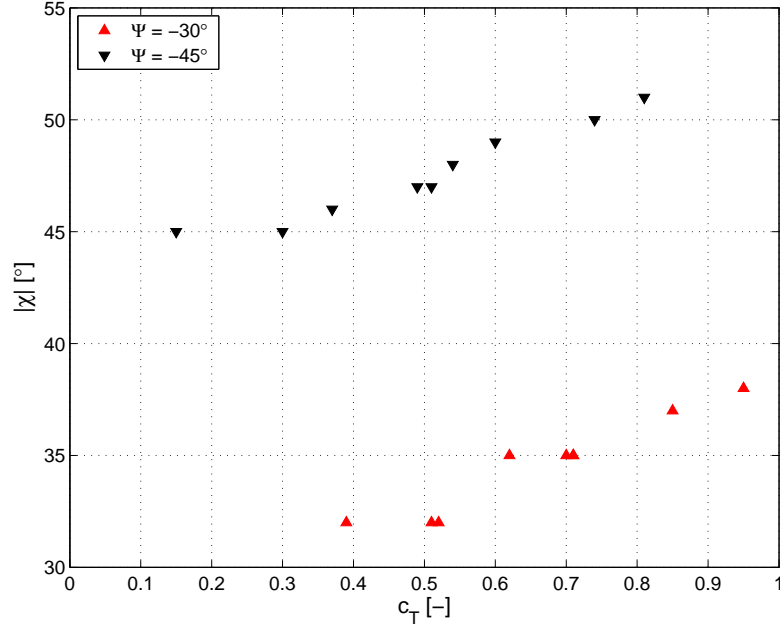
Figure 6.5: Wake skew angle $|\chi|$ versus C_T for all measured rotor operating conditions at $\Psi = -15°$, $-30°$, $-45°$.

for BEM methods to use χ as input to an empirical correction model for induced velocity nonuniformity in yaw, recall the review in Section 2.1.2.

In BEM models, χ is defined at a given annulus using the flow velocity at the rotor plane,

$$\chi = atan\left(\frac{U_m}{W_m}\right), \tag{6.4}$$

with U_m and W_m the velocity in the directions parallel and normal to the rotor plane, respectively, in accordance with the orientation of the (x_m, y_m, z_m)-coordinate system shown in Figure 3.3.

Since U_m and W_m are not measured, χ is defined differently for the flow visualization experiments, see Figure 6.2; tip vortex centers on the upwind and downwind side that have the same wake age are connected with straight lines[1]. A minimum of two of these tip vortex lines can be drawn per rotor operating condition. The wake skew axis is subsequently given by the straight line intersecting the rotor hub that fits best to the midpoints of the tip vortex

---

[1]These lines connect tip vortices of the same wake age since a *two*-bladed rotor is tested. It can in fact be shown that this holds for rotors with an even number of blades, when assuming that the tip vortices are convected in the flow visualization plane (here, the (x_m, z_m)-plane) only.

122

lines. χ is defined as the angle between the normal to the rotor plane and the wake skew axis. The flow visualization measurements hence yield a single χ-value per rotor operating condition, in contrast to BEM-based models where a χ-value per annulus is derived.

As expected from the definition of χ, the measurements yield $|\Psi| < |\chi|$, see Figure 6.5. Furthermore, a relation between χ, measured in the near-wake region that extends up to about $2R_t$ downstream of the rotor, and C_T is established; with the rotor set to given Ψ, a variation in the rotor operating conditions that yields larger C_T also results in a $|\chi|$-increase. The χ-observations confirm the positive correlation found between changes in the skewed wake expansion and C_T-variations and can be explained with Glauert's momentum model for the actuator disc.
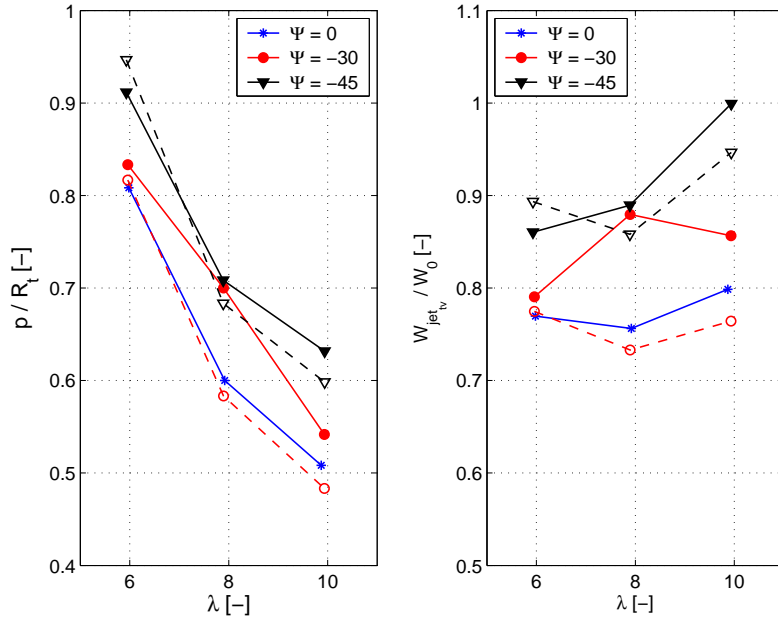
Figure 6.6: p/R_t (left plot) and $W_{jet_{tv}}/W_0$ (right plot) as a function of Ψ and λ for $\beta_{pitch} = 2°$. Dashed lines, open symbols and solid lines, filled symbols for the downwind and upwind side, respectively.

The asymmetry of the wake associated with a yawed rotor results in a tip vortex pitch p that depends on the θ_b-coordinate where the tip vortices trail the blade. The (x_m, z_m)-measurement plane allows p to be determined for the tip vortices trailing the blade at $\theta_b = 90°$ and $270°$, see Figure 6.2. The two values for the corresponding tip vortex convection velocity in the z_{jet}-direction, $W_{jet_{tv}}$, are subsequently derived using Equation [5.1]. Note that p

and $W_{jet_{tv}}$ are determined for the first rotational cycle only, due to the limited downstream extent of the measurement domain.

The conclusion drawn from the axial flow discussion in Section 5.2 that the main variable governing p is λ also holds for the yawed flow condition, compare Figures 5.5 and 6.6. For clarity, p and $W_{jet_{tv}}$ are plotted in Figure 6.6 as a function of Ψ and λ only, with constant $\beta_{pitch} = 2°$. Though not shown here, trends in p and $W_{jet_{tv}}$ are compared to C_T-variations resulting from changes in Ψ as well as β_{pitch} at given λ to find that p and $W_{jet_{tv}}$ depend on C_T for given λ, as has already been concluded in the axial flow discussion.

For a given rotor operating condition, p and $W_{jet_{tv}}$ are generally larger for tip vortices trailing the blade at the upwind rather than the downwind position, see Figure 6.6. The measured results hence suggest that induced axial velocity in the tip region is highest on the downwind side, thereby confirming the empirical induced velocity nonuniformity correction models of the Glauert type as used in BEM methods, refer to Section 2.1.2. Responsible for the increased induced axial velocity near the tip with the blade oriented downwind is the on average shorter distance between given blade section and the tip vortices, compared to that with the blade pointing upwind, see Figure 6.7.
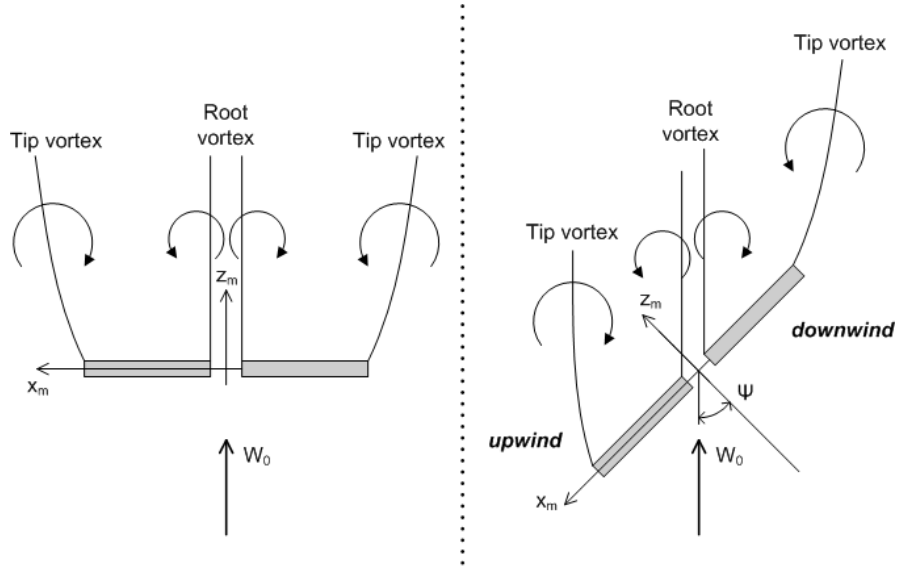

Figure 6.7: Schematic top view of the root and tip vortices trailing from the rotor. Left plot: axial flow, right plot: yawed flow.

124

6.3 Near-wake velocity field

The analysis of the measured tip vortex paths in Section 6.2 gives insight into the skewed wake expansion for the model rotor in yaw. Zooming in from the contours of the skewed near-wake, given by the tip vortex paths, this section focusses on the near-wake inflow distribution. The PLA three-dimensional flow velocity field, obtained from CTA measurements, is assessed for yaw misalignment effects.

Table 6.2: Rotor operating conditions of the three CTA cases

	λ [-]	β_{pitch} [°]	$k_{0.7R}$ [-]	$Re_{0.7R} \cdot 10^{-5}$ [-]		C_T [-]
				max	min	
$\Psi = 0°$	7.9	2.0	-	1.63	-	0.78
$\Psi = 30°$	8.0	2.0	0.09	1.77	1.49	0.70
$\Psi = 45°$	8.1	2.0	0.09	1.82	1.42	0.53

The number of rotor operating conditions studied is limited to three, due to the extremely time-consuming nature of the CTA measurements. The two yawed flow conditions are derived from the baseline axial flow condition of $\Psi = 0°$, $\lambda = 7.9$, $\beta_{pitch} = 2°$, discussed in Section 5.3, by selecting $\Psi = 30°, 45°$, whilst keeping Ω and β_{pitch} constant. A summary of the three settings, including the corresponding C_T, is given in Table 6.2. The small variations in λ result from application of non-constant wind tunnel wall corrections to the constant uncorrected $\lambda = 8$.

The rotor operating conditions are selected with the aim of obtaining non-stalled blades, in order not to complicate the analysis of yaw misalignment effects on the near-wake flow velocity field. The conclusion in Section 5.3.4 that $\alpha < \alpha_{stall}$ anywhere across the blade span indeed suggests that the baseline axial flow condition yields non-stalled blades. Evidence for the absence of significant spanwise regions of dynamic stall during a blade cycle with the $\Psi = 45°$-case will be presented in Section 6.4. Note however that owing to the small model size, detailed blade load measurements that could verify wether a blade section is stalled are not performed.

First, averaged flow velocity results are studied in Section 6.3.1. Thereafter, PLA results are analyzed; in Section 6.3.2 the PLA flow velocity at the blade passage is discussed and in Section 6.3.3 the PLA flow velocity field is analyzed. The present discussion is based on the second article in a series of two on the CTA measurements [79].

Before kicking-off the analysis, note an essential difference between axial and yawed flow conditions, addressed in Appendix B; whereas axial flow conditions yield rotating stationary near-wake flow, yaw results in cyclicly unsteady

near-wake flow for an observer rotating with the blades.

6.3.1 Averaged velocity

The study of yaw misalignment effects on the near-wake flow velocity commences with a discussion on averaged results. Two PLA flow velocity averages are defined;

- **the annular averaged PLA flow velocity**, introduced in Section 5.3.1 and obtained by averaging the PLA flow velocity on the annular circle with given radius r/R_t and distance z/R_t from the rotor plane for given blade orientation θ_b, see Equation [6.5].

$$\overline{<\vec{V}>}_{ann}(r, z, \theta_b) = \frac{1}{2\pi} \int_0^{2\pi} <\vec{V}> (r, \theta, z, \theta_b)\,\mathrm{d}\theta. \qquad (6.5)$$

- **the cycle averaged PLA flow velocity**, obtained by averaging the PLA flow velocity at given wake location $(r/R_t, \theta, z/R_t)$ during a full blade cycle, see Equation [6.6].

$$\overline{<\vec{V}>}_{cycle}(r, \theta, z) = \frac{1}{2\pi} \int_0^{2\pi} <\vec{V}> (r, \theta, z, \theta_b)\,\mathrm{d}\theta_b \qquad (6.6)$$

For perfect near-wake measurements on the rotor operating in the wind turbine state subject to perfectly axial flow conditions, the annular averaged PLA flow velocity equals the cycle averaged PLA flow velocity and is a function of r and z only. Such measurements hence result in an axisymmetric distribution of the average flow velocity.

Experimental reality is not perfect. Deviations from axisymmetry observed for the axial flow cases of Figures 6.8 (annular averaged) and 6.9 (cyclic averaged) are attributed to the interaction of the rotor with the nonuniform empty tunnel jet, discussed in Section 3.1, and to measurement uncertainty, discussed in Section 4.4.4.

Division of the averaged PLA axial flow velocities by the component of the undisturbed velocity normal to the rotor plane yields the associated dimensionless axial induction factors,

$$a_{ann, cycle} = 1 - \frac{\overline{<V_z>}_{ann, cycle}}{W_0 cos\Psi}. \qquad (6.7)$$

Subsequent studies present $a_{ann, cycle}$, rather than their dimensional counterparts.

Figure 6.8: a_{ann}-distribution. Each row and column represent a Ψ-case and a downstream distance z/R_t, respectively. Viewpoint is upstream of the rotor, looking downstream, the blades rotate clockwise. The undisturbed velocity component parallel to the rotor plane, $W_0 sin\Psi$, is from left to right. Note that a $(r/R_t, \theta)$-point in the domain does not indicate a wake location, an annular circle with radius r/R_r for the blade at $\theta_b = \theta$ is referred to instead.

127

annular averaged axial induction factor

The relevance of studying the annular averaged axial induction factor a_{ann}-distribution stems from BEM-based rotor aerodynamics codes. Using a BEM-based method, the rotor plane is divided into concentric annuli. At each time step, the wake momentum deficit per annulus is formulated using the annular averaged axial velocity at the rotor plane, as discussed in Chapter 2.

The a_{ann}-distributions do not display consistent yawed flow effects, see Figure 6.8. The main trend appears to be a quasi axisymmetric, radially dependent a_{ann}-distribution for both axial and yawed flow conditions, for all downstream measurement planes. Hence at an annular circle with given radius r/R_t and distance z/R_t from the rotor plane, a_{ann} is quasi-steady during a rotational cycle. The unsteadiness appears to increase for $\Psi = 45°$, compared to $\Psi = 0°, 30°$.

cycle averaged axial induction factor

Yaw misalignment of the rotor results in an asymmetric wake as can clearly be observed from a_{cycle}-distributions in Figure 6.9. For the axial flow condition, the a_{cycle}-distributions at all three downstream measurement planes are approximately axisymmetric. The a_{cycle}-patterns in the near-wake of a yawed rotor are significantly more asymmetric than those of the baseline axial flow condition.

The availability of three measurement planes allows observation of the downstream development of a_{cycle} in the near-wake. For the axial flow case, the nearly axisymmetric a_{cycle}-distributions display radial trends that are similar for all measurement planes including the one furthest downstream, at $z/R_t = 0.150$. For the yawed flow cases however, the trends seen in the a_{cycle}-distributions at $z/R_t = 0.0583$ are not consistent when going further downstream. Apparently, the flow in the near-wake behind the yawed rotor is highly nonlinear.

Derivation of the inflow at the rotor plane from downstream velocity measurements hence is complicated in yaw. Inflow trends at the rotor plane are expected to be best represented by the data closest to the rotor plane, at $z/R_t = 0.0583$. Indeed, for both yawed flow cases a_{cycle} at $z/R_t = 0.0583$ qualitatively corresponds to that at the rotor plane, derived with experimental studies [152] and with theoretical models that include the effect of the root vortex [176].

Towards the tip, a_{cycle} at a circle with given radius r/R_t, located $z/R_t = 0.0583$ downstream of the rotor plane, roughly adopts a sinusoidal function of θ, with highest axial induction factors at the downwind half. For $\Psi = 30°$, the sinusoidal distribution is approached more closely than for $\Psi = 45°$,
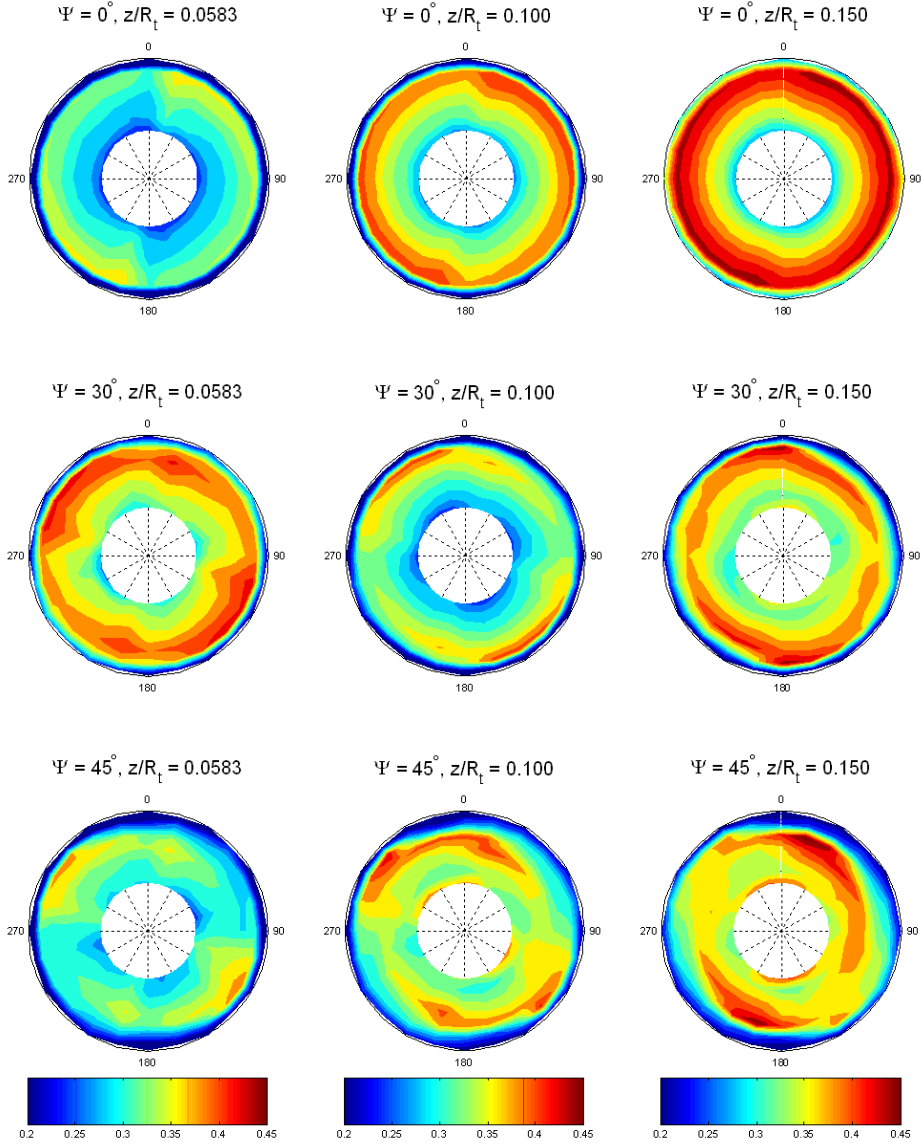
128

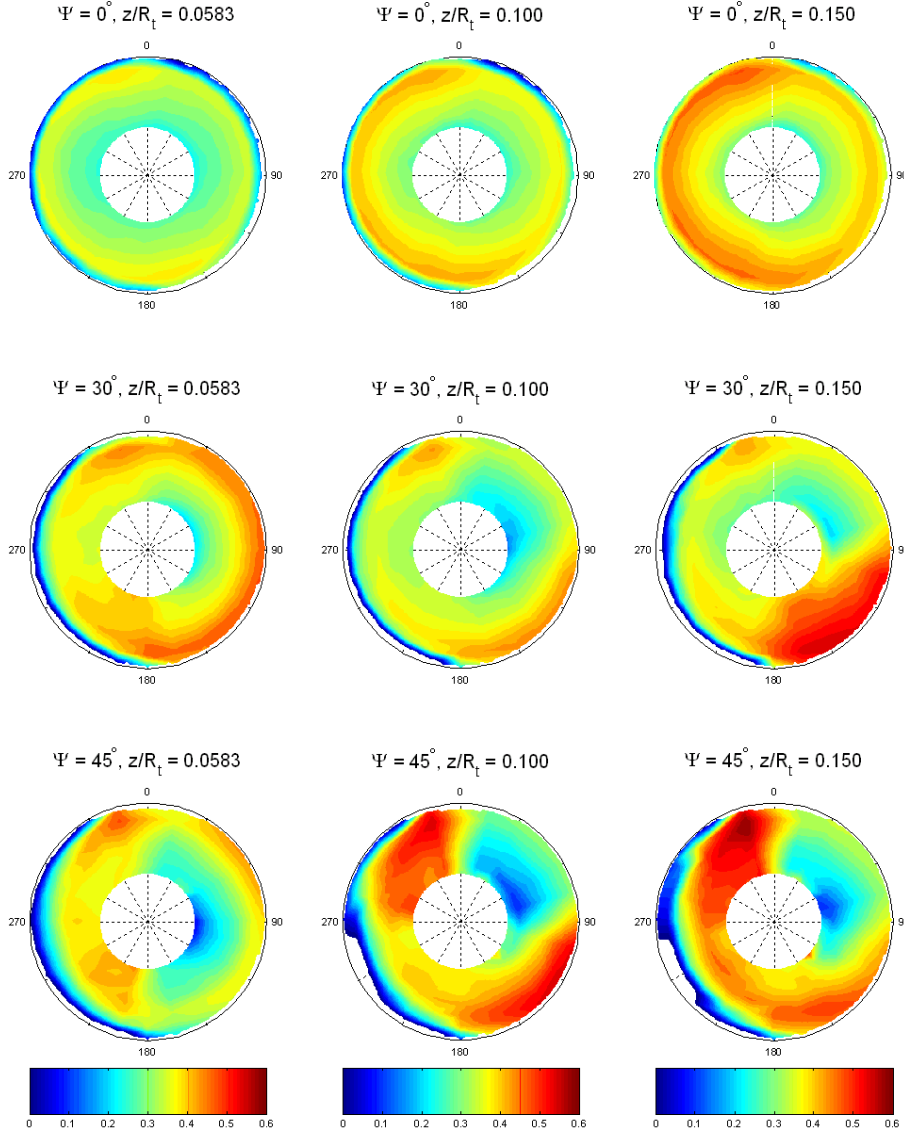Figure 6.9: a_{cycle}-distribution. Each row and column represent a Ψ-case and a downstream distance z/R_t, respectively. Viewpoint is upstream of the rotor, looking downstream, the blades rotate clockwise. The undisturbed velocity component parallel to the rotor plane, $W_0 sin\Psi$, is from left to right. In contrast to Figure 6.8, a $(r/R_t, \theta)$-point in the domain now *does* indicate a wake location.

probably due to stronger subharmonic effects in the near-wake at larger Ψ. A sinusoidal inflow distribution in the rotor plane for a yawed rotor is generally acknowledged; refer e.g. to Glauert's empirical inflow correction model for skewed wake effects given in Equation 2.30.

The roughly sinusoidal a_{cycle}-distribution, measured $z/R_t = 0.0583$ downstream of the rotor plane, results from the skewed downstream convection of the tip vortices in yaw, see Figure 6.7. The tip vortices are on average closer to the downwind half of the measurement plane than to the upwind half. Consequently, a_{cycle} in the outboard region at the downwind half is higher than at the upwind half. This effect is responsible for the higher blade loads near the tip with the blade at an upwind than at a downwind position, resulting in a restoring contribution to the yawing moment M_{yaw} about the y_m-axis, see Figure 3.3 for the orientations used. Yaw misalignment generally results in a restoring yaw moment on the rotor, $M_{yaw} < 0$ for $\Psi > 0°$, as has been verified in the European Commission JOULE project 'Dynamic inflow' [179, 157].

The significant a_{cycle}-reduction in the downwind, inboard region, seen for both yaw conditions at $z/R_t = 0.0583$, is due to the skewed root vortices, as shown by e.g. Snel [176] with a simplified numerical vortex wake model. In yaw, the root vortex paths are skewed towards the downwind half of the rotor plane, see Figure 6.7. The root vortices induce a significant axially downstream flow in the inboard, downwind region of the measurement plane, because of their close proximity to this region. Loads in the blade root region are thus increased when the blade points downwind. The skewed root vortex effect hence yields a destabilizing M_{yaw}-contribution, as has been verified with field tests on wind turbines in the Dutch national Annexlyse project [153, 159].

6.3.2 PLA velocity at blade passage

The inflow employed by the blade models that are used in BEM and vortex wake codes does not contain a contribution induced by the local bound vortex. An impression of the inflow at the rotor plane is obtained by reducing flow velocity recorded at the $z/R_t = 0.0583$-measurement plane to determine the PLA tangential and axial flow velocity at blade passage without a contribution induced by the local bound vortex, $<V_\theta>_{blade}$ and $<V_z>_{blade}$, respectively. The procedure to arrive at the blade passage velocities is described in Section 5.3.4. To present dimensionless quantities, $<V_\theta>_{blade}$ is divided by $W_0 sin\Psi$, $<V_z>_{blade}$ is rewritten into the axial induction factor at blade passage a_{blade} analogous to Equation [6.7]. a_{blade}- and $[<V_\theta>_{blade}/(W_0 sin\Psi)]$-distributions are plotted in Figures 6.10 and 6.11, respectively.

From physical intuition, the a_{blade}- and a_{cycle}-distributions are expected
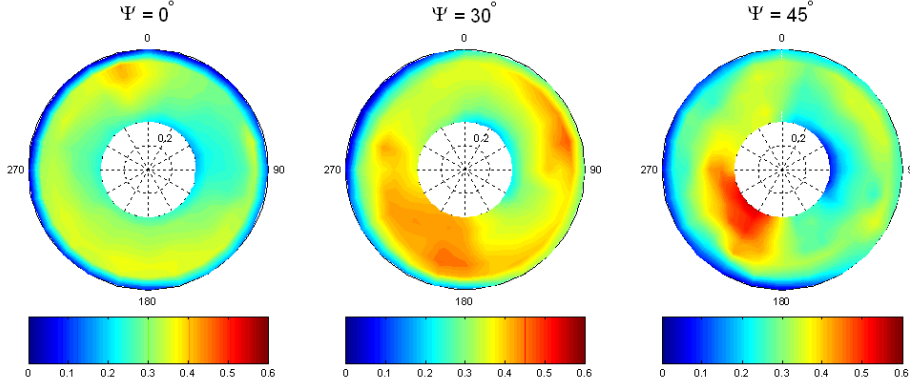
Figure 6.10: $[1- <V_z>_{blade} / (W_0 cos\Psi)]$-distribution in the measurement plane $z/R_t = 0.0583$ downstream of the rotor during a rotational cycle for all three cases.

to be comparable.[2] Prior to a detailed analysis of a_{blade}, it can be seen that the a_{blade}-distributions are less smooth than the a_{cycle}-distributions, compare Figures 6.9 and 6.10. This is thought to be the consequence of taking a snapshot[3] with a_{blade}, instead of an average for a_{cycle}.

The level and trends of the a_{cycle}-distributions at $z/R_t = 0.0583$ are generally similar to those of the a_{blade}-distributions. The a_{cycle}- and the a_{blade}-distribution are approximately axisymmetric and of comparable magnitude for the axial flow condition. With the rotor in yaw, the a_{blade}- and the a_{cycle}-reduction in the inboard, downwind region are similar. The reduction is attributed to the skewed paths of the root vortices, as discussed in Section 6.3.1. Outboard, the agreement between a_{cycle} and a_{blade} is worse than in the inboard, downwind region; the roughly sinusoidal a_{cycle}-distribution at given radius seen with $\Psi = 30°$ is not clearly reproduced for a_{blade}. At $\Psi = 45°$, both distributions do not show sinusoidal behavior. Note that the high a_{blade}-values seen in the outboard, downwind region result from the induced velocity contribution of the skewed tip vortices, as discussed in Section 6.3.1.

The contribution induced by the bound vortex to the azimuthal velocity is symmetric about the blade passage, see i.e. Figure 5.16. In contrast to the axial flow velocity, the bound vortex effect is hence not averaged out

---

[2]Reasons are that both a_{blade} and a_{cycle} are determined per point, not annulus, that the axial velocity peaks induced by the local bound vortex are approximately averaged out for a_{cycle} and that the velocity induced at a point by wake vorticity is approximately constant over a rotational cycle.

[3]Actually, instead of a single snapshot per blade passage, the values at two adjacent θ_b-positions are averaged, see Figure 5.16.
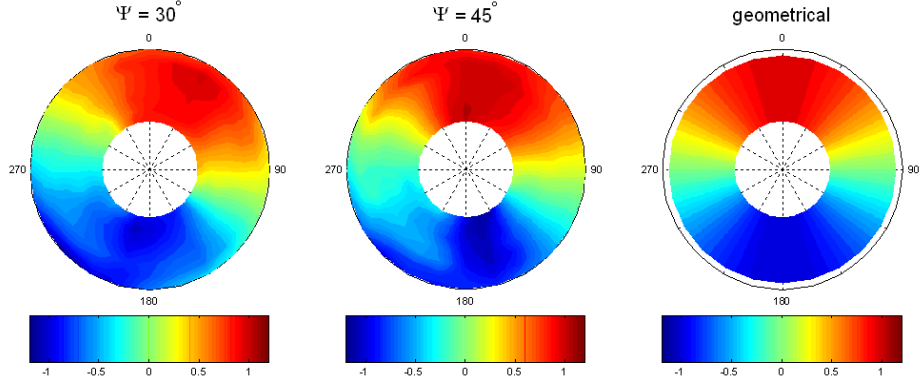
131

Figure 6.11: $<V_\theta>_{blade}/(W_0 sin\Psi)$-distribution in the measurement plane $z/R_t = 0.0583$ downstream of the rotor during a rotational cycle for all three cases. The right plot shows $<V_\theta>_{blade,geo}$, see Equation [6.8].

when determining the cycle averaged azimuthal velocity from Equation [6.6]. Whereas a_{cycle} and a_{blade} are expected to be similar, $\overline{<V_\theta>}_{cycle}$ and $<V_\theta>_{blade}$ should be different. Only the latter could be representative for the tangential velocity at the blade.

In yaw, the undisturbed flow component parallel to the rotor plane, $W_0 sin\Psi$, yields a purely geometrical contribution to $<V_\theta>_{blade}$, given by

$$<V_\theta>_{blade,geo} = W_0 sin\Psi cos\theta_b. \qquad (6.8)$$

For the relatively large yaw angles currently studied, the $<V_\theta>_{blade}$-distribution at $z/R_t = 0.0583$ is dominated by $<V_\theta>_{blade,geo}$, see Figure 6.11. Velocity contributions induced by wake vorticity yield second order effects.

6.3.3   PLA three-dimensional velocity field

The unsteady near-wake flow field is shown in Figure 6.12. Note that the complete unsteady wake cycle is covered with snapshots at $\theta_b = 90°$, $136°$, $180°$ and $226°$, representing half a rotation, since the PLA flow field at given inertial location in the near-wake behind the *two*-bladed model rotor is cyclic over $180°$, recall the discussion in Chapter 2.

The successive local $<V_z>$-maximum and -minimum induced by the bound vortex with the blade passing a given $(r/R_t, \theta, z/R_t)$-location, observed for the axial flow condition in Section 5.3.3, are seen for the yawed flow cases as well. Using $(W_0 cos\Psi)$ to make the axial flow velocity dimensionless, amplitudes of blade-passage maxima and minima generally are of similar magnitude for the

132

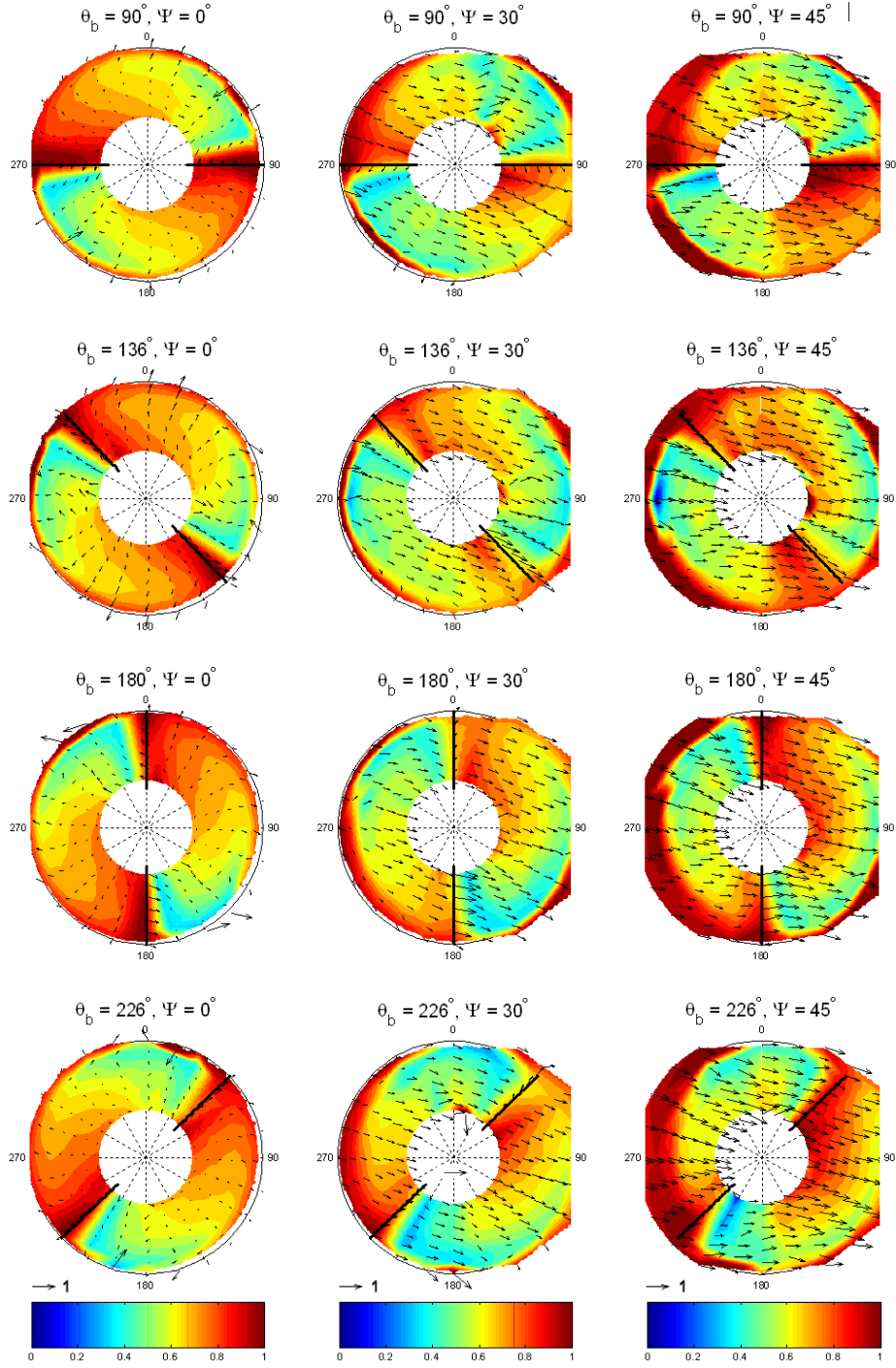Figure 6.12: $<\vec{V}>$ z/R_t=0.0583 downstream of the rotor. $<V_z>$-contour and $[<V_r>, <V_\theta>]$-vectors are plotted, both nondimensionalized with $W_0 cos\Psi$. Each row and column represent a θ_b-instant and a Ψ-case, respectively.

133

three cases considered. The difference between blade passage maxima and minima, expressed using Figure 5.16 as

$$\Delta <V_z>_{blade} = <V_z>_{max} - <V_z>_{min}, \qquad (6.9)$$

at given distance downstream of the rotor is a measure of the bound vortex circulation strength. With increased Ψ, similar $(\Delta <V_z>_{blade})/(W_0 cos\Psi)$ is found, see Figure 6.12. Because the denominator of this term reduces with larger Ψ, the finding translates to reduced $\Delta <V_z>_{blade}$, which in turn suggests lower bound vortex circulation strength. Ultimately, this leads to reduced blade loads. The C_T-measurements presented in Section 6.1 confirm current analysis.

For an observer rotating with the blades, the PLA flow velocity at $z/R_t = 0.0583$ varies minimally during the rotational cycle for the axial flow case; the flow is approximately rotating stationary[4]. With the rotor set to yaw, the PLA flow velocity becomes cyclicly unsteady for the rotating observer as a result of the skewed wake associated with yawed flow conditions.

The in-plane flow velocity patterns are influenced by Ψ, see the vectors in Figure 6.12. As expected, yaw misalignment yields a general downwind orientation of the in-plane flow. For the axial flow condition, the flow at the blade passage is accelerated in the direction opposite to the blade rotation, $<V_\theta> < 0$. With the rotor set to $\Psi \neq 0°$, the azimuthal acceleration of the flow at the blade passage is affected by the general downwind direction of the flow. Yaw misalignment hence results in a θ_b-dependent in-plane velocity at the blade passage; in the advancing blade region, $90° \leq \theta_b \leq 270°$, the flow acceleration in the direction opposite to the blade rotation is strengthened, in the retreating blade region, $270° \leq \theta_b \leq 360° \cup 0° \leq \theta_b \leq 90°$, it is counteracted.

6.4   Blade boundary layer state

Yaw misalignment introduces unsteady blade loads. The occurrence of dynamic stall is of particular importance in this respect, since it can yield significantly higher aerodynamic blade forces than for static stall. The phenomena governing dynamic stall, modeling aspects and its appearance on rotating wind turbine blades are discussed in Chapter 2.

In this Section, the focus is on the assessment of the spanwise location of stalled blade flow during a rotational cycle with the model rotor subject to yawed flow conditions. Dynamic stall regions are determined with both

---

[4]an apparent violation of rotating stationary flow is seen for the in-plane flow vectors at the blade passage, compare e.g. the plots with $\theta_b = 180°$ and $226°$. Next to measurement uncertainty, these effects originate from the finite spatial resolution of the measurements.

tuft visualization on the blade and CTA in the near-wake, see Section 3.2.4. Detailed blade loads are not recorded.

Accurate computation of the blade loads during a dynamic stall event requires precise prediction of the spanwise and temporal extent of the dynamic stall region. Even with the more modest goal of obtaining the correct sign of the aerodynamic damping term in aero-elastic modeling, dynamic stall regions should be predicted accurately. Measurements of the dynamic stall region are hence relevant for the validation and construction of rotor aerodynamics models. For an example hereof, refer to e.g. Munduate and Coton [133], who validate dynamic stall onset predictions of a BEM-based model with the NREL phase II and IV experiments. Present experimental analysis of dynamic stall occurrence is based on Haans *et al.* [76, 77], where a comparison to BEM results is also included.

A brief supplement to the description of the experimental setup given in Sections 3.1 and 3.2.4 is discussed first in Section 6.4.1. Thereafter, dynamic stall indicators are identified for both measurement techniques in Section 6.4.2. The section concludes with a discussion on the measured dynamic stall regions in Section 6.4.3.

6.4.1 Experimental setup: trip strips

Three rotor operating conditions are examined, see Table 6.3 for an overview. The $k_{0.7R}$-value of 0.09 for both rotor operating conditions indicates that the blade flow truly is unsteady; a quasi-steady aerodynamic approach is not valid [109]. When blade stall were to occur during the rotational cycle, it would have a dynamic rather than a static character. Note that strain gauge measurements are not performed; experimental C_T is not available. It can be estimated from Figure 6.1 however that for all three cases, $C_T \approx 0.5$.

Table 6.3: Rotor operating conditions of the two boundary layer state cases. For both cases, trip strips are glued to the blade.

	Ψ	β_{pitch}	trip strip	$k_{0.7R}$	$Re_{0.7R} \cdot 10^{-5}$	
					max	min
	[∘]	[°]	[-]	[-]	[-]	[-]
$\lambda = 8.1$	45	2.0	no	0.09	1.82	1.42
$\lambda = 8.1$	45	2.0	yes	0.09	1.82	1.42
$\lambda = 5.5$	45	2.0	yes	0.09	1.93	1.35

The $\lambda = 8.1$-case has also been studied with CTA measurements, as discussed in Section 6.3. Measurements of the dynamic stall region allow the non-stalled blades hypothesis, posed for this case in Section 6.3, to be tested;

135

recordings on the $\lambda = 8.1$-case are compared to those on an operating condition that should lead to a substantial dynamic stall region. The latter operating condition is defined by a reduced λ from 8.1 to 5.5, whilst keeping all other setting constant, see Table 6.3. The α-increase associated with a λ-reduction for a given yawed rotor operating condition increases the likelihood of a dynamic stall event during the rotational cycle.

The $Re_{0.7R}$-variations between the two rotor operating conditions are relatively small. The Re-estimate along the span is of $O(10^5)$ though, which could give rise to the formation of laminar separation bubbles on the NACA0012 airfoil. Laminar separation bubbles would further complicate the already complex dynamic stall process. Moreover, the significant impact bubbles have on the rotor flow field, combined with their sensitivity to small but inevitable flow condition variations during testing, introduces measurements uncertainties.
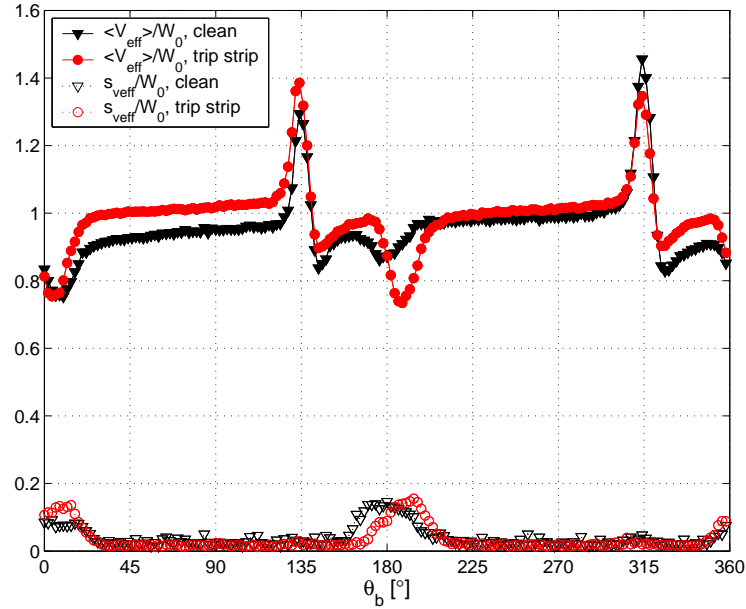
Figure 6.13: $<V_{eff}>$ and s_{Veff} at $(r/R_t, \theta, z/c) = (0.8, 135°, 0.44)$ for $\Psi = 45°$, $\lambda = 8.1$, $\beta_{pitch} = 2°$ and setups with clean blades and with trip strips glued to the blades. Blade passage: $\theta_{b_{blade}} = 135°, 315°$, wake passage: $\theta_{b_{wake}} \approx 180°, 360°$.

For a rotor with identical blades that are all set to the same β_{pitch}, an observer in an inertial frame of reference expects to see near-wake PLA flow patterns during a rotor cycle that are repetitive with the number of blades. The PLA flow in the near-wake of such a B-bladed rotor would thus be cyclic with period $2\pi/(B\Omega)$ for the non-moving observer. Note that when e.g. β_{pitch}

varies between the blades, the observer would still see cyclic flow, but now with period $2\pi/\Omega$.

Measuring the clean $\lambda = 8.1$-condition, i.e. the first case in Table 6.3 without trip strips, disturbances that went unnoticed while testing cause the two blades to yield distinctly different blade and wake passages though, see Figure 6.13 for an example.[5] The $<V_{eff}>$-peaks at the blade passage are different, as are the phase lags between passage of the blade trailing edge and the viscous wake $\Delta\theta_{b_{wake}}$, given in Equations [5.11] and [5.12].

The blades are fitted with trip strips in an attempt to avoid the formation of laminar separation bubbles through forced boundary layer transition to a turbulent state, see Figure 3.13. Across the entire span, a $2\ mm$ thick zig-zag type trip strip is glued to the surface at 10 % chord. The presence of laminar separation bubbles and the state of the boundary layer with and without trip strips are not examined experimentally. Evidence of the effect of trip strips is found from hot-film measurements in the near wake instead.

Application of trip strips to the $\lambda = 8.1$-case yields a marked reduction of the differences in the $<V_{eff}>$-patterns between the two sets of blade and wake passages at a given near-wake location. The $<V_{eff}>$-distribution returns to a period of π/Ω, from $2\pi/\Omega$ without strips.

The unintend variations in velocity patterns between the two blades contributes to measurement uncertainty, since it adds to data scatter with repeated measurements. Application of trip strips improves experiment repeatability and thereby reduces measurement uncertainty. Going forward, the study in this Section thus only considers cases where blades have trip strips.

6.4.2 Detection of stalled blade flow

The spanwise location of stalled blade flow during a rotational cycle is determined with tuft visualization on the blades and hot-film CTA in the near-wake. Both methods suffer from uncertainties in interpreting the measurement data. Comparison of the two resulting stalled blade flow regions for each rotor operating condition should give insight into the data interpretation of each method.

The main forces acting on tufts glued to a rotating blade are aerodynamic and centrifugal forces, the latter causing the tuft orientation to be biased radially outboard. The tufts could thus act as vortex generators that postpone flow separation [218, 37]. When flow separation does occur, the flow velocity relative to the tuft and consequently the aerodynamic force acting on the tuft are greatly reduced. The tuft is oriented in the radially outboard direction

---

[5]Both dynamic stall and PLA flow velocity measurements are conducted for the rotor operating condition of $\Psi = 45°$, $\lambda = 8$, $\beta_{pitch} = 2°$. In contrast to the dynamic stall measurements however, the $<V_{eff}>$-patterns of the PLA flow velocity measurements are not markedly different for the two blades, when testing the clean configuration.

due to the dominant centrifugal force. A tuft pointing radially outboard could however indicate radial, attached flow as well as flow separation.
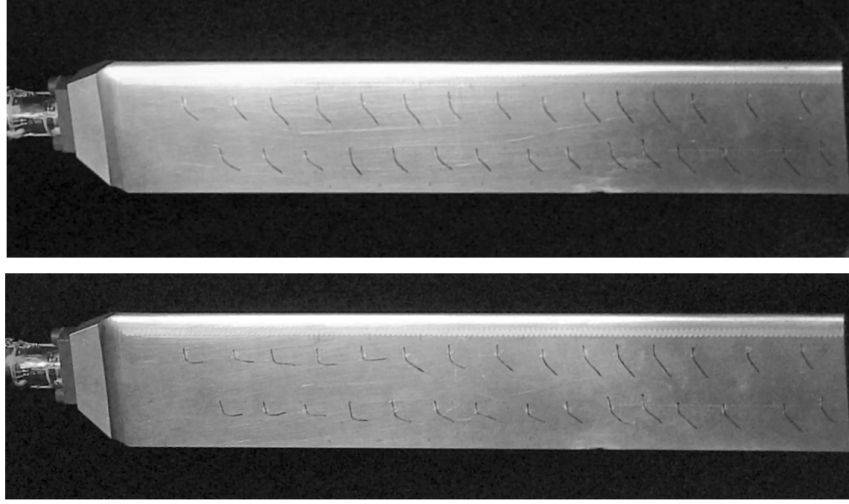

Figure 6.14: Tuft recordings at $\theta_b = 60°$, for $\lambda = 8.1$ (top) and 5.5 (bottom). For both: $\Psi = 45°$, $\beta_{pitch} = 2°$. With $\lambda = 5.5$, stall is identified on the first 5 and 4 inboard tufts for the leading and trailing edge rows of tufts, respectively.

With tuft recordings alone, no discrimination between the two flow conditions, separation or attached radial flow, can be made. Blade stall is thus tentatively identified by tufts pointing (almost) purely in the radial direction, see Figure 6.14. This indicator of blade stall is used by Vermeer and Timmer [205] in their study on the same rotor as used at present but then subject to axial flow conditions.

The near-wake flow velocity trends are studied with the phase-locked average $<V_{eff}>$ and phase-locked standard deviation s_{Veff} that are derived from the 54 hot-film V_{eff}-recordings per $(r/R_t, \theta, z/c, \theta_b)$-point, with z/c fixed at 0.44. The peaks in s_{Veff} indicate viscous wake passages, recall Figure 5.9.

Depending on the operating condition and the position in the wake, one of two typical θ_b-distributions of $<V_{eff}>$ and s_{Veff} is found at the blade and wake passages, see Figure 6.15. Typical signals I and II are given in the left and right plot, respectively. The differences between the two typical signals concern

- **wake passage**: $\theta_{b_{wake}}$, $(s_{Veff})_{max}$ and the wake width are different. For typical signal I, a clear phase lag $\Delta\theta_{b_{wake}}$ between the blade and wake

138
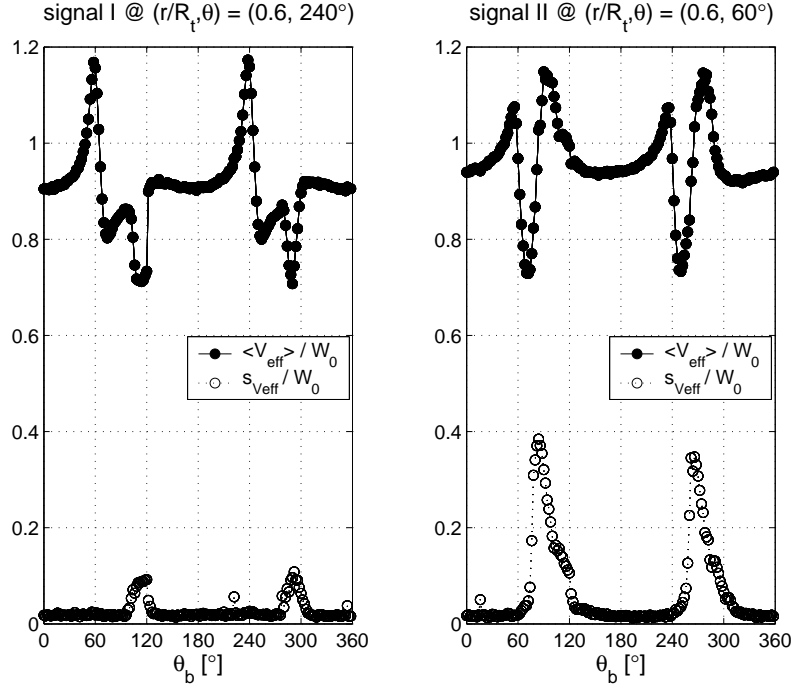
Figure 6.15: $<V_{eff}>$ and s_{Veff} for $\Psi = 45°$, $\lambda = 5.5$, $\beta_{pitch} = 2°$. Left plot: $(r/R_t, \theta, z/c) = (0.6, 240°, 0.44)$, typical signal I, indicating a non-stalled blade section. Right plot: $(r/R_t, \theta, z/c) = (0.6, 60°, 0.44)$, typical signal II, indicating a stalled blade section. For both plots, blade passage: $\theta_{b_{blade}} = 60°, 240°$.

passage is observed [6]. For typical signal II, blade and wake passages merge, $\theta_{b_{wake}} \approx \theta_{b_{blade}}$. $(s_{Veff})_{max}$ is substantially higher for typical signal II than I.

- **blade passage**: $\langle V_{eff} \rangle_{max}$ is lower for typical signal II than I.

Typical signal II appears to indicate a stalled blade section, since stall is associated with a large chordwise region of separated, unsteady flow at the blade causing a relatively low but fluctuating bound circulation and a large unsteady wake shed from the blade. Typical signal I seems to correspond to a fully attached or mostly attached flow on the blade, outside the stall regime. At all measurement locations in the wake, the recorded signals are checked for occurrences of typical signal II. When identified, the blade section passing given measurement position with coordinates r_1/R_t, θ_1 is flagged to be stalled,

---

[6] $\Delta\theta_{b_{wake}}$ is defined in Equations [5.11] and [5.12]

hence the blade section at spanwise station r_1/R_t for the blade oriented at $\theta_b = \theta_1$.

6.4.3 Dynamic stall regions

Analysis of the results for the two rotor operating conditions obtained with the two experimental techniques, plotted in Figure 6.16, learns that the region of blade stall is significantly less extensive for the $\lambda = 8.1$-case than for the $\lambda = 5.5$-case. Dynamic stall is de facto absent for the $\lambda = 8.1$-case; the blade stall region found from hot-film measurements for the innermost part of the blade is not confirmed by tuft recordings. The hypothesis of non-stalled blades for the $\lambda = 8.1$-case, posed in Section 6.3, is hence confirmed by present results. The substantially larger region of blade stall for the $\lambda = 5.5$-case is in agreement with the expected α-increase during a rotational cycle when lowering λ.
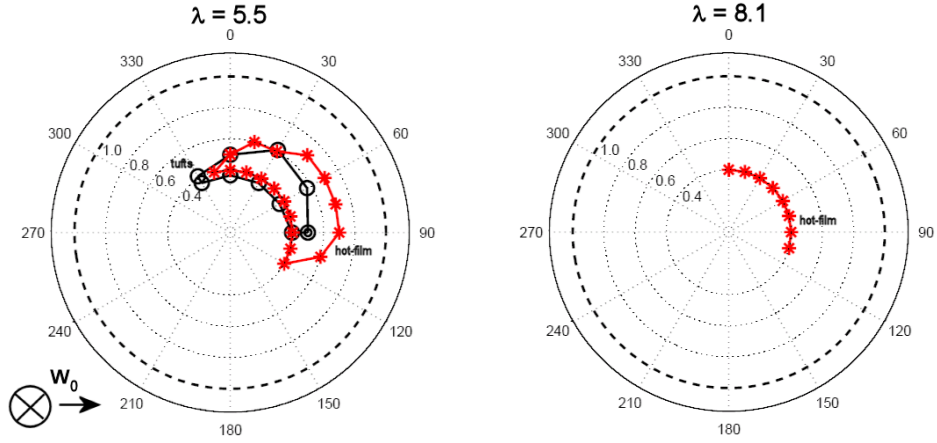
Figure 6.16: Boundary of the stall region on the blades for a full cycle, observed with two experimental techniques: tufts ($\circ$) and hot-film anemometry ($*$). Left plot:$\lambda = 5.5$, right plot:$\lambda = 8$. For both plots, $\Psi = 45°$, $\beta_{pitch} = 2°$.

For $\lambda = 5.5$, the observations from the hot-film measurements yield a significantly larger blade stall area than those from tuft experiments, see Figure 6.16. Part of the discrepancy can be attributed to resolution differences between the methods; tuft photos are taken with $\Delta\theta_b = 30°$, hot-film measurements with $\Delta\theta_b = 15°$. The tuft spacing is approximately $\Delta r/R_t = 0.02$, whereas hot-film recordings are made with $\Delta r/R_t = 0.1$.

When tuft measurements indicate that stall occurs on a given blade section during the rotational cycle, the onset of stall derived from tuft experiments is estimated at approximately equal θ_b as that found for the hot-film measurements, see Figure 6.16 with the note that the blades rotate clockwise.

Inboard, up to $r/R_t = 0.5$, flow reattachment θ_b found with tuft measurements is comparable to that derived with hot-film CTA, when taking into account the θ-resolution differences.

The radial extent of the blade stall region is underpredicted however with tufts, compared to hot-films. Three possible causes are identified; first, the purely radial tuft direction that should indicate stall could be to stringent. Second, the tufts could act as a vortex generator on the blade, thereby postponing stall [218, 37]. Third, V_{eff}, recorded at a near-wake position with given r-coordinate, is influenced not only by the blade flow conditions at the given r-section, but also by all other blade sections. The small downstream distance of the hot-films from the rotor plane, $z/R_t = 0.0583$, limits this effect.

Concluding, the uncertainties regarding the interpretation of the recordings for both tuft and CTA measurements cannot be completely eliminated based on the available data. Blade stall regions found with tuft and hot-film measurements generally overlap though. An overall positive correlation between tuft and hot-film results is hence achieved, in accordance with the correlation found by Vermeer and Timmer for the rotor in axial flow [205].

More insight into the ability of the experimental techniques to detect blade stall could be obtained when CTA is performed for a blade with tufts attached. Possible stall postponement effects from the tufts acting as vortex generators could then be assessed. Furthermore, to study the significance of blade flow conditions at other sections influencing the hot-film measurement at a given blade station, recordings at various downstream locations should be taken. As a final remark, the spatial resolution of the two experimental techniques should be equal to avoid the uncertainty introduced by the unavailability of either measurement at a given blade station and phase angle.

6.5   Conclusions

The assessment of both C_T and near-wake tip vortex center locations for a range of yawed rotor operating conditions yields valuable insight into yaw misalignment effects on the near-wake tip vortex paths. Observed trends in the wake expansion and wake skew correlate well with C_T-variations. The tip vortex pitch is governed by both λ and C_T. The larger pitch observed for vortices trailing the blade at the upwind than at the downwind side correspond to the expected nonuniform induced velocity in the wake.

The annular averaged axial flow velocity in the near-wake does not show clear yaw misalignment effects. Near-wake PLA induced axial flow velocity in the outboard region is smaller at the upwind than at the downwind side, attributed to the skewed tip vortex paths. In the inboard, downwind region however, a significant reduction of the induced axial flow velocity is observed

that is associated with the skewed root vortex paths. Due to the highly non-linear flow field downstream of a yawed rotor, the measurements closest to the rotor plane should be used directly instead of extrapolating the data at different downstream distances to get an impression of the flow in the rotor plane.

Tuft and CTA measurements are used to detect blade stall during a rotational cycle. Reasonable agreement between the results obtained with the two techniques is found. The measurements confirm that the yawed rotor operating conditions used for the PLA flow velocity measurements are free of dynamic stall.

Whilst the near-wake behind a wind turbine rotor model and its relation to rotor thrust are studied for yaw misalignment effects, measured blade loads are not available. Wake aerodynamics are however coupled to blade aerodynamics. With inflow at the rotor plane and blade loads, more comprehensive assessment of yawed flow conditions would be possible.

Chapter 7

The inverse vortex wake model: a rotor wake measurement analysis tool

The model rotor measurements discussed in Chapters 3 to 6 aim to enhance our insight into rotor aerodynamics. The combined recording of blade loads and the rotor wake is desired, because of the coupled blade and wake aerodynamics. The measurements focus on the rotor near-wake. Detailed blade loads are not recorded, as the small size of the rotor blades prohibits the installation of pressure orifices. The TUDelft rotor wake measurements are not unique in this respect; most other wind tunnel studies of model rotors either focus on detailed blade loads or the rotor wake, as can be concluded from the discussion in Chapter 2. A notable exception are the MEXICO measurements [181], conducted in December 2006, where for the first time both blade loads and the rotor wake are recorded in detail, including the inflow at the rotor plane.

The blade loads and inflow at the rotor plane that are not measured with rotor wake experiments can be estimated instead using rotor wake measurement analysis tools. Vermeer and Van Bussel [208], Vermeer [207] and Mast *et al.* [120, 122] have developed these tools with increasing complexity, as discussed in Chapter 2.

The measurement analysis tool discussed in this Section is presented under the name 'inverse vortex wake model' by Haans *et al.* [81, 80]. This model is capable of deriving blade loads and the inflow at the rotor plane from rotor wake measurements with the rotor subject to both axial and yawed flow conditions. The concept of the inverse vortex wake model is explained first in Section 7.1. Thereafter, the model is constructed using the present rotor wake measurements in Section 7.2. Verification and validation of the model are discussed in Section 7.3.

7.1 Model concept

The inverse vortex wake model is based on the same aerodynamic theory as
'ordinary' vortex wake models. The general vortex wake system as discussed
in the review of predictive vortex wake models, given in Section 2.1.3, holds
for the inverse vortex wake model as well, refer to the summary in Section
7.1.1. The inverse approach that distinguishes the inverse from an ordinary
vortex wake model is presented in Section 7.1.2.

7.1.1 Vortex wake theory revisited

Vortex wake theory and models are introduced abundantly in literature. Refer
e.g. to the textbook by Katz and Plotkin [101], which also forms the reference
of the basic overview given here.

   The inverse vortex wake model is based on the assumption that the rotor
flow field can be modeled by an incompressible, irrotational flow. Source
singularities are not included in the model, thickness effects are hence not
accounted for. Only vorticity effects are incorporated. Vorticity is lumped
into vortex segments on the blade lifting line and in the wake; the vortex
wake system consists of vortices with circulation Γ, both on the blades in the
form of lifting line bound vortices with circulation Γ_b and in the wake in the
form of trailed and shed vortices with circulation Γ_t and Γ_s, respectively. The
geometry of the vortex wake system is illustrated in e.g. Figure 5.13.

   In material coordinates, circulation is conserved, according to Kelvin's
theorem

$$\frac{D\Gamma}{Dt} = 0. \tag{7.1}$$

Consequently, at time $t = t_1$ and blade position $r = r_1$, the bound circulation
$\Gamma_b(r, t)$ is related to the circulation trailed and shed from the trailing edge at
$r = r_1$, $d\Gamma_t(r_1, t_1)$ and $d\Gamma_s(r_1, t_1)$, respectively, with

$$d\Gamma_t(r_1, t_1) = -\left(\frac{\partial \Gamma_b(r, t)}{\partial r}\right)_{r_1, t_1} dr \tag{7.2}$$

and

$$d\Gamma_s(r_1, t_1) = -\left(\frac{\partial \Gamma_b(r, t)}{\partial t}\right)_{r_1, t_1} dt. \tag{7.3}$$

   The flow velocity induced by a three-dimensional vortex segment with
circulation Γ is determined by the classical Biot-Savart law, derived for an
incompressible, inviscid flow, integrated over the length of the vortex segment,

$$\vec{v} = \int \frac{\Gamma}{4\pi} \frac{d\vec{s} \times \vec{r}}{r^3}. \tag{7.4}$$

Here, $d\vec{s}$ is an element of the vortex segment and $\vec{r}$ is the distance between the point at which the induced velocity is determined and $d\vec{s}$.

For $\vec{r} = 0$, a singular point exists. In reality however, the vortex has a viscous core with finite flow velocity. To model the flow velocity in the viscous core, thereby preventing the singular behavior, Equation [7.4] is modified to include a viscous core model K_v,

$$\vec{v} = \int K_v \frac{\Gamma}{4\pi} \frac{d\vec{s} \times \vec{r}}{r^3}. \qquad (7.5)$$

A number of viscous core models are discussed by Leishman *et al.* [112].

The total flow velocity at any given point in the domain is the summation of the undisturbed velocity and the velocity induced by all vortex segments in the vortex wake system, both at the lifting line and in the wake;

$$\vec{V} = \vec{V}_0 + \sum \vec{v}. \qquad (7.6)$$

7.1.2 Inverse approach

An 'ordinary' vortex wake model is generally used as a prediction tool; blade loads are computed for a given rotor at a given rotor operating condition without a priori experimental knowledge. The inverse vortex wake model on the other hand is a rotor wake measurement analysis tool. Estimates of the blade loads and the inflow at the rotor plane that are obtained with the inverse vortex wake model complement rotor wake measurements for a given rotor at a given rotor operating condition.

Rotor wake measurements should meet two criteria in order to allow definition of the corresponding inverse vortex wake model:

- the rotor wake measurements should enable reconstruction of the location, orientation and convection velocity of the vortex wake.

- it should be possible to determine the induced velocity vector from rotor wake measurements.

Conservation of circulation implies that Γ_t and Γ_s can both be expressed in terms of Γ_b when the vortex segments are trailed and shed into the wake, according to Equations [7.2] and [7.3]. Furthermore, the circulation of the vortex segments remains unchanged once trailed and shed into the wake. The first criterion hence allows all circulation in the vortex wake system to be expressed in terms of Γ_b.

Consequently, the velocity induced by any segment of the vortex wake is a function of Γ_b. Summation of the contributions from all vortex segments yields the total induced velocity, expressed in terms of Γ_b, that, according to

Equation [7.6], should be equal to the difference between the local flow velocity and the undisturbed wind $(\vec{V} - \vec{V}_0)$,

$$f(\Gamma_b) = \vec{V} - \vec{V}_0. \tag{7.7}$$

f denotes the functional acting on Γ_b. Discretization of the vortex wake system and determination of the induced velocity for multiple data points at which the flow velocity is measured yields an algebraic, linear system of equations having the following general form

$$A[\Gamma_b] = [\vec{V} - \vec{V}_0]. \tag{7.8}$$

An overdetermined system of equations is constructed in order to reduce the dependency of the unknown Γ_b on a faulty measurement at a particular data point that went unnoticed. The system of equations [7.8] can subsequently be solved for Γ_b with the Least-Squares method. Hence the bound circulation is derived without the need for an airfoil model.

7.2   Model construction

The inverse vortex wake method can in principle be applied to any rotor operating condition, provided that the vortex wake system represents an acceptable approximation to the flow and that the rotor wake measurements meet the two criteria discussed above. Wind shear and dynamic blade pitch conditions could e.g. be studied. At present however, the inverse vortex wake method is constructed for yawed flow conditions, the focal topic of this thesis.

The general discrete system of equations [7.8] is specified for yawed rotor operating conditions and the implementation of conservation of circulation is discussed in Section 7.2.1. The reconstruction of discretized vortex wake geometries from the rotor wake measurements is presented in Section 7.2.2 and the procedure to select flow velocity recordings is outlined in Section 7.2.3.

7.2.1   Discretized system of equations in yaw

For yawed flow conditions, Γ_b at given blade position is assumed to be cyclic with the rotor period $T_{rotor-cycle}$ that is defined in Equation [4.1]. Time t in Equations [7.2] and [7.3] can be replaced by the blade azimuth angle θ_b, with $\theta_b \in [0°, 360°)$. θ_b is subsequently discretized by selecting m θ_b-instants using a constant $\Delta\theta_b$-interval.

At each of the m θ_b-instants, p data points are selected, where a data point is a component of the PLA flow velocity measured at a (r, θ, z)-position for the given θ_b-instant. For each data point, a relation is constructed that equates

the computed induced velocity, expressed in terms of Γ_b, to the measured PLA induced velocity.[1] For yawed rotor operating conditions, the discretized system of equations [7.8] can hence be written as

$$
\begin{bmatrix}
a_{1,1,1,1} & \cdot & a_{n,1,1,1} & \cdot & a_{1,m,1,1} & \cdot & a_{n,m,1,1} \\
\vdots & \cdot & \vdots & \cdot & \vdots & \cdot & \vdots \\
a_{1,1,1,p} & \cdot & a_{n,1,1,p} & \cdot & a_{1,m,1,p} & \cdot & a_{n,m,1,p} \\
\vdots & \vdots & \vdots & \vdots & \vdots & \vdots & \vdots \\
\vdots & \vdots & \vdots & \vdots & \vdots & \vdots & \vdots \\
a_{1,1,m,1} & \cdot & a_{n,1,m,1} & \cdot & a_{1,m,m,1} & \cdot & a_{n,m,m,1} \\
\vdots & \cdot & \vdots & \cdot & \vdots & \cdot & \vdots \\
a_{1,1,m,p} & \cdot & a_{n,1,m,p} & \cdot & a_{1,m,m,p} & \cdot & a_{n,m,m,p}
\end{bmatrix}
\begin{bmatrix}
\Gamma_{b_{1,1}} \\
\vdots \\
\Gamma_{b_{n,1}} \\
\vdots \\
\Gamma_{b_{1,m}} \\
\vdots \\
\Gamma_{b_{n,m}}
\end{bmatrix}
=
\begin{bmatrix}
<V_{1,1}> \\
\vdots \\
<V_{1,p}> \\
\vdots \\
\vdots \\
<V_{m,1}> \\
\vdots \\
<V_{m,p}>
\end{bmatrix}
- \vec{V}_0. \quad (7.9)
$$

The size of influence matrix A is $(p*m) \times (n*m)$. Its indices $a_{i,j,k,l}$ indicate: circulation related to the bound circulation at blade segment i $(i = 1, \ldots, n)$ for blade azimuth angle $\theta_{b,j}$ $(j = 1, \ldots, m)$, equation set up for blade azimuth angle $\theta_{b,k}$ $(k = 1, \ldots, m)$ and for velocity component l $(l = 1, \ldots, p)$. An overdetermined system, hence with $p > n$, is set up to reduce the sensitivity of the system to the an unforeseen outlier measurement. System of equations [7.9] is solved for Γ_b with the Least-Squares method.

The vortex wake system that is required to express all circulation in the wake in terms of Γ_b is discretized using vortex rings with constant circulation, see Figure 7.1. Amongst models that also employ the vortex ring approach are e.g. the AWSM-code by Van Garrel [55]. The blade is represented by a line of vortex rings; spanwise vortex segments located on the $1/4c$-line and on the trailing edge are connected with chordwise vortex segments to form a blade vortex ring. At each θ_b-instant, vortex rings are shed from the blade trailing edge into the wake, where they connect with the vortex rings shed at the previous instant through shared corner nodes. The vortex rings representing the blade and wake form a vortex lattice of rectilinear vortex segments with piecewise constant circulation.

The circulation strength of a vortex ring is expressed as $\Gamma_{k,i,l}$, with k indicating the instant θ_{b_k} at which the vortex wake system is considered, $k = 1, \ldots m$, i the numbering of the rings in the spanwise direction, $i = 1, \ldots n$, and l the numbering of the rings in the downstream direction, with $l = 1$ the ring on the blade. A vortex ring consists of four rectilinear vortex segments that are connected at the end points. The velocity induced by a rectilinear vortex

---

[1]Each equation is set up to compute a *component* of the induced flow velocity vector at given wake location, not the magnitude of the induced flow velocity *vector*. It's not required to set up equations for all three induced flow velocity components per wake location. One can hence pick the induced flow velocity components with lowest measurement uncertainty.
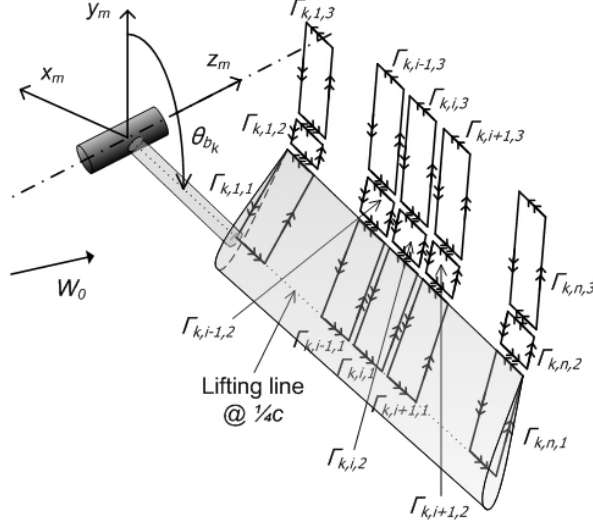
Figure 7.1: Schematic of the vortex wake system, discretized with vortex rings. For clarity, the vortex rings are drawn as individual elements, whilst in practice, the vortex rings share common segments.

segment with constant circulation Γ is given by

$$\vec{v} = K_v \frac{\Gamma}{4\pi} \left(\frac{\left(|\vec{a}| + |\vec{b}| \right) \left(|\vec{a}||\vec{b}| - \dot{\vec{a}b} \right)}{|\vec{a}||\vec{b}||\vec{a} \times \vec{b}|^2} \right) \left(\vec{a} \times \vec{b} \right). \tag{7.10}$$

For the definition of the vectors used, see Figure 7.2. A derivation of Equation [7.10] can e.g. be found in Conlisk [36].

Recall that K_v is the viscous core model. Numerous models are available. The selection of a model is not crucial to the inverse vortex wake model however, since the points at which the induced velocity is computed are not located within the viscous core of the vortex segments, as will be discussed in Section 7.2.3. The model proposed by Vatistas [200] is employed,

$$K_v = \frac{h^2}{(r_c^{2n} + h^{2n})^{1/n}}, \tag{7.11}$$

with h the distance between the vortex segment and the point $\vec{P}_r$ at which the induced velocity is determined, shown in Figure 7.2, r_c the vortex core radius and n an integer determining the flow velocity shape. r_c is assumed to be constant and equal to the airfoil thickness, $r_c = 0.12c$; vortex stretching and diffusion hence are ignored. Furthermore, $n = 2$ is selected, which yields an algebraic approximation to the Lamb-Oseen vortex [109].
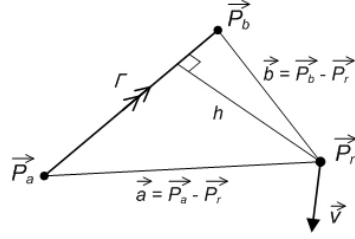
148

Figure 7.2: The velocity induced by a rectilinear constant circulation strength vortex segment.

When representing the vortex wake system in terms of vortex rings, the circulation Γ_b on the lifting line follows from the circulation strength of the blade vortex rings,

$$\Gamma_{b_{i,k}} = \Gamma_{k,i,1}. \tag{7.12}$$

$\Gamma_{b_{i,k}}$ denotes the circulation on a lifting line segment, with i the lifting line segment number in the spanwise direction, $i = 1, \ldots n$, and k indicating the instant θ_{b_k} at which the vortex wake system is considered, $k = 1, \ldots m$, see Figure 7.3. To construct the inverse vortex wake model given by Equation [7.8], the circulation on both the blade and the wake vortex rings should be expressed in terms of Γ_b. The relation between the circulation on the blade and wake vortex rings should thus be determined.
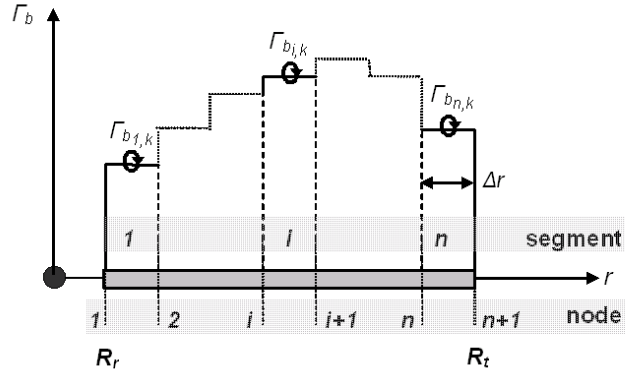

Figure 7.3: Schematic of the bound vortex spanwise discretization.

The relations between the circulation on the lifting line Γ_b and the circulation trailed and shed into the wake Γ_t and Γ_s given in Equations [7.2] and [7.3], respectively, are based on conservation of circulation. When discretizing

149

a given vortex wake system with blade vortex rings, conservation of circulation is automatically satisfied for Γ on the vortex segments that trail the lifting line, as each vortex ring is a closed path with constant Γ. A relation derived from Equation [7.2] that defines Γ_t is hence not required.

The circulation of the vortex rings that trail from the trailing edge into the wake must be explicitly related to that of the blade vortex rings though. Discretization of Equation [7.3] yields

$$\Gamma_{k,i,1} = \Gamma_{k,i,2}, \tag{7.13}$$

$$\Gamma_{k,i,l} = \Gamma_{k+1,i,l+1}, \quad l = 2, 3, \dots \tag{7.14}$$

The circulation strength of the first vortex ring downstream of the blade hence equals that of the corresponding blade vortex ring (Equation [7.13]), while the wake vortex rings are convected downstream (Equation [7.14]). Note that condition given by Equation [7.13]) results in $\Gamma = 0$ at the trailing edge. The circulation of all vortex rings can hence be expressed in terms of Γ_b using Equations [7.13] - [7.14].

When discretizing the vortex wake system, special care should be given to the wake age of the shed vortex segments. The vorticity shed from the trailing edge between $\theta_{b_{k-1}}$ and θ_{b_k} is lumped into shed vortex segments that are subsequently integrated in wake vortex rings. The contribution from the shed vortex segments to the induced velocity at the lifting line depends on their mutual distance, which is directly related to the wake age of the shed vortex segments. In accordance with vortex lattice modeling practise, see e.g. the discussion by Katz and Plotkin [101], the wake age of the first shed vortex segments downstream of the trailing edge is set to $0.25\Delta\theta_b$, see e.g. Figure 7.1.

7.2.2 Discretized vortex wake geometry

The circulation of each vortex ring that is shed into the wake from the blade trailing edge can be expressed in terms of Γ_b, as discussed in Section 7.2.1. When the vortex rings can furthermore be tracked while convecting downstream, the left-hand side of the inverse wake model given by Equation [7.9] can be constructed.

Vortex ring tracking requires the location, orientation and convection velocity of the vortex ring nodes in Figure 7.1 to be known for the rotor operating condition studied. Rotor wake measurements should hence allow discretized reconstruction of the vortex wake geometry. The approach followed depends on the available measurements. At present, the reconstruction of the vortex wake geometry is demonstrated for the rotor operating conditions summarized in Table 6.2, since for these conditions both the flow velocity and tip vortex center locations are measured in the near-wake.
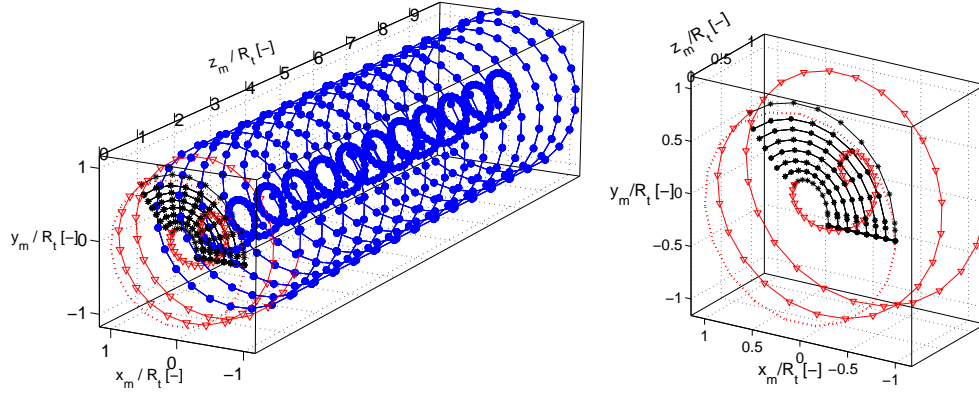
150

Figure 7.4: The vortex wake from a single rotor blade, for the axial flow condition with the blade at $\theta_b = 90°$. Left plot: overview, right plot: detail of the very-near-wake and the near-wake.

Consistent with the near-wake measurements, the vortex wake geometry is reconstructed from three 'building blocks', the root vortex, the vortex sheet and the tip vortex. With the blade modeled by n vortex rings, $n+1$ nodes can be identified on the blade in the spanwise direction, see Figures 7.1 and 7.3. When trailed into the wake, the path of each of the nodes is prescribed by one of the three 'building blocks', with the node numbering given in Figure 7.3;

- **root vortex**: most inboard node, $j = 1$,

- **vortex sheet**: midspan nodes, $j = 2, 3, \ldots, n$

- **tip vortex**: most outboard node, $j = n + 1$

Furthermore, the vortex wake geometry is reconstructed by dividing the wake into three downstream sections, see Figure 7.4;

- **a very-near-wake**, for $0 \leq z/R_t \lessgtr 1.50 \cdot 10^{-1}$, containing estimated root vortex paths, measured vortex sheet paths and measured tip vortex paths,

- **a near-wake**, for $1.50 \cdot 10^{-1} \lessgtr z/R_t \lessgtr 1$, containing estimated root vortex paths and measured tip vortex paths,

- **a far-wake**, for $1 \lessgtr z/R_t$, containing estimated root and tip vortex paths.

The vortex sheet paths are found by tracking the viscous wake, since wake vorticity is concentrated in the viscous wake, as argued in Section 5.3.3. The

151

viscous wake is tracked using the hot-film CTA measurements; the distinct increase in the phase-locked standard deviation s_{Veff}-distributions is a measure for the viscous wake location, as can be seen in Figure 5.9. The viscous wake convection velocity $\vec{V}_{wc}$ is subsequently derived, as explained in Section 5.3.6.

The hot-film CTA measurement plane furthest downstream of the rotor plane is located at $z/R_t = 1.50 \cdot 10^{-1}$. Downstream hereof, the vortex sheet is assumed to roll up into tip and root vortices. The wake age $\Delta\theta_{b_{wake}}$ of a vortex sheet node at $z/R_t = 1.50 \cdot 10^{-1}$ generally is a function of the spanwise node number and of the instant at which the node has trailed the blade. Since the vortex ring representation discussed in Section 7.2.1 requires all vortex sheet nodes that trail the blade at a given instant to have identical $\Delta\theta_{b_{wake}}$ at roll-up, the vortex sheet does not roll up at the plane $z/R_t = 1.50 \cdot 10^{-1}$ downstream. Roll-up is imposed for the vortex sheet nodes at constant $\Delta\theta_{b_{wake,1}}$ instead, with $\Delta\theta_{b_{wake,1}}$ the wake age at $z/R_t = 1.50 \cdot 10^{-1}$ of the vortex sheet node that convects downstream the slowest. The vortex sheet paths hence generally extend further downstream then $z/R_t = 1.50 \cdot 10^{-1}$.

The tip vortices are assumed to trail from the trailing edge at the blade tip, $r/R_t = 1$. The tip vortex paths in the very-near-wake and the near-wake are reconstructed from measured tip vortex center locations, see e.g. Figure 7.5 for the $\Psi = 30°$-case; tip vortex centers in the (x_m, z_m)-plane on the upstream and downstream side with identical wake age are connected with straight lines, as has also been done in Section 6.2 to determine the wake skew angle χ. For each tip vortex pair, a 'tip vortex circle' is constructed in the plane defined by the tip vortex line and a line parallel to the y_m-axis that intersects the tip vortex line. The circle center coincides with the midpoint of the tip vortex line, while the circle diameter is equal to the length d of the tip vortex line.

No tip vortex measurements are available in the far-wake, starting at $z/R_t \approx 1$. The tip vortex paths in this region are hence estimated. The tip vortex convection velocity in the far-wake is assumed to be constant and equal to the distance between the centers of the two tip vortex circles furthest downstream, divided by $\Delta t = \pi/\Omega$, the time interval equivalent to $\Delta\theta_{b_{wake}} = 180°$. Tip vortex circles are consequently constructed in the far-wake, see Figure 7.5, where

$$\chi_{nw} = \chi_{fw}, \tag{7.15}$$

$$\beta_{nw} = \beta_{fw}, \tag{7.16}$$

$$p_{z_{nw}} = p_{z_{fw}}, \tag{7.17}$$

$$d_{nw} = d_{fw}, \tag{7.18}$$

with χ the wake skew angle, β the wake twist angle, p_z the z-pitch and d the tip vortex line length. Suffixes nw and fw indicate the measurements furthest downstream in the *near wake* and the estimates in the *far wake*, respectively.
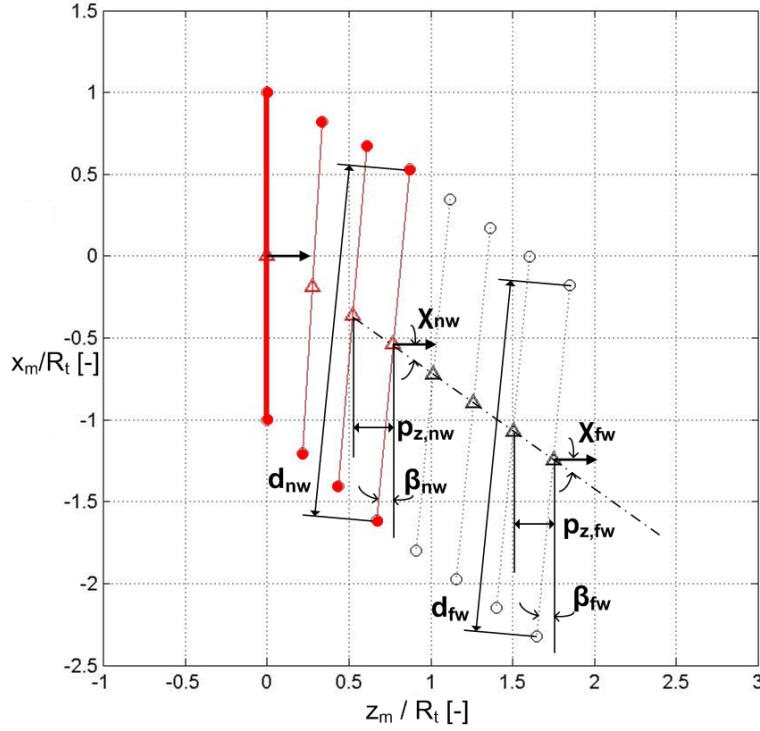
Figure 7.5: Tip vortex center locations in the (x_m, z_m)-plane for the $\Psi = 30°$ condition. Closed symbols, solid line: measurements. Open symbols, dotted lines: estimates.

Note that the far-wake tip vortex paths do not expand. All tip vortex circles combined outline the helical tip vortex paths.

The construction of the root vortex paths is based on assumptions only, since no root vortex measurements are performed. Vermeer *et al.* [204] discuss that the root vortex is difficult to detect experimentally. It is assumed that the root vortices trail from the trailing edge at the root, $r = R_r$, and that the root vortex paths do not expand. For the axial flow condition, the root vortex nodes are assumed to convect in the axial direction only, whilst their convection speed is determined from a study into the effect of variations in the root vortex convection speed on the fit between the measured and computed results, to be presented in Section 7.3.2. The results from this study will be used to define the root vortex paths for the yawed flow conditions.

At the boundary between the very-near-wake and the near-wake, the vortex sheet is forced to roll up into concentrated tip and root vortices, see Figure 7.6. Vortex wake roll-up in fact is a physical flow phenomenon. Van Dyke's

153
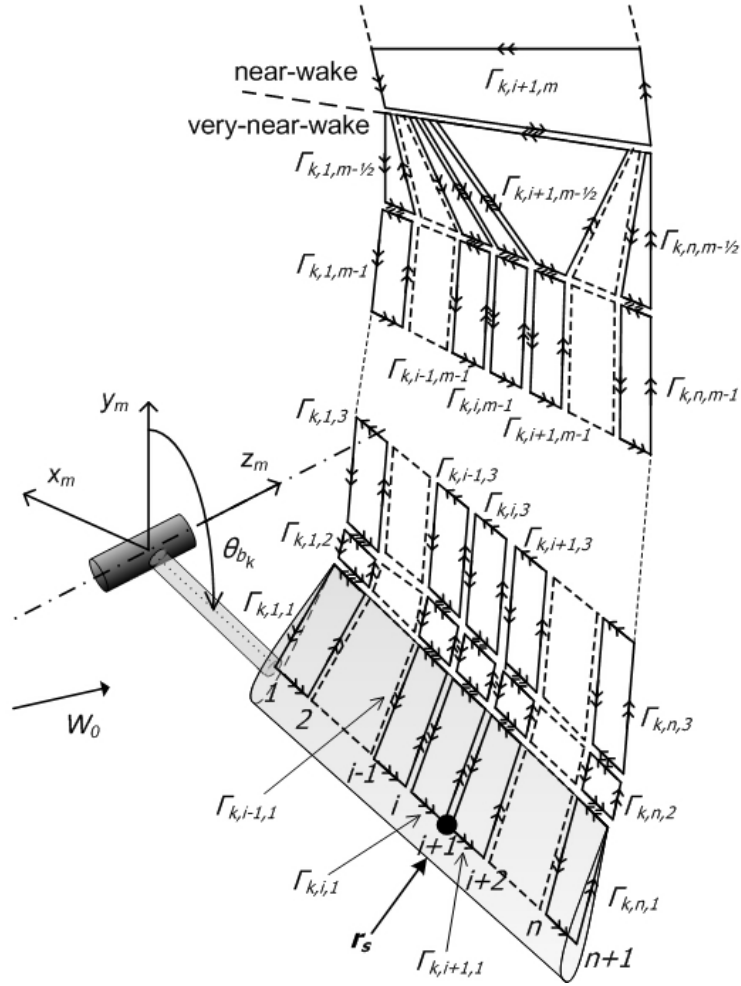
Figure 7.6: Schematic of the vortex sheet roll-up into concentrated tip and root vortices.

album of fluid motion [47] presents a visualization of the wake roll-up behind a translating wing (picture 84 by H. Bippes).[2]

The roll-up process for the vortex ring representation of the vortex wake system is illustrated using an additional row of vortex rings with downstream number $m-1/2$ and associated circulation strength $\Gamma_{k,i,m-1/2}$. The '$m-1/2$'-

---

[2]Take your time while you leaf through all the marvelous photographs in 'An album of fluid motion' [47]. Elaborating on the discussion by Vermeer *et al.* [204] regarding the difficulty to experimentally detect the root vortex for a model wind turbine, picture 75 'Vortices behind a rotating propeller' shows that root vortices are present in a rotating blade vortex system.

row of vortex rings is for illustration purposes only; in the actual inverse vortex wake model, roll-up is instantaneous and the '$m-1/2$'-row does not exist. A single vortex ring remains after roll-up. The other vortex rings are compressed in spanwise direction during the roll-up process, thereby canceling out the circulation on the coinciding vortex segments. Γ of the concentrated tip and root vortices after roll-up hence is of equal strength and opposite sign.

Γ of a concentrated tip vortex is the summation of Γ over all vortex sheet segments that roll up into the tip vortex and likewise for the concentrated root vortex. The boundary between the parts of the vortex sheet rolling up into the root and tip vortices should correspond to the spanwise location of maximum circulation on the bound vortex $\Gamma_{b,max}$. Consequently, $|\Gamma|$ of the tip and root vortices should be equal to the maximum circulation on the bound vortex $\Gamma_{b,max}$.

In the inverse vortex wake model, the fractions of the vortex sheet rolling up into the tip and root vortices are imposed a priori; a blade spanwise location r_s is preselected where the most outboard vortex segment rolling up into the root vortex trails the blade, see Figure 7.6. Having computed the corresponding Γ_b-distribution, r_s is compared a posteriori to the spanwise location of the vortex element with $\Gamma_{b,max}$. For $|\Gamma|$ of the tip and root vortices after roll-up to be equal to the maximum circulation on the bound vortex $\Gamma_{b,max}$, the inboard node of the bound vortex element with $\Gamma_{b,max}$ and r_s should coincide. This r_s-location is obtained for the axial flow condition using an iterative procedure, as will be shown in Section 7.3.2. The yawed flow conditions are tackled using the r_s-location found for the axial flow condition.

7.2.3 Velocity points selection

The inverse vortex wake model given by Equation [7.9] can in principle be constructed for any sample of (r, θ, z, θ_b)-points where a flow velocity component is measured. The suitability of a point is determined by the assumptions underlying the vortex wake modeling and the nature of the flow problem. Discussions by Vermeer [207] and Mast *et al.*[122] aid in the selection of (r, θ, z, θ_b)-points at which the induced velocity is reconstructed.

Vermeer [207] observes that when computing the spanwise distribution of the circulation on a bound vortex Γ_b from near-wake velocity measurements, the system of equations becomes ill-conditioned when the velocity points are selected at a single radial position r_1 only. The induced velocity at r_1 in the near-wake is dominated by bound vortex segments near r_1, contributions from bound vortex segments located away from r_1 quickly diminish with their distance to r_1, recall the $(1/r^3)$-relation in the Biot-Savart law [7.4]. Vermeer's analysis model only considers the contribution of bound circulation to induced velocity, wake circulation is not included. In essence however, the requirement

of selecting (r, θ, z, θ_b)-points at r-stations all along the blade also holds for the present, more extensive, inverse vortex wake model, in order to prevent an ill-conditioned system of equations. Points are hence selected at $r/R_t = 0.4, 0.5, \ldots, 0.9$; all r-stations at which the PLA flow velocity is recorded, except for the tip location $r/R_t = 1.0$, that is omitted because of the relatively large measurement uncertainty.
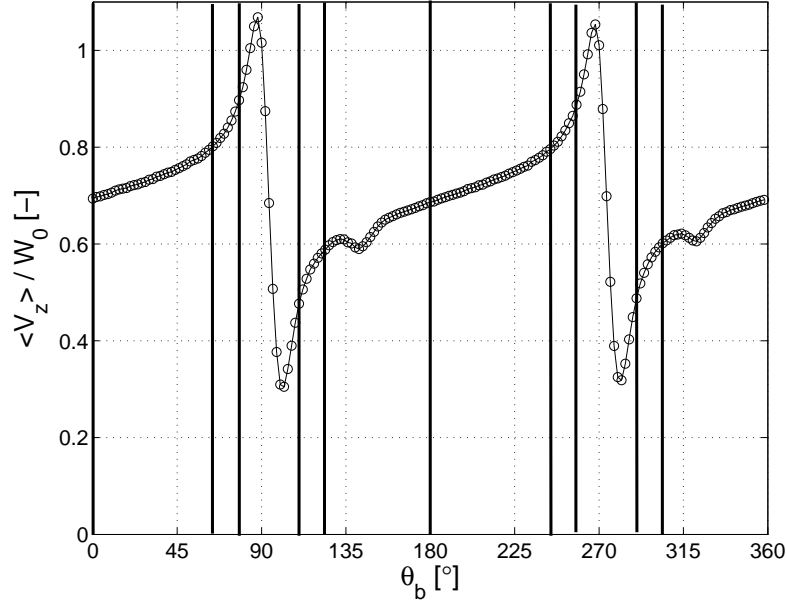

Figure 7.7: $\overline{< V_z >}/W_0$ versus θ_b at $(r/R_t, \theta, z/R_t) = (0.6, 90°, 0.0583)$ for the axial flow condition, with the solid vertical lines indicating the θ_b-values that are selected to construct the inverse vortex wake model.

Mast *et al.* [122] show that a lifting line model does not accurately predict the induced velocity in the proximity of a blade. For a given near-wake location, the local induced velocity minima and maxima associated with a blade passage are under-predicted by the lifting line model, when compared with XFOIL-results. Drela's airfoil code XFOIL [45], couples a panel method to an integral boundary layer method [3], resulting a.o. in a more realistic flow field near the blade. The difference between lifting line and XFOIL results is explained by the effects of airfoil thickness and distributed vorticity; whereas in XFOIL the airfoil surface is discretized with vorticity panels, effectively

---

[3]The general XFOIL methodology is given in Drela [45]. For more information on XFOIL and the software itself, available under the GNU General Public License, see http://raphael.mit.edu/xfoil/

modeling the surface as a streamline, this level of detail is lost in the lifting line method where the bound vorticity is lumped into a bound vortex at the chord line, $1/4c$ from the leading edge. The (r, θ, z, θ_b)-points should hence be positioned away from the local induced velocity maxima and minima at blade passage.

The singular character of a lumped vortex furthermore renders inadequate points at or in the direct vicinity of wake vortex segments. As discussed in Section 7.2.2, the very-near-wake vortex sheet is reconstructed by tracking the viscous wake with the CTA hot-film measurements. For a given (r, θ, z)-location, the points should hence not be located at or near the viscous wake passage $\theta_{b_{wake}}$. A typical example of (r, θ, z, θ_b)-points selected for construction of the inverse vortex wake model is given in Figure 7.7.

7.3 Model verification & validation

Prior to analyzing rotor wake measurements with the inverse vortex wake model, the quality of the numerical results should be assessed. In general, both measurements and numerical models are directed at uncovering the real world, as is depicted in Figure 7.8. The dotted arrow between 'measured data' and 'conceptual model' indicates that, whereas normally a conceptual model is based on analysis of the reality only, construction of the inverse vortex wake conceptual model requires measured data as well.
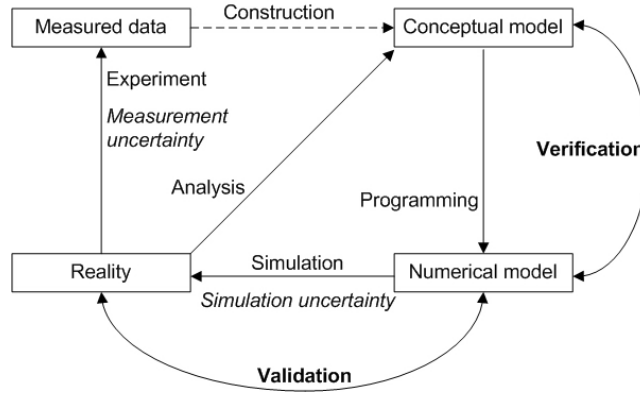

Figure 7.8: Relations between measurements, inverse vortex wake modeling and reality, edited from the AIAA Guide [2].

The true value that measurements and modeling aim to reveal normally is unknown. In order to assess the quality of the measurement and the numerical model, the errors between the true value on the one hand and the

157

measured and simulated values on the other hand must hence be estimated by the measurement and simulation uncertainty, respectively. The analysis of the measurement uncertainty has been discussed in Section 4.4 already.

The simulation uncertainty is obtained through verification and validation of the numerical model, see Figure 7.8 for their position within the modeling process. Verification is the process of judging wether the conceptual model has been solved correctly. It hence concerns the accuracy of solving the discretized continuum mathematics and the correctness of the computer code. Validation is the process of judging wether the mathematical model correctly and accurately describes the real world. Since measurements represent the real world, validation is affected by the associated measurement uncertainty.

With the emergence of numerical simulations in the last few decades, the field of verification and validation has developed accordingly. The importance of verification and validation has been acknowledged by the AIAA by publishing a Guide [2] on the topic.[4] The inverse vortex wake model defies the general verification and validation concepts however, since for each case considered, the model is constructed with experimental data obtained for that specific case; the inverse vortex wake model is a measurement analysis tool!

Verification, discussed in Section 7.3.1, is hence performed on a case for which an analytical solution exists; a translating lifting line with elliptic circulation distribution. When the model is constructed using the analytical solution instead of the measurements, the influence of the uncertain measurements is eliminated. Validation, discussed in Section 7.3.2, concerns sensitivity analyzes of parameters that cannot be derived from measurements on the simulation results and their agreement with measured data.

7.3.1   Model verification

Prandtl's lifting line theory yields an analytic relation for the downwash W at a translating wing as a function of the spanwise distribution $\Gamma_b = \Gamma_b(y)$, see Figure 7.9 for the (x, y, z)-coordinate system used. For the elliptic distribution

$$\Gamma_b(y) = \Gamma_{b_0} \sqrt{1 - \frac{2y}{b}}, \tag{7.19}$$

it can be proven that W is constant across the lifting line, with

$$W = -\frac{\Gamma_{b_0}}{2b}. \tag{7.20}$$

Here, b is the wing span. The derivation of Equation [7.20] can be found in aerodynamics textbooks [15, 101].

---

[4]The AIAA Guide [2] "does not recommend standards in these areas because a number of important issues are not yet resolved". While work hence is still in progress, useful verification and validation tools can be found in Oberkampf and Trucano [134].
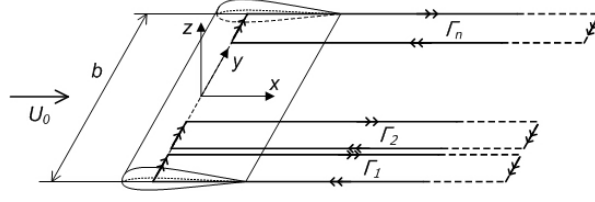
Figure 7.9: Translating lifting line, discretized with n vortex rings.

The elliptic lifting line problem is discretized using n vortex rings in the spanwise direction, see Figure 7.9. Since the flow condition is steady, vortex segments do not *shed* into the wake.[5] All vortex rings associated with a given bound vortex segment are thus merged into one ring. The wake vortex sheet remains in the (x, y)-plane and does not roll up. As regards the right-hand side of Equation [7.8], points are selected at the lifting line, with the 'measured' induced velocity equal to the downwash W, given in Equation [7.20].

The case with $b = 10\,m$, $U_0 = 20\,m/s$ and $W = -1\,m/s$ is studied. The numerical Γ_b-distribution obtained with the inverse vortex wake model approaches the analytic solution [7.19] when the number of spanwise bound vortex segments increases, see Figure 7.10. The conceptual inverse vortex wake model is hence solved correctly for this verification case.
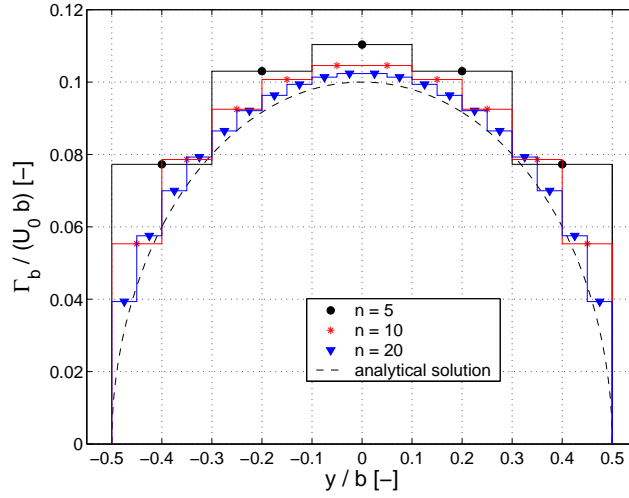

Figure 7.10: Spanwise $\Gamma_b/(U_0 b)$: numerical results versus the analytic solution.

---

[5]The only vortex shed into the wake is the start vortex that closes the vortex ring far downstream, see Figure 7.9.

7.3.2 Model validation

Near-wake flow velocity measurements and recordings of the tip vortex center locations are available for all three rotor operating conditions selected to be analyzed with the inverse vortex wake model. Vortex sheet roll-up and the root vortex convection velocity are not measured however. They need to be assumed in order to construct the inverse vortex wake model. Furthermore, the influence of the location where the vortex wake is truncated is unknown. Here, the sensitivity of these parameters is studied for the baseline axial flow condition; its conclusions are applied to the two yawed flow conditions.

The numerical grid is given by a spanwise resolution of vortex segment nodes at the lifting line of $\Delta(r/R_t) = 0.1$, with $r/R_t = 0.3, 0.4, \ldots, 1.0$, and a cyclic resolution of $\Delta\theta_b = 15°$, with $\theta_b = 0°, 15°, \ldots, 360°$. The grid comports with the spatial resolution of the hot-film CTA measurements.
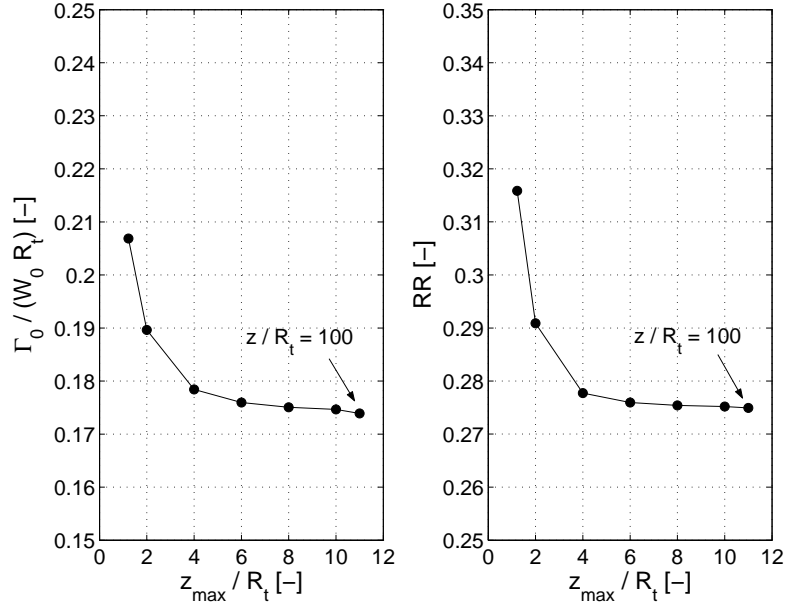
Figure 7.11: Influence of the axial location of the vortex wake downstream boundary, z_{max}/R_t, on $\Gamma_b/(W_0^* R_t)$ (left plot) and RR (right plot). First data point, at $z/R_t = 1.22$, corresponds to a vortex wake without a far-wake. Results from simplified model assuming spanwise constant Γ_b.

The sensitivity of the simulation result to the axial location at which the vortex wake is truncated, z_{max}, is studied using the simplification that Γ_b is constant across the lifting line. Both Γ_b and the relative solution residual RR

of the inverse vortex wake model [7.8],

$$RR = \left[\frac{\sum \left((\vec{V} - \vec{V_0}) - A\Gamma_b \right)^2}{\sum \left(\vec{V} - \vec{V_0} \right)^2} \right]^{1/2} , \quad (7.21)$$

show significant variations as a function of z_{max}, see Figure 7.11. Note that the relatively high RR-level could be a consequence of the simplification to enforce constant Γ_b across the span.

Γ_b converges as expected with increased z_{max}. The difference in Γ_b computed for $z_{max}/R_t = 10$ with that computed for a computationally impractical value of $z_{max}/R_t = 100$ is smaller than 0.5%. An acceptable compromise between accuracy and computational effort is hence obtained for $z_{max}/R_t = 10$, which is consequently selected for all three cases.
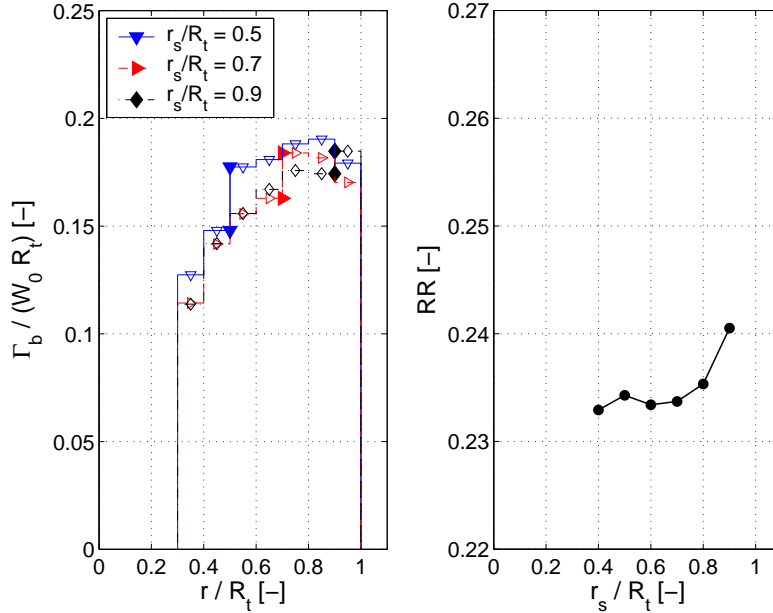
Figure 7.12: Effect of the spanwise trailing location of the most outboard vortex segment rolling up into the root vortex, r_s/R_t, on the Γ_b-distribution (left plot) and RR (right plot).

Prior to computing Γ_b with the inverse vortex wake model, the spanwise trailing location of the most outboard vortex segment rolling up into the root vortex, r_s, is selected, as discussed in Section 7.2.2. The most appropriate r_s-location is based both on physical and mathematical criteria. The former

161

implies that r_s should coincide with the inboard node of the bound vortex element with $\Gamma_{b_{max}}$. The latter concerns the agreement between measured and computed flow velocity, hence relates to RR.

Before assessing the sensitivity of the solution to r_s, note that the general shape of the Γ_b-distribution for the currently considered rotor operating condition near $c_{P_{max}}$ corresponds to that measured by e.g. Ebert and Wood [48] for a similar condition. The low sensitivity of both the computed Γ_b-distribution and RR to a r_s/R_t-variation, seen in Figure 7.12, can be explained by the approximately constant Γ_b-distribution from the midspan outboard. For $r_s/R_t = 0.7, 0.8, 0.9$, the physical criterion mentioned above is met; r_s coincides with the inboard node of the bound vortex element with $\Gamma_{b_{max}}$. Since $r_s/R_t = 0.7$ yields the lowest RR-value, see Figure 7.12, this r_s-location is selected to be used henceforwards. Note however that the relative RR-differences are small.

Even without the simplification of constant Γ_b, overall RR-levels are still substantial at $RR \approx 0.2$, compare Figures 7.11 and 7.12. This is at least in part attributed to measurement uncertainty of the PLA flow velocity, which typically amounts to $0.1W_0$ in axial flow, recall Section 4.4.4.

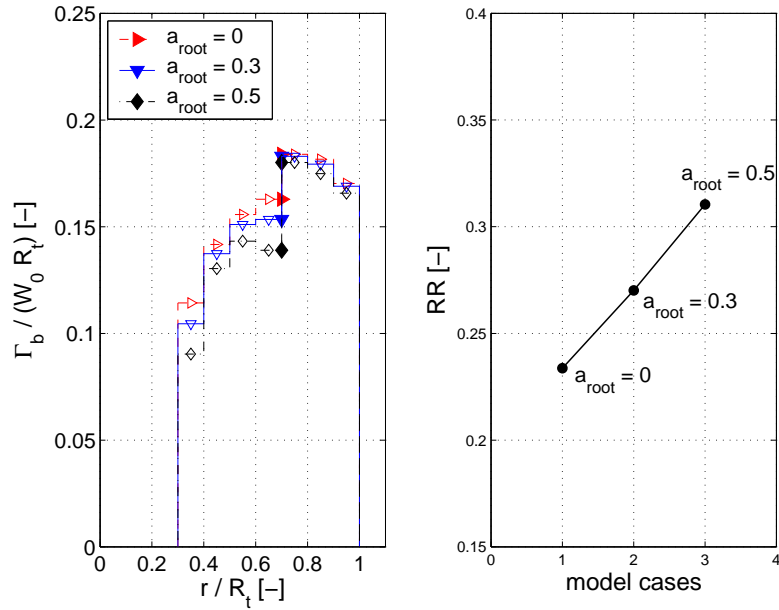No experimental data of the root vortex is available. The path of the

Figure 7.13: Effect of the axial induction factor at the root, a_{root}, on the Γ_b-distribution (left plot) and RR (right plot).

root vortex segments is modeled assuming that root vortex segments trail at R_r, that their paths do not expand and that their convection velocity $\vec{V}_{root}$ is constant. For the axial flow condition currently considered, the root vortex segments hence convect in the axial direction only; the root vortex convection axial velocity, $V_{z,root}$, is expressed in terms of the dimensionless axial induction factor at the root, $a_{root} = 1 - V_{z,root}/W_0$.

The sensitivity of the Γ_b-distribution to a_{root} is concentrated in the region where vortex segments trailing from the blade roll up into the root vortex, see Figure 7.13. Both RR, shown in Figure 7.13, and the flow velocity in the inboard region, illustrated in Figures 7.14 and 7.15, indicate that $a_{root} = 0$ yields the best agreement between measured and computed results.

Note the model does not capture measured V_θ-maxima near $\theta_b = 0°$ and $180°$. These maxima are related to the passage of the viscous wake, recall the discussion on PLA flow velocity trends in Section 5.3.3, which explains why they are not reproduced by the inviscid inverse vortex wake model.

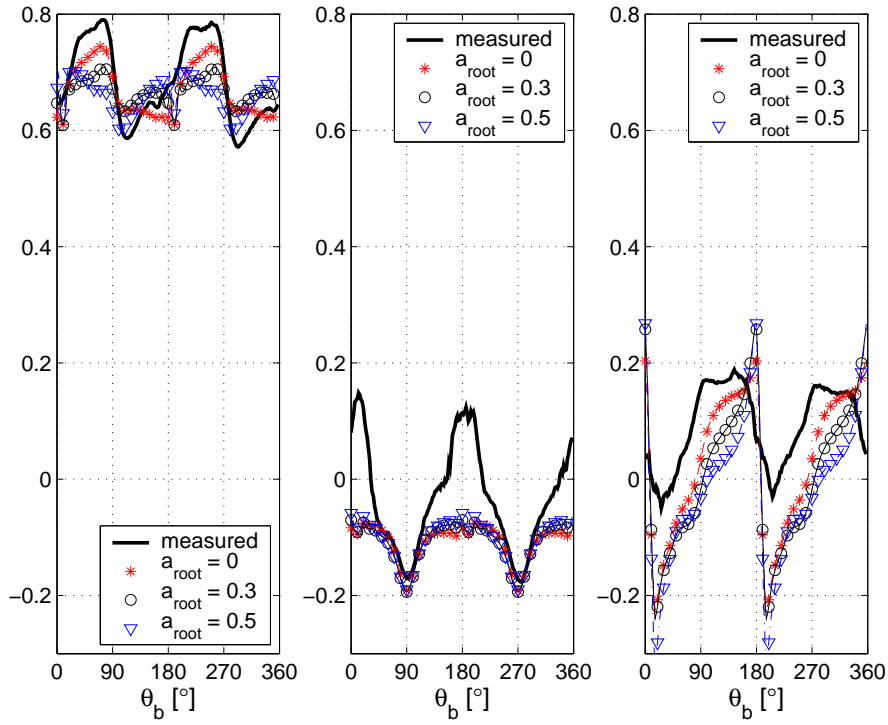Figure 7.14: Computed and measured $\vec{V}/W_0$ versus θ_b at $(r/R_t, \theta, z/R_t) = (0.4, 90°, 0.150)$. V_z/W_0, V_θ/W_0 and V_r/W_0 in the left, middle and right plot, respectively. For the computations, a_{root} is varied.

The (r, θ, z, θ_b)-points used to construct the inverse vortex wake model [7.8] are all within $0.150R_t$ of the rotor plane. The contribution from the root vortex to the induced velocity at the selected points is hence dominated by the root vortex segments in the near-wake. a_{root} is expected to be lowest in the near-wake, as across the span, a is known to decrease when going downstream, recall Figure 5.6. The best fit of computed with measured $< \vec{V} >$ and consequently the lowest RR-value is thus seen for $a_{root} = 0$.
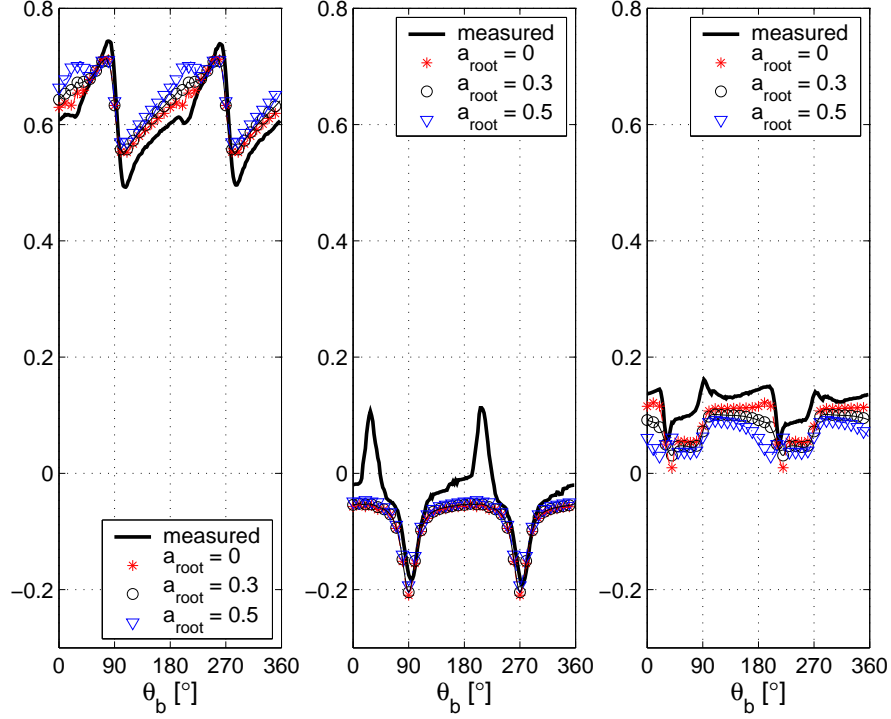
Figure 7.15: Idem as Figure 7.14, but then for $r/R_t, \theta, z/R_t) = (\mathbf{0.6}, 90°, 0.150)$.

All subsequent inverse vortex wake model results presented for the axial flow condition are hence computed using $a_{root} = 0$, which is equivalent to $V_{z,root} = W_0^*$. In yaw, $a_{root} = 0$ would yield root vortex convection parallel to the undisturbed flow, with $(V_{x,root}, V_{y,root}, V_{z,root}) = (W_0 sin\Psi, 0, W_0 cos\Psi)$. The root vortex path would intersect the tip vortex path, however. Root vortex segments in yaw are thus set to convect parallel to the skewed wake axis instead, see Figure 6.2, with $(V_{x,root}, V_{y,root}, V_{z,root}) = (W_0 sin\Psi, 0, W_0 sin\Psi/tan\chi)$. Since $|\Psi| < |\chi|$, as can bee seen in Figure 6.5, $V_{z,root} < W_0 cos\Psi$ or equivalently, $a_{root} > 0$ in yaw. The difference between Ψ and χ is small though; the root vortex segments hence are convected downstream at nearly the undisturbed

flow velocity.

Having determined the unknown parameters z_{max}, r_s and $\vec{V}_{root}$, the measured flow velocity at given points in the near-wake is compared to that computed with the inverse vortex wake model, see Figure 7.16. For a discussion on the trends observed for the measured flow velocity, the reader is referred to Section 5.3.3. The overall agreement between computed and measured flow velocity appears to be good, except the anticipated absence of local V_θ-maxima in the model results, as these are associated with viscous effects. Confidence in the quality of the inverse vortex wake model is strengthened by the good agreement. The model hence seems to be a promising measurement analysis tool that has the potential to enhance our insight into rotor wake aerodynamics by complementing rotor wake measurements with estimates for the unmeasured inflow at the rotor plane and blade loads.
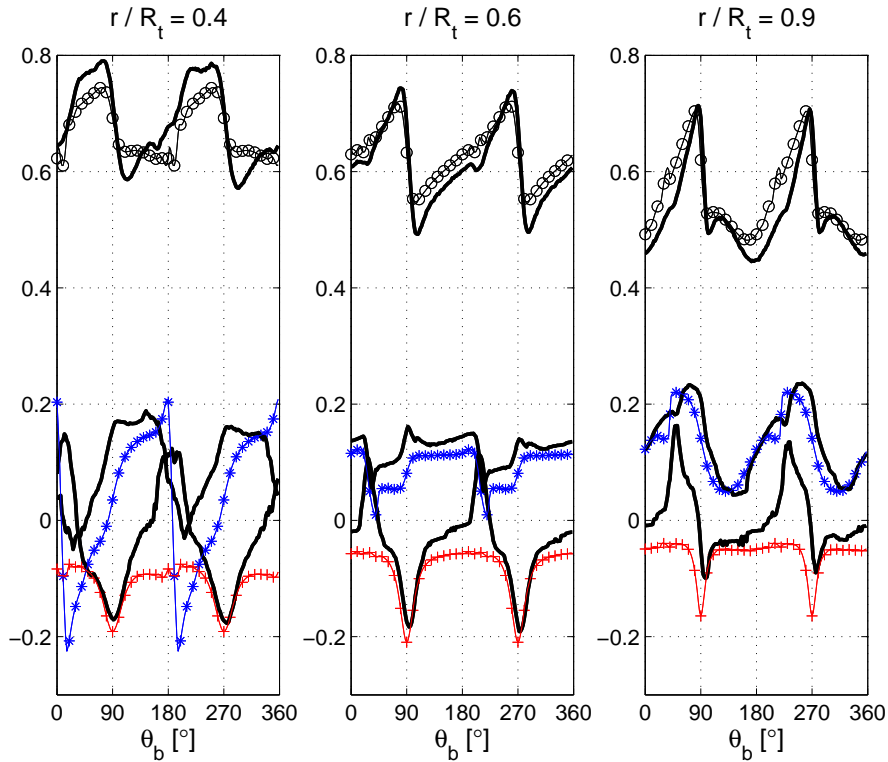

Figure 7.16: Nondimensional computed and measured velocity versus θ_b at $(\theta, z/R_t) = (90°, 0.150)$ for radial locations $r/R_t = 0.4, 0.6$ and 0.9. Computations are indicated with symbols: $V_r/W_0 : *$, $V_\theta/W_0 : +$, $V_z/W_0 : \circ$. Corresponding measurements are given by a solid line only.

165

Chapter 8

Inverse vortex wake model analysis of the rotor aerodynamics

The concept of the inverse vortex wake model, described in Section 7.1, can be applied to any operating condition that approximately satisfies the incompressible, irrotational flow field assumption associated with vortex wake modeling and for which both flow velocity measurements and experiments that enable reconstruction of the vortex wake are available. The inverse vortex wake model serves as a measurement analysis tool: it enables quantification of unmeasured flow variables.Compared to solely analyzing the rotor wake measurements, an additional assessment of results post-processed from the inverse vortex wake model hence yields an enhanced insight into aerodynamics of the rotor.

For the three rotor operating conditions summarized in Table 6.2, the near-wake measurements discussed in Chapters 5 and 6 allow construction of the inverse vortex wake model, as presented in Section 7.2. The results computed with the inverse vortex wake model are subsequently post-processed to arrive at the inflow at the rotor plane and blade loads; the baseline axial flow condition is discussed first in Section 8.1, yaw misalignment effects are analyzed thereafter in Section 8.2. Main conclusions drawn from the analysis with the inverse vortex wake model are given in Section 8.3.

The discussion in this Chapter builds upon those by Haans *et al.* [81, 80]. The discussion in this Chapter is based on the latest version of the model, as defined in Chapter 7, and should hence yield best results.

8.1 The axial flow condition

For the TUDelft rotor currently under consideration, the axial flow operating condition given by $\lambda = 7.9$, $\beta_{pitch} = 2°$ approximately yields $C_{P_{max}}$, as discussed in Section 5.1. Direct analysis of the measurements, presented in Section 5.3, suggests the absence of blade stall, as expected for a flow condition near $C_{P_{max}}$. Since blade loads are not measured, the suggestion can not be confirmed from measurements alone.

The availability of hot-film CTA measurements, recording the flow velocity, and quantitative smoke visualization, recording the tip vortex locations, for this axial flow rotor operating condition enables construction of the inverse vortex wake model, as discussed in Section 7.2. Having solved the inverse vortex wake model [7.9] for the unknown Γ_b-distribution, the results are post-processed to derive the inflow at the rotor plane, discussed in Section 8.1.1, and the blade loads, discussed in Section 8.1.2. The blade load estimate enable an assessment of blade stall occurrence.

8.1.1 Rotor plane inflow

The results obtained with the inverse vortex wake model are post-processed to determine two flow velocity variables at the rotor plane;

- **the annular averaged flow velocity** $\overrightarrow{V}_{ann}$, according to the definition in Section 6.3.1 with Equation [6.5]

- **the flow velocity at the lifting line**, relative to the rotating blade, $\vec{V}_{rel}$, shown in Figure 5.15.

The annular averaged axial flow velocity at the rotor plane and the lifting line axial flow velocity can be employed to estimate the angle of attack α using the annular averaged and the blade passage method respectively, as has been discussed in Section 5.3.4. Note that the name 'blade passage method' is not perfectly suited when deriving the flow velocity at the lifting line from the inverse vortex wake model instead of from measured blade passage signals. To be consistent with the measurement discussion in Section 5.3.4, the name has not been changed.

Application of the two methods to the axial flow velocity at the rotor plane derived with the inverse vortex wake model yields generally similar spanwise α-distributions, as can be seen in Figure 8.1. Substantial differences are observed near the root, at $r/R=0.35$, and near the tip, at $r/R_t=0.95$, though; at these blade sections, the blade passage method yields a more accurate α-estimate than the annular averaged method, since the local instead of the annular averaged flow velocity is considered, as has already been noted in Section
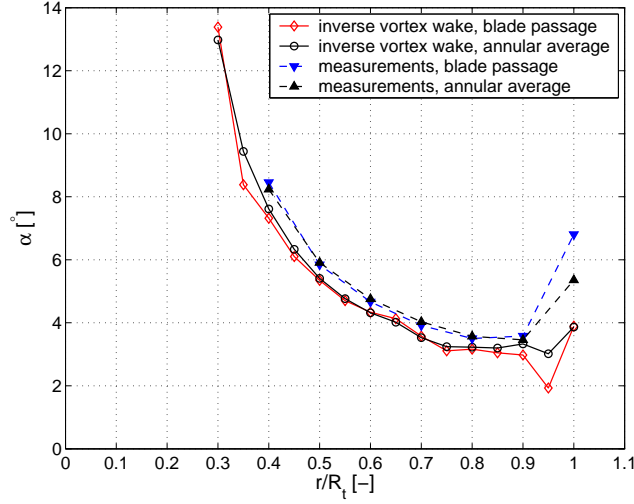
Figure 8.1: α versus r/R_t derived with the annular averaged and blade passage method, using the inverse vortex wake model and measurements.

5.3.4. Subsequent analyzes with the inverse vortex wake model hence make use of the blade passage method.

The axial flow velocity at the rotor plane, required by the annular averaged and blade passage methods to estimate α, can also be found from extrapolation of the near-wake flow velocity measurements to the rotor plane. The spanwise α-distributions that are obtained from this direct approach, given in Figure 5.17, are reproduced in Figure 8.1. The measurement extrapolation approach yields the same trends as the inverse vortex wake method. The offset between the two approaches suggests however that the extrapolation method underestimates α across the span, because the α-estimates obtained with the measurement extrapolation approach are expected to be less realistic than those derived from the physics-based inverse vortex wake model.

In the tip region, $0.9 < r/R_t \leq 1$, the measurement extrapolation and inverse vortex wake results seem to diverge. It must be noted though that the measurement extrapolation approach does not have a reading at $r/R_t = 0.95$. The divergence in the results near the tip could result from the high uncertainty associated with the hot-film measurement extrapolations at $r/R_t = 1$, as discussed in Section 5.3.4. The inverse vortex wake model results near the tip are also subject to model assumptions and limitations though; the vortex rings, constructed from rectilinear vortex segments that are connected at sharp angles, with the tip vortex trailing exactly at the blade tip trailing edge, are expected to represent the tip vortex trailing structure too simplistically.

169

The methods to derive α discussed up to here only require the axial induction factor a, the effect of the azimuthal induction factor a' on α is ignored. To properly assess the influence of a' on α for the axial flow condition under consideration, a' needs to be determined accurately. Whereas for the near-wake measurements, a' is estimated from visual inspection of the data, in combination with extrapolation to the rotor plane, recall Section 5.3.4, the inverse vortex wake model allows direct computation of a' at the lifting line. The latter approach is hence preferred to determine a'.

a' appears to be small along the entire span, with $a'_{max} = 0.019$. Consequently, the influence of a' on α is insignificant from root to tip, see Figure 8.2; the maximum difference observed when in- or excluding a' in the definition of α is $\Delta\alpha = 0.25°$. The small amplitude of a' derived for the current high λ-setting of $\lambda = 7.9$ is explained by inviscid momentum theory; for given a, a' is inversely proportional to $(\lambda\, r/R_t)^2$, refer e.g. to the textbook by Burton et al. [27].

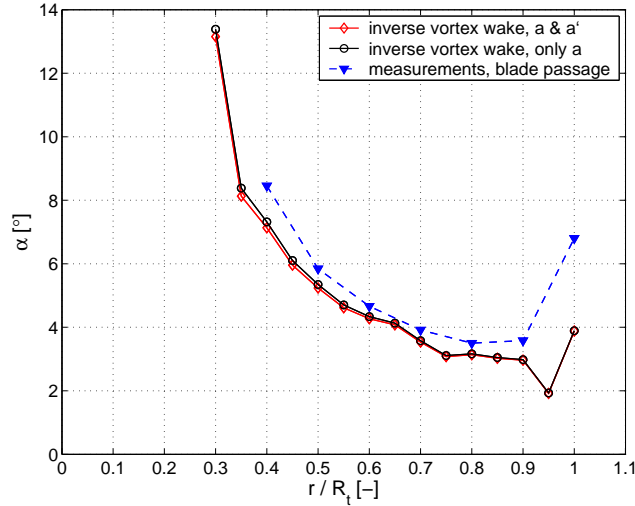Figure 8.2: α versus r/R_t derived with the blade passage method, using the inverse vortex wake model with and without the a'-contribution and the measurements.

8.1.2 Blade loads

With known Γ_b and the inflow at the lifting line, the blade lift L per unit span can be determined from the Kutta-Joukowsky law for a bound vortex [101, 15],

$$\vec{L} = \rho\vec{V}_{rel} \times \vec{\Gamma}_b, \tag{8.1}$$

170

with $\vec{V}_{rel}$ the flow velocity at the lifting line, relative to the rotating blade, as shown in Figure 5.15. $\vec{V}_{rel}$ hence is the summation of the undisturbed, the induced and the apparent flow velocity from blade rotation, the latter given by Ωr.

The corresponding lift coefficient c_l is found by combining Equation [8.1] with the definition of L [2.32],

$$c_l = \frac{2\,\Gamma_b}{c\,V_{rel}}. \tag{8.2}$$

L can furthermore be decomposed into a force per unit span normal and tangential to the rotor plane, F_z and F_θ respectively, using Equations [5.7] and [5.8]. Note that L and the related variables c_l, F_z and F_θ are derived from the inverse vortex wake model without the need for an airfoil model.
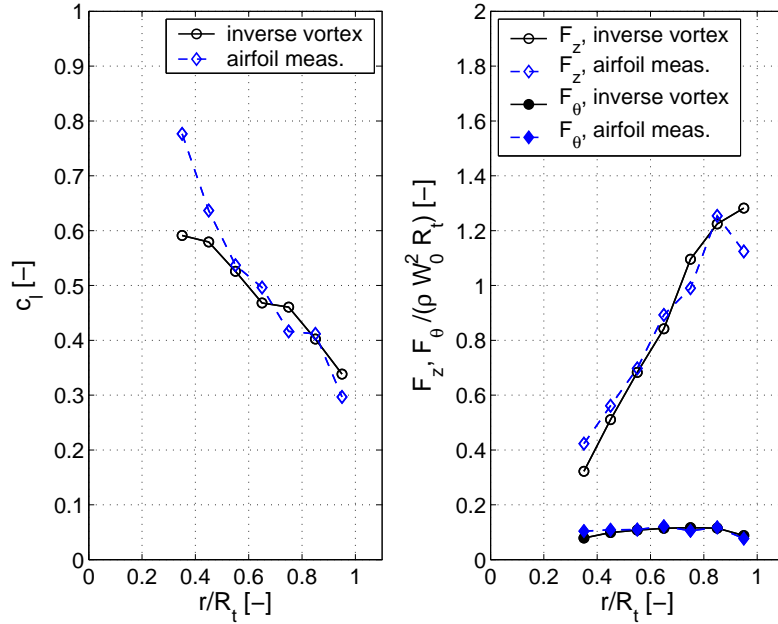
Figure 8.3: c_l (left plot) and F_z, F_θ (right plot, open en filled symbols, respectively) versus r/R_t. Inverse vortex wake method results: $\circ$, results obtained by applying an airfoil model to the inflow at the lifting line computed from the inverse vortex wake model: $\diamond$.

Spanwise distributions of c_l, F_z and F_θ derived from the inverse vortex wake model using Equation [8.1] are given in Figure 8.3, together with results obtained by applying a two-dimensional airfoil model to the inflow at the lifting line that is derived from the inverse vortex wake model. Here, the

airfoil model is given by the 2d-dimensional (α, c_l)-relation found from wind tunnel measurements on a NACA0012 airfoil at $Re_c = 1.5 \cdot 10^5$, refer to Section 3.1.

The spanwise c_l-distribution derived from the inverse vortex wake model generally exhibits two-dimensional behavior. In the root region however, c_l derived from the inverse vortex wake model is reduced significantly compared to the airfoil data. This c_l-reduction is found for $r/R_t \leq 0.45$ and includes sections where α is lower than the two-dimensional stall angle, $\alpha_{stall} = 10.6°$, compare Figures 8.1 and 8.3. A possible explanation could be that in the blade root region a three-dimensional flow disturbance, originating from the blunt blade cut-off at the root, results in early flow separation. More research is required, though. Besides this root-effect, the analysis with the inverse vortex wake model confirms that the blade flow is non-stalled, as has been suggested by the study of measurements only in Section 5.3.

Table 8.1: Computed and measured C_T and C_P.

	C_T	C_P
Inverse vortex wake model	0.76	0.48
Inverse vortex wake conditions with measured (α, c_l)	0.76	0.48
Wake measurements, 1d momentum (Section 5.3.1)	0.75	0.53
Wake measurements, measured (α, c_l) (Section 5.3.4)	0.86	0.61
Rotor measurements (Section 5.1)	0.78±0.08	0.32

Having derived the spanwise distributions of F_z and F_θ from the inverse vortex wake model, T and P can be determined with Equations [5.9] and [5.10], respectively. The corresponding C_T and C_P, obtained by substitution of Equation [5.9] and [5.10] in Equation [2.8] and [2.9], respectively, are given in Table 8.1, along with C_T and C_P obtained from measurements and modeling.

When applying the measured (α, c_l)-relation to the inflow conditions at the lifting line that are derived from the inverse vortex wake model, the resulting C_T and C_P are equal to those derived directly from the inverse vortex wake model, as is in line with the agreement seen in the right plot of Figure 8.3.

Next to the inverse vortex wake model, C_T and C_P are also estimated by direct assessment of the wake measurements. The latter approach is based on the extrapolation of near-wake flow velocity measurements to the rotor plane that allow C_T and C_P to be computed using either one-dimensional, inviscid momentum theory or (α, c_l)-measurements, as discussed in Sections 5.3.1 and 5.3.4 respectively. Both the inverse vortex wake model and the direct assessment of the wake measurements yield C_T-values that are within the 95% confidence uncertainty bounds of the C_T-measurement; the difference

between the results obtained by the two approaches hence is insignificant at the 95% confidence level. In general however, the inverse vortex wake model is expected to yield an improved approximation of the 'real' C_T compared to the direct analysis; the former approach is physics-based, the latter is linear extrapolation.

Although the C_P-estimate derived with the inverse vortex wake model shows a small improvement compared to the direct assessment, the discrepancy with the C_P-measurements remains substantial. The overestimation of C_P for both approaches is explained by their lack of viscous effects; blade torque and rotor power are known to be reduced under the influence of viscous drag.

8.2   The effects of yaw misalignment

Prior to a detailed discussion on yaw misalignment effects, it must be noted that the setup of the inverse vortex wake model for yawed flow conditions differs from that used for the axial flow condition. When the inverse vortex wake model is constructed using all three velocity components at a given point, the relative residual RR is found to be $0.24, 0.60, 0.73$ for the $\Psi = 0°$-, $30°$-, $45°$-cases, respectively. For the yawed flow cases, RR is deemed too large. Hence, whereas for the axial flow case the inverse vortex wake model is constructed using all three velocity components at a given point, for the yawed flow cases only the axial velocity component is used, resulting in $RR = 0.12, 0.40$ for the $\Psi = 30°$-, $45°$-cases, respectively.
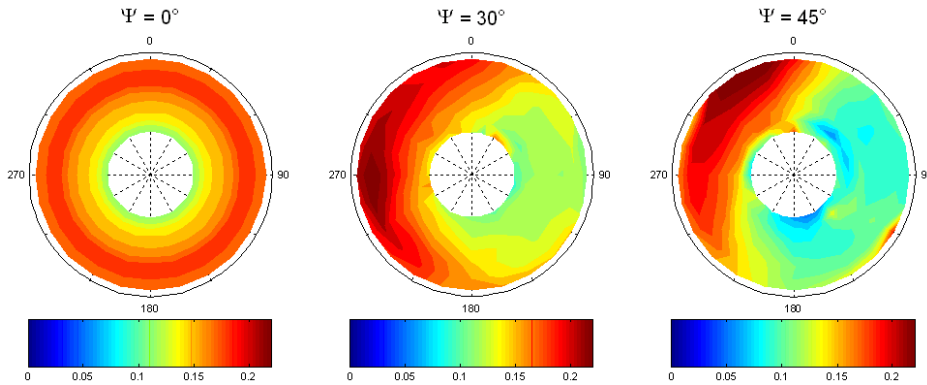

Figure 8.4: $\Gamma_b/(W_0 R_t)$-distribution at the blade lifting line during a rotational cycle for all three cases. Viewpoint is upstream of the rotor, looking downstream, the blades rotate clockwise. The undisturbed velocity component parallel to the rotor plane, $W_0 sin\Psi$, is from left to right.

The assessment of yaw misalignment effects is based on the spanwise Γ_b-distribution during a rotational cycle, plotted in Figure 8.4 for all three operating cases considered. Note that Γ_b is solved for directly by the inverse vortex wake model [7.9]. In contrast to the axial flow condition, the spanwise Γ_b-distributions associated with the yawed flow cases are cyclically unsteady; a characteristic feature of a rotor subject to yawed flow.

Having solved the inverse vortex wake model for Γ_b, the results can be post-processed to derive the inflow and blade loads. The inflow distributions at the rotor plane are introduced in Section 8.2.1. The induced velocity computed with the inverse vortex wake model is the summation of individual vortex segment contributions. In Section 8.2.2, the inflow at the rotor plane is decomposed; root, tip and vortex sheet contributions are identified and assessed for yaw misalignment effects. The effects of yaw misalignment on blade loads are discussed in Section 8.2.3.

8.2.1 Rotor plane inflow

The inflow at the rotor plane is analyzed using three flow velocity variables;

- **the annular averaged flow velocity** $\overline{\vec{V}}_{ann}$, according to the definition in Section 6.3.1 with Equation [6.5]

- **the cycle averaged flow velocity** $\overline{\vec{V}}_{cycle}$, according to the definition in Section 6.3.1 with Equation [6.6]

- **the flow velocity at the lifting line**, relative to the rotating blade, $\vec{V}_{rel}$, shown in Figure 5.15.

The axial and tangential flow velocity components are transformed into dimensionless axial and tangential induction factors a and a' respectively, using Equations 2.28 and 2.29. Additionally, for the yawed flow cases, $V_{\theta_{cycle}}$ and $V_{\theta_{rel}}$ are made dimensionless by division through the component of the undisturbed velocity parallel to the rotor plane, $W_0 sin\Psi$.

The study of $\overline{\vec{V}}_{ann}$ at the rotor plane is relevant for BEM-based rotor aerodynamic codes. At each time step for each concentric annulus, a BEM-based method equates the blade loads, computed by the Blade Element part, with the wake momentum deficit, formulated in terms of $\overline{\vec{V}}_{ann}$ at the rotor plane and computed by the Momentum part, as discussed in Section 2.1.2.

The a_{ann}- and a'_{ann}-distributions in the rotor plane, shown in Figure 8.5, appear to be nearly axisymmetric for both the axial and the yawed flow conditions. The inverse vortex wake model results hence confirm the conclusions drawn from the a_{ann}-distribution at $z/R_t = 5.83 \cdot 10^{-2}$ that is obtained directly

174
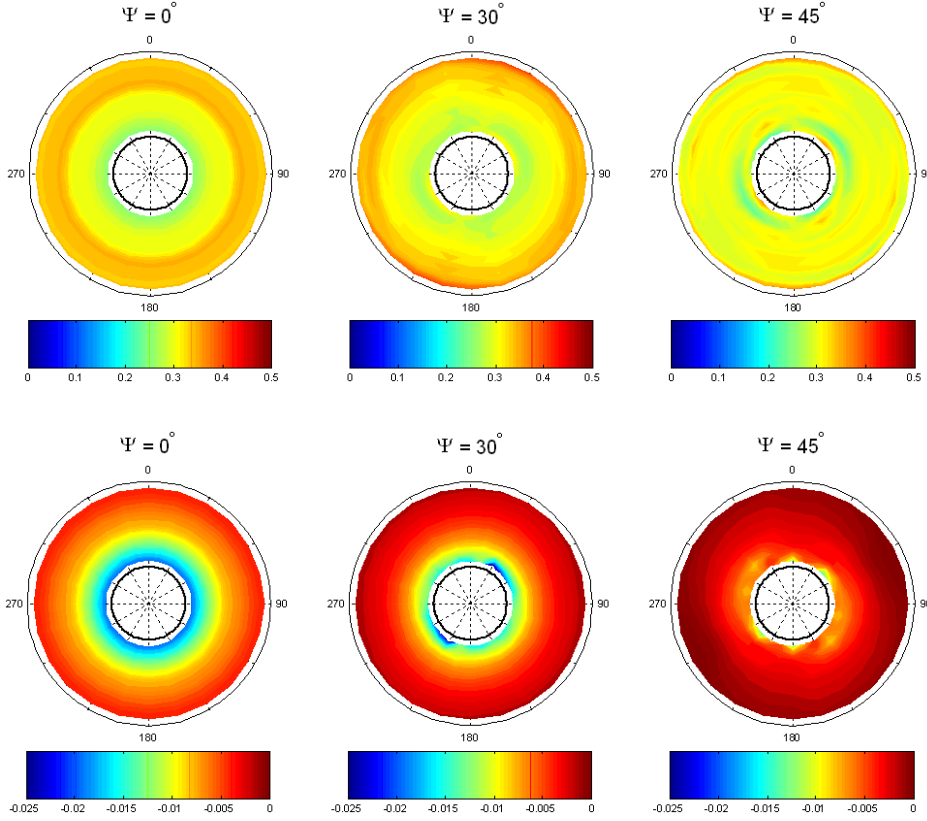
Figure 8.5: a_{ann}-distribution (top row) and a'_{ann}-distribution (bottom row) in the rotor plane for all three cases. A $(r/R_t, \theta)$-point refers to an annular circle with radius r/R_r for the blade at $\theta_b = \theta$.

from the near-wake measurements, see Figure 6.8. Yaw misalignment only introduces minor asymmetry. For an annular ring at a given radial coordinate r/R_t, a_{ann} and a'_{ann} thus are quasi-steady during a rotational cycle.

The annular averaged inflow does not reveal the flow conditions experienced by a blade section during its rotational cycle. Blade flow conditions should be assessed from cycle averaged and lifting line inflow instead. The relevance of studying blade flow conditions is rooted in the use of airfoil models within rotor aerodynamics codes; both BEM-based and vortex wake method employ airfoil models that require blade inflow conditions to compute blade loads.

The inflow asymmetry introduced by yaw misalignment can clearly be seen by the distributions of the cycle averaged and lifting line induction factors, shown in Figures 8.6 and 8.7 respectively. The asymmetric a- and a'-

175
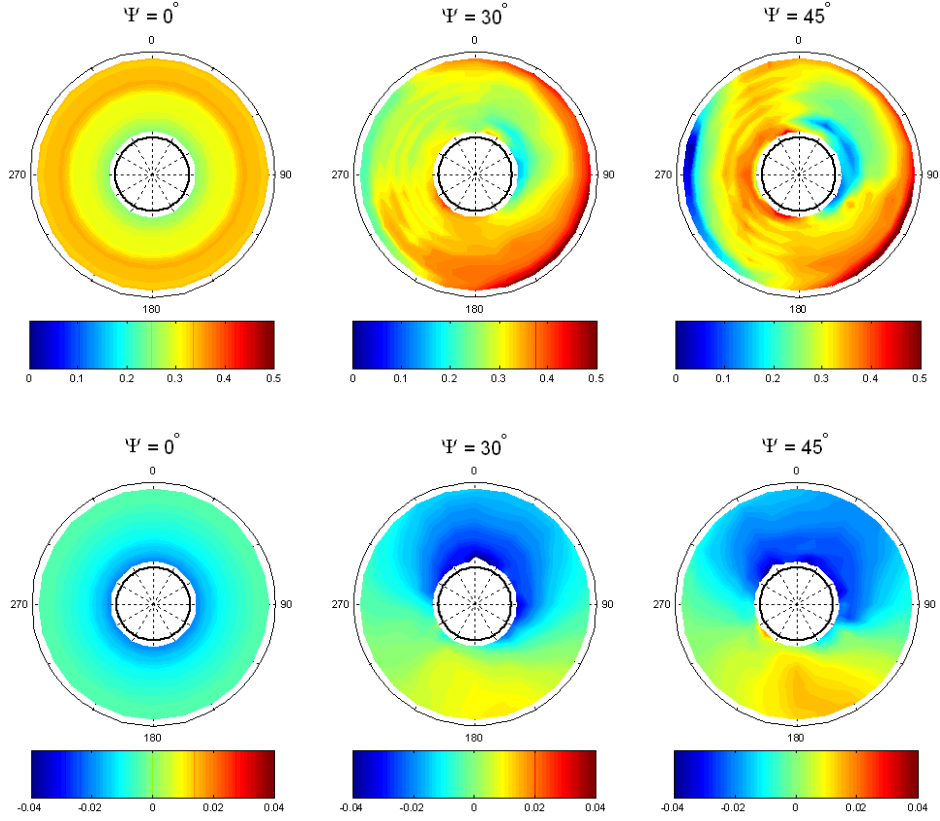
Figure 8.6: a_{cycle}-distribution (top row) and a'_{cycle}-distribution (bottom row) in the rotor plane for all three cases.

distributions for a rotor subject to yaw illustrate that the induced flow velocity at a blade section varies during the rotational cycle. The discussion of the flow phenomena governing the cyclic unsteadiness of the blade inflow is left for Section 8.2.2. It can already be concluded however that the distributions of the cycle averaged and lifting line inflow are similar. Furthermore, the trends observed in the inflow at the rotor plane derived with the inverse vortex wake model are comparable to those found from the near-wake measurements at $z/R_t = 0.0583$, compare Figures 8.6 and 8.7 with Figures 6.9 and 6.10.

With the rotor subject to yaw, the annular averaged inflow thus differs from the inflow locally at the blade for each section along the blade span, throughout the rotational cycle. The annular averaged inflow computed by the Momentum part of BEM-based methods is hence generally corrected for the unsteadiness resulting from yawed flow to derive the inflow at the blade that is required by the Blade Element part, refer to Section 2.1.2.

176
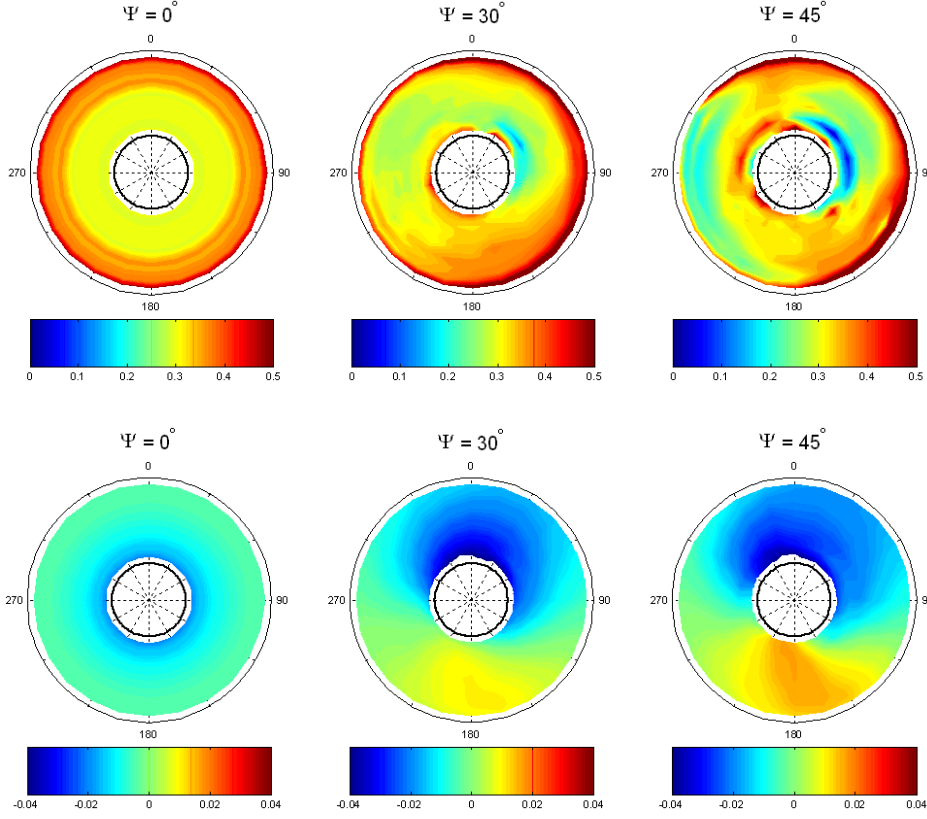
Figure 8.7: a_{rel}-distribution (top row) and a'_{rel}-distribution (bottom row) at the lifting line during a rotational cycle, for all three cases.

For the two yawed flow condition considered, the corrections to arrive at a_{rel} and a'_{rel} from a_{ann} and a'_{ann}, respectively, are readily available since a_{rel}, a'_{rel}, a_{ann} and a'_{ann} are derived with the inverse vortex wake mode. The correction terms in the axial and tangential directions are hence given by $(a_{rel} - a_{ann})$ and $(a'_{rel} - a'_{ann})$, respectively, see Figures 8.8 to 8.11.

The variation of the axial correction term is dictated by the a_{rel}-term, the a_{ann}-term mainly affects the mean level of the axial correction term. This observation also holds for the tangential correction term.

The trends observed with the axial correction term $(a_{rel} - a_{ann})$ depend on the blade spanwise section, see the right plots of Figures 8.8 and 8.9. For a given radial station, the two yawed flow cases yield similar trends, whilst the amplitude increases with larger yaw angle. Only for the most outboard section, at $r/R_t = 0.85$, a sinusoidal distribution is observed with a maximum at the downwind side near $\theta_b = 90°$ and a minimum at the upwind side near

177

Figure 8.8: a_{rel} (left plot) and $(a_{rel} - a_{ann})$ (right plot) versus θ_b at blade sections with $r/R_t = 0.45$, 0.65, 0.85 for the $\Psi = 30°$-case.

Figure 8.9: Idem as Figure 8.8, but then for the $\Psi = \mathbf{45°}$-case.

Figure 8.10: a'_{rel} (left plot) and $(a'_{rel} - a'_{ann})$ (right plot) versus θ_b at blade sections with $r/R_t = 0.45$, 0.65, 0.85 for the $\Psi = 30°$-case.

Figure 8.11: Idem as Figure 8.10, but then for the $\Psi = \mathbf{45°}$-case.
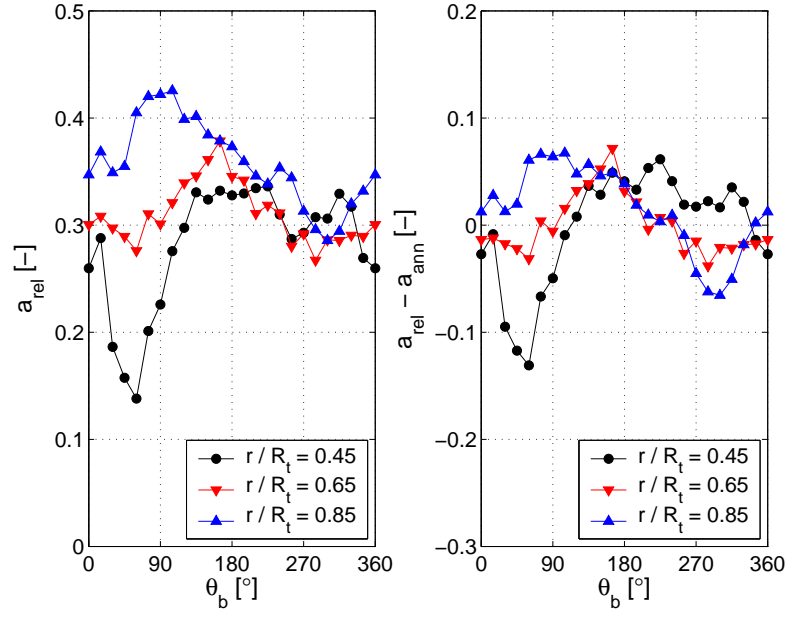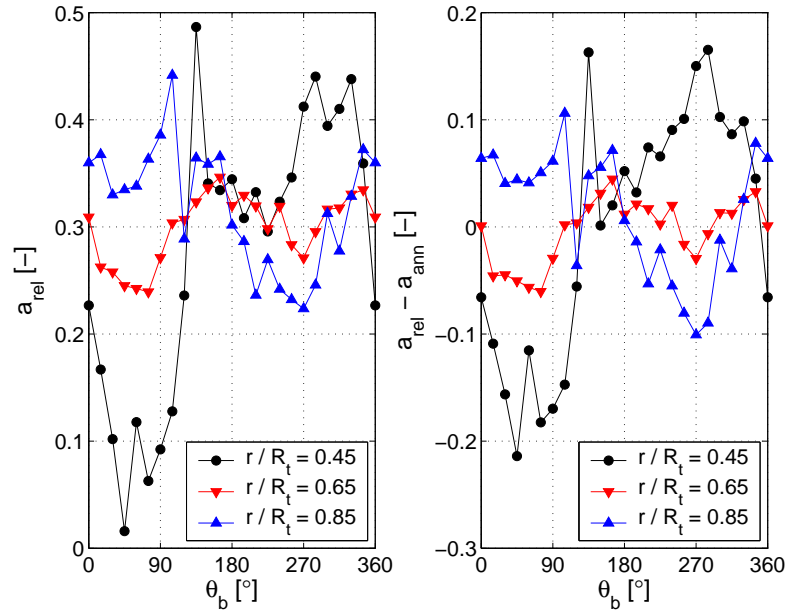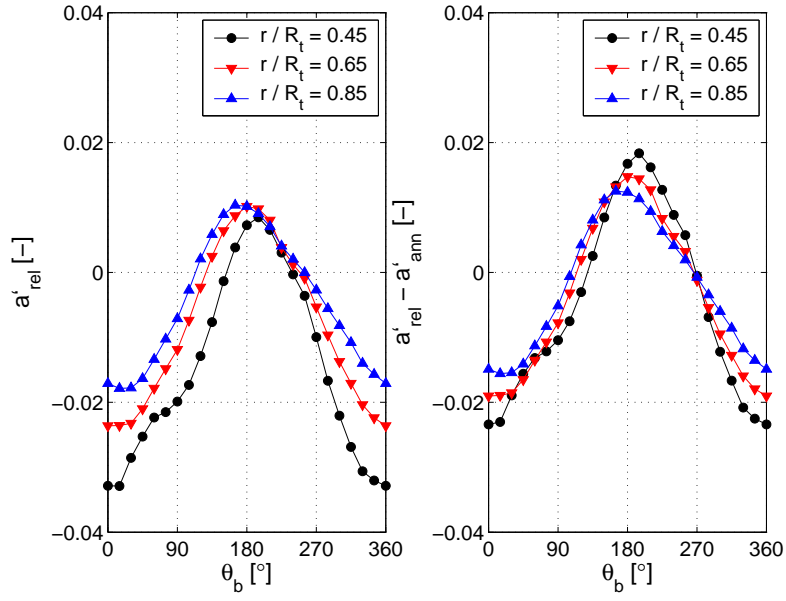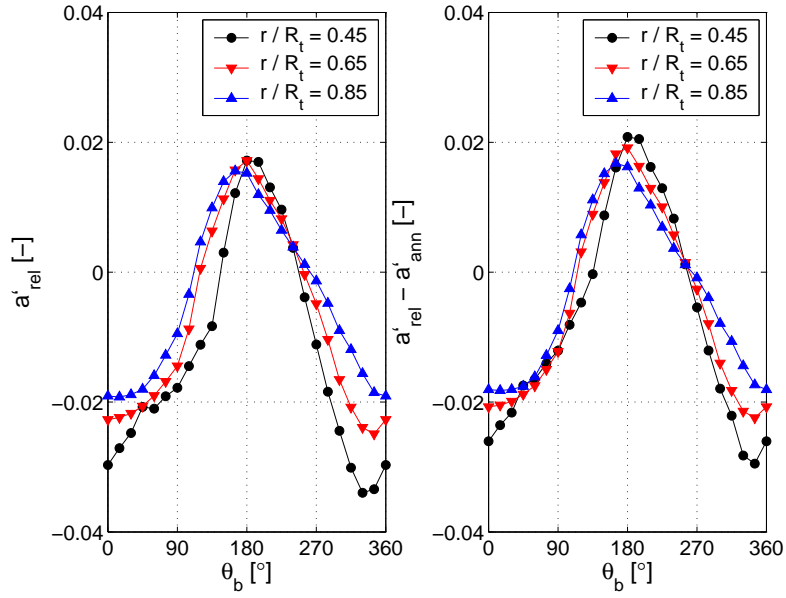
179

$\theta_b = 270°$, as predicted by the Glauert type models.

For the most inboard section, at $r/R_t = 0.45$, a minimum occurs in the downstream region, near $\theta_b = 90°$. The $\Psi = 45°$-case even displays a sinusoidal distribution, $180°$ out-of-phase with that at $r/R_t = 0.85$. The trends seen at $r/R_t = 0.45$ result from root vortex effects, as will be shown in Section 8.2.2. Note that the axial correction terms derived with the inverse vortex wake model are similar to those computed by Snel [176] using a simplified vortex wake model that includes root and tip vorticity only.

The tangential correction term $(a'_{rel} - a'_{ann})$ shows a sinusoidal distribution that is similar for all spanwise blade sections, with maxima near $\theta_b = 180°$ and minima near $\theta_b = 0°$. The amplitudes are larger for increasing Ψ.

It must be noted that the correction terms presented here are in principle valid only for the TUDelft rotor subject to the two yawed flow cases studied. The construction of an empirical correction model for use within a general BEM-based model to predict the loads on a rotor subject to yaw would require analysis of more cases with C_T- and Ψ-variations, preferably for several rotor models. As shown here, the inverse vortex wake model could be a suitable tool to derive the inflow at the rotor plane.

8.2.2 Wake circulation contributions to the lifting line inflow

The induced velocity is the vectorial summation of all vorticity contributions. The inverse vortex wake model enables the quantification of the contribution from each individual vortex segment to the induced velocity at any point in the flow domain. Vortex segment contributions are subsequently combined to form contributions from the bound vortex, the tip vortex, the root vortex, the trailed vortex sheet and the shed vortex sheet, in accordance with the model 'building blocks' discussed in Section 7.2.2. Equation 6.7 for a can hence be rewritten to

$$a = 1 - \frac{W_0 cos\Psi + V_{z_{bound}} + V_{z_{tip}} + V_{z_{root}} + V_{z_{sheet-trailed}} + V_{z_{sheet-shed}}}{W_0 cos\Psi}, \quad (8.3)$$

with $V_{z_{bound}}$ the axial flow velocity induced by the bound vortex etcetera, resulting in

$$a = a_{bound} + a_{tip} + a_{root} + a_{sheet-trailed} + a_{sheet-shed}, \quad (8.4)$$

with a_{bound} the axial induction factor resulting from the bound vortex, given by $a_{bound} = -V_{z_{bound}}/W_0 cos\Psi$, etcetera. An expression similar to Equation [8.4] can readily be derived for a'.

Here, the induced velocity at the lifting line is studied. The contribu-

tion to the induced velocity from the bound vortices thus is ignored [1]. The axial and tangential induction factors resulting from the tip and root vortices are given in Figures 8.12 and 8.13, respectively. As regards the vortex sheet, only the axial induction factor resulting from the trailed vortex sheet $a_{rel,sheet-trailed}$ contributes substantially, see Figure 8.14. The contributions from $a_{rel,sheet-shed}$, $a'_{rel,sheet-trailed}$ and $a'_{rel,sheet-shed}$ to a_{rel} and a'_{rel} are negligible and are hence not plotted. Note that the a_{rel}-range is set to 0.5 for each plot, enabling mutual comparison of all terms contributing to a_{rel}. For the same reason, the a'_{rel}-range is set to 0.12 throughout.

Figure 8.12: Tip vortex contribution to the total induction factor at the lifting line during a blade cycle a_{tip} (top row) and a'_{tip} (bottom row).

---

[1]In principle, only the contribution from the vortex element at the point of interest should be ignored. For the *two*-bladed rotor model currently studied, with blades $180°$ apart, all bound vortex segments from the two blades are located on a straight line; with the point of interest positioned at that line, the contribution from all bound vortex segments can hence be ignored.

The skewed tip vortices associated with yaw misalignment induce an approximately sinusoidal $a_{rel,tip}$-pattern for a blade section during the rotational cycle [2], with the maximum located downstream at $\theta_b \approx 90°$ and the minimum located upstream at $\theta_b \approx 270°$, see Figure 8.12. The a_{rel}-distribution in the outboard region is governed by tip vortex effects, as can be concluded from the agreement between a_{rel}- and $a_{rel,tip}$-trends, compare Figures 8.7 and 8.12. Recall from Section 6.3.1 that skewed tip vortices have already been held responsible for the sinusoidal a_{cycle}-distribution in the outboard region that is derived from direct assessment of the near-wake measurements. In contrast to the direct assessment however, the inverse vortex wake model allows decomposition of the induced velocity, thereby clearly identifying the causes for the observed trends.
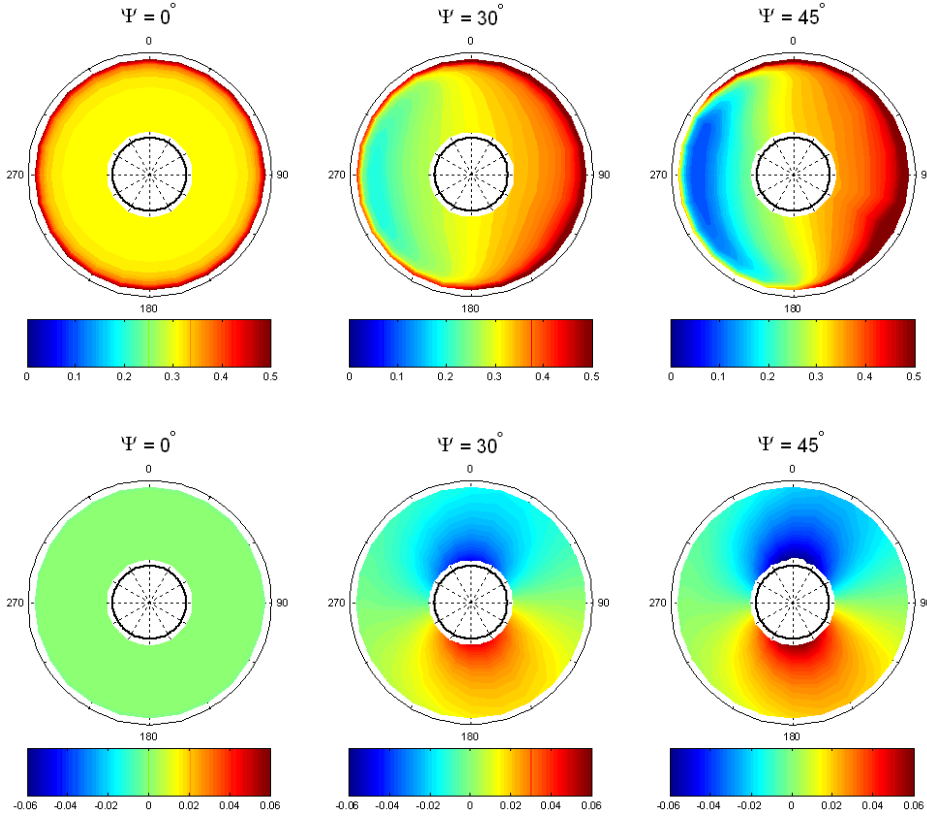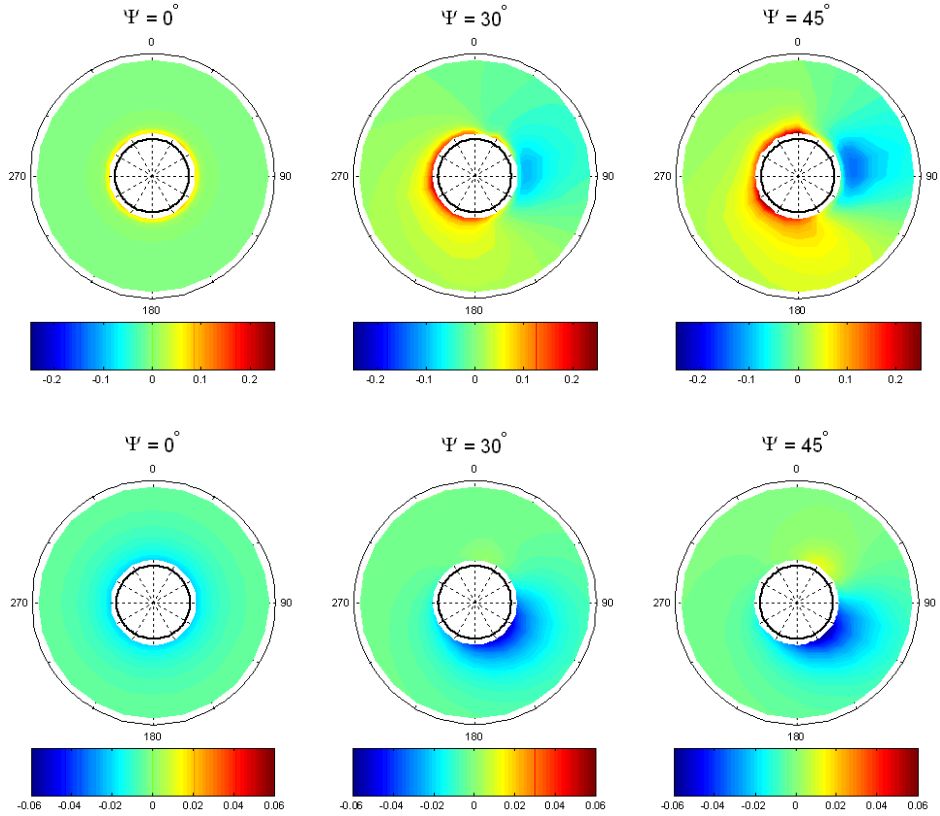

Figure 8.13: Root vortex contribution to the total induction factor at the lifting line during a blade cycle a_{root} (top row) and a'_{root} (bottom row).

---

[2]Ergo the agreement with the sinusoidal Glauert inflow correction model [60] that is based on smoke visualizations of fully rolled-up tip vortices for a helicopter in forward flight.

With the rotor subject to yaw, a blade section also experiences a sinusoidal $a'_{rel,tip}$-variation during the rotational cycle, as a result of the skewed tip vortices. The $a'_{rel,tip}$-maxima and -minima are located at $\theta_b \approx 180°$ and $\theta_b \approx 0°$, respectively, hence trailing the $a_{rel,tip}$-extremes by approximately $90°$. In contrast to a_{rel} that is dominated by tip vortex effects in the outboard region only, $a'_{rel,tip}$ governs a'_{rel} in the whole rotor plane, compare Figures 8.7 and 8.12.

The skewed root vortices clearly induce negative $a_{rel,root}$, hence accelerate the blade flow in the downstream direction, for the inboard sections of the blade during the downstream phase of its rotational cycle, see Figure 8.13. The $a_{rel,root}$-distributions explain the local a_{rel}-reduction in the inboard, downstream region. Furthermore, they confirm numerical studies by e.g. Øye [136] and Snel [176] that acknowledge the skewed root vortex effect using simplified vortex wake models, recall Section 6.3.1. Note that the negative $a_{rel,root}$ for the inboard sections of the blade when oriented downstream results in a destabilizing contribution to the yawing moment. A secondary skewed root vortex effect is the positive $a_{rel,root}$ for the inboard section of the blade when oriented upstream.

In contrast to $a'_{rel,tip}$, the skewed root vortex contribution to a' is concentrated in the inboard, downstream region, compare Figures 8.12 and 8.13. The difference is explained with the definition of a', given by Equation 2.29; whereas for $a'_{rel,tip}$, both the denominator, Ωr, and the numerator, $-V_{\theta_{tip}}$, decrease when going inboard from the tip, for $a'_{rel,root}$, the denominator increases while the numerator decreases when going outboard from the root.
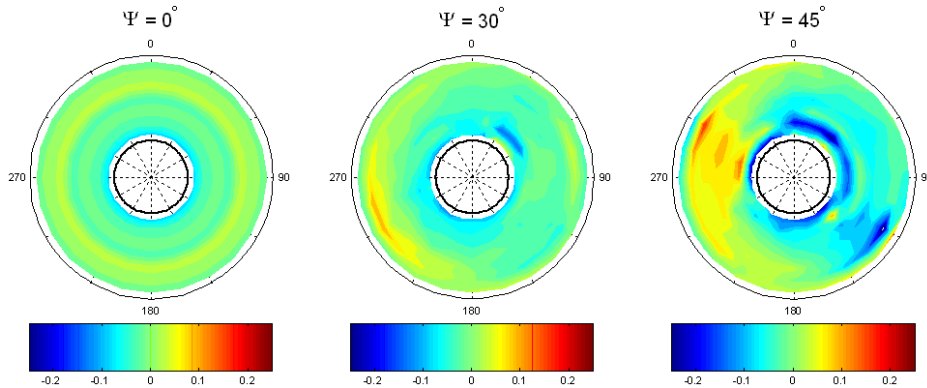
Figure 8.14: Trailed vortex sheet contribution to the total induction factor at the lifting line during a blade cycle $a_{sheet-trailed}$.

The yaw misalignment effects associated with the trailed vortex sheet can be considered a combination of the skewed tip and root effects, compare Figure

183
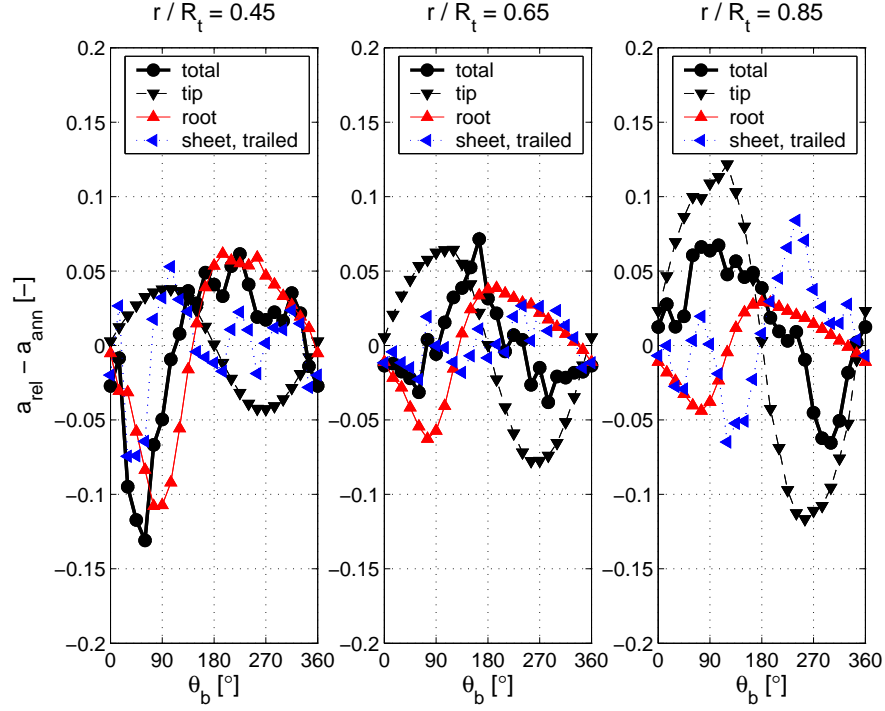
Figure 8.15: Contribution to $(a_{rel} - a_{ann})$ from the tip vortex; $(a_{rel,tip} - a_{ann,tip})$, the root vortex: $(a_{rel,root} - a_{ann,root})$ and the trailed vortex sheet: $(a_{rel,sheet-trailed} - a_{ann,sheet-trailed})$ at blade sections with $r/R_t = 0.45$, 0.65, 0.85 for the $\Psi = 30°$-case.

8.14 with Figures 8.12 and 8.13, since in general vortices with the circulation direction of both the tip and the root vortex trail the blade at a given instant. The tip effect shows from the positive $a_{rel,sheet-trailed}$ found at the outboard sections for the blade oriented upstream, wile the root effect appears through the negative $a_{rel,sheet-trailed}$ at the inboard sections for the blade oriented downstream. Note however that the sinusoidal variation of the velocity induced by the skewed tip vortices is absent.

To assess the influence of the various wake elements on the axial correction term $(a_{rel}-a_{ann})$, discussed in Section 8.2.1, the contributions $(a_{rel,tip}-a_{ann,tip})$, $(a_{rel,root}-a_{ann,root})$ and $(a_{rel,sheet-trailed}-a_{ann,sheet-trailed})$ are given in Figures 8.15 and 8.16. Here, $a_{ann,tip}$ is the annular averaged axial induction factor when only considering the flow velocity induced by the tip vortex etcetera.

The correction term plots confirm the discussion that is based on the contour plots given in Figures 8.12 to 8.14; the skewed tip vortex yields an ap-

184
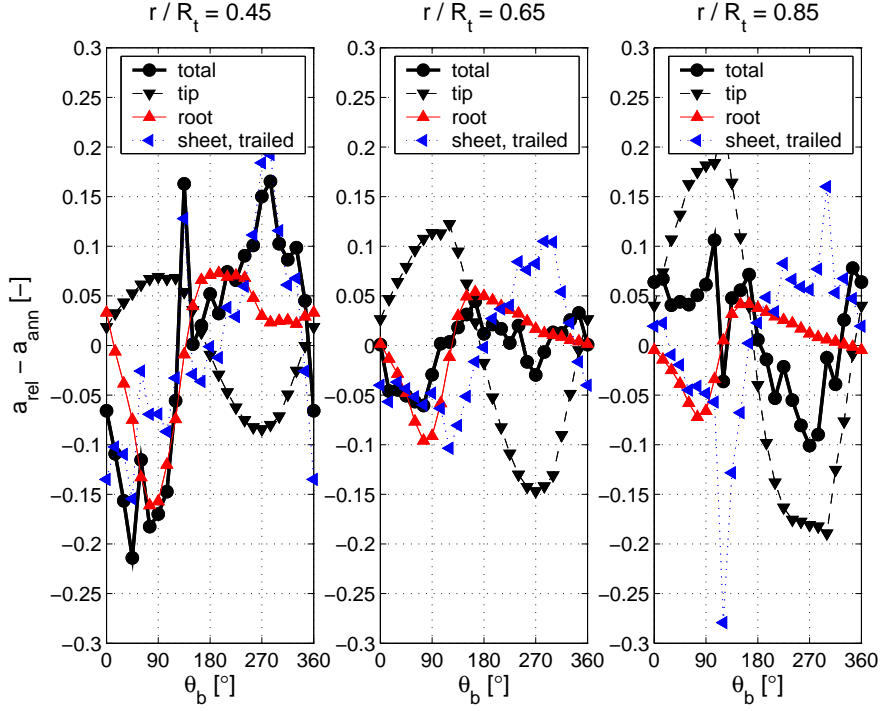
Figure 8.16: Idem as Figure 8.15, but then for the $\Psi = \mathbf{45}^\circ$-case.

proximately sinusoidal contribution with maxima and minima at $\theta_b \approx 90^\circ$ and $\theta_b \approx 270^\circ$ that increase in amplitude towards the tip. The skewed root vortices also induce a $1P$-cyclic variation. A sinusoidal shape is not found however; minima and maxima are located at $\theta_b \approx 90^\circ$ and $\theta_b \approx 180^\circ$ respectively and, especially for the inboard sections, are not of comparable amplitude.

The availability of all relevant contributions to the correction term in a single plot, in contrast to contour plots of each individual contribution, enables an improved assessment of the contribution from the trailed vortex sheet. Instead of a combination of both tip and root vortex effects, the trends seen for the trailed vortex sheet appear to correlate best with the root vortex effects alone.

The breakdown of the axial correction term $(a_{rel}-a_{ann})$ into its constituting components shows the significance of skewed root vortex effects. Understanding of the physical characteristics of the root vortex can be obtained experimentally. Root vortex measurements for wind turbine rotors are rare though; to the author's knowledge, only Ebert and Wood [50] study root vortices for a rotor in axial flow conditions and no root vortex measurements have been

185

published at all for yawed flow conditions. Conducting detailed root vortex measurements, in axial and yawed flow, would thus be recommendable.

Furthermore, the decomposition of $(a_{rel} - a_{ann})$ could serve as a basis to develop empirical inflow correction models for use in BEM-based codes. The model should accurately represent both skewed tip and root vortex effects to obtain representative inflow corrections along the entire blade span.

8.2.3 Blade loads

When computing the blade loads from the Γ_b-distribution shown in Figure 8.4, it must be realized that the Kutta-Joukowsky law [8.1] holds for steady flow conditions only. To determine the unsteady blade loads associated with yawed flow conditions, the Kutta-Joukowsky law is modified [101],

$$\vec{L} = \rho \left[\vec{V}_{rel} \times \vec{\Gamma}_b + \frac{\partial \Gamma_b}{\partial t} \, d\vec{r} \times \vec{c} \right], \qquad (8.5)$$

Here, the first term concerns the lift due to the instantaneous circulation and is hence called circulatory lift. The second term concerns the lift from fluid acceleration and is known as non-circulatory lift. The circulatory lift is oriented normal to the relative flow velocity, whilst the non-circulatory lift acts normal to the chord line; $\vec{c}$ is the chord line vector, pointing from the leading to the trailing edge, and $d\vec{r}$ is a vector of unit length along the lifting line, pointing outboard. Once L is known, c_l, F_z and F_θ can subsequently be determined. It must be noted that the circulatory lift appears to be dominant over the non-circulatory lift for the yawed flow cases considered at present [3].

The asymmetric α-, c_l-, F_z- and F_θ-contours shown in Figures 8.17 to 8.20 clearly illustrate the periodically unsteady flow conditions at the lifting line resulting from yaw misalignment. Furthermore, the results found for the $\Psi = 30°$-case and the $\Psi = 45°$-case yield similar trends. Application of the inverse vortex wake model to the three selected operating conditions hence allows a consistent view of yaw misalignment effects on the flow conditions in the rotor plane at high λ-setting, $\lambda = 8$, for a baseline axial flow condition near $c_{P_{max}}$.

For wind tunnel measurements on a NACA0012 airfoil at $Re = 1.5 \cdot 10^5$, which is within the Re-range for the present near-wake rotor measurements, stall is observed at $\alpha_{stall} = 10.6°$, see Figure 3.5. The two yawed flow cases considered here result in $\alpha < \alpha_{stall}$ along the span during the entire rotational cycle, see Figure 8.17. The rotor blades are hence not expected to have undergone substantial dynamic stall events during the near-wake measurements

---

[3]The importance of the non-circulatory lift increases with larger reduced frequency k. For both yawed flow cases, $k_{0.7R} = 0.09$ is estimated, see Table 6.2. Only for $k \geq 0.2$, the non-circulatory lift starts to become the dominant term, according to Leishman [109].
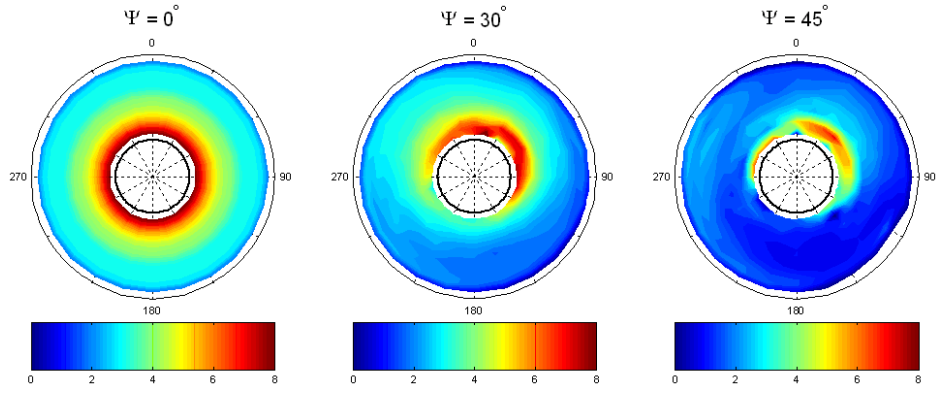
Figure 8.17: α-distribution at the lifting line during a rotational cycle for all three cases.
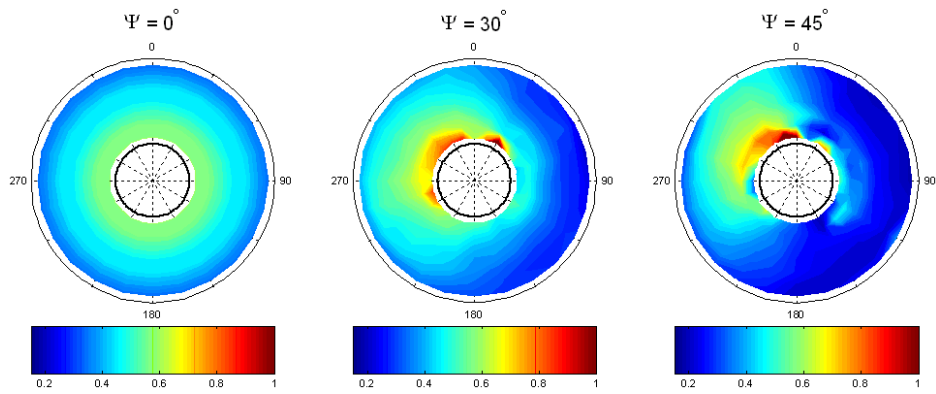
Figure 8.18: c_l-distribution at the lifting line during a rotational cycle for all three cases.
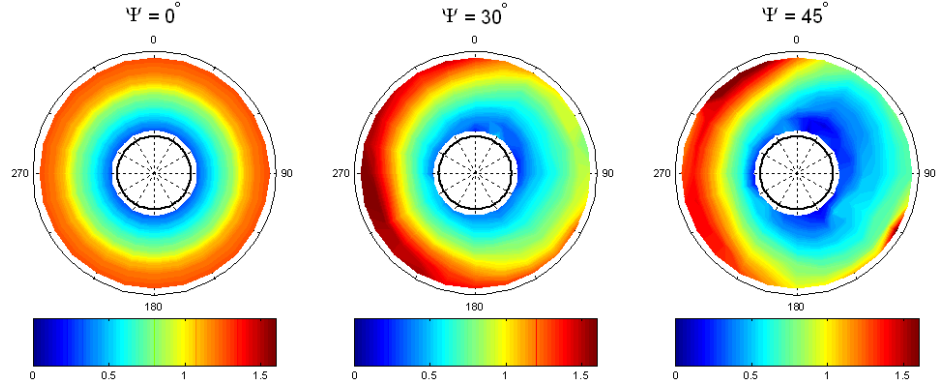
Figure 8.19: F_z-distribution at the lifting line during a rotational cycle for all three cases.
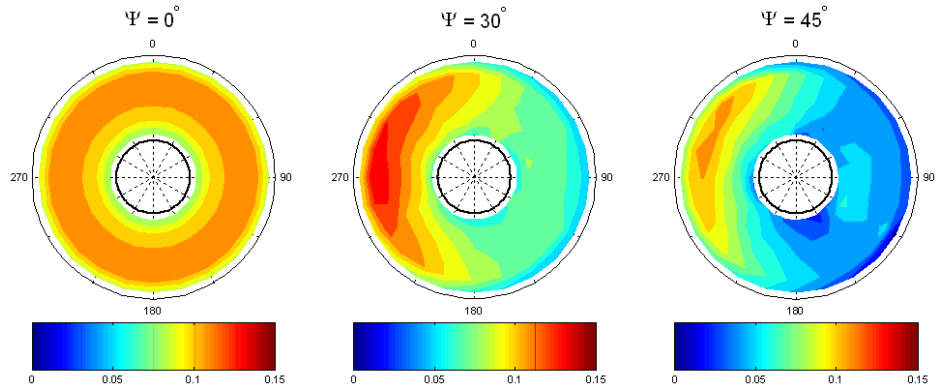
Figure 8.20: F_θ-distribution at the lifting line during a rotational cycle for all three cases.

that are currently analyzed with the inverse vortex wake model. The absence of dynamic stall should reduce the complexity of the inflow distribution in the rotor plane.
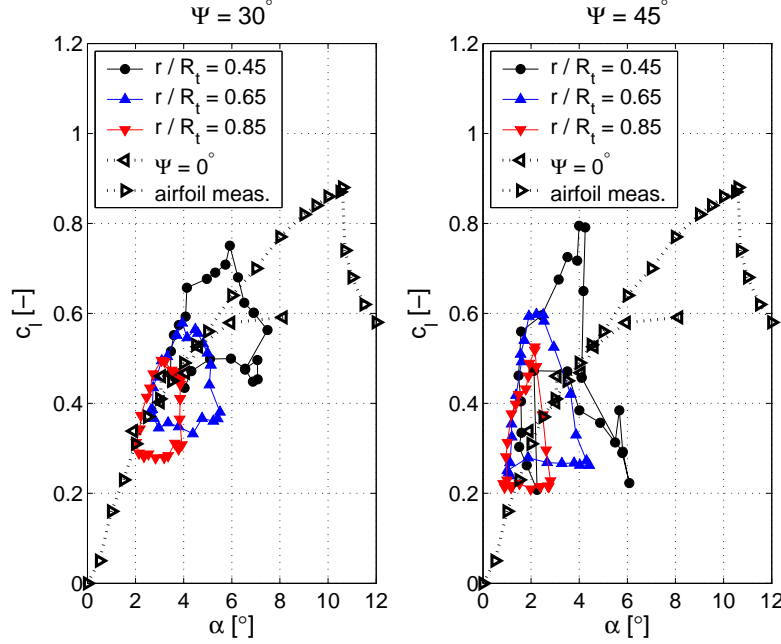
Figure 8.21: c_l versus α during a rotational cycle at radial stations $r/R_t = 0.45, 0.65, 0.85$ for the $\Psi = 30°$-case (left plot) and the $\Psi = 45°$-case (right plot). All hysteresis loops rotate clockwise.

The non-stalled flow conditions still yield lift hysteresis though, see Figure 8.21; the unsteady α observed at a given blade section causes an out-of-phase c_l-response. The hysteresis loops at all computed blade sections, for both yawed flow cases, rotate clockwise and are centered around the steady (α, c_l)-data.

The periodic unsteadiness of the rotor aerodynamics results in θ_b-dependent C_T and C_P that are derived from the loads on all blades. For the two-bladed TUDelft rotor, the phase difference between the blades is $\Delta\theta = 180°$. At given $\theta_b = \theta_{b_1}$, the spanwise load distribution of the first blade is hence given in Figures 8.19 and 8.20 for $\theta = \theta_{b_1}$, whilst that of the second blade is found for $\theta = (\theta_{b_1} + 180°)\, mod\, 360°$. Having determined the load distribution of both blades at θ_{b_1}, the procedure discussed in Section 8.1.2 is applied to arrive at $C_T(\theta_{b_1})$ and $C_P(\theta_{b_1})$, see Figure 8.22. The two blades that are 180° out-of-phase yield the 2P-frequency observed for the C_T- and C_P-signals. Subsequent

189

averaging over the rotational cycle yields the values given in Table 8.2.

Table 8.2: Computed and measured C_T and C_P for both yawed flow cases.

	$\Psi = 30°$		$\Psi = 45°$	
	C_T	C_P	C_T	C_P
Inverse vortex wake model	0.74	0.41	0.63	0.29
Rotor measurements (Section 6.1)	0.70 ± 0.07	-	0.53 ± 0.06	-

For the $\Psi = 30°$-case, the cycle averaged C_T derived from the inverse vortex wake model is within the 95% confidence uncertainty limit of the measured C_T. The computations furthermore learn that C_T is nearly constant during a rotational cycle. For the $\Psi = 45°$-case, the difference observed between measured and computed C_T is significant, suggesting that the inverse vortex wake model should be improved for this case. Recall that of the three cases considered, RR is highest for the $\Psi = 45°$-case. As a result of a higher degree of unsteadiness with larger yaw misalignment, the $\Psi = 45°$-case yields larger C_T-variations during a rotational cycle than the $\Psi = 30°$-case. Not only the blades are hence dynamically loaded for the $\Psi = 45°$-case, the unsteady C_T induces a dynamic load on the entire rotor structure.

C_P is not measured for the yawed flow cases. Consistent with the axial flow case however, the 'true' C_P is expected to be overestimated by the computational results, since viscous drag is ignored by the inverse vortex wake model.

8.3   Conclusions

The near-wake measurements of the TUDelft rotor lack recordings of the inflow at the rotor plane and blade loads. Application of the inverse vortex wake model to the near-wake measurements enables the corresponding inflow at the rotor plane and the blades loads to be estimated instead.

The derivation of the angle of attack α from the inverse vortex wake model is of particular importance, because of the difficulty to determine α from measurements and the dependence on α of rotor aerodynamics models. For the baseline axial flow condition near $c_{P_{max}}$ presently considered, with $\lambda = 7.9$, $\beta_{pitch} = 2.0°$ yielding $C_T = 0.78$, the spanwise α-distribution derived at the lifting line closely corresponds to that derived from an annular averaged approach. Furthermore, the effect of the azimuthal induction factor on α is negligible along the entire blade span. Both observations are attributed to the high λ-setting of the two-bladed rotor.
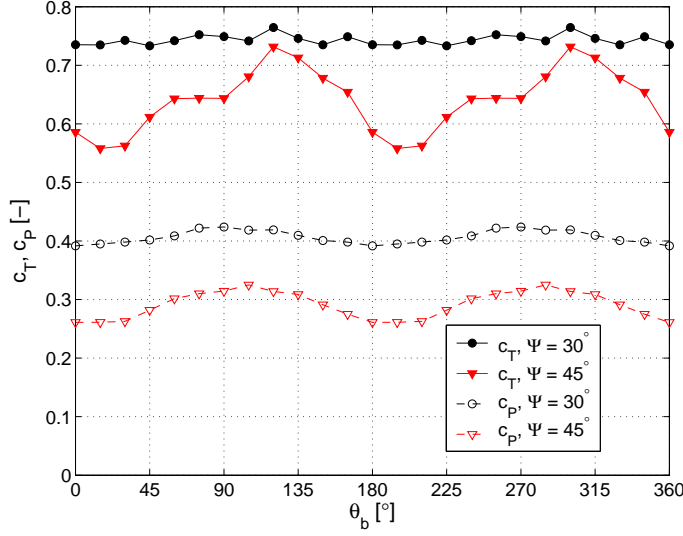
Figure 8.22: Computed C_T & C_P during a rotation for both yawed flow cases.

The Kutta-Joukowsky law is applied to the results derived with the inverse vortex wake model to find the lift coefficient c_l. An airfoil model based on α is hence not required to determine c_l. For the axial flow condition, general agreement is found with the spanwise c_l-distribution found from application of airfoil (α, c_l)-measurements to α derived with the inverse vortex wake model. The flow on the rotating blade generally exhibits two-dimensional behavior for the operating condition studied. The spanwise α- and c_l-distributions derived with the inverse vortex wake model furthermore confirm the suggestion from the direct assessment of the near-wake measurements that the blade flow is non-stalled, as is expected for the operating condition near $c_{P_{max}}$.

The baseline axial flow condition is set to a nonzero yaw angle Ψ to arrive at two yawed flow conditions: $(\Psi, \lambda, \beta_{pitch}) = (30°, 8.0, 2.0°)$ and $(45°, 8.1, 2.0°)$ that yield 0.70 and 0.53, respectively.

The spanwise α-distribution at the blade lifting line remains below the static, two-dimensional stall angle during the entire rotational cycle for both yawed flow conditions. Substantial dynamic stall events are hence not antici-pated. To compute c_l for the unsteady blade flow conditions associated with yaw, the Kutta-Joukowsky law is modified to account for non-circulatory lift. The unsteady blade flow conditions yield lift hysteresis. Consistent with the conclusion drawn from the α-distribution, no substantial dynamic stall regions are observed for the lift hysteresis loops. The absence of dynamic stall should reduce the complexity of the inflow distribution at the rotor plane.

Whereas the annular averaged inflow at the rotor plane is quasi-steady during a rotational cycle for the yawed flow conditions, the inflow at the lifting line is cyclically unsteady. The difference between the annular averaged inflow and the inflow locally at the blade can be considered a correction term for the annular averaged axial and tangential induction factors that are computed with the Momentum part of a BEM-based code.

The phenomena governing the unsteady inflow can be assessed with the inverse vortex wake model, since the induced velocity at the lifting line can be decomposed into contributions from the tip vortex, root vortex and the vortex sheet.

Skewed tip vortices induce a sinusoidal variation of the axial induction factor locally at a blade section a_{rel}, the amplitude of which increases towards the tip. Maxima and minima are found for the blade in the downstream and upstream position, respectively. Skewed root vortices induce a local a_{rel}-minimum for the blade in the downstream position and a local a_{rel}-maximum near the transition between the downstream and upstream region; the pattern hence is not of a sinusoidal character. The amplitude of the extremes increases towards the root. The a_{rel}-pattern induced by the trailed vortex sheets is roughly similar to that induced by the root vortices.

Decomposition of the axial correction term reveals that the effects from both the skewed tip and root vortices should be included to obtain a representative inflow correction across the blade span. The corrections derived with the inverse vortex wake model could serve as the basis for an empirical inflow correction model. It must be noted that only two operating conditions, on a single rotor model, are available. Additional analysis of more operating conditions, with Ψ- and C_T-variations, on several rotor models, should increase the confidence in the empirical correction model.

Chapter 9

Comparison of rotor aerodynamics models with experiments

Rotor measurements generally have two objectives: to enhance understanding of flow phenomena governing the aerodynamics of the rotor and to serve as a base for comparison with and construction of aerodynamic models. The associated requirement for controlled, known operating conditions has led to a trend to move from field tests on full-scale turbines to wind tunnel measurements on scaled model rotors, recall Chapter 2.

The near-wake experiments discussed in this thesis fit within the tendency of going back-to-basics in the wind tunnel. Having analyzed the flow physics in Chapters 5, 6 and 8, in this Section the focus is on the comparison of measurements with rotor aerodynamics models. The validity of the BEM approach for rotors subject to yaw is discussed in Section 9.1 by assessing the Glauert momentum equation, where both blade loads and wake momentum deficit are derived from the inverse vortex wake model. The implications of dynamic stall model selection on rotor aerodynamics model predictions are assessed in Section 9.2; the actuator line model, formulated with either the Øye or the Beddoes-Leishman dynamic stall model, is compared with the near-wake measurements and the inflow at the rotor plane and blade loads that are derived from the inverse vortex wake model.

The model rotor suffers from lack of similitude[1] with full-scale turbines; Re is substantially smaller in the wind tunnel than in the field. The rotor aerodynamics models should hence employ airfoil models with appropriate Re to allow comparison with the measurements. The conclusions obtained from the comparisons should however be translated to the full-scale situation with

---

[1]similitude: geometric, kinematic and dynamic similarity, see Section 1.2.2.

due care.

Note that use of the near-wake measurements is not limited to researchers that are affiliated to the TUDelft; Gupta and Leishman [71] validate a free-vortex wake model using measurements of C_T and the tip vortex center locations, while Masson and Sibuet Watters [117] compare a moving actuator model with measurements of C_T, C_P and the near-wake flow velocity. Discussion hereof is outside of the scope of this thesis though.

9.1   Blade-Element Momentum method

The basis of a BEM method is formed by the Glauert momentum equation, given in Equation 2.13, which expresses the wake axial momentum deficit in terms of the inflow at the rotor [27, 86, 147]. Within a BEM model, the wake axial momentum deficit as given by the Glauert momentum model is equated to the rotor thrust found from the blade loads. The Glauert momentum relation reduces to theoretical equations for $\Psi = 0°$, $90°$ only and is assumed to hold for $0° < \Psi < 90°$ as well, recall the discussion in Section 2.1.1. Comparison
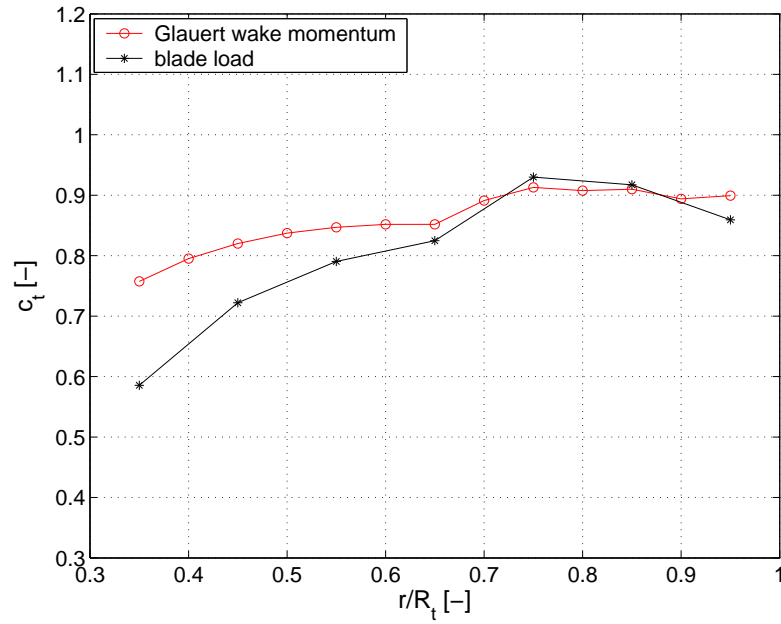
Figure 9.1: Sectional thrust coefficient c_t versus r/R_t for the axial flow condition in Table 6.2. c_t determined from blade loads: $*$ and derived from the inflow at the rotor plane using Glauert's momentum equation: $\circ$.
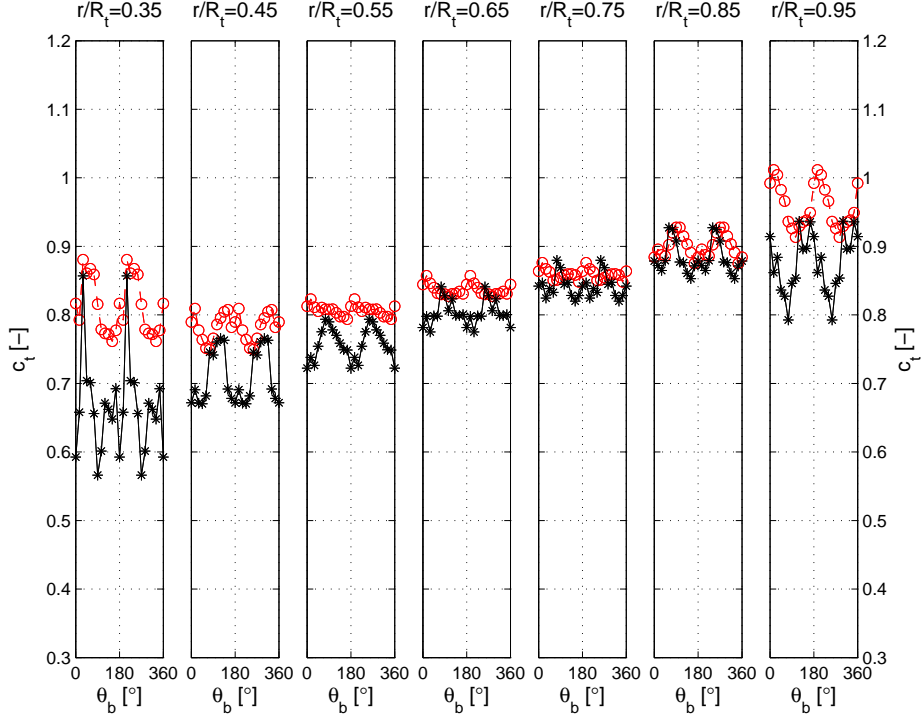
Figure 9.2: Sectional thrust coefficient c_t during a rotational cycle for a range of spanwise locations for the $\Psi = 30°$-case. c_t determined from blade loads: $*$ and derived from the inflow at the rotor plane using Glauert's momentum equation: $\circ$.

of the Glauert momentum equation with measurements across a range of yaw angles would enable this assumption, which essentially forms the foundation of BEM models, to be validated.

Measurements can only be used to assess the validity of the Glauert momentum equation, when both the experimental blade loads and inflow at the rotor plane are available. Through application of the inverse vortex wake model as a post-processing tool, the current wake experiments qualify for validation of the Glauert momentum equation. All three operating conditions for which the inverse vortex wake model has been constructed are analyzed, see Table 6.2 for the settings.

The Glauert momentum equation is validated per annulus; for each discrete blade azimuth position, the experimental sectional thrust coefficient c_t is determined, both from the blade loads and from the Glauert wake momentum deficit model. Note that the Glauert momentum model employs annular
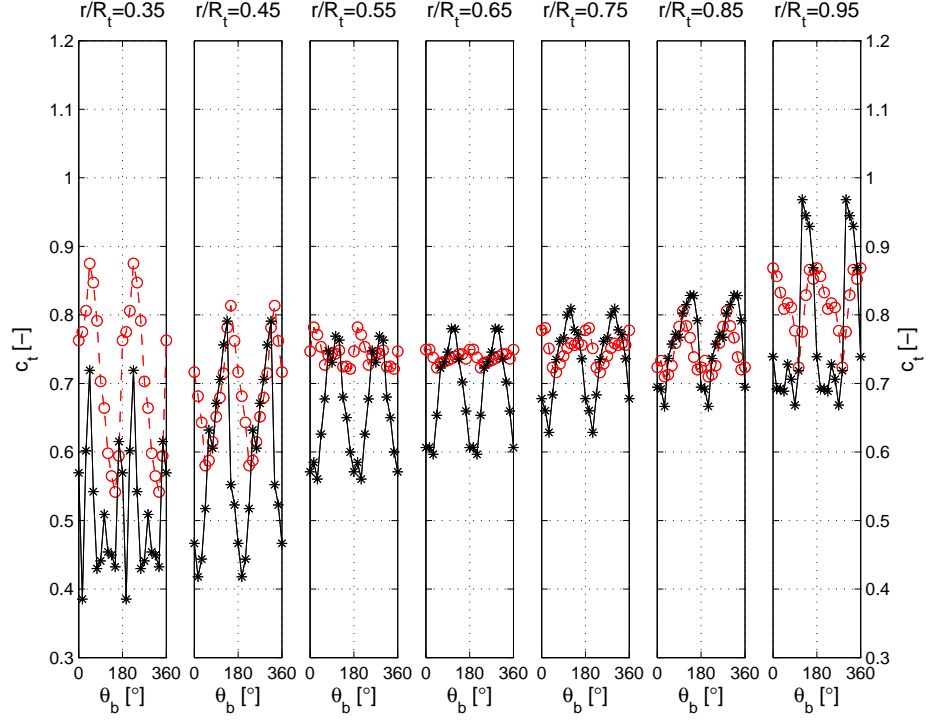
Figure 9.3: Idem as Figure 9.2, but then for the $\Psi = \mathbf{45}°$-case.

averaged inflow.

For the axial flow condition, where the Glauert relation reduces to the one-dimensional, inviscid momentum equation, c_t derived from blade loads corresponds with that found from the wake momentum deficit model, see Figure 9.1. Especially in the outboard regions, good agreement is observed. The selected axial flow condition hence can be modeled adequately with the Glauert momentum model, which is expected from the proximity of the operating condition to the C_P-optimum of the model rotor[2].

Whereas the axial flow condition considered can be assumed to result in a rotating stationary flow field, yawed flow conditions induce rotating unsteady flow. Consequently, the Glauert momentum equation at a given annulus is a function of θ_b. c_t derived from the Glauert wake momentum deficit model and that determined from the blade loads are given across the blade span during a full rotation in Figures 9.2 and 9.3 for the operating conditions with $\Psi = 30°$

---

[2]Note that the trends in c_t correspond with those of Figure 5.19, where blade loads and wake momentum deficit are derived from linear extrapolation of the near-wake measurements in combination with an airfoil model, instead of the inverse vortex wake model.
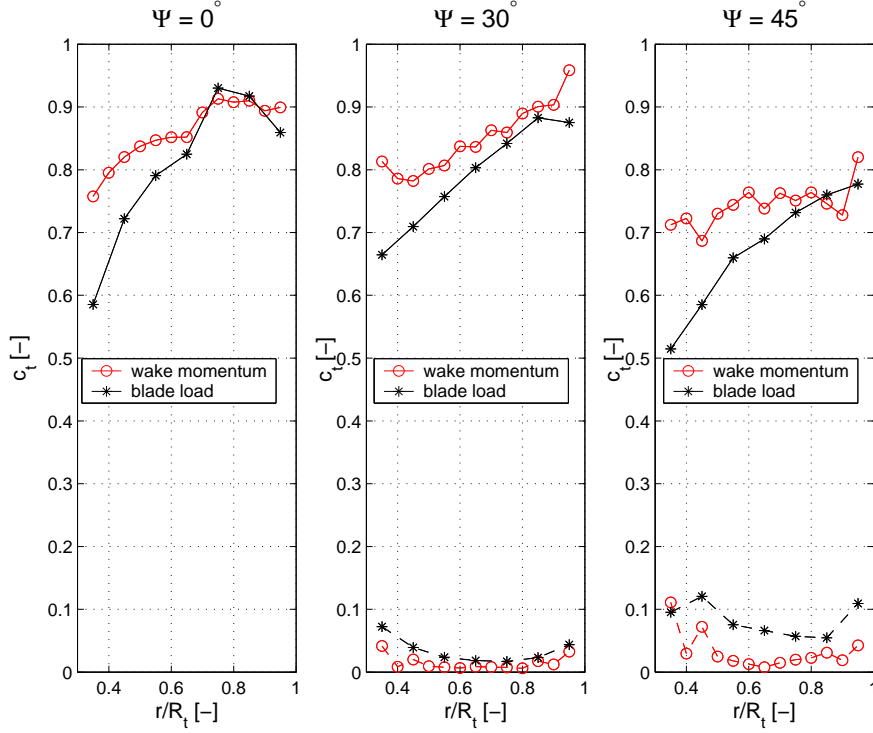
Figure 9.4: Sectional thrust coefficient c_t versus r/R_t for all three cases. Average (solid lines) and standard deviation (dashed lines) over a rotational cycle are given. Standard deviation here is a measure of cyclic unsteadiness in c_t.

and 45°, respectively. Cycle averaged results are given in Figure 9.4.

The unsteadiness in c_t increases with larger Ψ, as expected. For both yawed flow cases however, reasonable agreement is found, especially in the outboard regions. The wake axial momentum deficit of the two yawed flow conditions studied here, that both yield non-stalled blade flow as has been concluded in Section 8.2.3, can hence be modeled adequately with the Glauert momentum equation.

This result disputes that obtained by Sant [148, 147], who, *based on the same near-wake measurements*, concludes that the Glauert momentum equation has limited capability in modeling yawed flow conditions and consequently proposes a correction parameter. This paradox is hypothesized to result from the method used to arrive at the inflow in the rotor plane; in contrast to the physics-based, non-linear inverse vortex wake model used in the current study, Sant's analysis is based on linear extrapolation of the near-wake mea-

surements. Especially in yaw, linear extrapolation does not seem to do justice to the highly non-linear near-wake downstream development, as illustrated in Figures 6.8 and 6.9.

9.2   Actuator line method

Blade aerodynamics modeling is a major source of the generally large uncertainties of today's BEM and vortex wake models, refer e.g. to the discussion in Section 2.2.2 on the origins of the modeling uncertainties found with the NREL blind comparison. The effect of blade model selection on the uncertainty of rotor aerodynamics models cannot be assessed independently of the wake modeling contribution to the overall uncertainty, since the blade and wake models are coupled.

To focus on the uncertainty of the blade model, the uncertainty contribution of the wake model should be minimized. The contribution from the wake model to the overall uncertainty would be minimal when the wake would be modeled by the RANS equations instead of the wake models used with the BEM and vortex wake methods, most notably for unsteady, skewed wakes.

A rotor aerodynamics model that couples a blade model to a RANS model of the rotor wake is the actuator line method, introduced by Sørensen and Shen [186] and further developed by Mikkelsen [128]. The RANS equations govern the flow within a numerical domain that encompasses the rotor. Each rotor blade is represented by a line, named actuator line. The flow velocity relative to the actuator lines is determined and the corresponding blade forces, computed by a blade model, are introduced to the RANS equations as volume sources.

Two unsteady blade models are currently selected for use with the actuator line model; the Øye [135] and the Beddoes-Leishman [113, 114] dynamic stall models. Whilst the Øye model is relatively simple, mainly aiming to derive lift overshoot trends during dynamic stall, the Beddoes-Leishman model is more comprehensive, modeling a range of unsteady flow phenomena in order to derive the lift, drag and moment of an airfoil, not only during dynamic stall, but during unsteady conditions in general. For steady conditions, the Øye and the Beddoes-Leishman dynamic stall models presently reduce to the same static blade model that is derived from airfoil measurements.

The relevance of analyzing the Øye and Beddoes-Leisman dynamic stall models stems from their widespread use in wind turbine aero-elastic modeling and their representativeness for the range of complexity seen with semi-empirical dynamic stall modeling. The modeling results are compared mutually as well as to the near-wake measurements for both axial and yawed flow conditions. The comparison is aimed at improving the understanding of the

dependency of blade model uncertainty on the blade model selected and the operating condition considered.

The comparison for the axial flow conditions is given in Section 9.2.1. Predicted and measured yawed flow results, including a dynamic stall event, are compared in Section 9.2.2. The current focus hence is on the analysis of the results obtained with the actuator line model. Backgrounds on the actuator line model can be found in the appendices; the model concept and the numerical model used currently are discussed in Appendix C, whilst Appendix D concentrates on the airfoil models implemented in the actuator line code for the present study.

The work by Haans and Mikkelsen [72] forms the basis of the present discussion. Note that, where an older version of the inverse vortex wake model has been used in [72], the results discussed in this Section are derived with the latest version of the model, as defined in Chapter 7.

9.2.1 Axial flow comparison

The near-wake experiments in axial flow conditions are modeled with the actuator line method assuming rotating stationary flow and using static airfoil data measured at a single operating condition. The validity of this approach is assessed by comparison of computational with measured results. First however, a typical result is shown in Figure 9.5 to get a feeling for the capabilities of the actuator line model.

Rotor performance

To obtain an impression of the overall agreement between measurements and computations, the measured and computed rotor performance is compared in Figure 9.6. All computed C_T-values are within the 95% confidence measurement uncertainty bounds. The differences are thus insignificant at the 95% confidence level. Notwithstanding this conclusion, the actuator line model consistently under-predicts C_T at $\lambda \approx 6$, which could be related to stall delay effects in the blade root region that are not accounted for by the actuator line model. A stall delay model should be implemented with further studies to check this hypothesis. Further note the relatively large difference in C_T at $\lambda = 9.6$, $\beta_{pitch} = 0°$, that could be attributed to the violation of the modeling assumption of rotating stationary flow, since the measurements suggest that this setting, with $C_T = 0.97$, is on the verge of the turbulent wake state. Further actuator line computations based on the unsteady formulation and applied to a numerical domain without a symmetry plane[3] should verify this assumption.

---

[3]The yawed flow conditions are computed with this type of model.
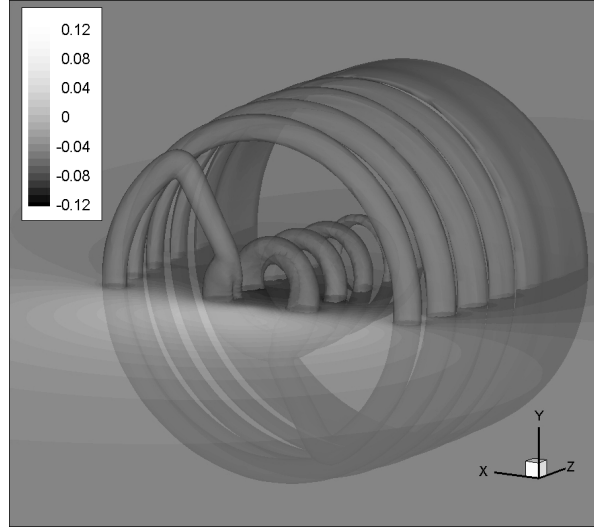
Figure 9.5: Actuator line model results for the axial flow condition with $\lambda = 7.9$, $\beta_{pitch} = 2.0°$. The vorticity isosurface illustrates bound, tip and root vortices, whilst the pressure contour shows the pressure jump across the rotor plane.

The comparison of measured and computed C_P yields mixed results, see Figure 9.6. An assessment into the causes of the differences is complicated by the absence of measurement uncertainty intervals with Vermeer's experiments. The actuator line method is expected to yield more realistic estimates of C_P than the inverse vortex wake model and direct assessment of the wake measurements however, recall the overestimates for C_P in Table 8.1, since the actuator line method is the only model of the three to include viscous airfoil drag.

The availability of the near-wake measurements for the operating condition with $\lambda = 7.9$ and $\beta_{pitch} = 2.0°$, combined with the inverse vortex wake model, enable a detailed comparison between experimental and actuator line results at this setting. Note that both C_T and C_P show good agreement between measurements and modeling at this setting, see Figure 9.6. Further note that consistent with the measurements, the actuator line model predictions of C_P suggest that this operating condition is near $C_{P_{max}}$.

Near-wake flow velocity

The quality of the RANS computations of the rotor wake can be assessed by comparison of the measured near-wake flow velocity with the actuator line results, see Figure 9.7. At present, the focus is on the comparison of measured
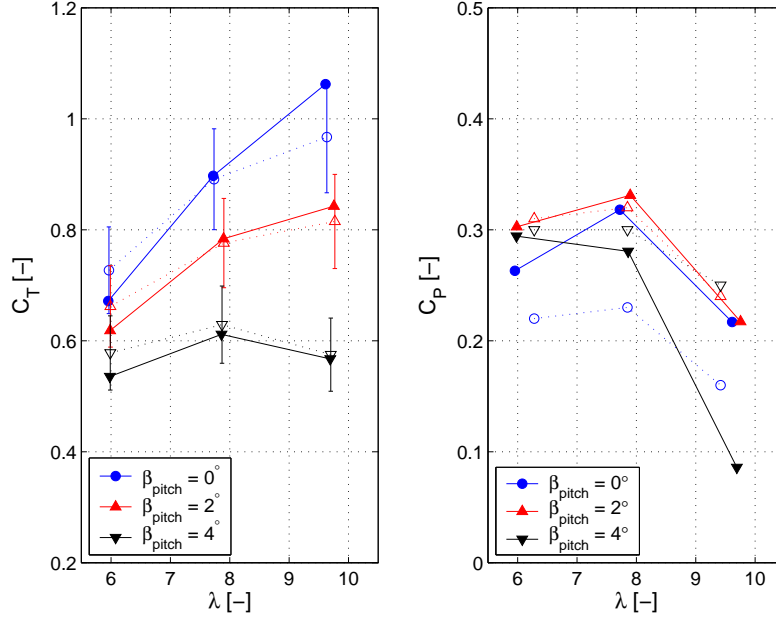
Figure 9.6: C_T and C_P versus λ and β_{pitch} for axial flow conditions. Actuator line computations: filled symbols, solid line. Measurements: open symbols, dotted line. Recall from Section 5.1 that, in contrast to C_T, C_P is not measured during the current experimental campaign, but is recorded by Vermeer [202] instead.

and computed results; the trends observed for the measured flow velocity have been discussed in Section 5.3.3.

Whilst the level of the computed axial and tangential flow velocity components generally corresponds to that of the measurements, the radial flow velocity component appears to be underpredicted in the inboard and midspan regions. The trends measured near the blade passages at $\theta_{b_{blade}} = 90°, 270°$, which are associated with inviscid vorticity effects, are reproduced by the computations. Near the wake passages, that are identified in Figure 9.7 by the measured local V_θ-maxima and V_r-minima, the agreement in the trends is below par however. The actuator line model does not capture the measured local V_θ-maxima which are associated with viscous effects; a result that is similar to that obtained with the inverse vortex wake model, compare Figures 7.16 and 9.7. Whereas the inviscid inverse vortex wake model is expected not to predict this viscous wake pattern, its absence with the RANS-based actuator line model is explained by the representation of the blades with actuator lines; a boundary layer that trails the blade to form the viscous wake, is not resolved
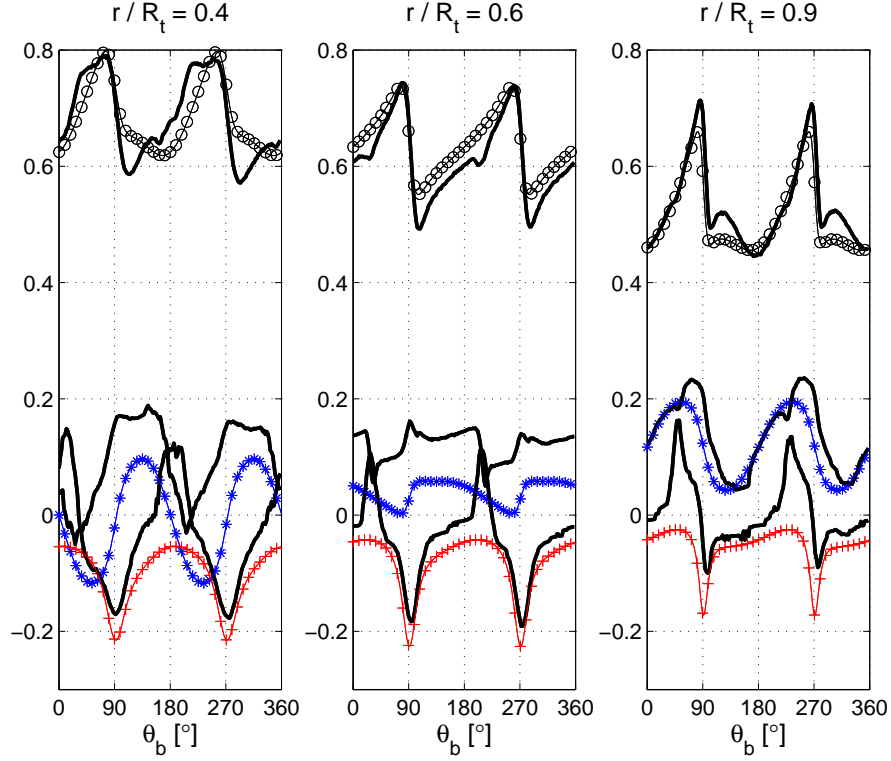
Figure 9.7: Nondimensional computed and measured velocity versus θ_b at $(\theta, z/R_t) = (90°, 0.150)$ for radial locations $r/R_t = 0.4, 0.6$ and 0.9. $\lambda = 7.9$, $\beta_{pitch} = 2°$. Actuator line computations: symbols, $V_r/W_0 : *$, $V_\theta/W_0 : +$, $V_z/W_0 : \circ$. Corresponding measurements: solid line only.

by the actuator line model[4].

    Whilst viscous wake effects are not represented adequately, the generation of vorticity at the actuator line and its downstream convection appear to be modeled realistically, also see Figure 9.5. The actuator line model does not capture the measured wake passage trend in the mid-span region however of a local V_r-maximum, followed by a local V_r-minimum, that is associated with wake vorticity effects[5], see the plot at $r/R_t = 0.6$ in Figure 9.7. The computed trailed vortex sheet in the mid-span region appears to be nearly completely diffused at $z/R_t = 0.150$ downstream already, as a result of the substantially

---

[4]Viscosity is only present to stabilize the solution, not to accurately model viscous phenomena, as noted in Appendix C.2.

[5]Note that the inviscid inverse vortex wake model does capture this wake vorticity related wake passage effect, compare Figures 7.16 and 9.7 for the plots at $r/R_t = 0.6$.

reduced value of $Re_r = 2 \cdot 10^3$ compared to the actual experimental value of $Re_r = 2 \cdot 10^5$. Despite the discrepancies in the wake passage effects, it can nonetheless be concluded that the actuator line computations of the near-wake flow velocity generally correspond to the measurements.

Angle of attack

A critical issue in rotor aerodynamics is the determination of α at a blade section, since the airfoil models implemented in BEM, vortex wake and actuator line methods require α to determine the sectional blade loads. The determination of α is complicated for two reasons; the definition of α on a rotating blade is debatable and direct measurements of α are not possible. A detailed discussion, including an overview of proposed approaches to derive α, is given in Section 5.3.4.

The actuator line model predicts α from the computed flow velocity at the lifting line, analogous to the blade passage method[6] that is used with the near-wake measurements. Two approaches to the blade passage method are employed for comparison with the α-distribution, predicted by the actuator line model; extrapolation of the near-wake flow velocity to the rotor plane and the inverse vortex wake model, see Figure 9.8. A comparison between the two experimental approaches, given in Section 8.1.1, suggests that the inverse vortex wake model yields a more accurate estimate of α than the extrapolation method.

The close correspondence of the actuator line model prediction with the inverse vortex wake model estimate, shown in Figure 9.8, confirms that the inverse vortex wake model is the preferred method to derive α from the near-wake measurements; in contrast to the linearized extrapolation method, the inverse vortex wake model seems to capture the nonlinear wake flow physics, that is realistically modeled by the RANS-based actuator line model.

When approaching the tip, the estimate obtained from the inverse vortex wake model first diverges from the actuator line predictions at $r/R_t = 0.95$, whereafter convergence is observed at $r/R_t = 1.0$. The overall match between the results from the two models across the blade span suggests that the divergence at $r/R_t = 0.95$ could be associated with the relatively coarse spanwise resolution of the inverse vortex wake model near the tip.

---

[6]The blade passage method determines α from the flow velocity at the blade, in contrast to the annular averaged method, that uses the annular averaged flow velocity in the rotor plane to find α, see Section 5.3.4.
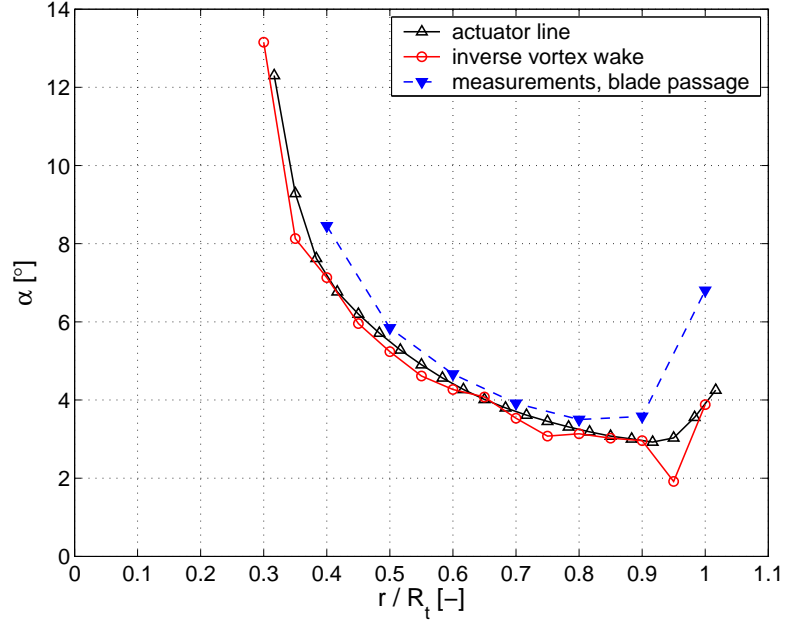
Figure 9.8: α versus r/R_t derived with the blade passage method, using the actuator line model, the inverse vortex wake model and the measurements. $\lambda = 7.9$, $\beta_{pitch} = 2°$.

Blade loads

The actuator line model couples an airfoil model with the RANS-based wake model to predict the blade loads. Loads are derived from the rotor measurements as well; strain gauge recordings yield the rotor thrust, with good agreement found between measured and predicted C_T for the currently considered flow condition of $\lambda = 7.9$ and $\beta_{pitch} = 2.0°$, see Figure 9.6. Sectional blade loads are not measured directly, since the blades are not equipped with pressure orifices. They are estimated instead from the near-wake measurements using the inverse vortex wake model, as has been discussed in Section 8.1.2.

To summarize, the inverse vortex wake model derives the circulation of and the inflow at the bound vortices. Two approaches are subsequently employed to determine the blade loads; the direct approach, where the circulation of and the inflow at the bound vortex are substituted into the Kutta-Joukowsky law [8.1] and the indirect approach, where an airfoil model is applied to the inflow at the lifting line. Note that the selected airfoil model is identical to
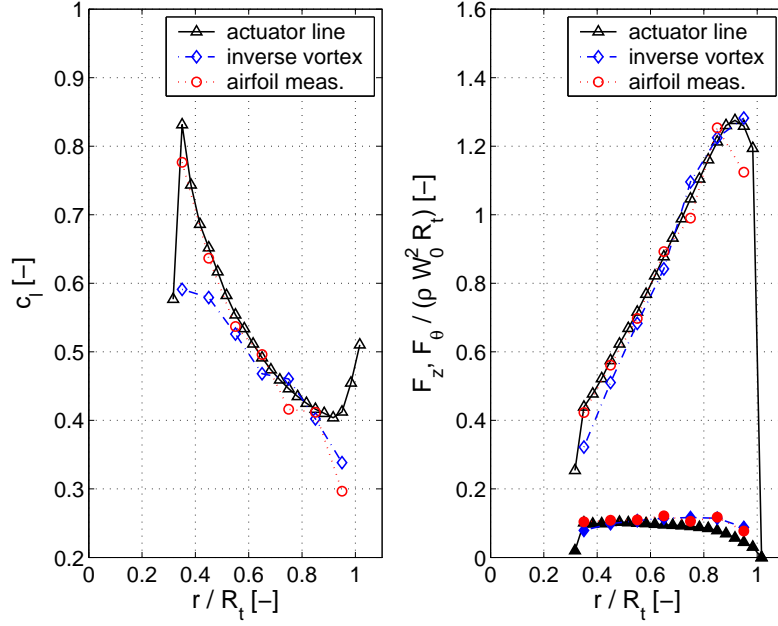
Figure 9.9: c_l (left plot) and F_z, F_θ (right plot, open and filled symbols, respectively) versus r/R_t. $\lambda = 7.9$, $\beta_{pitch} = 2°$. Actuator line results: $\triangle$, inverse vortex wake method results: $\diamond$, results from application of an airfoil model to the inflow at the lifting line computed from the inverse vortex wake model: $\circ$.

that used with the actuator line model[7].

Direct derivation of the blade loads from the inverse vortex wake model does not require the selection of an airfoil model, whilst three-dimensional, rotational blade load effects are inherently included. Comparison of the loads predicted by the actuator line model with those derived directly from the inverse vortex wake model should thus give insight into the suitability of the airfoil model used with the actuator line model to represent the actual blade loads.

The spanwise distributions of c_l, F_z and F_θ derived with the actuator line model and the two inverse vortex wake model approaches are given in Figure 9.9. The actuator line model prediction of c_l generally resembles that found

_____

[7]In fact, the airfoil models are not exactly the same; whereas the one used with the actuator line model includes both lift and drag, the one applied to the inverse vortex wake model only incorporates lift, because direct derivation of blade loads from the inverse vortex wake model also only yields the lift.

with the indirect inverse vortex wake model approach[8], as can be understood from the overall similarity in α between the actuator line model prediction and the inverse vortex wake model estimate shown in Figure 9.8.

The actuator line model prediction of c_l coincides with that derived directly from the inverse vortex wake model in the midspan region, given by $0.55 \leq r/R_t \leq 0.85$, suggesting that the airfoil model is adequate here. The actuator line model does not predict however that c_l levels off in the root region, given by $0.35 \leq r/R_t < 0.55$, as is observed with direct derivation from the inverse vortex wake model. Only at the most inboard node, where α exceeds the static stall angle of the airfoil model, the actuator line model predicts a decreased c_l. The airfoil model hence does not seem to accurately model c_l in the root region. The differences in the tip region cannot be assessed properly, since the spanwise resolution of the inverse vortex wake model is too coarse; only a single point, at $r/R_t = 0.95$, is available.

Good agreement is found between the spanwise distributions of F_z and F_θ predicted by the actuator line model and derived directly from the inverse vortex wake model, see Figure 9.9. The inadequacy of the airfoil model to predict c_l in the root region yields minor local differences in F_z and F_θ, because of the relatively low dynamic pressure at the blade in the root region.

It must be noted however that F_z and F_θ are determined by the actuator line model using both c_l and c_d, whereas the inverse vortex wake model approaches incorporate c_l only. F_z and F_θ predicted with the actuator line model are dominated by the contribution of c_l though; the only apparent effect of c_d is the reduction in the actuator line prediction of F_θ, compared to the inverse vortex wake model estimates, in the outboard region.

The airfoil model implemented in the actuator line model thus appears to predict a realistic spanwise blade load distribution for the model rotor at the axial flow condition of $\lambda = 7.9$ and $\beta_{pitch} = 2.0°$. Based on the present analysis, the airfoil model is furthermore expected to generally yield realistic blade loads when the model rotor is subject to operating conditions that result in steady inflow well below the airfoil static stall angle.

9.2.2 Yawed flow comparison: influence of dynamic stall model

Unsteady inflow conditions at a blade induce an unsteady blade aerodynamic response. A rotor aerodynamics code should therefore employ an unsteady blade model when computing rotor operating conditions that yield unsteady blade inflow, such as yaw misalignment. The near-wake measurements in yawed flow conditions are hence modeled with the actuator line method using

---

[8]The resemblance consequently results in an overlap between the present blade loads discussion on actuator line model predictions and that in Section 8.1.2 concerning estimates obtained with the inverse vortex wake model indirect approach.

either the Øye or the Beddoes-Leishman dynamic stall model. Note that whereas for axial flow conditions the actuator line model assumes rotating stationary flow, this assumption must be abandoned in yaw, see Appendix C.2 for more details.

The modeling results obtained with the Øye and Beddoes-Leishman dynamic stall models are compared to the near-wake measurements for the yawed flow conditions summarized in Table 9.1. With λ set to the relatively high value of $\lambda = 8$, dynamic stall is virtually absent as has been concluded from the inverse vortex wake model (Section 8.2.3) and tuft and hot-film recordings (Section 6.4.3) for the clean and rough configuration, respectively. The non-stalled yawed flow conditions with $\lambda = 8$ are assessed first, after which the focus is on the more complex dynamic stall conditions. The comparison should contribute to improved insight into the relation between an unsteady blade model and the uncertainty of a rotor aerodynamics model.

Table 9.1: Rotor operating conditions of the experimental yawed flow cases that are computed with the actuator line method.

Ψ [°]	λ [-]	β_{pitch} [°]	$k_{0.7R}$ [-]	$Re_{0.7R} \cdot 10^{-5}$ [-]		C_T [-]	blade
				max	min		layout
30	8.0	2.0	0.09	1.77	1.49	0.70	clean
45	8.1	2.0	0.09	1.82	1.42	0.53	clean
45	8.1	2.0	0.09	1.82	1.42	0.5 (estimate)	strip
45	5.5	2.0	0.09	1.93	1.35	0.5 (estimate)	strip

Non-stalled unsteady blade flow

Figures 9.10 to 9.12 present the spanwise distributions of α, c_l and F_z during a rotational cycle for the $\Psi = 30°$, $\lambda = 8.0$ operating condition; each of the figures shows the data computed with the actuator line model using the Beddoes-Leishman and the Øye dynamic stall models and that derived from the near-wake measurements with the inverse vortex wake model. The $\Psi = 45°$, $\lambda = 8.1$ operating condition is given in Figures 9.13 to 9.15. Note that the dynamic stall models are based on clean static airfoil data, in accordance with the clean configuration used for both experimental operating conditions.

The experimental results, derived with the inverse vortex wake model, have been discussed extensively in Section 8.2.3. The present analysis can hence focus on the comparison of measurements with models.

To begin with, the presence of dynamic stall in the actuator line results is studied, as the measurements have clearly indicated that the blade flow is

Figure 9.10: α-distribution at the actuator/lifting line during a rotational cycle for the actuator line model with the Beddoes-Leishman and Øye dynamic stall models and the inverse vortex wake model, for the $\Psi = 30°$-case.

Figure 9.11: Idem as Figure 9.10, but then the c_l-distribution.

Figure 9.12: Idem as Figure 9.10, but then the F_z-distribution.

non-stalled. For each of the two yawed flow conditions, the α-distributions computed using both dynamic stall models remain well below the airfoil static stall angle of $\alpha_{stall} = 10.6°$ across the span during a rotational cycle[9]. The actuator line models hence are in agreement with the experimental observation that both yawed flow cases concern non-stalled blade flow.

In the absence of dynamic stall, the actuator line model yields similar results at a given yawed flow condition when implementing either the Øye or the Beddoes-Leishman dynamic stall model. Trends observed in the actuator line results furthermore generally correlate well with those seen in the experimental results, derived with the inverse vortex wake model.

Detailed comparisons of the unsteady blade aerodynamics learn however that the computed lift hysteresis is significantly less than that derived using the inverse vortex model, see Figure 9.16. The actuator line results obtained with both dynamic stall models show minor lift hysteresis for both rotor operating conditions, at both spanwise sections considered. Note that the predicted dynamic lift responses are subtlety different for the two dynamic stall models; whereas the Beddoes-Leishman results closely follow the static data, the Øye results show over- and undershoots, suggesting that the effective time constant associated with the Øye modeling results is larger than that of the Beddoes-Leishman modeling results.

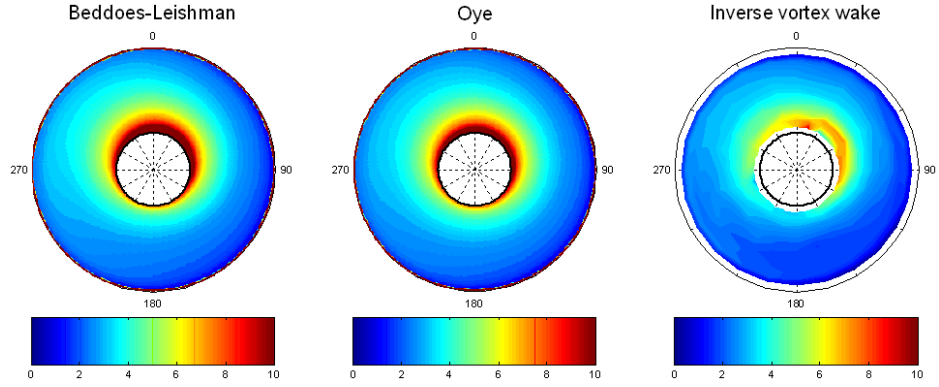[9]except *at* the blade root, see Figures 9.10 and 9.14

Figure 9.13: α-distribution at the actuator/lifting line during a rotational cycle for the actuator line model with the Beddoes-Leishman and Øye dynamic stall models and the inverse vortex wake model, for the $\Psi = 45°$-case.
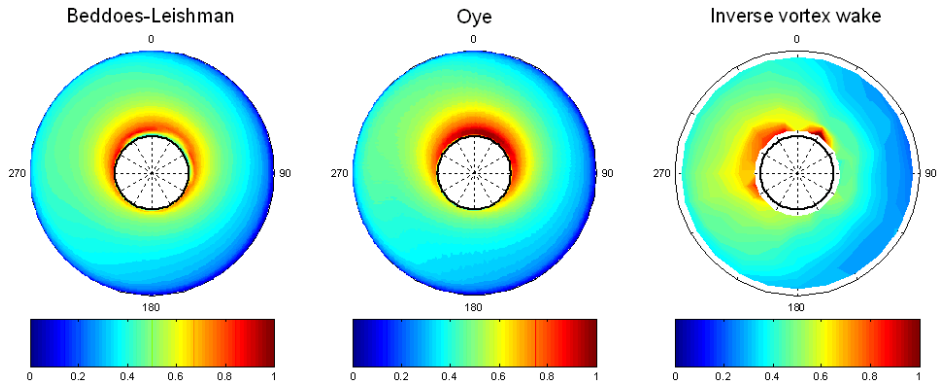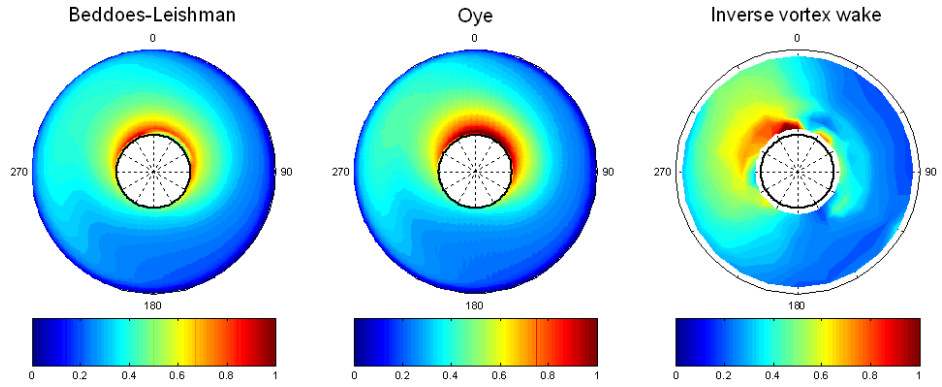

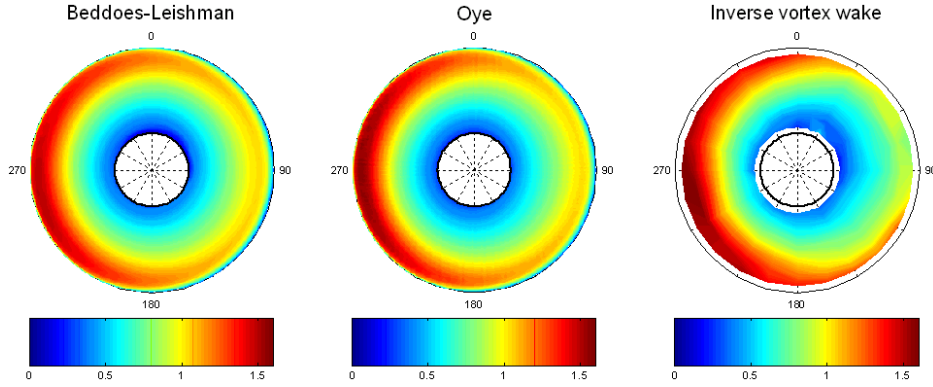Figure 9.14: Idem as Figure 9.13, but then the c_l-distribution.
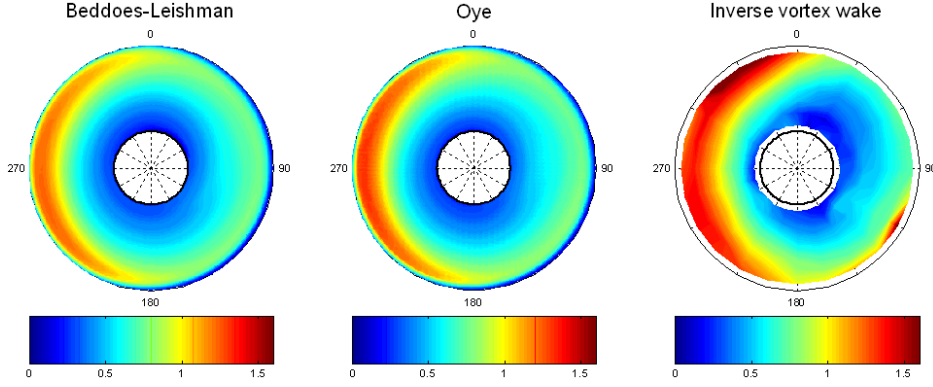
Figure 9.15: Idem as Figure 9.13, but then the F_z-distribution.

Focussing on the inflow, the induced axial and tangential flow velocity at the blade during a rotational cycle are found to agree when computed using either the Beddoes-Leishman or the Øye dynamic stall models, see Figures 9.17 and 9.18. The modeling results furthermore correlate with those derived from the measurements using the inverse vortex wake model;

- all three a_{rel}-plots show local minima in the outboard region near $\theta_b = 270°$ and in the inboard region near $\theta_b = 90°$

- all three a'_{rel}-plots show a local minimum near $\theta_b = 0°$ and a local maximum near $\theta_b = 180°$.

Note that in contrast to the inverse vortex wake model, the Navier-Stokes based flow modeling of the actuator line method does not allow the induced velocity to be decomposed in the vortex contributions. The induced velocity can hence not be compared at the level of vortex contributions.

The actuator line results obtained using the Beddoes-Leishman dynamic stall model are expected to have lower uncertainty than those found with the Øye model, as the former model is the more advanced one. The mutual agreement of the actuator line results is better however than that of the measurements with the Beddoes-Leishman modeling results; the measurements hence cannot confirm or rebut the reduced modeling uncertainty of the Beddoes-Leishman dynamic stall model actuator line results, compared to those obtained with the Øye dynamic stall model, as the measurement uncertainty appears to be larger than that of both modeling results.

211
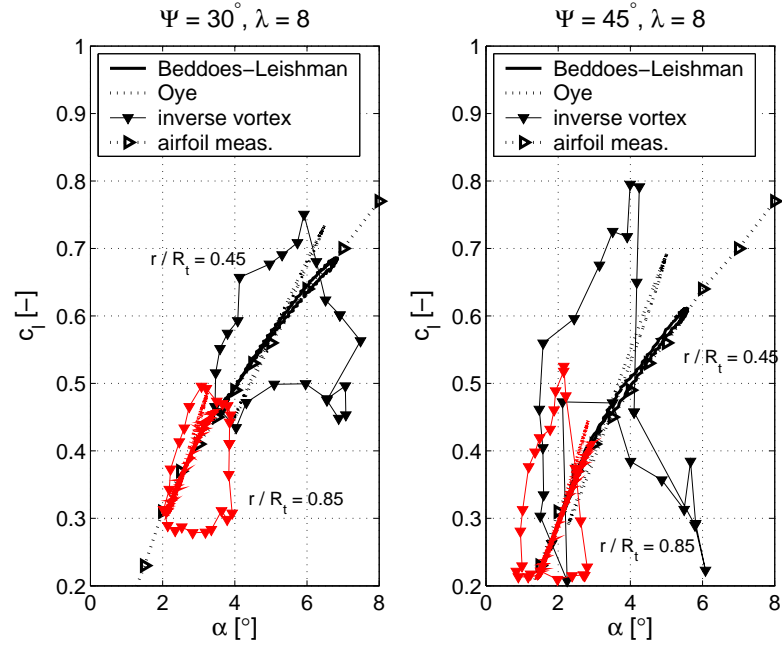
Figure 9.16: c_l versus α at $r/R_t = 0.45, 0.85$ during a rotational cycle, for the actuator line model with the Beddoes-Leishman (solid lines) and Øye (dotted lines) dynamic stall model and the inverse vortex wake model (∇), for the $\Psi = 30°$-case (left plot) and the $\Psi = 45°$-case (right plot). All hysteresis loops rotate clockwise.
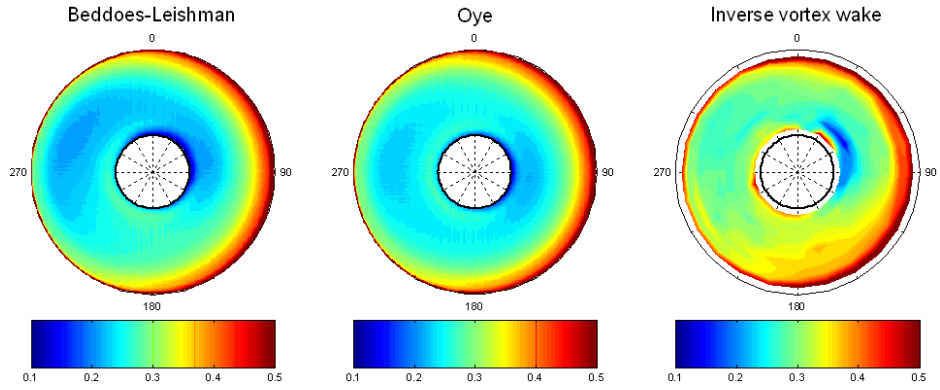
Figure 9.17: a_{rel}-distribution at the actuator/lifting line during a rotational cycle for the actuator line model with the Beddoes-Leishman and Øye dynamic stall models and the inverse vortex wake model, for the $\Psi = 30°$-case.
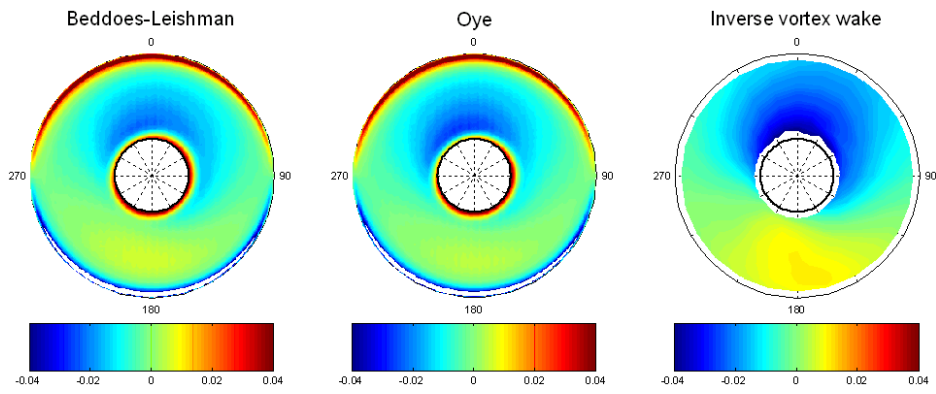
Figure 9.18: Idem as Figure 9.17, but then the a'_{rel}-distribution.

Dynamically stalled blade flow

Experiments, presented in Section 6.4.3, indicate that reducing λ from 8 to 5.5 with $\Psi = 45°$ and $\beta_{pitch} = 2°$ results in dynamic stall flow conditions. Two experimental methods, tuft recordings and near-wake flow measurements, yield similar regions of dynamically stalled flow. Comparison of the measurements with actuator line modeling allows an assessment of the relative performance of the Øye and Beddoes-Leishman dynamic stall models for a dynamic stall operating condition.

Whereas the experiments concern the rough configuration, the dynamic stall models are based on clean static airfoil data, as data for a rough NACA0012 at $Re \, \epsilon \, O(10^5)$ is unavailable. It is acknowledged that models based on clean instead of rough static airfoil data introduce additional uncertainty to the actuator line results. Dynamic stall experiments are performed for a rough instead of a clean configuration however, because the latter could introduce complex interactions between dynamic stall and boundary layer transition that are not accounted for by the dynamic stall models, thereby introducing a significant contribution to the measurement uncertainty, as has been discussed in Section 6.4.1.
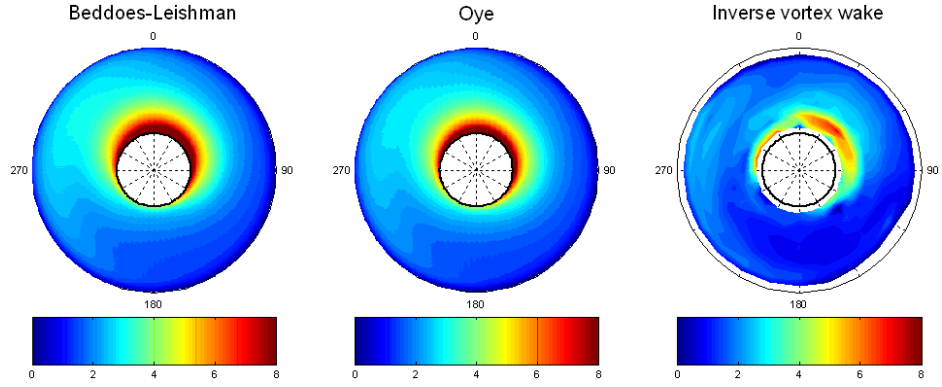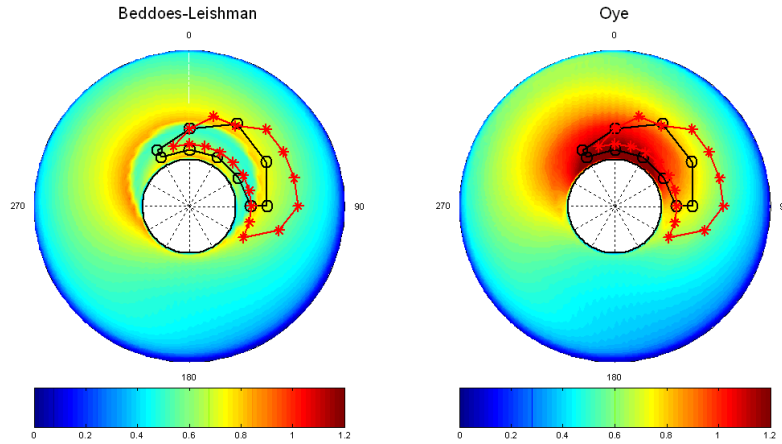

Figure 9.19: c_l-distribution at the actuator line during a rotational cycle for the actuator line model with the Beddoes-Leishman and Øye dynamic stall models, for the case with $\Psi = 45°$, $\lambda = 5.5$, $\beta_{pitch} = 2.0°$. Superimposed are regions of fully separated flow on the blade suction surface, observed with tuft visualization (∘) and hot-film anemometry (∗), as shown in Figure 6.16.

Where the two dynamic stall models yield similar results for conditions resulting in non-stalled unsteady blade flow, distinctly different results are obtained for the dynamic stall condition, see Figure 9.19. The Beddoes-Leishman

dynamic stall model results show an abrupt drop in c_l for the inboard region during a rotation. Smooth variations in c_l are observed instead for the same spanwise region, when computed with the Øye model, achieving higher $c_{l,max}$ in the process.

Both measurements indicate separated blade flow in the inboard region during part of the cycle. Although c_l could not be derived from the measurements, flow separation is generally associated with reduced c_l. The Beddoes-Leishman results hence correlate substantially better with the experimental observations than those computed with the Øye dynamic stall model, even though the phase angles of the computed and measured separated flow regions do not match.

The dynamic stall behavior of the NACA0012 airfoil is dominated by unsteady leading edge separation for the relatively low Re-numbers tested currently. The superior performance of the Beddoes-Leishman model is thus expected, as the Øye model only simulates unsteady trailing edge separation, whilst the Beddoes-Leishman model captures both trailing and leading edge separation.

215

Chapter 10

Conclusions & recommendations

This section reviews the results presented in the previous ones, in light of the objectives and scope formulated in Section 1.3. To refresh our minds after over 200 pages of text, a summary of results is presented first in Section 10.1. Conclusions are drawn in Section 10.2, whereafter Section 10.3 discusses recommendations.

10.1   Summary of results

Chapter 3:
The model rotor experiment

A model wind turbine rotor is tested in an open jet wind tunnel. The $1.2m$ diameter rotor has two twisted, nontapered blades, with $0.06m$ chord. Along the entire span, the NACA0012 airfoil is used. The wind tunnel tests are adequately documented enabling experimental repetition and/or modeling.

The wind tunnel tests are not designed to have perfect similitude - geometric, kinematic and dynamic similarity - with a MW-scale wind turbine. Instead, the aim is to study experimental rotor aerodynamics representative for a full scale turbine and to provide a base for model validation. The disparity in Reynolds number Re between the model rotor and a full-scale turbine is acknowledged. Possible effects hereof on dynamic stall behavior are mitigated through the application of trip strips in test conditions. Other than dynamic stall, Re-differences are not anticipated to cause fundamentally different rotor aerodynamics. The relevance of these experiments for wind turbine related flow physics studies and aerodynamic tool validation is thus not affected by Re-differences.

Both axial as well as yawed flow conditions are explored, with the yaw angle Ψ set to $0°$, $30°$ and $45°$. Strain gauges in the blade root are used to measure rotor thrust for design and off-design conditions, including yaw. The flow state on the blades in yaw is further investigated with tufts, visualizing dynamic flow separation during part of a rotational cycle. Tuft recordings are performed in combination with Phase-Locked Averaged PLA single-film hot-film Constant Temperature Anemometry CTA measurements in the near-wake, which together enable the study of flow separation from both the blade and wake perspective.

The near-wake is studied with quantitative smoke visualization of tip vortex paths for a range of axial and yawed flow conditions. PLA single-film hot-film CTA measurements are further conducted across 3 planes, located $z/R_t = 5.83 \cdot 10^{-2}$, $1.00 \cdot 10^{-1}$ and $1.50 \cdot 10^{-1}$ downstream of the rotor. The tunnel time required to complete a set of PLA CTA measurements at the 3 planes limits the number of cases to a single axial flow condition with tip speed ratio $\lambda = 8$, blade pitch angle $\beta_{pitch} = 2°$ and 2 yawed flow conditions; $\Psi = 30°$ and $45°$, both with $\lambda = 8$ and $\beta_{pitch} = 2°$. All three cases are anticipated to only yield a limited stall region across the blade span during a cycle, as the combination of $\lambda = 8$ and $\beta_{pitch} = 2$ results in near-optimum conditions for axial flow.

Chapter 4:
Experimental data reduction

Measurement data reduction covers three aspects; wind tunnel wall corrections, measurement uncertainties and derivation of the PLA three-dimensional velocity from the near-wake CTA recordings. Using a numerical Euler model of the simplified open jet wind tunnel, the traditional blockage correction as well as a nonuniformity correction specific for this tunnel are quantified. Combination of the effects amounts to a maximum correction of about 1-2% on the undisturbed wind speed.

Section 4.4 presents the measurement uncertainty analysis according to AIAA standards and guidelines [3, 4]. Bias and random contributions are combined to establish total measurement uncertainty bounds, all at 95% confidence level. A typical total uncertainty bound of 11% is found for C_T, as measured with strain gauges in the bade root. Measurement uncertainty bounds for near-wake tip vortex trajectories up to about $1.5R_t$ downstream, measured with quantitative smoke visualization, typically amount to $0.03R_t$ and $0.07R_t$ in the radial and axial direction, respectively. Lastly, uncertainty bounds for the PLA three-dimensional flow velocity in the near-wake is quantified; whilst the random component is a constant for given W_{jet}, the bias term is a function of the flow velocity vector. The total uncertainty bound for each of the three

velocity components typically is $0.1W_{jet}cos\Psi$ for axial flow and $0.2W_{jet}cos\Psi$ for the yawed flow condition with $\Psi = 45°$.

A novel method to derive the PLA three-dimensional flow velocity from PLA CTA measurements with a single wire/film is proposed in Section 4.2. Where the traditional approach needs three CTA measurements with the film in a unique orientation, the novel method requires six recordings. With the traditional method, only the magnitudes of the three flow velocity components can be computed; their directions need to be assumed. The novel method uses the asymmetric response of a parallel single-film probe - where the film is parallel to the longitudinal axis of the probe - to find both magnitude as well as direction of all three components of PLA flow velocity. The need to explicitly assume flow directions is hence obsoleted with the new method, as flow directions are implicitly computed.

Chapter 5:
Experimental analysis of the rotor near-wake in axial flow

Whilst the core of the thesis concerns the study of the asymmetric rotor aerodynamics in yaw, experimental results for the reference axial flow conditions are reviewed first. Starting with rotor performance in Section 5.1, C_T is analyzed across a wide operational range; current findings are further compared against those by Vermeer [202] on nearly identical conditions to find good agreement, easily within the uncertainty bounds of the current study. Note that the data published by Vermeer is not accompanied with uncertainty bounds.

Measured tip vortex trajectories, refer to Section 5.2, clearly demonstrate the expected expansion of the near-wake and increased tip vortex pitch with reduced λ. Trends in tip vortex paths with variations in λ and β_{pitch} further comply with those in C_T-recordings, confirming the coupling between blade and wake aerodynamics. Current recordings also agree with Vermeer's tip vortex location experiments, performed with PLA CTA [202], the differences between the two sets being generally smaller than the current measurement uncertainty.

The near-wake flow velocity is studied extensively for the axial flow condition with $\lambda = 8$ and $\beta_{pitch} = 2°$, where the performance is close to optimum. Introductory annular averaged results review the downstream development of the axial induction factor $a(r)$. Linear extrapolation is further employed to find $a(r)$ in the rotor plane; used in the Rankine-Froude one-dimensional actuator disc momentum equation, the resulting C_T matches its strain gauge counterpart; $C_T = 0.75$ versus $C_T = 0.78$. The differences between the two approaches that are smaller than the measurement uncertainty.

Turning the focus to PLA flow velocity, the proposed data reduction tech-

nique proves its value; when compared to the traditional approach, sample results demonstrate substantially reduced nonphysical wiggles for low amplitude velocity components and implicit determination of the direction of flow. Measured cyclic unsteadiness of the PLA near-wake flow velocity agrees with previously published experiments, refer to e.g. Vermeer [204], and its trends are explained with a vortex wake model. Note that present experiments reveal a substantial level of detail; even for the *radial* PLA flow velocity component, the smallest of the three, observed trends agree with vortex wake modeling.

The sectional angle of attack α is subsequently derived from the measured near-wake flow velocity, using both the annular averaged method by Hansen *et al.* [87] and a proposed blade passage method. Similar α-results are obtained across the span, except for those at the tip, where large uncertainties of both methods frustrate proper comparison. Lift and drag coefficients c_l and c_d obtained from wind tunnel measurements on a NACA0012 are subsequently applied to the estimated α-distributions to find blade loads. Resulting C_T just falls within the uncertainty bound of that from strain gauge measurements. Sectional c_t from blade load estimates are compared to that from one-dimensional actuator disc momentum theory, recall the derivation of the axial induction factor in the rotor plane. These two approaches to arrive at c_t represent the blade and wake part of BEM modeling. The agreement is reasonable in the mid span, but deteriorates towards the tip

Chapter 6:
Experimental analysis of yaw effects on the rotor near-wake

The thorough experimental analysis of reference axial flow conditions given in Chapter 5 forms a solid basis to explore the core of this thesis; yawed flow. Measured rotor performance in yaw is reviewed first in Section 6.1. The nonuniformity of the undisturbed flow field in the tunnel is seen to have minor impact on performance and thus rotor aerodynamics for $|\Psi| > 15°$, ergo the choice to only study conditions with $\Psi = 30°, 45°$.

Tip vortex trajectories, discussed in Section 6.2, demonstrate the skewness of the near-wake in yaw, meeting expectations from modeling and existing experimental literature. Skewed wake expansion correlates to the rotor thrust. Pitch and convection velocity of the tip vortices in the near-wake are further reported, with detailed explanation of the flow physics governing observed trends.

The near-wake flow velocity in yaw is addressed first through averages, using two approaches; the annular and the cycle averaged PLA flow velocity. Recall that the Glauert momentum model, used in BEM codes, employs the annular averaged velocity. Measurements indicate that in yaw, the annular averaged axial velocity at the three downstream planes is quasi-steady during

a cycle, for given annulus.

In contrast, the cycle averaged axial velocity in the near-wake is clearly asymmetric in yaw. The data confirms experiments and its trends can be explained with vortex wake models that include both the skewed tip and root vortices. Notably, the flow velocity develops strongly nonlinearly whilst convecting downstream.

The unsteady PLA flow velocity representative for that at the blade is presented during a cycle using the data nearest to the rotor plane, at $z/R_t = 5.83 \cdot 10^{-2}$. Both axial and tangential flow velocity are shown. For the axial component, unsteady flow velocity patterns are similar to those of the cycle averaged flow velocity. The tangential flow velocity at the blade is dominated by the undisturbed velocity component arising from yaw misalignment.

Widening the scope from the inflow at/near the blade to that in the downstream planes, the unsteady PLA flow velocity field clearly demonstrates the asymmetry in the skewed near-wake. Trends seen with blade and wake passages are influenced by yaw and effectively become dependent on the azimuth angle.

A complementary approach with tuft visualization of blade flow and hot-film CTA of near-wake flow quantifies the spanwise extent of the flow separation region during a cycle. Results obtained from the two techniques are in general agreement. These indicate the virtual absence of dynamic stall for the case with $\Psi = 45°$, $\lambda = 8$, $\beta_{pitch} = 2°$, thereby suggesting that stall is insignificant for the $\lambda = 8$, $\beta_{pitch} = 2°$ conditions with $\Psi = 30°, 0°$ as well. A reduction of λ to 5.5 triggers dynamic stall at the inboard region of the blade during the downwind part of the cycle.

Chapter 7:
The inverse vortex wake model: a rotor wake measurement analysis tool

Whilst blade and wake aerodynamics are strongly coupled, current model rotor measurements focus on the near-wake; only rotor thrust is recorded, no detailed blade loads. Analysis of wake data and insight into experimentally observed rotor aerodynamic phenomena is hampered by the absence of detailed blade measurements. This general remark is specially relevant for the present study, since loads are explicitly mentioned as a focal point. The remark would hold though for most wind tunnel tests on small scale rotors, say up to $2 - 3m$ diameter, as their size typically prohibits instrumentation with pressure sensors distributed across the blades.

A measurement analysis model is developed to fill the lacuna of spanwise distributed load recordings with model estimates. The tool is a lifting line vortex wake model. When a vortex wake model is used in predictive mode,

blade aerodynamics are specified to compute the wake structure and associated induced flow velocity field. In contrast, this measurement analysis version feeds wake recordings to the model, using them to reconstruct the vortex wake structure and induced flow velocity field, whereafter the spanwise load distribution is derived. Since the approach essentially reverse engineers the wake, the measurement analysis tool is named inverse vortex wake model.

No blade or section aerodynamic data is needed to estimate loads, as these implicitly result from the circulation at the blades, i.e. bound circulation, the inflow at the blade, both of which are derived with the model, and the Kutta-Joukowsky law. The tool can handle both axial as well as yawed flow conditions, using a discrete formulation.

Prandtl's classical translating wing example of his lifting line theory, for which an analytic solution exists, is used to verify the model, with success. Model validation is performed on present near-wake flow velocity measurements; using the reconstructed vortex wake, i.e. both geometry and circulation strength, the unsteady flow velocity during a blade rotation is computed at selected inertial locations in the near-wake and compared to experimental findings. The model is seen to capture those driving flow phenomena that are of inviscid nature. Model validation thus shows good agreement between measurements and the inverse vortex wake model.

Chapter 8:
Inverse vortex wake model analysis of the rotor aerodynamics

Application of the inverse vortex wake model to present near-wake experiments commences with an analysis of the near-optimal axial flow condition, where $\lambda = 8$, $\beta_{pitch} = 2°$. Sectional α is seen to be marginally underpredicted with the crude linear extrapolation technique of Chapter 5, when compared with the nonlinear inverse vortex wake model estimates. Estimates of the spanwise blade load distribution reveal the presence of a three-dimensional flow phenomenon in the blade root that yields reduced local performance. Integrated over the rotor, the estimated C_T aligns well with that found from direct strain gauge measurements and alternative estimates based on one-dimensional momentum theory.

In yaw, the estimated spanwise distribution of bound circulation demonstrates cyclic unsteadiness. The annular averaged flow velocities in the rotor plane are, for given annulus, quasi-steady though during a blade cycle. Note that the measurement analysis tool allows estimates *in* the rotor plane, whilst the near-wake measurements only come up to $z/R_t = 3.58 \cdot 10^{-2}$ hereof.

Estimates of the cycle averaged flow velocity in the rotor plane, as well as that at the lifting line, do demonstrate the cyclic variation of the induced velocity at a blade section associated with yaw. Both flow velocity estimates

resemble the near-wake measurements closest to the rotor plane, at $z/R_t = 3.58 \cdot 10^{-2}$.

Availability of both annular averaged and lifting line flow velocity estimates allows quantification of the nonuniformity corrections as used in BEM modeling. Present measurements and the associated estimates from the inverse vortex wake model confirm that the characteristic shape of the corrections for the axial induction factor varies between in- and outboard annuli; the sinusoidal form, which is the basis of much-used Glauert type corrections, is only established outboard. Inboard, significant higher harmonics are found.

Consistently applying conservation of circulation in the inverse vortex wake model enables reconstruction of the contribution from the various vortices to the induced velocity. As a first result, the influence from shed vorticity on the inflow at the lifting line is observed to be negligible across the axial and yawed flow cases studied. Contributions from the tip and root vortices, as well as the trailed vortex sheet, are all found to be substantial for the three flow conditions.

In yaw, tip vortex contributions to the induced flow velocity at the lifting line are nearly sinusoidal during a blade cycle, with increasing amplitude towards the blade tip and highest axial induction factors during the downwind part of the cycle. The root vortices induce a generally weaker flow velocity than the tip vortices. The exception is found in yaw, where during the downwind phase of the cycle relatively strong negative axial induction factors are found at the blade inboard section. Induced velocity contributions from the trailed vortex sheet are found to generally comply with the effects seen for root vortices.

The estimated bound circulation and inflow at the blades can readily be translated into loads using the Kutta-Joukowski law modified for unsteadiness. Again note that the inverse vortex wake model does not require airfoil tables or dynamic stall models to estimate blade loads. The two yawed flow conditions studied lead to sectional α during the blade cycle that remain below the static stall angle. Ergo, no substantial dynamic stall is expected. Even without stall, c_l hysteresis is found across the blade span. The blade aerodynamics hence is truly unsteady. Resulting C_T compares reasonably well with that found from strain gauge recordings, where it must be noted that at $\Psi = 30°$, the discrepancy is within the measurement uncertainty whilst at $\Psi = 45°$, it is somewhat larger than that.

Chapter 9:
Comparison of rotor aerodynamics models with experiments

Where previous Chapters focus on the interpretation of the current near-wake measurements, Chapter 9 discusses the comparison of these measurements to

existing rotor aerodynamics (sub)models. Blade as well as wake modeling are considered. Note that comparisons published by other researchers between current measurements and their models are out-of-scope; the comparisons discussed here only refer to those (co-)performed by the author of this thesis.

Starting with blade modeling, the measurements are used to review the results from a rotor aerodynamics tool where a "normal" blade model is coupled to a RANS model of the rotor wake. This approach goes by the name actuator line model.

The RANS formulation of the wake flow should reduce the wake contribution to modeling uncertainty, when compared to the wake formulations used in vortex wake and especially BEM models. The dominant source of actuator line modeling uncertainty is thus anticipated to be the blade model, which is identical to that used with BEM and vortex wake methods.

The comparison of measurements with actuator line modeling thus aims to review blade modeling uncertainty. Two common models are used; the simple Øye and the comprehensive Beddoes-Leishman dynamic stall models. Note the context; instead of two-dimensional wind tunnel conditions as used for airfoil tests, the three-dimensional unsteady, rotating environment of a blade is analyzed, since the latter condition is considered to be most challenging, but also most relevant.

Axial flow modeling goes with the assumption of steady inflow for given blade section during a rotation. The two dynamic stall models thus return to the same static airfoil table, resulting in identical predictions for the two actuator line predictions. Good agreement is found between measured and predicted C_T across a range of axial flow conditions. Zooming in on the case with $\lambda = 7.9$, $\beta_{pitch} = 2°$, the measured three-dimensional PLA near-wake flow velocity generally agrees with predictions. The same holds for sectional α and loads. The static airfoil table used thus presents itself as a sound base for the dynamic stall models.

The model is compared to near-wake flow measurements at the yawed flow conditions with $\lambda = 8$, $\beta_{pitch} = 2°$ and $\Psi = 40°, 45°$, where stall is experimentally observed to be virtually absent. Modeling results comply with this experimental observation. For both conditions, reasonable correlation is found between measured inflow and loads and actuator line modeling using the two dynamic stall methods. The measurement uncertainty is larger though than the differences between the two modeling results; the measurements are hence inconclusive on the reduced modeling uncertainty of the Beddoes-Leishman dynamic stall model actuator line results, compared to those obtained with the Øye dynamic stall model.

Reduction of λ to 5.5, with other settings unchanged, is experimentally observed to trigger substantial flow separation during part of a rotation for inboard blade sections. Distinctly different blade aerodynamics are found from

224

the actuator line codes with Øye and Beddoes-Leishman dynamic stall models. The former demonstrates smooth blade load unsteadiness, thereby surpassing static $c_{l,max}$ at inboard sections. Clear indications of stall are not found, though. In contrast, the Beddoes-Leishman dynamic stall model does yield abrupt c_l-reduction at inboard sections just after sectional $c_{l,max}$, i.e. stall.

The actuator line tool with Beddoes-Leishman dynamic stall model agrees best with measurements. This does not come as a surprise though, since for the NACA0012, stall at the relatively low Reynolds numbers of the experiments is governed by leading edge separation. This phenomenon is included with the Beddoes-Leishman, not with the Øye dynamic stall model.

Wake modeling is addressed through a comparison of the Glauert momentum equation with near-wake measurements for two yawed and a reference axial flow condition. For all annuli, sectional c_t is determined directly from blade loads as well as from the Glauert momentum equation. Both avenues use the inverse vortex wake model; the momentum deficit requires estimates of the annular averaged axial induction factor, whilst blade loads are estimated from the unsteady Kutta-Joukowski law. Note that in yaw, sectional c_t exhibits cyclically unsteady behavior.

In axial flow, the empirical Glauert momentum equation reduces to the theoretical one-dimensional Rankine-Froude actuator disc model. The good agreement found for the sectional c_t, especially outboard, between that from blade loads and the wake momentum deficit, the latter according to the Glauert momentum equation, for the axial flow condition with $\lambda = 7.9$, $\beta_{pitch} = 2°$ is encouraging; it demonstrates the suitability of the classical one-dimensional actuator disc model in our reference, near-optimum axial flow condition.

Turning to yaw, with $\Psi = 30°, 45°$ whilst maintaining $\lambda = 8$ and $\beta_{pitch} = 2°$, the general agreement in sectional c_t between that from blade loads and the Glauert momentum equation is reasonable. Averaged over a rotor cycle, the two approaches yield reasonable agreement for outboard sections. Discrepancies increase with larger Ψ, where wake asymmetries are stronger and uncertainties of the results are higher. The match still is reasonable though for outboard annuli at the most demanding $\Psi = 45°$-case.

The PLA sectional c_t-estimates exhibit substantial cyclic unsteadiness, with clear 2P-periodicity as a result of the rotor having two blades. Unsteadiness increases with larger Ψ. Particularly in the mid-span region, the wake deficit based c_t fails to capture the full extent of the variations as estimated from blade loads. This limitation of the Glauert momentum model is also anticipated from annular averaging of the measured near-wake flow velocity in Section 6.3.1, which is quasi steady during a rotation for given annulus.

10.2   Conclusions

This Section reflects on the results of the thesis, as summarized in Section 10.1, in the context of the objectives and scope formulated in Section 1.3. Recall the three objectives;

1. quantify the effects of experimentally observed yaw misalignment on rotor inflow and blade loads

2. identify the aerodynamic mechanisms governing the effects of yaw misalignment on rotor inflow and blade loads

3. assess the validity of semi-empirical submodels, used to patch BEM-theory; the Glauert momentum equation for yaw, induction non-uniformity corrections in yaw, airfoil dynamic stall models.

The accomplishment of these objectives requires intermediate milestones related to the execution and direct analysis of the experiments, presented in Section 10.2.1. The first objective is achieved with the implementation of the inverse vortex wake model, refer to Section 10.2.2. Objectives 2 and 3 are addressed in Section 10.2.3.

10.2.1   The rotor experiment

The objective of experimentally quantifying rotor inflow and blade loads first of all requires wind tunnel measurements on a model rotor. Present measurements in an open jet wind tunnel on a $1.2m$ diameter rotor fit this requirement. Their adequate documentation, including the assessment of wind tunnel wall corrections and measurement uncertainty, adds value for the scientific community, as it allows replication and modeling.

   The traditional technique to derive the Phase Locked Average PLA three-dimensional flow velocity from the single-film CTA measurements only solves for the magnitude of the flow velocity; the direction is left for the experimenter to specify. This limitation severely hampers quantification of the flow velocity and subsequent identification of flow phenomena in the skewed near-wake. The data reduction technique proposed in this thesis is shown to derive both magnitude and direction of the PLA flow velocity. This novel technique thus is pivotal to achieve the three objectives.

   Measurements focus on yaw. Their credibility is based though on the quality of the reference axial flow recordings. Present recordings are satisfactory in that respect; trends in measured C_T, tip vortex paths and near-wake flow velocity are generally as expected from previously published experiments and models. Further, C_T measured from strain gauges and that obtained from

one-dimensional inviscid actuator disc theory agree within measurement uncertainty for a near-optimum operating condition.

Analysis of the experiments in yaw reveal the phenomena typically associated with misaligned rotors; measured tip vortex paths are skewed and the inflow in the near-wake behind the rotor plane is asymmetric. Experimentally observed trends are as expected from previously published rotor measurements.

The present suite of experiments in yaw yields a rather rare set of data, especially with the inclusion of PLA three-dimensional flow velocity in the skewed near-wake. In fact, the only other experiment known to yield PLA three-dimensional flow velocity in yaw is the 2006 EU-funded test campaign MEXICO, where data reduction and analysis are organized in IEA Annex XXIX Mexnext that is still ongoing at the time of writing this conclusion.

10.2.2 The inverse vortex wake model

Recordings at three planes parallel to the rotor, with downstream distances of $3.5 \cdot 10^{-2}$, $6.0 \cdot 10^{-2}$ and $9.0 \cdot 10^{-2} R_t$, where R_t is the rotor radius, clearly demonstrate the nonlinear downwind convection of the skewed wake. Consequently, the inflow *at* the rotor plane cannot be distilled in a straightforward manner from the near-wake measurements. Linear extrapolation would e.g. not do justice to the nonlinearities.

This observation affects meeting the objectives defined for this thesis, as all relate to rotor inflow. The objectives furthermore require blade loads, which are not recorded along the span. To enable both rotor inflow and sectional loads to be estimated from recordings, the inverse vortex wake model, a TUDelft physics-based measurement analysis tool, is further developed. Main current improvements include the discrete formulation and especially the extension towards cyclic unsteadiness, e.g. yaw.

The method works by first reconstructing the vortical wake structure from experiments. Conservation of circulation, the Biot-Savart law and measurements of the induced velocity are then combined to result in a system of equations, which is solved for the unknown bound circulation. Successful verification and validation aids to establish confidence in the method.

The inverse vortex wake model is applied to a reference, near-optimum axial flow condition and two yawed flow conditions with marginal dynamic stall, as experimentally observed. With the resulting estimates of the inflow in the rotor plane and at the lifting line and of sectional blade loads, the first objective of the thesis is effectively achieved.

10.2.3   Flow mechanisms & assessment of predictive models

Analysis of blade loads and rotor inflow for the reference axial condition and the two yawed flow cases is generally performed in the context of Blade Element Momentum BEM modeling. To give a concrete example; the mechanisms driving the patterns in the annular averaged axial induction factor are studied, since this variable is associated with the wake momentum deficit model in BEM. The efforts to achieve the second and third objective listed above are thus typically intertwined.

The inverse vortex wake model is first employed to study flow phenomena in the reference near-optimum axial flow condition. The findings from this tool confirm the quality of the axial flow measurements established from the direct analysis of measurements. Next, it can be concluded that the flow physics of this condition are generally captured adequately with the one-dimensional BEM model. Moreover, the near-wake flow is found to convect quasi-linearly downstream. Lastly, this reference axial flow condition is demonstrated to yield marginal flow separation and stall; only towards the root, sectional lift coefficient c_l is found to be reduced compared to that expected from airfoil tables at given angle-of-attack α, an effect driven by three-dimensional flow disturbances.

Turning to yawed flow conditions, the inverse vortex wake model estimates of blade loads and inflow in the rotor plane and at the lifting line offer a unique chance to study flow phenomena in the skewed wake. The study focusses on three elements; the unsteady blade aerodynamics and resulting loads, the relation between wake momentum loss and induced flow velocity at the rotor plane and the mechanisms driving the cyclic unsteadiness of the inflow at the lifting line. From the viewpoint of BEM modeling, these items address the validity of unsteady airfoil models, the Glauert momentum model and non-uniformity corrections to the induced velocity.

Unsteady blade aerodynamics & resulting loads

The blade loads analysis first of all confirms the direct observation of near-wake flow velocity measurements that the yawed flow cases considered do not yield substantial spanwise regions of dynamic stall during a rotation. Its absence eliminates the additional complexity that dynamic stall would pose to the analysis of the aerodynamics of the yawed rotor.

Also without dynamic stall, yaw introduces unsteady blade loads. The experimental c_l-hysteresis found with the inverse vortex wake model increases going inboard and to more severe yaw angle. Actuator line modeling with either the Øye or the Beddoes-Leishman dynamic stall model does note reproduce the extent of the experimental hysteresis. Differences are hypothesized

to originate from measurement uncertainty and from not applying trip strips on the model blades; unsteady boundary layer phenomena related to the relatively low Reynolds numbers of the experiments, which are not included in the unsteady blade models, could have occurred in the tests. None of these hypotheses can be ruled out at present state.

Wake momentum loss

The study on wake momentum loss in yaw compares the sectional thrust coefficient c_t obtained from blade load estimates with that found from the Glauert momentum equation. The latter approach feeds the annular averaged induced axial velocity in the rotor plane, estimated from the inverse vortex wake model, to the Glauert momentum equation to compute c_t. Even up to the most severe yaw angle of $45°$, the agreement in c_t is reasonable across the blade span, especially outboard. It can thus be concluded that the empirical Glauert momentum equation holds, by approximation, for given yawed rotor measurements.

Based on these findings, BEM codes do not require an engineering correction to the Glauert momentum model. Sant [147] concludes from the same set of measurements that this momentum equation needs tuning. This paradox stems from the means to determine the inflow in the rotor plane; where Sant linearly extrapolates the measured near-wake flow velocity, here the nonlinear inverse vortex wake model is used. Adequately accounting for the nonlinearity in the skewed wake hence drives the physical interpretation.

Nonuniform inflow

In yaw, the induced velocity in the rotor plane is distributed nonuniformly for given annulus, driven by the asymmetric vortical wake. Analysis of present measurements with the inverse vortex wake model yields this nonuniformity. Even more so, this study is the first to break down experimental induction factors into their constituting components from the tip and root vortices, trailed and shed mid-span vortex sheet.

Whilst the shed vortex sheet induces a marginal contribution to the total induced flow velocity at the rotor plane, the effects of the trailed vortex sheet and especially root and tip vortices are relevant. Tip vortices induce an approximately 1P-sinusoidal flow field at the rotor plane. The distribution of flow velocity induced by root vortices is characterized by higher (than 1P) harmonics; notably, a strong local minimum of the axial induction factor is found inboard, with the blade oriented downwind.

Experimental induced axial velocity trends in the yawed rotor plane generally confirm those predicted with simplified vortex wake models, developed

to derive induced flow nonuniformity corrections for BEM in yaw, when these not only include tip but also root vortices. For the developers of these corrections models, current measurements are valuable; the estimated experimental sectional blade loads and rotor inflow allow them to further develop and/or validate their models. Especially the breakdown of induced flow velocity at the rotor plane into its constituting elements is an insightful experimental asset.

10.3 Recommendations

Before diving into the deep with detailed recommendations on yawed flow aerodynamics, let's start to advocate good rotor measurement practise;

1. Provide a description of the experimental geometry and flow conditions that is adequate for independent modeling of the tests

2. Acknowledge Reynolds number disparity between measurements and full-scale and anticipate need for mitigation of Reynolds effects

3. Quantify wind tunnel interference, addressing both general blockage phenomena as well as specifics of the wind tunnel setup used; e.g. relative position of instruments

4. Perform rotor thrust - and optionally also power - coefficient recordings across range of operating conditions that is preferably substantially wider than that used for the detailed rotor measurements

5. Quantify wind tunnel interference, addressing both general blockage phenomena as well as specifics of the wind tunnel setup used; e.g. relative position of instruments. For the method to derive the general interference, refer to e.g. Glauert [62], where detailed quantification might require numerical flow modeling

6. Use structured methods, e.g. AIAA standard [3] and guide [4], to a-priori design for controlled, acceptable measurement uncertainty and to posteriori quantify effective measurement uncertainty

Items 1-3 allow the setup of an independent model, aimed to reproduce the measurements. Items 4 - 6 then enable quantified model validation.

A next recommendation is the rather trivial suggestion that wind tunnel studies of rotor aerodynamics should encompass both experimental wake flow as well as blade loads. Though trivial, its implications are rather dramatic, as typically small-scale rotor models do not allow the instrumentation to record detailed loads. The development of the inverse vortex wake model in this thesis is a direct consequence hereof. When detailed load recordings are not

available, the experimenter is advised to employ such a model in order to estimate the experimental blade loads.

In yaw, the use of an inverse vortex wake model is of particular relevance to estimate blade loads and inflow in the rotor plane, as the analyzes in this thesis clearly demonstrate the nonlinearity of the near-wake. Without a tool to adequately capture these nonlinear effects, the experimenter might draw conclusions from his experiments that prove to be substantially off the mark.

A further recommendation concerns the selection of the appropriate technique to record the flow velocity in the rotor wake. Current experimental campaign employs hot-film CTA to this end. At first sight, this technique might appear out-of-date compared to Particle Image Velocimetry PIV, which is a trending topic amongst wind tunnel experimentalists. On second thought though, hot-film CTA enables use of an inverse vortex wake model as a measurement analysis tool, because experimental *PLA*, *three*-dimensional flow velocity can be quantified.

Compared to hot-film CTA, PIV is known to non-intrusively and more efficiently record the flow velocity, as a certain area - or volume with stereo-PIV - is recorded at once, instead of the point recording with CTA. Further, PIV allows measurements in the rotor plane, in proximity to the blades. Acknowledging these features of PIV and their potential to capture detailed flow phenomena, it's perfectly justifiable to use PIV instead of CTA for rotor wake studies.

An inverse vortex wake model remains a valuable approach though to analyze the rotor flow recorded with PIV; availability of the experimental vortex system implicitly aids the understanding between recorded flow phenomena and vortex dynamics. Furthermore, the analysis tool facilitates direct comparison to BEM models. When aiming to use an inverse vortex wake model with PIV measurements of the rotor wake, the PIV method should allow for derivation of the PLA three-dimensional flow velocity.

The final recommendations appeal to developers and users of BEM methods. The assessments done in this thesis suggest that for the 2 yawed flow cases studied in detail, Glauert momentum model predictions agree reasonably with measured wake deficit. These results do not justify any significant modification to the Glauert momentum model.

Furthermore, this thesis addresses the nonuniformity correction that modifies the annular averaged induction factor to that at the blade. The nonuniformity is experimentally confirmed to be governed by a sinusoidal effect from tip vortices and higher harmonics from root vortices, with a particularly strong negative axial induction factor in the inboard region, with the blade oriented downwind. The BEM modeling community is encouraged to implement nonuniformity correction methods that comply with given tip and root vortex effects.

Appendix A

Test matrix

The experimental campaign on the model rotor in the TUDelft open jet wind tunnel is summarized in Table A.1. All test conditions are corrected for wind tunnel interference, except those at $\Psi = 15°$, where such corrections are not available. The term "blade" under the heading "test conditions" refers to use of trip strips on the blade nose; these are applied to prevent unsteady laminar separation bubbles during dynamic stall events.

The last four columns of the table refer to the experimental techniques used, with abbreviations

- **C_T**: rotor thrust coefficient measurements using strain gauges in the blade root

- **flow vis**: quantitative visualization of the tip vortex paths up to about 1 rotor radius R_t downstream using smoke

- **tufts**: visualization of flow separation on the blade suction side along its span using wool tufts

- **CTA**: three-dimensional flow velocity measurements at three near-wake planes, with $z/R_t = 5.83 \cdot 10^{-2}$, $1.00 \cdot 10^{-1}$ and $1.50 \cdot 10^{-1}$ using Constant Temperature Anemometry with a single-sensor hot-film

- **qualitative CTA**: single-sensor hot-film CTA in the near-wake plane with $z/R_t = 5.83 \cdot 10^{-2}$, which is equivalent to $z/c = 4.38 \cdot 10^{-1}$, to record an effective flow velocity signal as qualitative measure of blade flow separation

All measurements are unsteady and reduced to Phase-Locked Averages. For C_T, test matrix A.1 further documents cyclic averages.

Test conditions				Measurements			
Ψ	λ	β_{pitch}	blade	C_T	flow viz	tufts	CTA
[°]	[-]	[°]	[-]				
0	5.9	0	clean	0.73	x		
0	5.9	2	clean	0.64	x		
0	5.8	4	clean	0.55	x		
0	7.9	0	clean	0.92	x		
0	7.9	2	clean	0.78	x		x
0	7.9	4	clean	0.62	x		
0	10.0	0	clean	1.02	x		
0	9.9	2	clean	0.83	x		
0	10.0	4	clean	0.58	x		
15	6	0	clean	0.72	x		
15	6	2	clean	0.64	x		
15	6	4	clean	0.55	x		
15	8	0	clean	0.90	x		
15	8	2	clean	0.76	x		
15	8	4	clean	0.60	x		
15	10	0	clean	0.99	x		
15	10	2	clean	0.78	x		
15	10	4	clean	0.52	x		
30	6.0	0	clean	0.71	x		
30	6.0	2	clean	0.62	x		
30	6.0	4	clean	0.52	x		
30	8.0	0	clean	0.85	x		
30	8.0	2	clean	0.70	x		x
30	8.0	4	clean	0.51	x		
30	10.0	0	clean	0.95	x		
30	10.0	2	clean	0.71	x		
30	10.1	4	clean	0.39	x		
45	5.5	2	strip			x	x[a]
45	6.1	0	clean	0.59	x		
45	6.1	2	clean	0.49	x		
45	6.1	4	clean	0.37	x		
45	8.1	0	clean	0.73	x		
45	8.1	2	clean	0.53	x		x
45	8.1	2	strip			x	x[a]
45	8.1	4	clean	0.30	x		
45	10.1	0	clean	0.81	x		
45	10.1	2	clean	0.52	x		
45	10.1	4	clean	0.15	x		

[a] qualitative CTA

Table A.1: Summary test matrix

Appendix B

Near-wake flow symmetry

Consider a rotor operating in the wind turbine state, with coordinate systems as sketched in Figure B.1. Axial flow conditions, with $\Psi = 0°$, ideally result in stationary flow variables in the near-wake for an observer rotating with the blades.

The number of degrees-of-freedom is consequently reduced from four to three,

$$X\left(r, \theta, z, \theta_b\right) = X\left(r, \Delta\theta, z\right),$$
(B.1)

with $\Delta\theta = \left(\theta_b - \theta\right) mod\, 360°$ and X a flow variable. X can be substituted by e.g. the static pressure p or the flow velocity $\vec{V}$.
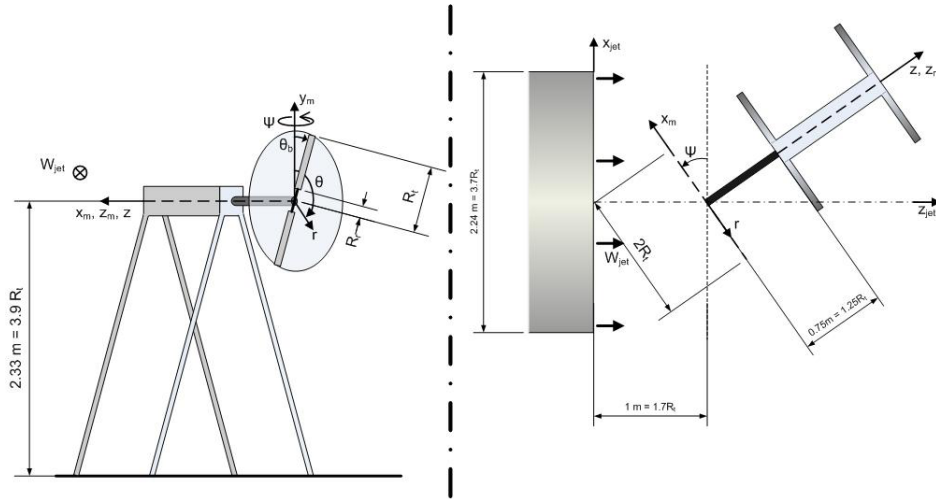
Figure B.1: A schematic rotor, the free stream wind and related coordinate systems. Left plot: front view, looking in downwind direction, right plot: top view.

The flow field satisfying Equation [B.1] is named rotating stationary. Note that the term axisymmetric would not be appropriate, since the axisymmetry condition $\partial X / \partial \theta = 0$ generally does not hold.

In yaw, the near-wake is asymmetric, i.e. skewed. Consequently, Equation [B.1] does not hold for $\Psi \neq 0°$. For an observer rotating with the blades, the near-wake flow in yawed flow conditions is not rotating stationary, but cyclicly unsteady.

Appendix C

Actuator line model

C.1   Model concept

The actuator line method, introduced by Sørensen and Shen [186], couples a blade model to a rotor wake that is modeled by the NS equations. Originally, the NS equations are expressed in the $(V - \omega)$-formulation, with ω the vorticity. Mikkelsen [128] rewrites the method in $(p - V)$-formulation, with p the pressure, and combines it with EllipSys3D, a general purpose incompressible RANS flow solver developed by Sørensen [189] and Michelsen [126, 127]. The EllipSys3D code allows for parallel computing. As a further development of the actuator line technique, Shen *et al.* [169] propose the implementation of a new tip loss correction model. Present results are based on Mikkelsen's version of the actuator line method and are in part obtained using a cluster of computers.

The three-dimensional NS equation that governs conservation of fluid momentum accounts for blade loads $\vec{f}_b$ by introducing the body force $\vec{f}$ as a source term along lines representing the blades; the actuator lines,

$$\rho \frac{D\vec{V}}{Dt} = \vec{f} - \nabla p + \mu \nabla^2 \vec{V}. \tag{C.1}$$

$\vec{f}$ is derived from $\vec{f}_b$ that is in turn determined from the velocity computed along the actuator lines using a blade model, similar to the procedure for a BEM or vortex wake model.

To avoid singular behavior, whilst conserving the integrated loading, the blade load $\vec{f}_b$ is introduced as the source term $\vec{f}$ that is smoothly distributed instead of concentrated along a line, taking the convolution of $\vec{f}_b$. The body force $\vec{f}_\epsilon{}^i$ at point $\vec{x}$ associated with the blade load per unit span at a given radial station $\vec{r}$ of an actuator line $\vec{f}_b{}^i$ is given by

$$\vec{f}_\epsilon{}^i(\vec{x}) = \vec{f}_b{}^i(\vec{r}) \otimes \eta_\epsilon(d), \qquad \eta_\epsilon(d) = \frac{1}{\epsilon^3 \pi^{3/2}} \exp\left[- (d/\epsilon)^2 \right]. \tag{C.2}$$

Here, the suffix i indicates the actuator line considered, with $i = 1, \ldots, B$ and B the number of actuator lines, η_ϵ is a regularization kernel, d is the distance between $\vec{x}$ and $\vec{r}$ and ϵ is a constant that serves to adjust the concentration of $\vec{f}_\epsilon^{\,i}$. The regularized body force at $\vec{x}$ resulting from the blade force acting on all actuator line radial stations hence becomes

$$\vec{f}_\epsilon(\vec{x}) = \sum_{i=1}^{B} \int_0^{R_t} \vec{f^i}(r)\eta_\epsilon d d r. \tag{C.3}$$

For a 'normal' RANS model, the blade loads are found by solving the flow field around the blades, requiring a fine grid near the blades to capture the details of the flow. The actuator line model allows the grid resolution near the blades to be coarser than that for a 'normal' RANS model, since blade loads are derived from a blade model instead. The actuator line code hence yields a relatively economic means of numerically studying wake aerodynamics in RANS-formulation.

C.2 Numerical domain & boundary conditions

The wind tunnel experiments on the TUDelft model rotor are modeled with the actuator line method. The open jet wind tunnel is not included in the modeling, the flow conditions corrected for wind tunnel wall effects are computed instead. Two types of numerical domains are used, see Figure C.1;

- **axial flow**: the operating conditions are assumed to yield rotating stationary flow, refer to Appendix B. Half of the physical domain is hence discretized for the two-bladed rotor model. The numerical domain is a cylinder with a semi-circular cross-section that rotates with the blades and extends $10R_t$ upstream, $15R_t$ downstream and $16R_t$ outboard of the rotor hub.

- **yawed flow**: lack of flow symmetry in yaw requires the full physical domain to be discretized. The numerical domain is a rectangular box that measures $32R_t$ in height, $32R_t$ in width and $30R_t$ in length (direction of the undisturbed flow), with the rotor located at the box center.

Grid cells are concentrated in the near domain extending from about $1R_t$ upstream to $1R_t$ downstream of the rotor plane and $1R_t$ radially outboard from the rotor hub, see Figure C.1, to accurately capture the near-wake flow. Grid nodes in the near domain are distributed equidistantly in each direction, with the rotor radius discretized by 31 nodes. Outside of the near domain, cells are stretched towards the outer boundaries. Domain and grid dependency studies
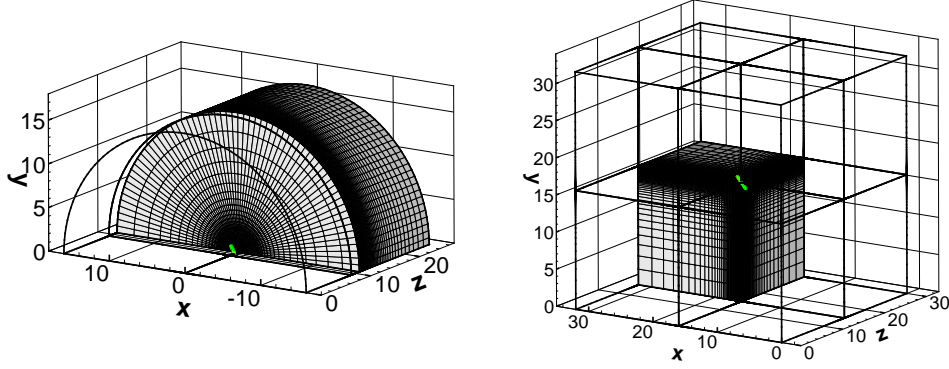
Figure C.1: Grids for the actuator line method, with nodes concentrated near the actuator lines. Left: cylindrical grid, with symmetry plane, used for axial flow conditions. Right: rectangular box grid, used for yawed flow conditions.

suggest that the domain dimensions and grid resolutions presented here are an acceptable compromise between accuracy and computational cost.

The boundary conditions imposed at the domain boundaries are:

- for both axial and yawed flow domains:

  - at the **upstream boundary**: inflow condition, uniform and constant velocity, equal to undisturbed velocity, $V_z = W_0$, $V_{x,y} = 0$.

  - at the **downstream boundary**: outflow condition, zero velocity gradient normal to the downstream boundary, $\partial \vec{V}/\partial z = 0$.

- for the axial flow domain:

  - at the **outer boundary**: far-field condition, uniform and constant velocity, equal to undisturbed velocity, $V_z = W_0$, $V_{x,y} = 0$.

  - at the **symmetry plane**: cyclic condition

- for the yawed flow domain:

  - at the **lateral boundaries**: cyclic condition,

  - at the **top & bottom boundaries**: far-field condition

It must be noted that the diffusion term $\mu\nabla^2\vec{V}$ in the NS-equations [C.1] is at present only intended to stabilize the solution; the present grid resolution is too coarse to model turbulence. The laminar formulation of the NS equations

239

is consequently employed [1]. The rotor Reynolds number, $Re_r = \rho W_0 R_t / \mu$, is set to $Re_r = 2 \cdot 10^3$, which is substantially lower than the actual experimental value for Re_r. Sørensen and Shen [186] discuss however that, equivalent to bluff bodies, the effect of Re_r on the flow behavior is limited when a given threshold is exceeded. At the blades, where vorticity is produced, Re-effects are considered through application of Re_c-dependent airfoil data in the blade models, with Re_c the chord Reynolds number. Note that for actuator line simulations of the Tjæreborg rotor, Mikkelsen [128] also applies $Re_r = 2 \cdot 10^3$.

---

[1] The laminar formulation is not used by default; Troldborg *et al.* [198] e.g. describe a version of the actuator line model where turbulence is modeled using a Large Eddy Simulation.

Appendix D

Airfoil dynamic stall models

D.1   Steady baseline: measurements

The axial flow conditions are computed using an airfoil model that is given by static NACA0012 characteristics at $Re_c = 1.5 \cdot 10^5$ measured by Timmer and Vermeer, see Figure D.1 and recall Section 3.1. The measurements show an abrupt stall behavior. The sudden c_l-loss at the stall angle of attack, $\alpha_{stall} = 10.6°$, can be attributed to bursting of the laminar separation bubble on the airfoil suction surface leading edge. Laminar separation bubbles are also responsible for the nonlinear c_l-variation at low α.

The model does not account for Re_c-variations; whilst the Re_c-range across the blade, for all axial flow conditions considered, is estimated at $0.6 \cdot 10^5 \leq Re_c \leq 2.9 \cdot 10^5$, the data measured at $Re_c = 1.5 \cdot 10^5$ is used throughout. Furthermore, the stall delay effect in the root region, named also after its discoverer the Himmelskamp effect [90], is not corrected for. Both unsteady airfoil models studied currently are based on the static measurement data as well.

D.2   Øye dynamic stall model

The first unsteady airfoil model to be selected for actuator line computations of the yawed flow conditions is the semi-empirical dynamic stall model proposed by Øye [135], based on unsteady trailing edge separation only. Trailing edge separation is the phenomenon that the boundary layer detaches from the airfoil upstream of the trailing edge, resulting in a loss of lift compared to the fully attached potential flow situation. In general, the separation point moves upstream gradually when α is increased. While progressive trailing edge separation generally results in static stall[1] on relatively thick airfoils, at $Re_c > 10^6$, most other airfoils also experience trailing edge separation to some extent.

---

[1]Hence the term trailing edge stall

Figure D.1: Measured NACA0012 airfoil characteristics at $Re_c = 1.5 \cdot 10^5$. Left: c_l versus α, right: the drag polar.

The separation point does not respond instantaneously to varying flow conditions. When an airfoil is subject to unsteady flow conditions, the *dynamic* separation point thus lags the corresponding *static* separation point. In the Øye model [135], a first order Ordinary Differential Equation (ODE) describes the lag in the dynamic separation point. The ODE requires an empirical time constant τ. Currently, $\tau = 4c/|V_{rel}|$ is selected.

The lag in the dynamic trailing edge separation point for an airfoil subject to unsteady inflow conditions results in a lift overshoot from the static stall value when dynamically exceeding the static stall angle. The lift overshoot hysteresis loops provide aerodynamic damping to a rotor aero-elastic model[2]. Airfoil load predictions obtained with the relatively simple Øye model are not expected to closely match measurements however, since the dynamic stall vortex that significantly affects the airfoil loads is not modeled.

---

[2]The development of the Øye model was driven by the lack of aerodynamic damping present in wind turbine aero-elastic computations of dynamic stall conditions using static airfoil data only, compared to field measurements.

D.3 Beddoes-Leishman dynamic stall model

Leishman and Beddoes [113, 114] elaborate on a model developed by Beddoes [21] to arrive at a comprehensive semi-empirical dynamic stall model[3]. The Beddoes-Leishman dynamic stall model is selected to be the second unsteady airfoil model used for actuator line computations of the yawed flow conditions. The method combines four semi-empirical models of physical phenomena [110]; an unsteady potential flow model for linear loads, an unsteady trailing edge separation model for nonlinear loads, an unsteady leading edge pressure model for dynamic stall onset and a dynamic stall model for load associated with the dynamic stall vortex. At present, the Beddoes-Leishman model is implemented in the indicial formulation.

Tuning of the model responses for a specific airfoil at a specific Mach number M and Re_c is done through a limited number of empirical coefficients that depend on both static and unsteady airfoil measurements. The present discussion focusses on the considerations driving the quantification of the empirical coefficients, without first introducing them in detail. For an in-depth introduction, the interested reader is referred to Leishman and Beddoes [113, 114], where the notations of the empirical coefficients correspond to those used here[4].

Only for a selected number of airfoils, at selected M and Re_c, all empirical coefficients are readily available. The coefficients for other airfoils and/or operating conditions should either be derived from dedicated airfoil measurements or be estimated. For the yawed flow cases computed with the actuator line model, the operating conditions across the blade are estimated at $M \leq 0.15$ and $0.5 \cdot 10^5 \leq Re_c \leq 2.7 \cdot 10^5$. The static NACA0012 airfoil data measured for low speed flow conditions with $Re_c = 1.5 \cdot 10^5$, see Figure 3.5, are considered to be representative for this range of modeled operating conditions. The static empirical coefficients shown in Table D.1 that are derived from this data set are consequently used throughout the computations.

Quantification of the two remaining static empirical coefficients η and C_{n_1}, given in Table D.2, is based on Leishman and Beddoes [113, 114] instead. The

---

[3]The Beddoes-Leishman dynamic stall model has initially been developed for helicopters, hence its focus on the airfoil pitching moment, that is not discussed here as it is not essential to wind turbines.

[4]It should be noted that Leishman and Beddoes [113, 114] do not introduce C_3, a_3, S_3 and α_2, given in Table D.1. These coefficients are associated with a minor modification; Equation [D.1] is extended with a third term,

$$f = \begin{cases} C_1 + a_1 \, exp \left[(\alpha - \alpha_1) / S_1 \right] & \alpha \leq \alpha_1 \\ C_2 + a_2 \, exp \left[(\alpha_1 - \alpha) / S_2 \right] & \alpha_1 \leq \alpha \leq \alpha_2 \\ C_3 + a_3 \, exp \left[(\alpha_2 - \alpha) / S_3 \right] & \alpha \geq \alpha_2 \end{cases} \tag{D.1}$$

.

Table D.1: Beddoes-Leishman empirical coefficients based on *static* airfoil data. Values derived from NACA0012 data for $Re_c = 1.5 \cdot 10^5$, shown in Figure 3.5.

c_1	a_1	S_1	c_2	a_2	S_2	c_3	a_3	S_3	α_1	α_2
1.0	-0.3	0.8	0.1	0.6	4.6	0.0	0.24	0.5	3.81°	10.6°

recovery factor η accounts for not realizing the chord force that would be obtained in static potential flow. Leishman and Beddoes [114] suggest that $\eta = 0.95$ is a typical value.

The critical normal force coefficient C_{n_1} is the normal force coefficient C_n at the onset of static leading edge separation. Pierce [139] notes that when the flow around an airfoil is characterized by a reattaching separation bubble (as is the case here) or gentle trailing edge separation, c_N obtained for fully attached flow should be extrapolated to the angle of attack at maximum c_N to arrive at c_{N_1}, instead of choosing the maximum value of c_N for c_{N_1}. Hence although the NACA0012 airfoil measurements at $Re_c = 1.5 \cdot 10^5$, shown in Figure 3.5, yield $C_n = 0.87$ at stall, presently $C_{n_1} = 1.45$ is selected, which corresponds to that given by Leishman and Beddoes [113] for a NACA0012 airfoil at $M = 0.3$, $Re_c = 2.4 \cdot 10^6$.

Table D.2: Beddoes-Leishman empirical coefficients based on *static* airfoil data. η suggested in [114], C_{n_1} given in [113] for NACA0012 at $M = 0.3$, $Re_c = 2.4 \cdot 10^6$.

η	C_{n_1}
0.95	1.45

The five unsteady empirical coefficients, given in Table D.3, are related to the time scales of unsteady separated flow phenomena and are quantified using contributions from unsteady airfoil measurements. No unsteady empirical coefficients are available for the NACA0012 airfoil within the range of modeled operating conditions, however. The unsteady empirical coefficients presented by Beddoes and Leishman [113] for validation experiments on the NACA0012 at $M = 0.30$, $Re_c = 2.4 \cdot 10^6$ are used instead across the blade, for all yawed flow conditions studied, notwithstanding the significant differences between the operating conditions; more appropriate data was not available to the author at the time of performing the research. Validation studies of the Beddoes-Leishman dynamic stall model [113, 70] suggest however that the variation in the unsteady empirical constants over a range of operating conditions and

airfoils is minor. It must be noted that future studies on the aerodynamics of (model) wind turbines using the Beddoes-Leishman dynamic stall model could benefit from model improvements for low M conditions proposed recently by Sheng, Galbraith and Coton for dynamic stall onset [170, 171] and stall recovery [172].

Table D.3: Beddoes-Leishman empirical coefficients based on *unsteady* airfoil data. Values given in [113] for NACA0012 at $M = 0.3$, $Re_c = 2.4 \cdot 10^6$.

T_p	T_f	T_{vl}	T_v	D_f
1.7	3.0	7.0	6.0	8.0

Bibliography

[1] *Climate change: Commission welcomes final adoption of Europe's climate and energy package.* European Commission, reference: IP/08/1998 17/12/2008.

[2] Aiaa guide for the verification and validation of computational fluid dynamics simulations. Technical Report G-077-1998, AIAA, Reston, VA., USA, January 1998.

[3] Assessment of experimental uncertainty with application to wind tunnel testing. Technical Report S-071A-1999, AIAA, Reston, VA., USA, 1999.

[4] Assessing experimental uncertainty - supplement to aiaa s-071a-1999. Technical Report G-045-2003, AIAA, Reston, VA., USA, 2003.

[5] *External Costs. Research results on socio-environmental damages due to electricity and transport.* EU 20198. European Commission, 2003.

[6] *Guideline for the certification of wind turbines. Edition 2003 with supplement 2004.* Germanischer Lloyd, Hamburg, Germany, 2004.

[7] *Climate Change 2007: Synthesis Report. Contribution of Working Groups I, II and III to the Fourth Assessment Report of the Intergovernmental Panel on Climate Change.* Intergovernmental Panel on Climate Change, Geneva, Switzerland, 2007.

[8] E-126 prototype - world's most powerful wind turbine installed near emden. Windblatt, Issue 04, 2007.

[9] *Key world energy statistics 2008.* International Energy Agency, 2008. For online statistics, see: $http://www.iea.org/Textbase/stats/index.asp$.

[10] *Pure Power. Wind energy scenarios up to 2030.* European Wind Energy Association, March 2008.

[11] *Global wind report, annual market update 2010.* Global Wind Energy Council, March 2011.

[12] *International Energy Annual 2006.* United States Department of Energy, Energy Information Administration, June-December 2008.

[13] Nuclear Energy Agency & International Energy Agency. *Projected costs of generating electricity - 2005 update.* Organisation for Economic Co-Operation and Development, 2005.

[14] I. Ammara, C. Leclerc, and C. Masson. A viscous three-dimensional differential/actuator disc method for the analysis of wind farms. *Journal of Solar Energy Engineering*, Vol. 124, No. 4:345–356, 2002.

[15] J.D. Anderson. *Fundamentals of Aerodynamics, second edition.* McGraw-Hill, New York, NY., USA, 1991.

[16] G. Arsuffi. A general formulation for aerodynamic analysis of wind turbine. In *Proceedings of the second IEA symposium on the aerodynamics of wind turbines*, Lyngby, Denmark, 1988. IEA.

[17] A. Bagai and J.G. Leishman. Rotor free-wake modelling using a pseudo-implicit technique-including comparisons with experimental data. *Journal of the American Helicopter Society*, 40:29–41, July 1995.

[18] M. Baragona. *Unsteady characteristics of laminar separation bubbles - an experimental and numerical investigation.* PhD thesis, Delft Technical University, Delft, The Netherlands, December 2004.

[19] R. Bareiss and S. Wagner. Free wake/hybrid code rovlm - a tool for aerodynamic analysis of wind turbines. In *Proceedings 1993 European Community wind energy conference*, pages 424–427, Lűbeck-Traveműnde, Germany, March 1993.

[20] R. Bareiss and S. Wagner. A hybrid wake model for hawt. In K. McAnulty, editor, *Proceedings of the sixth IEA symposium on the aerodynamics of wind turbines*, pages 7.1–7.10, Lyngby, Denmark, 1993. IEA.

[21] T.S. Beddoes. Representation of airfoil behavior. *Vertica*, Vol. 7:183–197, 1983.

[22] A. Betz. Das maximum der theoretisch moglichen ausnutzung des windes durch windmotoren. *Zeitschrift für das gesamte Turbinenwesen*, pages 307–309, 1920.

[23] A.R.S Bramwell. Some remarks on the induced velocity field of a lifting rotor and on glauert's formula. Technical Report Current Papers: C.P. no. 1301, Aeronautical Research Council, 1974.

248

[24] A.R.S. Bramwell. *Helicopter dynamics*. Edward Arnold Publishers Ltd, 1976.

[25] J.A. Brander and M.S. Taylor. The simple economics of easter island: A ricardo-malthus model of renewable resource use. *The American economic review*, Vol. 88, Issue 1:119–138, 1998.

[26] H. H. Bruun. *Hot-Wire Anemometry*. Oxford Science Publications, Oxford, England, 1995.

[27] Tony Burton, David Sharpe, Nick Jenkins, and Ervin Bossanyi. *Wind Energy Handbook*. Wiley, Chichester, England, 2001.

[28] G.J.W. van Bussel. Induced velocity distributions and axial loads on yawed rotors. In *EWEC*, Thessaloniki, Greece, October 1994.

[29] G.J.W. van Bussel. *The aerodynamics of horizontal axis wind turbine rotors explored with asymptotic expansion methods*. PhD thesis, Delft University of Technology, Delft, The Netherlands, 1995.

[30] C.P. Butterfield, W.P. Musial, G.N. Scott, and D.A. Simms. Nrel combined experimental final report - phase ii. Technical Report NREL/TP-442-4807, NREL, Golden, CO., USA, 1992.

[31] C.P. Butterfield, D.A. Simms, W.P. Musial, and G.N. Scott. Nrel combined experiment - phase i final report. Technical Report NREL/TP-257-4655, NREL, Golden, CO., USA, 1992.

[32] J.J. Chattot. Design and analysis of wind turbines using helicoidal vortex model. *Computational Fluid Dynamics Journal*, Vol. 11, Issue 1:50–54, 2002.

[33] J.J. Chattot. Optimization of wind turbines using helicoidal vortex model. *Journal of solar energy engineering*, Vol. 125, Issue 4:418–424, 2003.

[34] J.J. Chattot. Helicoidal vortex model for steady and unsteady flows, aiaa-2004-0829. In *23rd ASME Wind Energy Symposium, 42nd Aerospace Sciences Meeting and Exhibit*, Reno, NV., USA, January 2004.

[35] R.P. Coleman, A.M. Feingold, and C.W. Stempin. Evaluation of the induced velocity field of an idealised helicopter rotor. Technical Report NACA WRL-126, NACA, 1945.

[36] A.T. Conlisk. Modern helicopter rotor aerodynamics. *Progress in Aerospace Sciences*, 37:419–476, 2001.

249

[37] G.P. Corten. *Flow Separation on Wind Turbine Blades.* PhD thesis, Utrecht University, Utrecht, The Netherlands, 2001.

[38] F.N. Coton and T. Wang. The prediction of horizontal axis wind turbine performance in yawed flow using an unsteady prescribed wake model. *proc. of the institution of mechanical engineers, part a, journal of power and energy*, 213:33–43, 1999.

[39] F.N. Coton, T. Wang, and R.A. McD. Galbraith. An examination of key aerodynamic modelling issues raised by the nrel blind comparison. *Wind Energy*, Vol. 5, No. 2-3:199–212, April - September 2002.

[40] C. Crawford and J. Platts. Updating and optimization of a coning rotor concept. *Journal of Solar Energy Engineering*, Vol. 130, No. 3, 2008.

[41] C.A. Crawford. *Advanced Engineering Models for Wind Turbines with Application to the Design of a Coning Rotor Concept.* PhD thesis, University of Cambridge, Cambridge, England, October 2006.

[42] J. Å. Dahlberg and D. Medici. Potential improvement of wind turbine array efficiency by active wake control (awc). In *Proceedings of the European Wind Energy Conference and Exhibition*, Madrid, Spain, June 2003.

[43] H. Dexin, C. Ming, J-Å Dahlberg, and G. Ronsten. Flow visualization on a rotating wind turbine blade. Technical Report FFA TN 1993-28, FFA, Bromma, Sweden, 1993.

[44] K.R. Dixon. The near wake structure of a vertical axis wind turbine, including the development of a 3d unsteady free-wake panel method for vawts. Master's thesis, Faculty of Aerospace Engineering, Delft University of Technology, Delft, The Netherlands, 2008.

[45] M. Drela. Xfoil: An analysis and design system for low reynolds number airfoils. In T.J. Mueller, editor, *Low Reynolds number aerodynamics : proceedings of the conference*, Berlin, New York, 1989. Springer Verlag.

[46] E.P.N. Duque, M.D. Burklund, and W. Johnson. Navier-stokes and comprehensive analysis performance predictions of the nrel phase vi experiment, aiaa-2003-0355. In *41st AIAA Aerospace Sciences Meeting and Exhibit*, Reno, NV., USA, January 2003.

[47] M. Van Dyke. *An album of fluid motion.* The parabolic press, Stanford, CA., USA, 2002.

[48] P.R. Ebert and D.H. Wood. The near wake of a model horizontal-axis wind turbine-i. experimental arrangements and initial results. *Renewable Energy*, Vol. 12, No. 3:225–243, 1997.

[49] P.R. Ebert and D.H. Wood. The near wake of a model horizontal-axis wind turbine-ii. general features of the three-dimensional flowfield. *Renewable Energy*, Vol. 18, No. 4:513–534, 1999.

[50] P.R. Ebert and D.H. Wood. The near wake of a model horizontal-axis wind turbine part 3: Properties of the tip and hub vortices. *Renewable Energy*, Vol. 22, No. 4:461–472, 2001.

[51] G. Espana, S. Aubrun, and P. Devinant. Is the meandering of a wind turbine wake due to atmospheric length scales? In J. Peinke, M. Oberlack, and A. Talamelli, editors, *Proceedings of the iTi conference in turbulence 2008*, pages 91–94, Bertinoro, Italy, 2008.

[52] L.J. Fingerish, D. Simms, M. Hand, D. Jager, J. Cotrell, M. Robinson, S. Schreck, and S. Larwood. Wind tunnel testing of nrel's unsteady aerodynamics experiment, aiaa-2001-0035. In *20th ASME Wind Energy Symposium, 39th AIAA Aerospace Sciences Meeting and Exhibit*, Reno, NV., USA, January 2001.

[53] O. Fleig, M. Iida, and C. Arakawa. Wind turbine blade tip flow and noise prediction by large-eddy simulation. *Journal of Solar Energy Engineering*, Vol. 126, Issue 4:1017–1024, November 2004.

[54] R.E. Froude. On the part played in propulsion by difference in pressure. *Transaction of the Institute of Naval Architects*, Vol. 30:390–423, 1889.

[55] A. van Garrel. Development of a wind turbine aerodynamics simulation module. Technical Report ECN-C–03-079, ECN, Petten, The Netherlands, August 2003.

[56] A. van Garrel. Integral boundary layer methods for wind turbine aerodynamics; a literature survey. Technical Report ECN-C–04-004, ECN, Petten, The Netherlands, December 2003.

[57] B.S. Gerber, J.L. Tangler, E.P.N. Duque, and J.D. Kocurek. Peak and post-peak power aerodynamics from phase vi nasa ames wind turbine data. *Journal of Solar Energy Engineering*, Vol. 127, No. 2:192–199, May 2005.

[58] B.M. Geurts. Modeling of a horizontal axis wind turbine with smart actuators. Master's thesis, Faculty of Aerospace Engineering, Delft University of Technology, Delft, The Netherlands, 2009.

251

[59] H. Glauert. The analysis of experimental results in the windmill brake and vortex ring states of an airscrew. Technical Report Technical Report No. 1026, Aeronautical Research Committee, London, UK, 1926.

[60] H. Glauert. A general theory for the autogyro. Technical Report ARC R & M 786, ARC, 1926.

[61] H. Glauert. *The elements of aerofoil and airscrew theory, second edition.* Cambridge University Press, Cambridge, England, 1947.

[62] H. Glauert. Airplane propellers. In W.F. Durand, editor, *Aerodynamic Theory*, chapter Division L, pages 169–360. Dover Publications, New York, NY., USA, 1963.

[63] G.H. Goankar and D.A. Peters. Effectiveness of current dynamic-inflow models in hover and forward flight. *Journal of American Helicopter Society*, Vol. 31, No. 2, 1986.

[64] G.H. Goankar and D.A. Peters. Review of dynamic inflow modelling for rotorcraft flight dynamics. *Vertica*, Vol. 2, No. 3:213–242, 1988.

[65] A. Gonzalez and X. Munduate. Three-dimensional and rotational aerodynamics on the nrel phase vi wind turbine blade. *Journal of solar energy engineering*, Vol. 130, Issue 3, 2008.

[66] I. Grant, M. Mo, X. Pan, P. Parkin, J. Powell, H. Reinecke, K. Shuang, F. Coton, and D. Lee. An experimental and numerical study of the vortex filaments in the wake of an operational, horizontal-axis, wind turbine. *Journal of wind engineering and industrial aerodynamics*, Vol. 85, No. 2:177–189, 2000.

[67] I. Grant and P. Parkin. A dpiv study of the trailing vortex elements from the blades of a horizontal axis wind turbine in yaw. *Experiments in Fluids*, Vol. 28, No. 4:368–376, 2000.

[68] I. Grant, P. Parkin, and X. Wang. Optical vortex tracking studies of a horizontal axis wind turbine in yaw using laser-sheet, flow visualisation. *Experiments in Fluids*, Vol. 23, No. 6:513–519, 1997.

[69] S. Gupta and J.G. Leishman. Comparison of momentum and vortex methods for the aerodynamic analysis of wind turbines, aiaa-2005-0594. In *24th ASME Wind Energy Symposium, 43th AIAA Aerospace Sciences Meeting and Exhibit*, Reno, NV., USA, January 2005.

[70] S. Gupta and J.G. Leishman. Dynamic stall modelling of the s809 aerofoil and comparison with experiments. *Wind Energy*, Vol. 9, No. 6:521–547, November/December 2006.

[71] S. Gupta and J.G. Leishman. Validation of a free-vortex wake model for wind turbines in yawed flow, aiaa-2006-0389. In *25th ASME Wind Energy Symposium, 44th AIAA Aerospace Sciences Meeting and Exhibit*, Reno, NV., USA, January 2006.

[72] W. Haans and R. Mikkelsen. Airfoil models in the actuator line code assessed with near-wake measurements on a yawed rotor, aiaa-2007-0424. In *26th ASME Wind Energy Symposium, 45th AIAA Aerospace Sciences Meeting and Exhibit*, Reno, NV., USA, January 2007.

[73] W. Haans, T. Sant, G.A.M. van Kuik, and G.J.W. van Bussel. Measurement and modelling of tip vortex paths in the wake of a hawt under yawed flow conditions, aiaa-2005-0590. In *24rd ASME Wind Energy Symposium, 43th AIAA Aerospace Sciences Meeting and Exhibit*, pages 136–145, Reno, NV., USA, January 2005.

[74] W. Haans, T. Sant, G.A.M. van Kuik, and G.J.W. van Bussel. Measurement of tip vortex paths in the wake of a hawt under yawed flow conditions. *Journal of Solar Energy Engineering*, Vol. 127, No. 4:456–463, November 2005.

[75] W. Haans, T. Sant, G.A.M. van Kuik, and G.J.W. van Bussel. Velocity measurements in the near wake of a horizontal axis wind turbine. In *31st European Rotorcraft Forum*, pages 61.1–61.14, Florence, Italy, September 2005.

[76] W. Haans, T. Sant, G.A.M. van Kuik, and G.J.W. van Bussel. Stall in yawed flow conditions: A correlation of blade element momentum predictions with experiments. *Journal of Solar Energy Engineering*, Vol. 128, No. 4:472–480, November 2006.

[77] W. Haans, T. Sant, G.A.M. van Kuik, and G.J.W. van Bussel. Stall in yawed flow conditions: a correlation of blade element momentum predictions with experiments, aiaa-2006-0200. In *44th AIAA Aerospace Sciences Meeting and Exhibit*, Reno, NV., USA, January 2006.

[78] W. Haans, T. Sant, G.A.M. van Kuik, and G.J.W. van Bussel. Hawt near-wake aerodynamics, part i: axial flow conditions. *Wind Energy*, Vol. 11, Issue 3:245–264, 2008.

[79] W. Haans, T. Sant, G.A.M. van Kuik, and G.J.W. van Bussel. Hawt near wake aerodynamics, part ii: Yawed flow conditions. *Wind Energy*, Under review:Under review, Under review.

253

[80] W. Haans, G.A.M van Kuik, and G.J.W. van Bussel. Experimentally observed effects of yaw misalignment on the inflow in the rotor plane. *Journal of Physics: Conference Series*, Vol. 75:012012, 2007.

[81] W. Haans, G.A.M. van Kuik, and G.J.W. van Bussel. The inverse vortex wake model: a measurement analysis tool, aiaa-2007-0422. In *26th ASME Wind Energy Symposium, 45th AIAA Aerospace Sciences Meeting and Exhibit*, Reno, NV., USA, January 2007.

[82] M.M. Hand, D.A. Simms, L.J. Fingersh, D.W. Jager, and J.R. Cotrell. Unsteady aerodynamics experiment phase v: test configuration and available data campaigns. Technical Report NREL/TP-500-29491, NREL, Golden, CO., USA, August 2001.

[83] M.M. Hand, D.A. Simms, L.J. Fingersh, D.W. Jager, J.R. Cotrell, S. Schreck, and S.M. Larwood. Unsteady aerodynamics experiment phase vi: wind tunnel test configurations and available data campaigns. Technical Report NREL/TP-500-29955, NREL, Golden, CO., USA, December 2001.

[84] A.C. Hansen. Yaw dynamics of horizontal axis wind turbines. Technical Report NREL/TP-442-4822, National Renewable Energy Laboratory, Golden, CO., USA, 1992.

[85] M.O.L. Hansen. *Aerodynamics of wind turbines*. James & James Ltd, London, UK, 2000.

[86] M.O.L. Hansen, J.N. Sørensen, S. Voutsinas, N. Sørensen, and H.Aa. Madsen. State of the art in wind turbine aerodynamics and aeroelasticity. *Progress in aerospace sciences*, Vol. 42:285–330, 2006.

[87] M.O.L. Hansen, N.N. Sørensen, J.N. Sørensen, and J.A. Michelsen. Extraction of lift, drag and angle of attack from computed 3-d viscous flow around a rotating blade. In *EWEC 1997*, pages 499–501, Dublin, Ireland, October 1997.

[88] M.O.L. Hansen, N.N. Sørensen, J.N. Sørensen, and J.A. Michelsen. A global navier-stokes rotor prediction model, aiaa-1997-0970. In *35th AIAA Aerospace Sciences Meeting and Exhibit*, Reno, NV., USA, January 1997.

[89] E. Hau. *Windkraftanlagen*. Springer Verlag, Berlin, New York, 1988.

[90] H. Himmelskamp. *Profiluntersuchungen an einem umlaufenden Propeller (Profile Investigations on a Rotating Airscrew)*. PhD thesis, University of Göttingen, Göttingen, Germany, 1945.

[91] J.G. Holierhoek. *Aeroelasticity of large wind turbines.* PhD thesis, Delft University of Technology, Delft, The Netherlands, 2008.

[92] Y. Hua, W.Z. Shen, J.N. Sørensen, and W.J. Zhu. Determination of the angle of attack on the mexico rotor using experimental data. In *The Science of Making Torque from Wind*, Heraklion, Crete, Greece, June 2010.

[93] M.K. Hubbert. Nuclear energy and the fossil fuels. *American Petroleum Institute Drilling and Production Practice*, Vol. 23:7–25, 1956.

[94] M. Iida, C. Arakawa, and H. Matsumiya. Three dimensional navier-stokes flow-field computations through horizontal axis wind turbine blade, aiaa-2001-0058. In *39th AIAA Aerospace Sciences Meeting and Exhibit, 20th ASME Wind Energy Symposium*, Reno, NV., USA, January 2001.

[95] S. Ivanell. *Numerical Computations of Wind Turbine Wakes.* PhD thesis, Linné Flow Centre, KTH Mechanics, Stockholm, Sweden, 2009.

[96] S. Ivanell, R. Mikkelsen, J.N. Sørensen, and D. Henningson. Numerical analysis of the tip and root vortex position in the wake of a wind turbine. *Journal of Physics: Conference Series*, Vol. 75, 2007.

[97] S. Ivanell, R. Mikkelsen, N.J. Sørensen, and D. Henningson. Three-dimensional actuator disc modeling of wind farm wake interaction. In T. Chaviaropoulos, editor, *The proceedings of the European wind energy conference and exhibition EWEC 2008 Brussels*, Brussels, Belgium, 2008. EWEC.

[98] S. Ivanell, R.F. Mikkelsen, J.N. Sørensen, and D. Henningson. Stability analysis of the tip vortices of a wind turbine, aiaa-2008-1322. In *46th AIAA Aerospace Sciences Meeting and Exhibit*, Reno, NV., USA, January 2008.

[99] E.N. Jacobs and A. Sherman. Airfoil section characteristics as affected by variations of the reynolds number. Technical Report NACA-TR-586, NACA, Langley Field, VA., USA, 1937.

[100] N.E. Joukowsky. Windmill of the nej type. *Transactions of the Central Institute for Aero-Hydrodynamics of Moscow*, 1920.

[101] J. Katz and A. Plotkin. *Low-Speed Aerodynamics.* Cambridge University Press, Cambridge, England, 2001.

[102] D. Kocurek. Lifting surface performance analysis for horizontal axis wind turbines. Technical Report NREL/STR-217-3163, National Renewable Energy Laboratory, Golden, CO., USA, 1987.

[103] G.A.M. van Kuik. *On the limitations of Froude's actuator disc concept.* PhD thesis, Eindhoven University of Technology, Eindhoven, The Netherlands, 1991.

[104] G.A.M. van Kuik. The lanchester-betz-joukowsky limit. *Wind Energy*, Vol. 10:289–291, 2007.

[105] F.W. Lanchester. A contribution to the theory of propulsion and the screw propeller. *Transaction of the Institution of Naval Architects*, Vol. 56:98–116, 135–153, 1915.

[106] G.C. Larsen, H. Aa. Madsen, K. Thomsen, and T.J. Larsen. Wake meandering: a pragmatic approach. *Wind Energy*, Vol. 11, Issue 4:377–395, 2008.

[107] C. Leclerc and C. Masson. Predictions of aerodynamic performances and loads of hawts operating in severe unsteady conditions. *AIAA-paper*, 1999-0066, 1999.

[108] J.G. Leishman. Seed particle dynamics in tip vortex flows. *Journal of aircraft*, Vol. 33:823–825, 1996.

[109] J.G. Leishman. *Principles of Helicopter Aerodynamics.* Cambridge University Press, Cambridge, England, 2000.

[110] J.G. Leishman. Challenges in modelling the unsteady aerodynamics of wind turbines. *Wind Energy*, 5:85–132, april-september 2002.

[111] J.G. Leishman and A. Bagai. Challenges in understanding the vortex dynamics of helicopter rotor wakes. *AIAA journal*, Vol. 36, Issue 7:1130–1140, July 1998.

[112] J.G. Leishman, A. Baker, and A. Coyne. Measurements of rotor tip vortices using three-component laser doppler velocimetry. *Journal of the American Helicopter Society*, Vol. 41, No. 4:342–353, 1996.

[113] J.G. Leishman and T.S. Beddoes. A generalised model for airfoil unsteady aerodynamic behaviour. In *42nd. Annual Forum of the American Helicopter Society*, pages 243–265, Washington, DC., USA, June 1986.

[114] J.G. Leishman and T.S. Beddoes. A semi-empirical model for dynamic stall. *Journal of the American Helicopter Society*, 34:3–17, July 1989.

256

[115] David JC MacKay. *Sustainable energy without the hot air*. UIT Cambridge Ltd., Cambridge, England, 2008.

[116] H. A. Madsen, N.N. Sorensen, and S. Schreck. Yaw aerodynamics analyzed with three codes in comparison with measurements. *AIAA-paper*, 2003-0519:94–103, 2003.

[117] C. Masson and C. Sibuet Watters. Moving actuator surfaces: a new concept for wind turbine aerodynamic analysis. In *Internacional Conference on Renewable Energies and Power Quality ICREP08*, Santander, Spain, March 2008.

[118] F. Massouh and I. Dobrev. Investigation of wind turbine near wake. In *International conference on jets, wakes and separated flows, ICJWSF-2005*, Toba-shi, Mie, Japan, October 2005.

[119] F. Massouh, I. Dobrev, and M. Rapin. Experimental and numerical survey in the wake of a wind turbine, aiaa-2007-0423. In *26th ASME Wind Energy Symposium, 45th AIAA Aerospace Sciences Meeting and Exhibit*, Reno, NV., USA, January 2007.

[120] E.H.M. Mast. Estimating the circulation distribution using near wake velocity measurements, we03190. Master's thesis, Wind Energy, Delft University of Technology, Delft, The Netherlands, 2003.

[121] E.H.M. Mast, G.A.M. van Kuik, and M.B. Zaayer. Offshore wind energy policies and their effects: Experiences in denmark and the uk and prospects for the netherlands. In T. Chaviaropoulos, editor, *Proceedings of the 2007 European Wind Energy Conference & Exhibition in Milan*, pages 1–10, Brussels, Belgium, May 2007. EWEA.

[122] E.H.M. Mast, L.J. Vermeer, and G.J.W. van Bussel. Estimation of the circulation distribution on a rotor blade from detailed near wake velocities. *Wind Energy*, Vol. 7, No. 3:189–209, July/September 2004.

[123] D. Medici and P.H. Alfredsson. Measurements on a wind turbine wake: 3d effects and bluff body vortex shedding. In *The science of making torque from wind*, Delft, The Netherlands, April 2004.

[124] D. Medici and P.H. Alfredsson. Measurements on a wind turbine wake: 3d effects and bluff body vortex shedding. *Wind Energy*, Vol. 9:219–236, 2006.

[125] D. Medici and P.H. Alfredsson. Measurements behind model turbines: further evidence of wake meandering. *Wind Energy*, Vol. 11, Issue 2:211–217, 2008.

[126] J.A. Michelsen. Basis3d - a platform for development of multiblock pde solvers. Technical Report Report AFM-92-05, Department of Fluid Mechanics, Technical University of Denmark, Lyngby, Denmark, 1992.

[127] J.A. Michelsen. Block structured multigrid solution of 2d and 3d elliptic pde's. Technical Report Report AFM-94-06, Department of Fluid Mechanics, Technical University of Denmark, Lyngby, Denmark, 1994.

[128] R. Mikkelsen. *Actuator disc methods applied to wind turbines*. PhD thesis, Technical University of Denmark, Lyngby, Denmark, June 2003.

[129] R. Mikkelsen and J.N. Sørensen. Yaw analysis using a numerical actuator disc model. In *14th. IEA Symposium on the Aerodynamics of Wind Turbines*, pages 53–59, Boulder, CO., USA, January 2001.

[130] R. Mikkelsen, J.N. Sørensen, and W.Z. Shen. Modelling and analysis of the flow field around a coned rotor. *Wind Energy*, Vol. 4:121–135, 2001.

[131] R. Mikkelsen, J.N. Sørensen, and N. Troldborg. Analysis of power enhancement for a row of wind turbines using the actuator line technique. *Journal of Physics: Conference Series*, Vol. 75, 2007.

[132] B. Montgomerie and J-Å Dahlberg. Vortex system studies on small wind turbines. Technical Report FOI-R–0936–SE, ISSN 1650-1942, FOI, Stockholm, Sweden, September 2003.

[133] X. Munduate and Frank N. Coton. Identification of dynamic stall regions on horizontal axis wind turbines, aiaa-2000-0039. In *19th ASME Wind Energy Symposium, 38th Aerospace Sciences Meeting and Exhibit*, pages 168–171, Reno, NV., USA, January 2000.

[134] W.L. Oberkampf and T.G. Trucano. Verification and validation in computational fluid dynamics. *Progress in Aerospace Sciences*, Vol. 38:209–272, 2002.

[135] S. Øye. Dynamic stall simulated as time lag of separation. In U.F. McAnulty, editor, *Proceedings of the 4th IEA Symposium on the Aerodynamics of Wind Turbines*, Rome, Italy, November 1991. IEA.

[136] S. Øye. In J.G. Schepers, editor, *Minutes of the 12th plenary meeting of the Joule project joint investigation of dynamic inflow effects, ECN-DE-Memo-94-50*, Petten, The Netherlands, July 1994.

[137] P. Parkin, R. Holm, and D. Medici. The application of piv to the wake of a wind turbine in yaw. In *Proceedings of the 4th International Symposium on Particle Image Velocimetry*, Gottingen, Germany, September 2001.

[138] S.D. Pesmajoglou and J.M.R. Graham. Prediction of aerodynamic forces on horizontal axis wind turbines in free yaw and turbulence. *Journal of wind engineering and industrial aerodynamics*, Vol. 86:1–14, 2000.

[139] K.G. Pierce. Wind turbine load prediction using the beddoes-leishman model for unsteady aerodynamics and dynamic stall. Master's thesis, The University of Utah, Salt Lake City, UT., USA, 1996.

[140] D.M. Pitt and D.A. Peters. Theoretical predictions of dynamic inflow derivatives. *Vertica*, Vol. 5, No. 1:21–34, 1981.

[141] R.D. Preuss, E.O. Suciu, and L. Morino. Unsteady potential aerodynamics of rotors with applications to horizontal axis windmills. *AIAA Journal*, Vol. 18, No. 4:385–393, 1980.

[142] J.W.M. Rankine. On the mechnical principles of the action of propellers. *Transaction of the Institute of Naval Architects*, Vol. 6:13–39, 1865.

[143] D.J. Robison, F.N. Coton, R.A.McD. Galbraith, and M. Vezza. Application of a prescribed wake aerodynamic prediction scheme to horizontal axis wind turbine in axial flow. *Wind Engineering*, Vol. 19, Issue 1, 1995.

[144] D.J. Robison, F.N. Coton, R.A.McD. Galbraith, and M. Vezza. The development of a prescribed wake model for performance prediction in steady yawed flow. In *Proceedings of the 14th ASME/ETCE wind energy symposium*, Houston, TX., USA, 1996.

[145] G. Ronsten. Static pressure measurements on a rotating and a non-rotating 2.375 m wind turbine blade. *Journal of wind engineering and industrial aerodynamics*, Vol. 39:105–118, 1992.

[146] R.P.J.O.M. van Rooij, W.A. Timmer, and A. Bruining. Determination of the local inflow angle on rotating blades. In *Proceedings of the World Wind Energy Conference and Exhibition*, Berlin, Germany, July 2002.

[147] T. Sant. *Improving BEM-based aerodynamic models in wind turbine design codes*. PhD thesis, Delft University of Technology, Delft, The Netherlands, 2007.

[148] T. Sant, G. van Kuik, and G. van Bussel. Using near wake measurements to improve bem engineering models for yawed wind turbines. In *2004 European Wind Energy Conference & Exhibition*, pages 117–123, London, England, November 2004.

[149] T. Sant, G.A.M. van Kuik, and G.J.W. van Bussel. Estimating the angle of attack from blade pressure measurements on the nrel phase vi rotor

259

using a free wake vortex model: axial conditions. *Wind Energy*, Vol. 9, No. 6:549–577, November/December 2006.

[150] T. Sant, G.A.M. van Kuik, and G.J.W. van Bussel. Estimating the angle of attack from blade pressure measurements on the national renewable energy laboratory phase vi rotor using a free wake vortex model: yawed conditions. *Wind Energy*, Vol. 12, No. 1:1–32, January 2009.

[151] G. Schepers, K. Boorsma, and H. Snel. Iea task 29 mexnext: analysis of wind tunnel measurements from the eu project mexico. In *The Science of Making Torque from Wind*, Heraklion, Crete, Greece, June 2010.

[152] J.G. Schepers. An engineering model for yawed conditions, developed on basis of wind tunnel measurements. *AIAA-paper*, 1999-0039:164–174, 1999.

[153] J.G. Schepers. Annexlyse: validation of yaw models, on basis of detailed aerodynamic measurements on wind turbine blades. Technical Report ECN-C–04-097, ECN, Petten, The Netherlands, September 2004.

[154] J.G. Schepers, A.J. Brand, A. Bruining, J.M.R. Graham, M.M. Hand, D.G. Infield, H.A. Madsen, T. Maeda, J.H. Paynter, R. van Rooij, Y. Shimizu, D.A. Simms, and N. Stefanatos. Final report of the iea annex xviii: enhanced field rotor aerodynamics database. Technical Report ECN-C–02-016, ECN, Petten, The Netherlands, February 2002.

[155] J.G. Schepers, A.J. Brand, A. Bruining, J.M.R. Graham, M.M. Hand, D.G. Infield, H.A. Madsen, R.J.H. Paynter, and D.A. Simms. Final report of the iea annex xiv: field rotor aerodynamics. Technical Report ECN-C–97-027, ECN, Petten, The Netherlands, May 1997.

[156] J.G. Schepers, L. Pascal, and H. Snel. First results from mexnext: analysis of detailed aerodynamic measurements on a 4.5 m diameter rotor placed in the large german dutch wind tunnel dnw. In *EWEC*, Warsaw, Poland, April 2010.

[157] J.G. Schepers and H. Snel. Dynamic inflow: yawed conditions and partial span pitch control. Technical Report ECN-C–95-056, ECN, Petten, The Netherlands, October 1995.

[158] J.G. Schepers and H. Snel. model experiments in controlled conditions. Technical Report ECN-E–07-042, ECN, Petten, The Netherlands, February 2007.

[159] J.G. Schepers and R.P.J.O.M. van Rooij. Final report of the annexlyse project - analysis of aerodynamic field measurements on wind turbines. Technical Report ECN-C–05-064, ECN, Petten, The Netherlands, June 2005.

[160] S. Schmitz and J.J. Chattot. A parallelized coupled navier-stokes/vortex-panel solver. *Journal of Solar Energy Engineering*, Vol. 127, No. 4:475–487, November 2005.

[161] S. Schreck. final report iea wind annex xx: Hawt aerodynamics and models from wind tunnel measurements. Technical Report also published under NREL/TP-500-43508, IEA wind, Vienna, Austria, December 2008.

[162] S. Schreck and M. Robinson. Rotational augmentation of horizontal axis wind turbine blade aerodynamic response. *Wind Energy*, 5:133–150, April-September 2002.

[163] S. Schreck and M. Robinson. Rotational augmentation of horizontal axis wind turbine blade aerodynamic response, aiaa-2002-0029. In *21th ASME Wind Energy Symposium, 40th AIAA Aerospace Sciences Meeting and Exhibit*, Reno, NV., USA, January 2002.

[164] S. Schreck, M. Robinson, M. Hand, and D. Simms. Hawt dynamic stall response asymmetries under yawed flow conditions. *Wind Energy*, 3:215–232, October-December 2000.

[165] S. Schreck, T. Sant, and D. Micallef. Rotational augmentation disparities in the mexico and uae phase vi experiments. In *The Science of Making Torque from Wind*, Heraklion, Crete, Greece, June 2010.

[166] S.J. Schreck, M.C. Robinson, M.M. Hand, and D.A. Simms. Blade dynamic stall vortex kinematics for a horizontal axis wind turbine in yawed conditions. *Journal of Solar Energy Engineering*, 123:272–281, November 2001.

[167] W.Z. Shen, M.O.L. Hansen, and J.N. Sørensen. Determination of angle of attack (aoa) for rotating blades. In *EUROMECH Colloquium 464b Wind Energy*, Oldenburg, Germany, October 2005.

[168] W.Z. Shen, R. Mikkelsen, and J.N. Sørensen. Tip loss corrections for wind turbine computations. *Wind Energy*, Vol. 8, Issue 4:457–475, 2005.

[169] W.Z. Shen, J.N. Sørensen, and R. Mikkelsen. Tip loss correction for actuator/navier-stokes computations. *Journal of Solar Energy Engineering*, Vol. 127, No. 2:209–213, May 2005.

[170] W. Sheng, R.A. Galbraith, and F.N. Coton. Improved dynamic-stall-onset criterion at low mach numbers. *Journal of Aircraft*, Vol. 44, No. 3:1049–1052, 2007.

[171] W. Sheng, R.A.McD. Galbraith, and F.N. Coton. A new stall-onset criterion for low speed dynamic-stall. *Journal of Solar Energy Engineering*, Vol. 128:461–471, November 2006.

[172] W. Sheng, R.A.McD. Galbraith, and F.N. Coton. A modified dynamic stall model for low mach numbers, aiaa-2007-0626. In *26th ASME Wind Energy Symposium, 45th AIAA Aerospace Sciences Meeting and Exhibit*, Reno, NV., USA, January 2007.

[173] D. Simms, S. Schreck, M. Hand, and L.J. Fingersh. Nrel unsteady aerodynamics experiment in the nasa-ames wind tunnel: A comparison of predictions to measurements. Technical Report NREL/TP-500-29494, NREL, Boulder, CO., USA, June 2001.

[174] D.A. Simms, M.M. Hand, L.J. Fingersh, and D.W. Jager. Unsteady aerodynamics experiment phases ii-iv test configurations and available data campaigns. Technical Report NREL/TP-500-25950, NREL, Golden, CO., USA, July 1999.

[175] H. Snel. Review of the present status of rotor aerodynamics. *Wind Energy*, 1:46–69, april 1998.

[176] H. Snel. Survey of induction dynamics modelling within bem-like codes: dynamic inflow and yawed flow modelling revisited, aiaa-2001-0027. In *20th ASME Wind Energy Symposium, 39th AIAA Aerospace Sciences Meeting and Exhibit*, Reno, NV., USA, January 2001.

[177] H. Snel. Review of aerodynamics for wind turbines. *Wind Energy*, 6, Issue 3:203–211, July/September 2003.

[178] H. Snel. A short history of wind turbine aerodynamics, or: From betz to better. In *The Science of Making Torque from Wind*, Lyngby, Denmark, August 2007.

[179] H. Snel and J.G. Schepers. Joint investigation of dynamic inflow effects and implementation of an engineering method. Technical Report ECN-C–94-107, ECN, Petten, The Netherlands, April 1995.

[180] H. Snel and J.G. Schepers. The mexico project: analysis of yaw measurement and comparison with existing models. In T. Chaviaropoulos, editor, *Proceedings of the 2008 European Wind Energy Conference & Exhibition in Brussels*, Brussels, Belgium, 31 March - 3 April 2008. EWEA.

[181] H. Snel, J.G. Schepers, and B. Montgomerie. The mexico project (model experiments in controlled conditions): The database and first results of data processing and interpretation. *Journal of Physics: Conference Series*, Vol. 75:012014, 2007.

[182] H. Snel, J.G. Schepers, and B. Montgomerie. The mexico project (model experiments in controlled conditions): The database and first results of data processing and interpretation. In *The Science of Making Torque from Wind*, Lyngby, Denmark, August 2007.

[183] J. N. Sørensen. Aerodynamic aspects of wind energy conversion. *Annual review of fluid mechanics*, Vol. 43:427–448, 2011.

[184] J.N. Sørensen and R. Mikkelsen. On the validity of the blade element momentum method. In *European Wind Energy Conference*, pages 362–366, Copenhagen, Denmark, 2001.

[185] J.N. Sørensen and V. Okulov. modelling of the far wake behind a wind turbine. In J. Peinke, P. Schaumann, and S. Barth, editors, *Proceedings of the Euromech colloquium on wind energy*, pages 245–248, Oldenburg, Germany, October 2006.

[186] J.N. Sorensen and W.Z. Shen. Numerical modeling of wind turbine wakes. *Journal of Fluids Engineering*, 124:393–399, June 2002.

[187] J.N. Sørensen, W.Z. Shen, and R. Mikkelsen. Wall correction model for wind tunnels with open test section. In *The Science of Making Torque from Wind*, Delft, The Netherlands, April 2004.

[188] J.N. Sorensen, W.Z. Shen, and X. Munduate. Analysis of wake states by a full-field actuator disc model. *Wind Energy*, 1:73–88, December 1998.

[189] N.N. Sørensen. *General purpose flow solver applied to flow over hills*. PhD thesis, Risø National Laboratory, Roskilde, Denmark, 1995.

[190] N.N. Sørensen and M.O.L. Hansen. Rotor performance predictions using a navier-stokes method, aiaa-1998-0025. In *36th AIAA Aerospace Sciences Meeting and Exhibit, 17th ASME Wind Energy Symposium*, Reno, NV., USA, January 1998.

[191] N.N. Sørensen, J.A. Michelsen, and S. Schreck. Navier-stokes predictions of the nrel phase vi rotor in the nasa ames 80 ft 120 ft wind tunnel. *Wind Energy*, Vol. 5:151–169, 2002.

[192] A.H.P. Swift. *The effects of yawed flow on wind turbine rotors*. PhD thesis, Washington University, St Louis, MO, 1981.

[193] J.L. Tangler. The nebulous art of using wind tunnel aerofoil data for predicting rotor performance. *Wind Energy*, Vol. 5, No. 2-3:245–257, April - September 2002.

[194] J.L. Tangler. Insight into wind turbine stall and post-stall aerodynamics. *Wind Energy*, Vol. 7:247–260, 2004.

[195] S. Toet and L.J. Vermeer. Modificaties blaaspijp instituut voor windenergie en beschrijving huidige situatie. Technical Report IW-91049M, Instituut voor Windenergie, Delft University of Technology, Delft, The Netherlands, September 1991.

[196] C. Tongchitpakdee, S. Benjanirat, and L.N. Sankar. Numerical simulation of the aerodynamics of horizontal axis wind turbines under yawed flow conditions. *Journal of Solar Energy Engineering*, Vol. 127, No. 4:464–474, November 2005.

[197] N. Troldborg. *Actuator line modeling of wind turbine wakes*. PhD thesis, Technical University of Denmark, Lyngby, Denmark, June 2008.

[198] N. Troldborg, J.N. Sørensen, and R. Mikkelsen. Actuator line simulation of wake of wind turbine operating in turbulent inflow. *Journal of Physics: Conference Series*, Vol. 75:012063, 2007.

[199] N. Troldborg, J.N. Sørensen, and R. Mikkelsen. Numerical simulations of wake characteristics of a wind turbine in uniform inflow. *Wind Energy*, Vol. 13, No. 1:86–99, 2010.

[200] G.H. Vatistas, V. Kozel, and W.C. Mih. A simpler model for concentrated vortices. *Experiments in Fluids*, Vol. 11, No. 1:73–76, 1991.

[201] H.F. Veldkamp. *Chances in Wind Energy. A probabilistic approach to wind turbine fatigue design*. PhD thesis, Delft University of Technology, Delft, The Netherlands, 2006.

[202] L.J. Vermeer. A review of wind turbine wake research at tudelft, aiaa-2001-0030. In *20th ASME Wind Energy Symposium, 39th Aerospace Sciences Meeting and Exhibit*, pages 1–11, Reno, NV., USA, January 2001.

[203] L.J. Vermeer and J.K. de Boer. Wake structure of a rotor model in yaw. In *EWEC*, Lűbeck-Traveműnde, Germany, March 1993.

[204] L.J. Vermeer, J.N. Sørensen, and A. Crespo. Wind turbine wake aerodynamics. *Progress in Aerospace Sciences*, 39/6-7:467–510, August-October 2003.

[205] L.J. Vermeer and W.A. Timmer. Identification of operational aerofoil state by means of velocity measuments. In *Proceedings of 1999 European Wind Energy Conference*, pages 168–171, Nice, France, March 1999.

[206] N. Vermeer. A new rotor model for aerodynamic measurements in the improved open jet wind tunnel. In *National Wind Energy Conference 1990*, pages 441–445, Lunteren, The Netherlands, 1990.

[207] N-J Vermeer. Local circulation on rotating wind turbine blades from velocity measurements in the wake of a model rotor. In *Proceedings of the 14th British Wind Energy Association Conference*, pages 117–121, Nottingham, England, March 1992.

[208] N-J. Vermeer and G.J.W. van Bussel. Velocity measurements in the near wake of a model rotor and comparison with theoretical results. In *1990 European Community Wind Energy Conference Proceedings*, pages 218–222, Madrid, Spain, September 1990.

[209] O. de Vries. Fluid dynamic aspects of wind energy conversion. Technical Report AGARD-AG-243, AGARD, Neuilly sur Seine, France, 1979.

[210] O. de Vries. wind-tunnel tests on a model of a two-bladed horizontal axis wind turbine and evaluation of an aerodynamic performance calculation method. Technical Report TR 79071 L, NLR, Amsterdam, The Netherlands, June 1979.

[211] J. Wale, C.J. Fisichella, and M.S. Selig. Correcting inflow measurements from wind turbines using a lifting-surface code. *Journal of solar energy engineering*, Vol. 122:196–202, 2000.

[212] T. Wang and F.N. Coton. Prediction of the unsteady aerodynamic characteristics of horizontal axis wind turbines including three-dimensional effects. *proc. of the institution of mechanical engineers, part a, journal of power and energy*, 214:385–400, 2000.

[213] J. Whale, C.G. Anderson, R. Bareiss, and S. Wagner. An experimental and numerical study of the vortex structure in the wake of a wind turbine. *Journal of Wind Engineering and Industrial Aerodynamics*, Vol. 84:1–21, 2000.

[214] F.M. White. *Viscous Fluid Flow, Second Edition*. McGraw-Hill, New York, NY., USA, 1991.

[215] R.E. Wilson and P.B.S. Lissaman. Applied aerodynamics of wind-power machines. Technical Report NTIS: PB-238-595, Oregon State University, Portland, OR., USA, 1974.

[216] G. Xu and L.N. Sankar. Computational study of horizontal axis wind turbines, aiaa-1999-0042. In *37th AIAA Aerospace Sciences Meeting and Exhibit, 18th ASME Wind Energy Symposium*, Reno, NV., USA.

[217] G. Xu and L.N. Sankar. Effects of transition, turbulence and yaw on the performance of horizontal axis wind turbines, aiaa-2000-0048. In *46th AIAA Aerospace Sciences Meeting and Exhibit*, Reno, NV., USA, January 2000.

[218] W-J. Yang. *Handbook of Flow Visualization.* Hemispere, New York, NY., USA, 1989.

[219] F. Zahle. *Wind Turbine Aerodynamics Using an Incompressible Overset Grid Method.* PhD thesis, Imperial College, London, England, 2006.

Author publications

Journal Articles

[1] W. Haans, T. Sant, G.A.M. van Kuik and G.J.W. van Bussel. Measurement of Tip Vortex Paths in the Wake of a HAWT Under Yawed Flow Conditions, *Journal of Solar Energy Engineering*, Vol. 127, No. 4:456 - 463, November 2005.

[2] W. Haans, T. Sant, G.A.M. van Kuik and G.J.W. van Bussel. Stall in Yawed Flow Conditions: A Correlation of Blade Element Momentum Predictions With Experiments. *Journal of Solar Energy Engineering*, Vol. 128, No. 4:472 - 480, November 2006

[3] W. Haans, T. Sant, G.A.M. van Kuik and G.J.W. van Bussel. HAWT Near Wake Aerodynamics, Part I: Axial Flow Conditions. *Wind Energy*, published online 7 January.

[4] W. Haans, G.A.M van Kuik and G.J.W. van Bussel. The inverse vortex wake model: a measurement analysis tool. *Journal of Solar Energy Engineering*, Vol. X, No. X, August 2008.

[5] W. Haans, T. Sant, G.A.M. van Kuik and G.J.W. van Bussel. HAWT Near Wake Aerodynamics, Part II: Yawed Flow Conditions. *Wind Energy*, under review.

Conference Proceedings

[1] W. Haans, H. Bijl, M.I. Gerritsma and B.W. van Oudheusden. Small scale flow phenomena of hole-suction type laminar flow control sailplanes. AIAA-2004-2312. In *2nd AIAA Flow Control Conference*, Portland, OR, June-July 2004.

[2] W. Haans, T. Sant, G.A.M van Kuik and G.J.W. van Bussel. Measurement and Modelling of Tip Vortex Paths in the Wake of a HAWT under Yawed Flow Conditions, AIAA-2005-0590. In *24rd ASME Wind Energy Symposium, 43th AIAA Aerospace Sciences Meeting and Exhibit*, pages 136 - 145, Reno, NV, January, 2005.

[3] W. Haans, T. Sant, G.A.M. van Kuik and G.J.W. van Bussel. Hotfilm anemometry in the wake of a HAWT. In *proceedings of the IEA Annex XI/XX experts meeting*, Pamplona, Spain, 2005.

[4] W. Haans, T. Sant, G.A.M. van Kuik and G.J.W. van Bussel. Velocity Measurements in the Near Wake of a Horizontal Axis Wind Turbine. In *31st European Rotorcraft Forum*, pages 61.1 - 61.14, Florence, Italy, September 2005.

[5] T. Sant, W. Haans, G.A.M. van Kuik and G.J.W. van Bussel. An approach for the verification and validation of rotor aerodynamics codes based on free-wake vortex methods. In *31st European Rotorcraft Forum*, Florence, Italy, September 2005.

[6] W. Haans, T. Sant, G.A.M. van Kuik and G.J.W. van Bussel. Stall in Yawed Flow Conditions: a Correlation of Blade Element Momentum Predictions with Experiments, AIAA-2006-0200. In *25th ASME Wind Energy Symposium, 44th AIAA Aerospace Sciences Meeting and Exhibit*, Reno, NV, January 2006.

[7] W. Haans, G.A.M. van Kuik and G.J.W. van Bussel. The near wake behind a model rotor: measurements and computations. In *proceedings of the IEA Annex XI/XX experts meeting*, Kiel, Germany, 2006.

[8] W. Haans, G.A.M. van Kuik and G.J.W. van Bussel. Analysis of rotor wake measurements with the inverse vortex wake model. In *proceedings of the 2nd EAWE PhD seminar on Wind Energy in Europe*, Roskilde, Denmark, 2006.

[9] W. Haans, G.A.M. van Kuik and G.J.W. van Bussel. The inverse vortex wake model: a measurement analysis tool, AIAA-2007-0422. In *26th ASME Wind Energy Symposium, 45th AIAA Aerospace Sciences Meeting and Exhibit*, Reno, NV, January 2007.

268

[10] W. Haans and R. Mikkelsen. Airfoil models in the actuator line code assessed with near-wake measurements on a yawed rotor, AIAA-2007-0424. In *26th ASME Wind Energy Symposium, 45th AIAA Aerospace Sciences Meeting and Exhibit*, Reno, NV, January 2007.

[11] W. Haans, G.A.M van Kuik and G.J.W. van Bussel. Experimentally observed effects of yaw misalignment on the inflow in the rotor plane. *Journal of Physics: Conference Series*, Vol. 75:012012, 2007.

[12] G. Politakis, G. van Bussel, G. van Kuik and W. Haans. Suppression of classical flutter using a 'smart' blade. AIAA-2008-1301. In *27th ASME Wind Energy Symposium, 46th AIAA Aerospace Sciences Meeting and Exhibit*, Reno, NV, January 2008.

Book Contributions

[1] W. Haans and G.J.W. van Bussel. Wind tunnel experiments on rotors and near wakes. Chapter in *VKI Lecture Series 'Wind turbines: a state-of-the-art'*, Rhode-St Genese, Belgium, 2007.

Curriculum vitae

Wouter Haans was born on February 21, 1978, in Haaren, The Netherlands, growing up with a younger sister and brother. In 1996, he obtained his high school diploma at the Maurick College (Gymnasium) in Vught, ranking in the top 3 of the school. That same year, he started his Masters in Aerospace Engineering at the Delft University of Technology. He ended the propaedeutic year *cum laude*. His studies included an internship at the aerodynamics department of Airbus in their Filton, UK site. In 2003, he obtained his MSc from the Aerodynamics group. His master thesis resulted in a publication in the proceedings of the second AIAA flow control conference.

In November 2003, he started his PhD research at the Wind Energy group of the Faculty of Civil Engineering, now located at Aerospace Engineering, of the TUDelft, under supervision of Gijs van Kuik and Gerard van Bussel. The work on rotor aerodynamics in yaw was organized as part of a duo PhD project together with Tonio Sant. Four journal articles, eleven conference proceedings an a course in rotor aerodynamics later, he left university end of 2007 with an unfinished thesis.

Early 2008, he joined General Electric to work on conceptual design for their wind energy division in Salzbergen, Germany. After two years of commuting to and from The Hague, his next career move took him to Garrad Hassan in 2010, where he currently works as an engineering consultant, advising clients on rotor aerodynamics and conceptual design.

Working in evening hours, weekends and holidays, he finished his PhD thesis in 2011. He lives in The Hague together with Irene and the product of their love; Valérie and Philippe.